SYNAPTIC VESICLE CYCLE AT NANO-RESOLUTION

by

Shigeki Watanabe

A dissertation submitted to the faculty of
The University of Utah
in partial fulfillment of the requirements for the degree of

Doctor of Philosophy

Department of Biology

The University of Utah

May 2013

The University of Utah Graduate School

STATEMENT OF DISSERTATION APPROVAL

The dissertation of **Shigeki Watanabe**

has been approved by the following supervisory committee members:

Erik M. Jorgensen	, Chair	**12/13/2012** Date Approved
Michael Bastiani	, Member	**12/13/2012** Date Approved
Adam Frost	, Member	**12/13/2012** Date Approved
Edward J. King	, Member	**12/13/2012** Date Approved
Robert Marc	, Member	**12/13/2012** Date Approved

and by **Neil J. Vickers** , Chair of

the Department of **Biology**

and by Donna White, Interim Dean of The Graduate School.

ABSTRACT

Electron microscopy can visualize synapses at nanometer resolution, and can thereby capture the fine structure of these contacts. However, this imaging method lacks three key elements: temporal information, protein visualization, and large volume reconstruction. For my dissertation, I developed three methods in electron microscopy that overcame these limitations. First, I developed a method to freeze neurons at any desired time point after a stimulus to study synaptic vesicle cycle. Second, I developed a method to couple super-resolution fluorescence microscopy and electron microscopy to pinpoint the location of proteins in electron micrographs at nanometer resolution. Third, I collaborated with computer scientists to develop methods for semi-automated reconstruction of nervous system.

I applied these techniques to answer two fundamental questions in synaptic biology. Which vesicles fuse in response to a stimulus? How are synaptic vesicles recovered at synapses after fusion? Only vesicles that are in direct contact with plasma membrane fuse upon stimulation. The active zone in *C. elegans* is broad, but primed vesicles are concentrated around the dense projection. Following exocytosis of synaptic vesicles, synaptic vesicle membrane was recovered rapidly at two distinct locations at a synapse: the dense projection

and adherens junctions. These studies suggest that there may be a novel form of ultrafast endocytosis.

TABLE OF CONTENTS

ACKNOWLEDGEMENTS

During my graduate work, I have received tremendous support from my thesis advisor, my committee members, my colleagues, my students, my collaborators, my friends, my family, and my girlfriend. First, I would like to thank Erik Jorgensen. I simply do not have enough space to list everything you did for me and cannot find any words to describe how thankful I am to have you as my thesis advisor. It was life-changing experience in your laboratory, and I will never forget my life in your laboratory. Your creativity and inspiration will shape my future scientific career. I would also like to thank my committee members, Michael Bastiani, Chi-Bin Chien, Adam Frost, Edward King, and Robert Marc for their guidance and their scientific inputs. I would like to send special thanks to Edward King for making sure that my body and "toys" are all healthy. I strongly wished that Chi-Bin were here to sign off my dissertation. I would like to thank the past and present members of the Jorgensen laboratory for scientific discussion and support: Amrita, Michael Ailion, Patrick Allaire, Ewa Bednarek, Eric Bend, Pin-An Chen, Wayne Davis, Catharine Dy, Carl Ebeling, Glen Ernstrom, Christian Frøkjær-Jensen, Manasa Gudheti, Marc Hammarlund, Hsiao-Fen Han, Robert Hobson, Mingyu Gu, Gunther Hollopeter, Edward Hujber, Maelle Jospin, Matthew Labella, Qiang Liu, Patrick McEachern, Sean Merrill, Yueqi Moon, Hoe Kam Ng, Paola Nix, Leo Parra, Kim Schuske, Matthew

Schwartz, Mark Palfreyman, Aude Peden, Randi Rawson, Robby Weimer, and Jamie White. Especially, I would like to thank Wayne for his creativity and guidance. I would not have been able to complete my thesis without your help. I would also like to send special thanks to Gunther, Rob, and Christian for providing me helpful advice and the worm strains; Michael, Glen, Marc, Mingyu, Maelle, Qiang, Kim, and Mark for working together on projects and being co-authors; Pin-An, Eddie, Hsio-Fen, Randi, and Kim for taking care of my cats while I was away; Carl and Manasa for helping me on the super-resolution imaging; and Robby for instructing me to become an electron microscopist. I would also like to warmly thank Becky McKean for supporting my mental health by taking care of all the administrative matters. I would also like to thank all the technicians and undergraduate research assistants who worked with me: Amrita, Yang Hui, Nels Jorgensen, Michael Prestgard-Duke, Jackson Richards, Nikita Thomas, and Changyu Zhu. I wish all of you the best in your future career. I would also like to acknowledge all my collaborators: Punge Annedore, Katrin Willig, and Stefan Hell for providing incredible images for my project; Elizabeth Jurrus, Jason Thummel, Tolga Tasdizen for the collaborations on the automated neuron tracing project; Skyler Jackman, Richard Kramer, Jason Pellettieri, Aljendro Sánchez Alvarado, Kang Shen and students in his laboratory, Gregory Oikonomou, Shai Shaham, Daniel Colon-Ramos, Zhiyong Shao, Jennifer Peterson, Daniel Choquet, Christian Rosenmund for allowing me to work on their projects; Joel Mancuso, Katya Rechav, and Michael Elbaum for providing serial-block face images; and Kent McDonald and Richard Fetter for providing helpful

advice and tips for electron microscopy. I would also like to thank Jean Stringfellow and the EMBO organization for providing financial support. I would also like to thank my friends who made my life enjoyable. I would like to specifically acknowledge Sarah Elliot for spending tremendous amount of time discussing science over coffee. I would also like to thank my parents, Yoshinobu and Yumiko Watanabe, and my siblings, Kaori, Nozomi, Toshihiko, and Shoya for understanding my decision to come to the States and being there for me whenever I need it. I am grateful that you are my family. I would also like to thank ShuShu and ChaCha for being so cute and relieving my stress. Finally and most importantly, I would like to thank my girlfriend, Diana Lee, for being with me for the entire time I was in the graduate school. You are the reason for my success. Thank you.

CHAPTER I

INTRODUCTION

If you touch a hot stove, you rapidly snap your hand away. This reflexive response is mediated by communication between neurons. Specifically, signals sent from sensory neurons activate motor neurons, which command muscles to contract. Communication between neurons, or neurotransmission, is fundamental for our behaviors. Neurotransmission is carried out by the release of chemical signals, neurotransmitters, from one neuron (presynaptic cell) at a contact site called the synapse. Neurotransmitters bind to receptors on the postsynaptic cell, modulating the activity of the target cell (Dale, 1914; Otto, 1921) The neurotransmitters are contained in membrane-bound organelles called synaptic vesicles (Hebb and Whittaker, 1958; Whittaker, 1959). These vesicles are clustered at presynaptic terminals (De Robertis and Bennett, 1954; de Robertis and Bennett, 1955; Palay and Palade, 1955) and fuse to the plasma membrane to release their neurotransmitter contents into the synaptic cleft (Heuser and Reese, 1981). This process is called exocytosis. The rate of exocytosis can be extremely high, reaching up to ~100-500 vesicles per second in some synapses (Kopp-Scheinpflug et al., 2008; Lorteije et al., 2009; Maeno-Hikichi et al., 2011). To sustain such high rates, synaptic vesicles are recycled

locally at the synapse. This process is called endocytosis. In this dissertation, two aspects of synaptic biology are investigated and discussed: functional organization of synaptic vesicles for exocytosis and mechanisms of endocytosis.

Synaptic vesicle exocytosis

Vesicle hypothesis of the transmitter release

The release of neurotransmitters from presynaptic terminals is quantal, meaning that the minimal postsynaptic response is unitary in size (Fatt and Katz, 1952). The ultrastructural analysis of synapses revealed membrane-bound organelles that are uniform in size (De Robertis and Bennett, 1954; de Robertis and Bennett, 1955; Palay and Palade, 1955). The appearance of such structures led to the hypothesis that synaptic vesicles are the storage organelles for neurotransmitters (Del Castillo and Katz, 1956). To test this model, Hebb and Whittaker purified synaptic vesicles from the cholinergic neurons of the electric organ of *Torpedo marmorata* and showed that acetylcholine was contained in the vesicles (Hebb and Whittaker, 1958). Kuffler and Yoshikami determined the amount of transmitters required for a quantum by the iontophoretic application of acetylcholine onto frog and snake muscles and estimated the number of transmitter molecules in each vesicle by determining the number of molecules required to generate a quantal current (Kuffler and Yoshikami, 1975). These results supported the model that synaptic vesicles contained neurotransmitters; however, how neurotransmitters were released from synaptic vesicles remained elusive.

Katz hypothesized that synaptic vesicles fuse to the plasma membrane for neurotransmission (Del Castillo and Katz, 1956). To test this model, frog neuromuscular junctions were stimulated, and the morphological change after synaptic transmission was observed by electron microscopy. These studies showed membrane turnover at the synapse following intensive repetitive stimulation (Ceccarelli et al., 1972; Heuser and Reese, 1973), suggesting that vesicles might undergo fusion and full collapse into the membrane. However, the fate of each vesicle at the moment of neurotransmission could not be determined due to the continuous transmitter release during the stimulation and delay in the fixation of tissues. To capture the synapse during transmitter release, Heuser and Reese developed a freeze-slammer, which was capable of freezing tissues following a single stimulus with a millisecond temporal resolution (Heuser et al., 1979). Using this device, Heuser and Reese demonstrated that synaptic vesicles fused to the plasma membrane for neurotransmission. Ceccarelli and his colleagues further showed that these morphological changes were correlated with the timing of the transmitter release measured by electrophysiology (Torri-Tarelli et al., 1985). Altogether, these experiments demonstrated that fusion of synaptic vesicles accounts for the quantal nature of synaptic transmission.

Synaptic vesicle pools

Synaptic vesicle fusion occurs in specialized sites at synapses, now called active zones (Couteaux and Pécot-Dechavassine, 1974). In the chemical synapse, exocytosis can occur following an action potential (Hodgkin and Huxley,

1936) or spontaneously at rest (Fatt and Katz, 1952). When an action potential arrives at the terminal, voltage-gated calcium channels open, allowing brief influx of calcium into the cell (Llinás et al., 1976, 1981). This rapid elevation of the internal calcium concentration induces the engagement of fusion machinery, resulting in the exocytosis of vesicles. These vesicles are called the readily-releasable pool of vesicles (Rosenmund and Stevens, 1996). Coherent transmitter release ensures the propagation of signals from one cell to another. On the other hand, spontaneous release occurs independent of an action potential (Fatt and Katz, 1952). Although these events may be vesicles that simply overcome the energy barrier to fusion, some argue that they play important roles at the synapse, including in maturation (Murphy et al., 1994), maintenance (McKinney et al., 1999; Verhage et al., 2000; Sutton et al., 2004) and facilitation of synapses (Jin et al., 2012). Spontaneous release may even trigger an action potential in some small postsynaptic neurons such as cerebellar interneurons (Carter and Regehr, 2002; Otsu and Murphy, 2003). Thus, two independent mechanisms for synaptic release seem to contribute differently to neuronal communication.

How are these two types of neurotransmission regulated? Both spontaneous and active release occur via synaptic vesicle fusion to the membrane. One potential mechanism is that synaptic vesicles committed to spontaneous or evoked release are organized into different pools at the synapse. Vesicles in the readily-releasable pool are thought to be touching or in the close association with the plasma membrane in the active zone (Stevens and

Tsujimoto, 1995; Schikorski and Stevens, 1997, 2001; Zenisek et al., 2000). The binding of calcium to the calcium sensor, synaptotagmin, is shown to be required for synchronous evoked release (Matthew et al., 1981; Perin et al., 1991; Brose et al., 1992). On the other hand, spontaneous release may draw vesicles from the reserve pool (Sara et al., 2005; Mathew et al., 2008; Fredj and Burrone, 2009; Chung et al., 2010) – a pool of vesicles that is not in close association with plasma membrane and is only mobilized during repetitive stimulation (Kuromi and Kidokoro, 2000; Rizzoli and Betz, 2005). Therefore, spontaneous and evoked release may be regulated by the differential morphological organization of vesicle pools. However, when recycling of synaptic vesicles is blocked, either spontaneous (Rizzoli and Betz, 2002) or evoked release (Ikeda and Bekkers, 2009) alone is capable of depleting synaptic vesicles completely from the terminal, indicating that there are no distinct pools. Consistent with this idea, several studies have shown that the same synaptic vesicles are used for both spontaneous and evoked release (Rizzoli and Betz, 2002; Groemer and Klingauf, 2007; Ikeda and Bekkers, 2009; Wilhelm et al., 2010).

In this dissertation, I investigated the morphological organization of spontaneous and evoked pools of vesicles in the neuromuscular junctions of *Caenorhabditis elegans* (Chapter 7). I developed a method to capture synaptic morphology during synaptic transmission or inhibition (Chapter 2). In brief, evoked neurotransmission was induced by the activation of channelrhodopsin, a light-activated cation channel (Nagel et al., 2002, 2003, 2005; Boyden et al., 2005). Spontaneous release was inhibited by the activation of halorhodopsin, a

light-activated chloride pump (Schobert and Lanyi, 1982; Zhang et al., 2007a). The synaptic morphology was captured immediately after the induction of evoked release or inhibition of spontaneous release using a high-pressure freezer. Using this technique, I found that the domain of spontaneous release and evoked release overlapped near presynaptic densities. Furthermore, exocytosis of synaptic vesicles was observed from a broader region likely due to the elevated calcium level in the terminal during the evoked release. These data suggest that the same vesicles are likely used for both types of neurotransmission and the amount of calcium influx may determine the number of synaptic vesicles that fuse.

Synaptic vesicle endocytosis

Following exocytosis, synaptic vesicles must be recycled locally at synapses. Synaptic vesicle proteins or precursors are generated in the cell body of neurons and transported to synapses. However, these processes are extremely slow, requiring hours to days. To sustain high rates of neurotransmission, neurons have developed a mechanism to recycle vesicles locally. This process is called synaptic vesicle endocytosis. Three models of endocytosis have been proposed based on the morphological analysis of stimulated neurons: clathrin-mediated endocytosis, kiss-and-run endocytosis, and bulk endocytosis.

Clathrin-mediated endocytosis

Clathrin-mediated endocytosis was first discovered by Heuser and Reese. To test the vesicle hypothesis, Heuser and Reese examined stimulated synapses by electron microscopy and found that vesicle membrane was incorporated into plasma membrane following repetitive stimulation and was retrieved ~20 s after stimulation (1973). Using a freeze-slammer (Heuser et al., 1979), they further demonstrated that synaptic vesicles progressively collapse into the plasma membrane over a period of 50 ms following a single stimulus (Heuser and Reese, 1981) and that vesicles were recovered at a distant site from active zones (Miller and Heuser, 1984). These results suggested that synaptic vesicles fully collapse into the plasma membrane and are recycled locally at synapses.

There were three unique features for clathrin-mediated endocytosis: morphology, time, and location. First, recycling membrane contained large particles, presumably vesicle proteins, and was surrounded by electron dense coats (Heuser and Reese, 1973; Miller and Heuser, 1984). Second, the prevalence of these pits peaks at 30 s after stimulation (Heuser and Reese, 1973; Miller and Heuser, 1984). Third, these endocytic structures were observed distant from active zones (Miller and Heuser, 1984). These observations led to a model in which synaptic vesicles are recycled in the peri-active zone slowly following stimulation via the coat proteins, clathrin. To date, clathrin-mediated endocytosis is thought to be the central pathway. The role of clathrin in synaptic vesicle endocytosis has been well established by a series of experiments. Maycox *et al.* purified coated vesicles from rat brain and showed that clathrin,

adaptor proteins, and synaptic vesicle proteins were present on the coated vesicles (Maycox et al., 1992). Furthermore, Takei et al. demonstrated that addition of clathrin and adaptor proteins purified from brain cytosol to liposomes is sufficient to generate vesicles (Takei et al., 1998). The functional studies also revealed the important role of clathrin in endocytosis. Synaptic vesicle endocytosis was severely blocked by knock-down of clathrin by RNA interference in cultured hippocampal cells (Granseth et al., 2006). Moreover, synaptic vesicles were not reformed in the fly neuromuscular junction when the clathrin complex was disrupted (Heerssen et al., 2008). Therefore, clathrin plays a crucial role in synaptic vesicle endocytosis.

However, clathrin-mediated endocytosis may not be the sole pathway for endocytosis for two reasons: first, regeneration of a synaptic vesicle via a clathrin scaffold requires about 15-20s (Heuser and Reese, 1973; Granseth et al., 2006; Balaji and Ryan, 2007); during high rates of release, faster and more robust mechanisms might be necessary to sustain neurotransmission (Dittman and Ryan, 2009). Second, perturbations of proteins that are thought to be involved in this process, such as AP2 (Gu et al., 2008; Kim and Ryan, 2009) and clathrin (Sato et al., 2009), do not completely block vesicle endocytosis. Thus, other pathways may operate at synapses.

Kiss-and-run endocytosis

Kiss-and-run endocytosis was proposed by Ceccarelli and his colleagues (Fesce et al., 1994). When neurons were stimulated at low frequency (2 Hz) for

a prolonged period of time, membrane invaginations with various neck sizes were found in active zones (Ceccarelli et al., 1972). Horseradish peroxidase was taken up into some of these invaginations, suggesting that these vesicles are in the process of recycling rather than fusing. The presence of endocytic intermediates in active zones and invaginations with a narrow neck led them to postulate that exocytosis and endocytosis are coupled via a transient fusion pore. To provide evidence for such a pathway, they applied a single stimulus to frog neuromuscular junctions and followed the morphological changes at a millisecond temporal resolution using a freeze-slammer (Torri-Tarelli et al., 1985). Based on Heuser and Reese's experiment (1981), an accumulation of exocytic figures with a wider neck was expected from 5 ms – 10 ms; however, the number of exocytic figures decreased during this time frame. They argued that this reduction was caused by the reversal of the fusion pore. These results were not convincing, but the idea that synaptic vesicles can be reused rapidly after fusion was favored as an alternative model of endocytosis.

The kiss-and-run pathway is thought to account for the rapid turnover of synaptic vesicles based on several experiments. Capacitance measurements of the Calyx of Held revealed two kinetic components for endocytosis: rapid and slow (Sun et al., 2002; Wu et al., 2005; Yamashita et al., 2005). Further experiments using optical tracers such as FM dyes (Pyle et al., 2000; Richards et al., 2000, 2005; Aravanis et al., 2003), pHluorin (Gandhi and Stevens, 2003), and quantum dots (Zhang et al., 2007b, 2009) also showed two kinetic components for vesicle recovery.

However, there are caveats to these experiments. For example, the fast component found in the pHluorin experiment (Gandhi and Stevens, 2003) was likely due to the small region of interest selected for the analysis; careful analyses with a larger region of interest showed a single component with a time constant of 15-20 s (Granseth et al., 2006; Balaji and Ryan, 2007). The physical constrains imposed by the size of quantum dots that are taken up into vesicles may prevent vesicles from collapsing into the membrane (Dittman and Ryan, 2009). Moreover, synaptic vesicles may not be recycled in active zones in the Calyx of Held despite the existence of two kinetic components (Wu and Wu, 2009). Thus, the existence of kiss-and-run is still under debate although the speed of kiss-and-run endocytosis can account for the rapid reuse of synaptic vesicles.

Bulk endocytosis

Bulk endocytosis is proposed based on the observations that bulk membrane was internalized into the cells during the intense repetitive stimulation (Heuser and Reese, 1973; Gad et al., 1998; Takei et al., 1998; Richards et al., 2000; Holt et al., 2003; Paillart et al., 2003; Teng et al., 2007; Clayton et al., 2010; Gaffield et al., 2011). These structures were originally thought to be recycling endosomes from which synaptic vesicles are regenerated following protein sorting (Heuser and Reese, 1973). However, the presence of bulk membrane invaginations on the surface (Koenig and Ikeda, 1996; Takei et al., 1998; Richards et al., 2000; Teng et al., 2007) led to the idea that infolding of

bulk membrane compensates for the increase of surface membrane during the high rate of neurotransmission (Royle and Lagnado, 2003). The infoldings could occur in active zones (Koenig and Ikeda, 1996) or in peri-active zones (Richards et al., 2000), and they are severed by dynamin (Clayton et al., 2010). Clathrin is likely required to regenerate synaptic vesicles from the internalized membrane (Heuser and Reese, 1973; Takei et al., 1998).

Bulk endocytosis is an attractive model for rapid retrieval of exocytic vesicle membrane following the exhaustive stimulation. The capacitance measurements in the Calyx of Held demonstrated that bulk membrane retrieval may occur within 50-300 ms in peri-active zones (Wu and Wu, 2007, 2009). However, this pathway may not account for the fast endocytic rate at synapses because synaptic vesicles are likely regenerated slowly from the internalized membrane by the clathrin complex (Heuser and Reese, 1973; Takei et al., 1998).

These ultrastructural studies led to the proposal of three models for endocytosis. However, in each case, repetitive intense stimulation was applied to samples under nonphysiological conditions. The fate of synaptic vesicles following exocytosis was obscured by the continuous synaptic vesicle fusion. In this dissertation, I investigated how membrane was retrieved following a single pulse using time-resolved electron microscopy. The clathrin model predicts that vesicles will collapse into the membrane, that membrane will endocytose lateral to the active zone, and that endocytosis will occur slowly (~20 s). By contrast, 'kiss-and-run' predicts that vesicles will not collapse into the membrane, that vesicles will endocytose at the site of release, that they will be the same size as

synaptic vesicles and endocytosis will be fast (~1 s). In contrast to these models, my new data demonstrate that following a single stimulus, vesicles collapse into the membrane, that membrane is endocytosed lateral to the fusion sites, but is recovered on an ultrafast timescale (~50 - 300 ms) using an unknown mechanism (Chapter 7). These morphological features are not consistent with clathrin model or kiss-and-run model and may suggest a novel endocytic pathway following a single stimulus.

Dissertation outline

In this dissertation, I will address two controversial issues in synaptic biology: 1) How are synaptic vesicles organized for exocytosis? 2) How does endocytosis take place? To address these questions, I developed two novel techniques in electron microscopy. In Chapter 2, I will describe a method to stimulate the synaptic terminal and observe vesicle fusion and recycling. In Chapter 3, I will present a technique to localize proteins in electron micrographs at nano-resolution. In Chapter 4, I will present an improved method for protein localization. In Chapter 5, I will describe a step-by-step protocol for correlative nanoscopy and electron microscopy. In Chapter 6, I will apply the correlative microscopy technique in mouse hippocampal neurons and describe five technical advancements. Using time-resolved electron microscopy and nano-fEM, I will address how exocytosis and endocytosis takes place in the neuromuscular junctions of *Caenorhabditis elegans* in Chapter 7. Finally, I will present my collaborative work on connectomes in Chapter 8 and Chapter 9 and discuss the

potential tools that need to be developed to address how neurons are wired properly. In the final chapter of this dissertation, I will discuss the interpretation of my findings and the future directions.

References

Aravanis, A.M., Pyle, J.L., and Tsien, R.W. (2003). Single synaptic vesicles fusing transiently and successively without loss of identity. Nature *423*, 643–647.

Balaji, J., and Ryan, T.A. (2007). Single-vesicle imaging reveals that synaptic vesicle exocytosis and endocytosis are coupled by a single stochastic mode. Proc. Natl. Acad. Sci. U.S.A *104*, 20576–20581.

Boyden, E.S., Zhang, F., Bamberg, E., Nagel, G., and Deisseroth, K. (2005). Millisecond-timescale, genetically targeted optical control of neural activity. Nat. Neurosci. *8*, 1263–1268.

Brose, N., Petrenko, A.G., Südhof, T.C., and Jahn, R. (1992). Synaptotagmin: a calcium sensor on the synaptic vesicle surface. Science *256*, 1021–1025.

Carter, A.G., and Regehr, W.G. (2002). Quantal events shape cerebellar interneuron firing. Nat. Neurosci. *5*, 1309–1318.

Del Castillo, J., and Katz, B. (1956). Biophysical aspects of neuro-muscular transmission. Prog Biophys Biophys Chem *6*, 121–170.

Ceccarelli, B., Hurlbut, W.P., and Mauro, A. (1972). Depletion of vesicles from frog neuromuscular junctions by prolonged tetanic stimulation. J. Cell Biol *54*, 30–38.

Chung, C., Barylko, B., Leitz, J., Liu, X., and Kavalali, E.T. (2010). Acute dynamin inhibition dissects synaptic vesicle recycling pathways that drive spontaneous and evoked neurotransmission. J. Neurosci. *30*, 1363–1376.

Clayton, E.L., Sue, N., Smillie, K.J., O'Leary, T., Bache, N., Cheung, G., Cole, A.R., Wyllie, D.J., Sutherland, C., Robinson, P.J., et al. (2010). Dynamin I phosphorylation by GSK3 controls activity-dependent bulk endocytosis of synaptic vesicles. Nat. Neurosci *13*, 845–851.

Couteaux, R., and Pécot-Dechavassine, M. (1974). [Specialized areas of presynaptic membranes]. C.R. Hebd. Seances Acad. Sci., Ser. D, Sci. Nat. *278*, 291–293.

Dale, H.H. (1914). The action of certain esters and ethers of choline, and their relation to muscarine. J Pharmacol Exp Ther *6*, 147–190.

Dittman, J., and Ryan, T.A. (2009). Molecular circuitry of endocytosis at nerve terminals. Annu. Rev. Cell Dev. Biol *25*, 133–160.

Fatt, P., and Katz, B. (1952). Spontaneous subthreshold activity at motor nerve endings. J. Physiol. (Lond.) *117*, 109–128.

Fesce, R., Grohovaz, F., Valtorta, F., and Meldolesi, J. (1994). Neurotransmitter release: fusion or "kiss-and-run"? Trends Cell Biol. *4*, 1–4.

Fredj, N.B., and Burrone, J. (2009). A resting pool of vesicles is responsible for spontaneous vesicle fusion at the synapse. Nat Neurosci *12*, 751–758.

Gad, H., Löw, P., Zotova, E., Brodin, L., and Shupliakov, O. (1998). Dissociation between Ca2+-triggered synaptic vesicle exocytosis and clathrin-mediated endocytosis at a central synapse. Neuron *21*, 607–616.

Gaffield, M.A., Romberg, C.F., and Betz, W.J. (2011). Live imaging of bulk endocytosis in frog motor nerve terminals using FM dyes. J Neurophysiol *106*, 599–607.

Gandhi, S.P., and Stevens, C.F. (2003). Three modes of synaptic vesicular recycling revealed by single-vesicle imaging. Nature *423*, 607–613.

Granseth, B., Odermatt, B., Royle, S.J., and Lagnado, L. (2006). Clathrin-mediated endocytosis is the dominant mechanism of vesicle retrieval at hippocampal synapses. Neuron *51*, 773–786.

Groemer, T.W., and Klingauf, J. (2007). Synaptic vesicles recycling spontaneously and during activity belong to the same vesicle pool. Nat. Neurosci. *10*, 145–147.

Gu, M., Schuske, K., Watanabe, S., Liu, Q., Baum, P., Garriga, G., and Jorgensen, E.M. (2008). Mu2 adaptin facilitates but is not essential for synaptic vesicle recycling in Caenorhabditis elegans. J. Cell Biol *183*, 881–892.

Hebb, C.O., and Whittaker, V.P. (1958). Intracellular distributions of acetylcholine and choline acetylase. J Physiol *142*, 187–196.

Heerssen, H., Fetter, R.D., and Davis, G.W. (2008). Clathrin dependence of synaptic-vesicle formation at the Drosophila neuromuscular junction. Curr. Biol. *18*, 401–409.

Heuser, J.E., and Reese, T.S. (1973). Evidence for recycling of synaptic vesicle membrane during transmitter release at the frog neuromuscular junction. J. Cell Biol *57*, 315–344.

Heuser, J.E., and Reese, T.S. (1981). Structural changes after transmitter release at the frog neuromuscular junction. J. Cell Biol *88*, 564–580.

Heuser, J.E., Reese, T.S., Dennis, M.J., Jan, Y., Jan, L., and Evans, L. (1979). Synaptic vesicle exocytosis captured by quick freezing and correlated with quantal transmitter release. J. Cell Biol *81*, 275–300.

Hodgkin, A.L., and Huxley, A.F. (1936). Action potentials recorded from inside a nerve fibre : Abstract : Nature.

Holt, M., Cooke, A., Wu, M.M., and Lagnado, L. (2003). Bulk membrane retrieval in the synaptic terminal of retinal bipolar cells. J. Neurosci. *23*, 1329–1339.

Ikeda, K., and Bekkers, J.M. (2009). Counting the number of releasable synaptic vesicles in a presynaptic terminal. Proc. Natl. Acad. Sci. U.S.A. *106*, 2945–2950.

Jin, I., Udo, H., Rayman, J.B., Puthanveettil, S., Kandel, E.R., and Hawkins, R.D. (2012). Spontaneous transmitter release recruits postsynaptic mechanisms of long-term and intermediate-term facilitation in Aplysia. PNAS.

Kim, S.H., and Ryan, T.A. (2009). Synaptic vesicle recycling at CNS snapses without AP-2. J. Neurosci *29*, 3865–3874.

Koenig, J.H., and Ikeda, K. (1996). Synaptic vesicles have two distinct recycling pathways. J. Cell Biol. *135*, 797–808.

Kopp-Scheinpflug, C., Tolnai, S., Malmierca, M.S., and Rübsamen, R. (2008). The medial nucleus of the trapezoid body: comparative physiology. Neuroscience *154*, 160–170.

Kuffler, S.W., and Yoshikami, D. (1975). The number of transmitter molecules in a quantum: an estimate from iontophoretic application of acetylcholine at the neuromuscular synapse. J. Physiol. (Lond.) *251*, 465–482.

Kuromi, H., and Kidokoro, Y. (2000). Tetanic stimulation recruits vesicles from reserve pool via a cAMP-mediated process in Drosophila synapses. Neuron *27*, 133–143.

Llinás, R., Steinberg, I.Z., and Walton, K. (1976). Presynaptic calcium currents and their relation to synaptic transmission: voltage clamp study in squid giant synapse and theoretical model for the calcium gate. Proc. Natl. Acad. Sci. U.S.A. *73*, 2918–2922.

Llinás, R., Steinberg, I.Z., and Walton, K. (1981). Presynaptic calcium currents in squid giant synapse. Biophys. J. *33*, 289–321.

Lorteije, J.A.M., Rusu, S.I., Kushmerick, C., and Borst, J.G.G. (2009). Reliability and precision of the mouse calyx of Held synapse. J. Neurosci *29*, 13770–13784.

Maeno-Hikichi, Y., Polo-Parada, L., Kastanenka, K.V., and Landmesser, L.T. (2011). Frequency-dependent modes of synaptic vesicle endocytosis and exocytosis at adult mouse neuromuscular junctions. J. Neurosci *31*, 1093–1105.

Mathew, S.S., Pozzo-Miller, L., and Hablitz, J.J. (2008). Kainate modulates presynaptic GABA release from two vesicle pools. J. Neurosci. *28*, 725–731.

Matthew, W.D., Tsavaler, L., and Reichardt, L.F. (1981). Identification of a synaptic vesicle-specific membrane protein with a wide distribution in neuronal and neurosecretory tissue. J. Cell Biol. *91*, 257–269.

Maycox, P.R., Link, E., Reetz, A., Morris, S.A., and Jahn, R. (1992). Clathrin-coated vesicles in nervous tissue are involved primarily in synaptic vesicle recycling. J. Cell Biol *118*, 1379–1388.

McKinney, R.A., Capogna, M., Dürr, R., Gähwiler, B.H., and Thompson, and S.M. (1999). Miniature synaptic events maintain dendritic spines via AMPA receptor activation. Nature Neuroscience *2*, 44–49.

Miller, T.M., and Heuser, J.E. (1984). Endocytosis of synaptic vesicle membrane at the frog neuromuscular junction. J. Cell Biol *98*, 685–698.

Murphy, T.H., Blatter, L.A., Bhat, R.V., Fiore, R.S., Wier, W.G., and Baraban, J.M. (1994). Differential regulation of calcium/calmodulin-dependent protein kinase II and p42 MAP kinase activity by synaptic transmission. J. Neurosci. *14*, 1320–1331.

Nagel, G., Brauner, M., Liewald, J.F., Adeishvili, N., Bamberg, E., and Gottschalk, A. (2005). Light activation of channelrhodopsin-2 in excitable cells of Caenorhabditis elegans triggers rapid behavioral responses. Curr. Biol. *15*, 2279–2284.

Nagel, G., Ollig, D., Fuhrmann, M., Kateriya, S., Musti, A.M., Bamberg, E., and Hegemann, P. (2002). Channelrhodopsin-1: a light-gated proton channel in green algae. Science *296*, 2395–2398.

Nagel, G., Szellas, T., Huhn, W., Kateriya, S., Adeishvili, N., Berthold, P., Ollig, D., Hegemann, P., and Bamberg, E. (2003). Channelrhodopsin-2, a directly light-gated cation-selective membrane channel. Proceedings of the National Academy of Sciences of the United States of America *100*, 13940 –13945.

Otsu, Y., and Murphy, T.H. (2003). Miniature transmitter release: accident of nature or careful design? Sci. STKE *2003*, pe54.

Otto, L. (1921). Uber humorale Ubertragbarkeit der Herznervenwirkung. Pflugers *189*, 239–242.

Paillart, C., Li, J., Matthews, G., and Sterling, P. (2003). Endocytosis and vesicle recycling at a ribbon synapse. J. Neurosci *23*, 4092–4099.

Palay, S.L., and Palade, G.E. (1955). The fine structure of neurons. J Biophys Biochem Cytol *1*, 69–88.

Perin, M.S., Brose, N., Jahn, R., and Südhof, T.C. (1991). Domain structure of synaptotagmin (p65). J. Biol. Chem. *266*, 623–629.

Pyle, J.L., Kavalali, E.T., Piedras-Rentería, E.S., and Tsien, R.W. (2000). Rapid reuse of readily releasable pool vesicles at hippocampal synapses. Neuron *28*, 221–231.

Richards, D.A., Bai, J., and Chapman, E.R. (2005). Two modes of exocytosis at hippocampal synapses revealed by rate of FM1-43 efflux from individual vesicles. J. Cell Biol *168*, 929–939.

Richards, D.A., Guatimosim, C., and Betz, W.J. (2000). Two endocytic recycling routes selectively fill two vesicle pools in frog motor nerve terminals. Neuron *27*, 551–559.

Rizzoli, S.O., and Betz, W.J. (2002). Effects of 2-(4-morpholinyl)-8-phenyl-4H-1-benzopyran-4-one on synaptic vesicle cycling at the frog neuromuscular junction. J. Neurosci. *22*, 10680–10689.

Rizzoli, S.O., and Betz, W.J. (2005). Synaptic vesicle pools. Nat. Rev. Neurosci *6*, 57–69.

De Robertis, E.D., and Bennett, H.S. (1954). A submicroscopic vesicular component of Schwann cells and nerve satellite cells. Exp. Cell Res. *6*, 543–545.

De Robertis, E.D., and Bennett, H.S. (1955). Some features of the submicroscopic morphology of synapses in frog and earthworm. J Biophys Biochem Cytol *1*, 47–58.

Rosenmund, C., and Stevens, C.F. (1996). Definition of the readily releasable pool of vesicles at hippocampal synapses. Neuron *16*, 1197–1207.

Royle, S.J., and Lagnado, L. (2003). Endocytosis at the synaptic terminal. J. Physiol. (Lond.) *553*, 345–355.

Sara, Y., Virmani, T., Deák, F., Liu, X., and Kavalali, E.T. (2005). An isolated pool of vesicles recycles at rest and drives spontaneous neurotransmission. Neuron *45*, 563–573.

Sato, K., Ernstrom, G., Watanabe, S., Weimer, R., Chen, C., Sato, M., Siddiqui, A., Jorgensen, E., and Grant, B. (2009). Differential requirements for clathrin in receptor-mediated endocytosis and maintenance of synaptic vesicle pools. Proceedings of the National Academy of Sciences *106*, 1139.

Schikorski, T., and Stevens, C.F. (1997). Quantitative ultrastructural analysis of hippocampal excitatory synapses. J. Neurosci *17*, 5858–5867.

Schikorski, T., and Stevens, C.F. (2001). Morphological correlates of functionally defined synaptic vesicle populations. Nat. Neurosci *4*, 391–395.

Schobert, B., and Lanyi, J.K. (1982). Halorhodopsin is a light-driven chloride pump. J. Biol. Chem. *257*, 10306–10313.

Stevens, C.F., and Tsujimoto, T. (1995). Estimates for the pool size of releasable quanta at a single central synapse and for the time required to refill the pool. Proc. Natl. Acad. Sci. U.S.A *92*, 846–849.

Sun, J.-Y., Wu, X.-S., and Wu, L.-G. (2002). Single and multiple vesicle fusion induce different rates of endocytosis at a central synapse. Nature *417*, 555–559.

Sutton, M.A., Wall, N.R., Aakalu, G.N., and Schuman, E.M. (2004). Regulation of dendritic protein synthesis by miniature synaptic events. Science *304*, 1979–1983.

Takei, K., Haucke, V., Slepnev, V., Farsad, K., Salazar, M., Chen, H., and De Camilli, P. (1998). Generation of coated intermediates of clathrin-mediated endocytosis on protein-free liposomes. Cell *94*, 131–141.

Teng, H., Lin, M.Y., and Wilkinson, R.S. (2007). Macroendocytosis and endosome processing in snake motor boutons. J. Physiol. (Lond.) *582*, 243–262.

Torri-Tarelli, F., Grohovaz, F., Fesce, R., and Ceccarelli, B. (1985). Temporal coincidence between synaptic vesicle fusion and quantal secretion of acetylcholine. J. Cell Biol *101*, 1386–1399.

Verhage, M., Maia, A.S., Plomp, J.J., Brussaard, A.B., Heeroma, J.H., Vermeer, H., Toonen, R.F., Hammer, R.E., Den, T.K. van, Berg, et al. (2000). Synaptic Assembly of the Brain in the Absence of Neurotransmitter Secretion. Science *287*, 864–869.

Whittaker, V.P. (1959). The isolation and characterization of acetylcholine-containing particles from brain. Biochem J. *72*, 694-706.

Wilhelm, B.G., Groemer, T.W., and Rizzoli, S.O. (2010). The same synaptic vesicles drive active and spontaneous release. Nat. Neurosci. *13*, 1454–1456.

Wu, W., and Wu, L.-G. (2007). Rapid bulk endocytosis and its kinetics of fission pore closure at a central synapse. Proc. Natl. Acad. Sci. U.S.A. *104*, 10234–10239.

Wu, W., Xu, J., Wu, X.-S., and Wu, L.-G. (2005). Activity-dependent acceleration of endocytosis at a central synapse. J. Neurosci. *25*, 11676–11683.

Wu, X.-S., and Wu, L.-G. (2009). Rapid endocytosis does not recycle vesicles within the readily releasable pool. J. Neurosci. *29*, 11038–11042.

Yamashita, T., Hige, T., and Takahashi, T. (2005). Vesicle endocytosis requires dynamin-dependent GTP hydrolysis at a fast CNS synapse. Science *307*, 124–127.

Zenisek, D., Steyer, J.A., and Almers, W. (2000). Transport, capture and exocytosis of single synaptic vesicles at active zones. Nature *406*, 849–854.

Zhang, F., Wang, L.-P., Brauner, M., Liewald, J.F., Kay, K., Watzke, N., Wood, P.G., Bamberg, E., Nagel, G., Gottschalk, A., et al. (2007a). Multimodal fast optical interrogation of neural circuitry. Nature *446*, 633–639.

Zhang, Q., Cao, Y.-Q., and Tsien, R.W. (2007b). Quantum dots provide an optical signal specific to full collapse fusion of synaptic vesicles. Proc. Natl. Acad. Sci. U.S.A *104*, 17843–17848.

Zhang, Q., Li, Y., and Tsien, R.W. (2009). The dynamic control of kiss-and-run and vesicular reuse probed with single nanoparticles. Science *323*, 1448–1453.

CHAPTER 2

TIME-RESOLVED ELECTRON MICROSCOPY: COUPLING OPTOGENETICS WITH HIGH-PRESSURE FREEZING

Summary

A complete understanding of neuronal functions requires observation of the synapse with high spatial and temporal resolution. Recently, we developed a method to combine optogenetics with electron microscopy to capture dynamic changes in synaptic morphology during neurotransmission. First we generated transgenic C. elegans animals expressing channelrhodopsin in specific neurons. We stimulated these neurons in intact animals using a home-built light stimulation device and modified specimen holders for the Leica EM Pact2 high-pressure freezer. Samples were subsequently frozen 20 ms after the light stimulus. We demonstrated that synaptic vesicle fusion intermediates could be captured using this technique. This method can be readily applied to other light-activatable molecules, such as caged compounds, light-switchable ligands, and photoactivatable proteins, to study dynamic changes in cells.

Introduction

Changes in membrane architecture can occur rapidly during trafficking through the secretory pathway. For example, regulated fusion at synapses is

extremely fast; the synaptic delay between stimulus and postsynaptic response is only 1ms (Eccles, 1964). Two problems arise for the visualization of such cellular events: size and speed. The synapse is too small to visualize membrane fusion using conventional light microscopes. Synapses in many organisms can be as small as a few hundred nanometers across, and synaptic vesicles are typically 30-40 nm in diameter; these sizes are far below the resolution limit of light microscopy. Thus, the morphology of a synapse is best imaged using electron microscopy.

Speed is the second hurdle for measuring certain cell biological processes. When neurons are stimulated, neurotransmitters are synchronously released into the synaptic cleft within a few milliseconds of the arrival of the action potential (Heuser et al., 1979). Conventional sample preparations for electron microscopy, unfortunately, rely on perfusion and diffusion of the fixative; these methods are too slow to capture rapid events and also introduce fixation artifacts. Worse yet, the fixatives used to prepare the samples cause the fusion of synaptic vesicles (Smith and Reese, 1980; Rosenmund and Stevens, 1997). Thus, capturing the very moment of vesicle fusion to the membrane seemed almost impossible. To overcome this limitation, Heuser and Reese developed the freeze-slammer. In this device, specimens were slammed against a metal block cooled to 4ºK by liquid helium (Heuser et al., 1979). Specimens were frozen near-instantaneously. By electrically stimulating the preparation at various time points before freezing, the temporal sequence of vesicle fusion was characterized with millisecond temporal resolution (Heuser et al., 1979; Heuser and Reese, 1981; Torri-Tarelli

et al., 1985). However, the freeze-slammer was only capable of freezing the surface of the specimen without ice crystals (up to 10 μm deep), and thus only dissected preparations of neurons (Heuser et al., 1979; Heuser and Reese, 1981; Torri-Tarelli et al., 1985) or very thin tissues (Kachar et al., 1986; Arsenault et al., 1988; Neill et al., 1988) could be analyzed. Moreover, the stimulation conditions required the use of potassium channel blockers and high calcium (Heuser et al., 1979; Heuser and Reese, 1981; Torri-Tarelli et al., 1985) and was thus not physiological. To apply rapid freezing methods to different model organisms two improvements were necessary: increased vitreous freezing depth and *in vivo* physiological stimulation protocols.

In recent years, a high-pressure freezing method was developed to improve the freezing depth (Moor and Riehle, 1968; Moor, 1987). Normally, when liquid water is cooled to freezing temperature, water molecules begin to form ice on a seed crystal or another nucleating structure (Dubochet, 2007). When ice crystals from, the local concentration of solutes increases because the solutes are excluded from the crystals (Dubochet, 2007). This increase alters the local osmotic pressure, eventually leading to the bursting of cellular membranes (Dubochet, 2007). In the absence of a nucleation site, water can stay in its super-cooled liquid phase (Dubochet, 2007) until the temperature reaches -40ºC, when it will crystallize even in the absence of a nucleus (Rasmussen et al., 1975). If a freezing rate of -10,000ºC/s can be achieved, super-cooled water can be vitrified, that is, the water will freeze in an unordered state. Liquid nitrogen can generate a cooling rate of -16,000ºC/s. However, due to the poor heat conductance of water,

the freezing rate of tissue 10 μm deep is very slow, and therefore thick samples (>10 μm) cannot be frozen without the formation of ice crystals. However, at 2100 bar (1 bar = atmospheric pressure at sea level), water can be super-cooled to -90ºC. Under these conditions, a freezing rate of -100ºC/s is sufficient to vitrify water. Thus, by freezing under high-pressure, biological tissues as thick as 500 μm can be frozen with reduced ice crystal formation, despite the poor heat conductance of water. Therefore, in principle, time-resolved imaging via electron microscopy can be performed in intact animals such as *Caenorhabditis elegans* using high-pressure freezing. However, neurons in intact animals are not readily accessible by an electrode. Therefore, an alternative stimulation method must be sought.

In the last decade, optogenetic techniques have been developed to apply non-invasive stimulation to neurons and precisely control neuronal activities (Yizhar et al., 2011). The discovery of light-activated sodium channels (Nagel et al., 2002, 2003b; Sineshchekov et al., 2002) and engineered variants such channelrhodopsin (Nagel et al., 2003b; Lin et al., 2009; Gunaydin et al., 2010; Govorunova et al., 2011; Lin, 2012) have made it possible to activate specific neurons in intact organisms by a simple flash of light (Boyden et al., 2005; Nagel et al., 2005b; Douglass et al., 2008; Liewald et al., 2008; Liu et al., 2009; Leifer et al., 2011). Therefore, by coupling light-induced stimulation with high-pressure freezing, temporal events in neurotransmission can be studied in intact animals under physiological conditions. Unfortunately, the current configurations of commercially available high-pressure freezers do not allow for light stimulation of

specimens.

We developed a device that couples optogenetics with high-pressure freezing. The device can preserve morphological changes that occur during neurotransmission with a temporal resolution of milliseconds. In this chapter, we describe the use of channelrhodopsin to stimulate neurons. The protocol is compatible with other methods that selectively activate or inactivate cellular activities by light, such as caged neurotransmitters (Walker et al., 1986; Milburn et al., 1989; Wieboldt et al., 1994), photo-switchable ligands (Bartels et al., 1971; Banghart et al., 2004), caged second messengers (cyclic nucleotides) (Adams and Tsien, 1993), and photoactivatable proteins (light-inducible protein interactions) (Levskaya et al., 2009; Yazawa et al., 2009; Kennedy et al., 2010). For example, time-resolved electron microscopy could be used to observe the dynamic reorganization of postsynaptic terminals that occurs when synaptic facilitation is induced by caged glutamate. Cells that are naturally responsive to light such as rod or cone cells in the retina can be studied using this method. Alternatively, rapid events in non-excitable cells such as cytoskeletal reorganizations or membrane trafficking can be studied using this technique. In summary, these methods can capture cellular dynamics with nanometer spatial resolution and millisecond temporal resolution.

Materials

High-pressure freezing

1. Leica EM Pact2 high-pressure freezer with or without rapid transfer system (Leica microsystems)
2. Specimen bayonet (Leica microsystems)
3. Specimen pods (Leica microsystems)
4. Sapphire end stones (#E2.08, Swiss Jewel company)
5. Custom-made screws
6. Two-part epoxy
7. Silver marking pen (fine point)
8. Sample cup ('membrane carriers', 100µm deep, #16707898, Leica microsystems)
9. Loading fork ("manual bayonet loading device", #16707828, Leica microscystems)
10. Tweezers (insulated, #16LZ01873KN, Leica microsystems)
11. Paint brush (#00)
12. Methylcyclohexane (#300306, Sigma-Aldrich)
13. Hexadecene (#H2131-100ML, Sigma-Aldrich)
14. Bovine serum albumin (A2153-10G, Sigma-Aldrich)
15. Liquid nitrogen

Light stimulation device

1. Modified specimen bayonet (Marine Reef International)
2. Modified specimen pods (Marine Reef International)
3. Light stimulation controller (Marine Reef International)
4. Lambda DG-4 light source (Sutter)

Freeze-substitution

1. Automated freeze-substitution unit (AFS 2, Leica microsystem)
2. Cryovials (#D9912, Nalgene)
3. Acetone (RT10016, EMS)
4. Ethanol (#459844-1L, Sigma-Aldrich)
5. Osmium tetroxide (crystals, 1/10 g; RT19134, EMS)
6. Glutaraldehyde in acetone (#16530, EMS)
7. Uranyl acetate (#21447-252, Polysciences)
8. Disposable transfer pipette (#14670-201, VWR)
9. Disposable pastuer pipette (Borosilicate glass; #13-678-20A, Fisher)

Plastic embedding

1. Epon-araldite (kit, #18028, Ted Pella)
2. BEEM capsule (#70010B, EMS)

Sectioning

1. Ultramicrotome (UC6, Leica microsystem)
2. Diamond knife (Ultra jumbo, 45º, 4.0 mm; DiATOME)
3. Glass strips (#8030, Ted Pella)
4. Glass knife boats (#123-3, Ted Pella)
5. Hair tool for manipulation of plastic sections
6. Razor blade (Double edge; #72000, EMS)
7. High profile microtome blades (#818, Leica microsystem)
8. TEM grids (single slot, #1GC12H, Ted Pella)
9. Formvar (0.5%, RT15820, EMS)

Imaging

1. Transmission electron microscope
2. Digital camera (Orius, Gatan)

Methods

Modification of specimen holders

A high-pressure freezer is capable of freezing a thick specimen with reduced ice crystal formation. However, specimens must be mounted within a closed compartment and cannot be illuminated (Fig. 2.1A, B). The Leica EM Pact2 was developed to allow direct observation of specimens under a light microscope up to a few seconds before freezing (McDonald et al., 2007; Müller-Reichert et al., 2008; Verkade, 2008). Specifically, specimens are loaded into an

open cup and capped with a black diamond on a specimen pod (Fig. 2.1B-D) just prior to freezing either manually or via a rapid transfer system (RTS). The transfer system screws down the black diamond anvil to cover the sample cup and drives the specimen bayonet into the freezing chamber automatically. The transfer system can be used to capture membrane dynamics at synapses ~2.5 s or greater after chronic or repetitive stimulation. An optical fiber with a filter cube can be mounted adjacent to the specimen loading path (Fig. 2.1E). Light stimulation can be applied either from a mercury lamp or a laser source before freezing the sample. However, to resolve the membrane dynamics involved in processes such as exocytosis and rapid forms of endocytosis requires millisecond temporal resolution (Heuser et al., 1979; Heuser and Reese, 1981; Miller and Heuser, 1984; Torri-Tarelli et al., 1985). To improve the temporal resolution, we built a device and computer program to stimulate samples milliseconds before freezing. In this chapter, we describe in detail how to build and operate this device.

First, we modified the specimen bayonet so that an LED bulb or an optical fiber could be mounted adjacent to the sample cup. To create this light path to the specimen, three modifications were required (Fig. 2.2). First, a hole was drilled into a specimen bayonet. A specimen bayonet (Fig. 2.2A) has six components: an insulating cover, a metal shaft, a metal chuck, a spring, a pin, and a cap (Fig. 2.2B). The metal chuck and spring are used to lock the specimen pod tightly at the tip of the bayonet. The metal shaft can be removed from the insulating cover, freeing the metal chuck and spring from the holder. The pin was

removed and a 2 mm hole drilled through the middle of the metal shaft to create a conduit for wires (Fig. 2.2C). Second, we replaced the metal chuck with a 3.2 mm LED bulb and a fabricated metal LED mount (Fig. 2.2D). Third, we fabricated a new screw for a specimen pod (Fig. 2.2E). The original screw has a black diamond anvil attached at the tip (Fig. 2.2E left). The fabricated screw has a bore with a diameter of 1.2 mm down the central axis and a countersink with a diameter of 2.08 mm at the tip of the screw (Fig. 2.2E right; see Notes 5.1). A transparent sapphire anvil with a diameter of 2.08 mm and a thickness of ~1 mm was glued in the countersink using two-part epoxy (see Notes 5.2). The modified specimen bayonet and pod were reassembled to the original configuration. The new specimen holder allows for the application of single-color light with an intensity as high as ~20 mW/mm^2.

An alternative assembly allows the application of light of multiple wavelengths. The bayonet in this configuration holds an optical fiber. In addition to the modifications described above, the pin was split into two halves and glued back into the shaft with two-part epoxy, leaving the central bore open for the optical fiber. An optical fiber with a diameter of 1.5 mm was placed in the central bore of the shaft, and the free end of the fiber was attached to a Lambda DG-4 light source. To house the optical fiber in the freezing path of the rapid transfer system, we had to remove the safety cover (Fig. 2.3). Because the safety lock was controlled by magnets attached to the cover, we removed the magnets from the cover and placed them directly on the sensor (Fig. 2.3 and Fig. 2.4A; see Notes 5.3). These modifications allowed the application of multiple colors of light

prior to freezing. However, we have not yet developed a computer interface to the Lambda DG-4 for high temporal resolution control.

Development of the light stimulation device

To observe membrane dynamics at synapses, light stimulation must be applied to specimens with millisecond temporal precision. For the EM Pact2 with a Rapid Transfer System attachment, a specimen bayonet is driven into the freezing chamber by pressing the start button on the LED display. The freezing process is initiated when the specimen bayonet is securely locked into position. For an EM Pact2 without the transfer attachment, a specimen bayonet is loaded directly into the freezing chamber. Pressing the start button will then initiate the freezing process. To achieve millisecond temporal resolution, the interval between when the start button is pressed and when the specimen is actually frozen must be determined. The manufacturer estimated this interval to be about 2.5 s for an EM Pact2 outfitted with the transfer system. Taking this estimate into account is adequate to achieve sub-second precision, but we sought an alternative method to achieve millisecond temporal precision.

To achieve higher temporal precision, we used an accelerometer to determine when the sample is fired down the rail, when it enters the freezing chamber, and when it is pressurized. A computer then controls when the light is switched on relative to these events. We installed an accelerometer on the bayonet holder on the transfer device (Fig. 2.4A). Interestingly, the readout of the accelerometer showed several intervals with multiple peaks indicating different

motions of the specimen bayonet (Fig. 2.4B). The first 70 ms of the recording (interval 1) reflects the deceleration of the specimen bayonet along the rail (the recording begins after the sample was fired down the rail). To reveal what the other intervals represent, we monitored the temperature change using a thermistor while videotaping the freezer. The response time of the thermistor is too slow to capture the rapid freezing rate, but we can approximate the time when freezing occurs based on the initial response recorded by the thermistor. We found that freezing was initiated roughly 200 ms after the specimen bayonet reached the freezing chamber. This suggests that the first downward deflection observed in interval 3 reflects when pressure was applied to the specimen since this peak appears nearly simultaneously with freezing (Fig. 2.4B). The pressure application, thus, occurred 1545 ms after the accelerometer detected the initial launch of the bayonet down the rail (see Notes 5.4). Telemetry from the high-pressure freezer further refines the interval between the application of pressure and freezing at a higher temporal resolution. This interval was consistently 7-8 ms from shot to shot (Fig. 2.4C; see Notes 5.5). Therefore, about 1555 ms is required to freeze the specimens after pressing the start button and launching the bayonet. These results suggest that if a light pulse of 20 ms is to be delivered 100 ms before freezing, light stimulation should be triggered 1435 ms after the initial reading from the accelerometer. Unfortunately, the time when the specimens are frozen varied from shot to shot by about 20 ms, so the light stimulation was not delivered consistently at the programmed time point (see Notes 5.4). Nevertheless, we can calculate the actual interval between

stimulation and freezing based on the accelerometer readings from each shot.

The Leica EM Pact2 can also be operated without the transfer system. In this configuration, the specimen bayonet is manually locked in the freezing chamber, and thus the accelerometer readout cannot be used to deliver the light stimulation at the desired time point. We consulted Leica technicians and obtained an interface to the computer in the instrument. We built an electronic light stimulation controller (Fig. 2.4D) to send a "start" signal for freezing, bypassing the necessity to press the start button on the display. The control box can apply light stimulation with sub-10 ms temporal resolution. Nevertheless, there is still a variable delay introduced by the freezer that must be accounted for (see Notes 5.4). The light stimulation controller and the customized specimen bayonet and pods are now commercially available from Marine Reef International (see Notes 5.6).

Light stimulation coupled high-pressure freezing

For light stimulation-coupled high-pressure freezing, specimens can be mounted into a sample cup using procedures appropriate for each model system. Procedures for mounting particular specimens have been described extensively (McDonald, 2007; McDonald et al., 2007, 2010; Mueller-Reichert, 2010). For *C. elegans*, animals expressing channelrhodopsin need to be placed on a plate containing trans-retinal at least 16 hours prior to the experiments (Liu et al., 2009). Once animals are transferred to a plate containing trans-retinal, they should be kept in darkness. The high-pressure freezing should also be performed

in a dim room to minimize light exposure. To freeze *C. elegans* animals, a 100 μm deep sample cup should be used. Bacteria (*E. coli*) or 20% BSA can be used to fill the cup and to act as a cryoprotectant (see Notes 5.7) (McDonald et al., 2007). We use a manual loading station to mount the specimen carrier into the specimen pod. Because specimens are inevitably exposed to light while mounting, once specimens are loaded into the pod, the pod should be placed in dark for at least 30 s to allow recovery. For freezers lacking the transfer system, the pod can be mounted onto the bayonet and directly inserted into the freezing chamber for this step. In the meantime, the stimulation protocol should be programmed and selected using the light stimulation controller (see Notes 5.8). Once the specimen bayonet is locked, light stimulation and freezing can be triggered by simply pressing the green button on the light stimulation device controller (Fig. 4d). Between each shot, testing the function of LED may be necessary, since freezing may damage the wiring or the LED itself. The frozen specimens can be processed using standard procedures for freeze-substitution and plastic embedding (Rostaing et al., 2004; McDonald et al., 2007, 2010; Mueller-Reichert, 2010; McDonald and Webb, 2011).

Application examples

Using the light stimulation device, we monitored membrane dynamics in *C. elegans* neurons expressing ChIEF (Lin et al., 2009), a variant of channelrhodopsin. We programmed our light stimulation device to fire a single 20 ms light pulse 20 ms before freezing. At 20 ms, vesicles can be observed

collapsing into the membrane [5] along the active zone of motor neurons (Fig. 2.5). This result suggested that a combination of high-pressure freezing and optogenetics is capable of capturing membrane dynamics with high temporal resolution.

Notes

5.1 The countersink of the screw must be fabricated precisely so that the surface is absolutely flat. An uneven surface will cause the sapphire anvil to be slightly tilted, resulting in a pressure leak from the specimen carrier while freezing. In addition, tilted sapphire anvils tend to shatter when subjected to high pressure.

5.2 The amount of two-part epoxy applied to the rim of the countersink should be minimal – just enough to cover the rim. Otherwise, the bottom surface of the sapphire that faces the light source will have a thick layer of glue, resulting in the reduction in the transmitted light intensity. A silver marking pen can be used to coat the side of the sapphire anvil with a reflective surface to maximize the light intensity transmitted to the specimen.

5.3 Because safety features are bypassed, you are responsible for any injury that may occur. Make sure you do not stick any part of your body near the moving parts if you are using an EM Pact2 with a Rapid Transfer System. Before the machine initiates freezing, it checks to determine that the specimen is loaded and the cover is closed. Therefore, although the specimen can be mounted onto the freezing device without opening the cover, the instrument needs to receive instructions that the cover has been opened and closed. Therefore, the magnet

should be removed once, indicating the opening of the cover, and placed back into position, indicating the closing of the cover. The freezing can then be triggered by pressing the start button. Finally, the optical fiber is heavy, and thus the specimen bayonet is not balanced on the bayonet holder. When the specimen bayonet comes out of the freezing chamber after freezing, the specimen pod may not fully rotate into the liquid nitrogen bath. We typically push the pod into the bath manually, but extra caution should be taken to stand away from the bayonet until it has been ejected from the freezing chamber because the chamber is under a great deal of pressure.

5.4 The interval between pressing the start button and freezing is ~1555 ms for the RTS EM Pact2 and ~180 ms for the non-RTS EM Pact2. However, these values vary by about 20 ms from shot to shot. These fluctuations are likely caused by the mechanism of the freezer: Before liquid nitrogen is applied to the specimens, the freezer must ensure that the pressure in the freezing chamber is correct. The pressure is dependent on multiple factors such as the amount of liquid nitrogen in the storage tank, the idling time between shots, and the working pressure of the compressor. Thus, the light stimulation can be triggered very close to the programmed time point, but it often varies by 20 ms. Therefore, we always calculate the time when the light stimulation was actually delivered in relationship to pressurization and freezing based on the accelerometer reading for the pressure application (the lowest peak indicated by a black arrow in interval 3 in Fig. 4B).

5.5 The data files can be exported as .DGM format from the high-pressure

freezer using a USB drive provided by the manufacturer. The file can then be converted into .CSV format using the software provided on the USB drive. By plotting the pressure data and the temperature data in Microsoft Excel, we calculated the average time required to freeze specimens to 0ºC from the time the pressure begins to increase. The average time was 8 ms ± 1 ms from 20 different freezes. This represents the shortest time interval between stimulation and freezing using this apparatus.

5.6 For a commercial version of light stimulation kits, contact Marine Reef international (sales@marinereef.com).

5.7 To maximize the exposure of the animals to the light, 20% BSA is preferable. However, specimens frozen with 20% BSA tend to stay stuck in the sample cup during the freeze-substitution and plastic embedding in BSA. Using force to retrieve the specimens from the carrier often results in the permanent damage to the tissues or, in the worst case scenario, permanent loss of the tissues. Thus, although some light may be scattered by bacteria during the stimulation, bacteria are better suited as space-fillers for light-coupled high-pressure freezing. Heat is conducted faster in bacteria than air, and thus the bacteria serves as a cryo-protectant.

5.8 The programming of light stimulation protocols is very flexible. For example, a single stimulus lasting 5 ms can be applied 20 ms before the freezing (see Notes 5.4). A train of stimuli can also be programmed (for example, 10Hz train for 30 s with the duration of each stimulus of 20 ms). Intervals between two trains of stimuli can also be programmed (for example, 10Hz for 30 s, 5 s rest, and a

single stimulus of 20 ms). These programs can be stored directly in the light stimulation controller and can be selected by pressing the white button (Fig. 4d).

Acknowledgements

We would like to thank the Grass Foundation and the Marine Biological Laboratory at Woods Hole for providing us space and equipment required for performing the freezing experiments. Qiang Liu performed freezing experiments using the optical fiber. We would like to thank Roger Y. Tsien for providing us a construct for ChIEF and Eddie Hujber for critical reading of the manuscript. The research was supported by the US National Institutes of Health (NS034307) and the Marine Biological Laboratory (The Dart Scholars Program and the Grass Fellowship). EMJ is an Investigator of the Howard Hughes Medical Institute.

References

Adams, S.R., and Tsien, R.Y. (1993). Controlling cell chemistry with caged compounds. Annu. Rev. Physiol. *55*, 755–784.

Aravanis, A.M., Pyle, J.L., and Tsien, R.W. (2003). Single synaptic vesicles fusing transiently and successively without loss of identity. Nature *423*, 643–647.

Arsenault, A.L., Ottensmeyer, F.P., and Heath, I.B. (1988). An electron microscopic and spectroscopic study of murine epiphyseal cartilage: analysis of fine structure and matrix vesicles preserved by slam freezing and freeze substitution. J. Ultrastruct. Mol. Struct. Res. *98*, 32–47.

Balaji, J., and Ryan, T.A. (2007). Single-vesicle imaging reveals that synaptic vesicle exocytosis and endocytosis are coupled by a single stochastic mode. Proc. Natl. Acad. Sci. U.S.A *104*, 20576–20581.

Banghart, M., Borges, K., Isacoff, E., Trauner, D., and Kramer, R.H. (2004). Light-activated ion channels for remote control of neuronal firing. Nat. Neurosci *7*, 1381–1386.

Bartels, E., Wassermann, N.H., and Erlanger, B.F. (1971). Photochromic activators of the acetylcholine receptor. Proc. Natl. Acad. Sci. U.S.A *68*, 1820–1823.

Boyden, E.S., Zhang, F., Bamberg, E., Nagel, G., and Deisseroth, K. (2005). Millisecond-timescale, genetically targeted optical control of neural activity. Nat. Neurosci. *8*, 1263–1268.

Brose, N., Petrenko, A.G., Südhof, T.C., and Jahn, R. (1992). Synaptotagmin: a calcium sensor on the synaptic vesicle surface. Science *256*, 1021–1025.

Carter, A.G., and Regehr, W.G. (2002). Quantal events shape cerebellar interneuron firing. Nat. Neurosci. *5*, 1309–1318.

del Castillo, J., and Katz, B. (1956). Biophysical aspects of neuro-muscular transmission. Prog Biophys Biophys Chem *6*, 121–170.

Ceccarelli, B., Hurlbut, W.P., and Mauro, A. (1972). Depletion of vesicles from frog neuromuscular junctions by prolonged tetanic stimulation. J. Cell Biol *54*, 30–38.

Chung, C., Barylko, B., Leitz, J., Liu, X., and Kavalali, E.T. (2010). Acute dynamin inhibition dissects synaptic vesicle recycling pathways that drive spontaneous and evoked neurotransmission. J. Neurosci. *30*, 1363–1376.

Clayton, E.L., Sue, N., Smillie, K.J., O'Leary, T., Bache, N., Cheung, G., Cole, A.R., Wyllie, D.J., Sutherland, C., Robinson, P.J., et al. (2010). Dynamin I phosphorylation by GSK3 controls activity-dependent bulk endocytosis of synaptic vesicles. Nat. Neurosci *13*, 845–851.

Couteaux, R., and Pécot-Dechavassine, M. (1974). [Specialized areas of presynaptic membranes]. C.R. Hebd. Seances Acad. Sci., Ser. D, Sci. Nat. *278*, 291–293.

Dittman, J., and Ryan, T.A. (2009). Molecular circuitry of endocytosis at nerve terminals. Annu. Rev. Cell Dev. Biol *25*, 133–160.

Douglass, A.D., Kraves, S., Deisseroth, K., Schier, A.F., and Engert, F. (2008). Escape behavior elicited by single, channelrhodopsin-2-evoked spikes in zebrafish somatosensory neurons. Curr. Biol. *18*, 1133–1137.

Dubochet, J. (2007). The physics of rapid cooling and its implications for cryoimmobilization of cells. Cellular Electron Microscopy 7.

Eccles, S.J.C. (1964). The physiology of synapses (Springer).

Fatt, P., and Katz, B. (1951). An analysis of the end-plate potential recorded with an intracellular electrode. J. Physiol. (Lond.) *115*, 320–370.

Fatt, P., and Katz, B. (1952). Spontaneous subthreshold activity at motor nerve endings. J. Physiol. (Lond.) *117*, 109–128.

Fesce, R., Grohovaz, F., Valtorta, F., and Meldolesi, J. (1994). Neurotransmitter release: fusion or "kiss-and-run"? Trends Cell Biol. *4*, 1–4.

Fredj, N.B., and Burrone, J. (2009). A resting pool of vesicles is responsible for spontaneous vesicle fusion at the synapse. Nat Neurosci *12*, 751–758.

Gad, H., Löw, P., Zotova, E., Brodin, L., and Shupliakov, O. (1998). Dissociation between Ca2+-triggered synaptic vesicle exocytosis and clathrin-mediated endocytosis at a central synapse. Neuron *21*, 607–616.

Gaffield, M.A., Romberg, C.F., and Betz, W.J. (2011). Live imaging of bulk endocytosis in frog motor nerve terminals using FM dyes. J Neurophysiol *106*, 599–607.

Gandhi, S.P., and Stevens, C.F. (2003). Three modes of synaptic vesicular recycling revealed by single-vesicle imaging. Nature *423*, 607–613.

Govorunova, E.G., Spudich, E.N., Lane, C.E., Sineshchekov, O.A., and Spudich, J.L. (2011). New channelrhodopsin with a red-shifted spectrum and rapid kinetics from Mesostigma viride. MBio *2*, e00115–00111.

Granseth, B., Odermatt, B., Royle, S.J., and Lagnado, L. (2006). Clathrin-mediated endocytosis is the dominant mechanism of vesicle retrieval at hippocampal synapses. Neuron *51*, 773–786.

Groemer, T.W., and Klingauf, J. (2007). Synaptic vesicles recycling spontaneously and during activity belong to the same vesicle pool. Nat. Neurosci. *10*, 145–147.

Gu, M., Schuske, K., Watanabe, S., Liu, Q., Baum, P., Garriga, G., and Jorgensen, E.M. (2008). Mu2 adaptin facilitates but is not essential for synaptic vesicle recycling in Caenorhabditis elegans. J. Cell Biol *183*, 881–892.

Gunaydin, L.A., Yizhar, O., Berndt, A., Sohal, V.S., Deisseroth, K., and Hegemann, P. (2010). Ultrafast optogenetic control. Nat. Neurosci. *13*, 387–392.

Hebb, C.O., and Whittaker, V.P. (1958). Intracellular distributions of acetylcholine and choline acetylase. J Physiol *142*, 187–196.

Heerssen, H., Fetter, R.D., and Davis, G.W. (2008). Clathrin dependence of synaptic-vesicle formation at the Drosophila neuromuscular junction. Curr. Biol. *18*, 401–409.

Heuser, J.E., and Reese, T.S. (1973). Evidence for recycling of synaptic vesicle membrane during transmitter release at the frog neuromuscular junction. J. Cell Biol *57*, 315–344.

Heuser, J.E., and Reese, T.S. (1981). Structural changes after transmitter release at the frog neuromuscular junction. J. Cell Biol *88*, 564–580.

Heuser, J.E., Reese, T.S., Dennis, M.J., Jan, Y., Jan, L., and Evans, L. (1979). Synaptic vesicle exocytosis captured by quick freezing and correlated with quantal transmitter release. J. Cell Biol *81*, 275–300.

Hodgkin, A.L., and Huxley, A.F. (1936). Action potentials recorded from inside a nerve fibre : Abstract : Nature.

Holt, M., Cooke, A., Wu, M.M., and Lagnado, L. (2003). Bulk membrane retrieval in the synaptic terminal of retinal bipolar cells. J. Neurosci. *23*, 1329–1339.

Ikeda, K., and Bekkers, J.M. (2009). Counting the number of releasable synaptic vesicles in a presynaptic terminal. Proc. Natl. Acad. Sci. U.S.A. *106*, 2945–2950.

Jin, I., Udo, H., Rayman, J.B., Puthanveettil, S., Kandel, E.R., and Hawkins, R.D. (2012). Spontaneous transmitter release recruits postsynaptic mechanisms of long-term and intermediate-term facilitation in Aplysia. PNAS.

Kachar, B., Christakis, N.A., Reese, T.S., and Lane, N.J. (1986). The intramembrane structure of septate junctions based on direct freezing. J. Cell. Sci. *80*, 13–28.

Kennedy, M.J., Hughes, R.M., Peteya, L.A., Schwartz, J.W., Ehlers, M.D., and Tucker, C.L. (2010). Rapid blue-light-mediated induction of protein interactions in living cells. Nat Meth *7*, 973–975.

Kim, S.H., and Ryan, T.A. (2009). Synaptic vesicle recycling at CNS snapses without AP-2. J. Neurosci *29*, 3865–3874.

Koenig, J.H., and Ikeda, K. (1996). Synaptic vesicles have two distinct recycling pathways. J. Cell Biol. *135*, 797–808.

Kopp-Scheinpflug, C., Tolnai, S., Malmierca, M.S., and Rübsamen, R. (2008). The medial nucleus of the trapezoid body: comparative physiology. Neuroscience *154*, 160–170.

Kuffler, S.W., and Yoshikami, D. (1975). The number of transmitter molecules in a quantum: an estimate from iontophoretic application of acetylcholine at the neuromuscular synapse. J. Physiol. (Lond.) *251*, 465–482.

Kuromi, H., and Kidokoro, Y. (2000). Tetanic stimulation recruits vesicles from reserve pool via a cAMP-mediated process in Drosophila synapses. Neuron *27*, 133–143.

Leifer, A.M., Fang-Yen, C., Gershow, M., Alkema, M.J., and Samuel, A.D.T. (2011). Optogenetic manipulation of neural activity in freely moving Caenorhabditis elegans. Nat. Methods *8*, 147–152.

Levskaya, A., Weiner, O.D., Lim, W.A., and Voigt, C.A. (2009). Spatiotemporal control of cell signalling using a light-switchable protein interaction. Nature *461*, 997–1001.

Liewald, J.F., Brauner, M., Stephens, G.J., Bouhours, M., Schultheis, C., Zhen, M., and Gottschalk, A. (2008). Optogenetic analysis of synaptic function. Nat. Methods *5*, 895–902.

Lin, J.Y. (2012). Optogenetic excitation of neurons with channelrhodopsins: Light instrumentation, expression systems, and channelrhodopsin variants. Prog. Brain Res. *196*, 29–47.

Lin, J.Y., Lin, M.Z., Steinbach, P., and Tsien, R.Y. (2009). Characterization of Engineered Channelrhodopsin Variants with Improved Properties and Kinetics. Biophysical Journal *96*, 1803–1814.

Liu, Q., Hollopeter, G., and Jorgensen, E.M. (2009). Graded synaptic transmission at the Caenorhabditis elegans neuromuscular junction. Proceedings of the National Academy of Sciences *106*, 10823 –10828.

Llinás, R., Steinberg, I.Z., and Walton, K. (1976). Presynaptic calcium currents and their relation to synaptic transmission: voltage clamp study in squid giant synapse and theoretical model for the calcium gate. Proc. Natl. Acad. Sci. U.S.A. *73*, 2918–2922.

Llinás, R., Steinberg, I.Z., and Walton, K. (1981). Presynaptic calcium currents in squid giant synapse. Biophys. J. *33*, 289–321.

Lorteije, J.A.M., Rusu, S.I., Kushmerick, C., and Borst, J.G.G. (2009). Reliability and precision of the mouse calyx of Held synapse. J. Neurosci *29*, 13770–13784.

Maeno-Hikichi, Y., Polo-Parada, L., Kastanenka, K.V., and Landmesser, L.T. (2011). Frequency-dependent modes of synaptic vesicle endocytosis and exocytosis at adult mouse neuromuscular junctions. J. Neurosci *31*, 1093–1105.

Mathew, S.S., Pozzo-Miller, L., and Hablitz, J.J. (2008). Kainate modulates presynaptic GABA release from two vesicle pools. J. Neurosci. *28*, 725–731.

Matthew, W.D., Tsavaler, L., and Reichardt, L.F. (1981). Identification of a synaptic vesicle-specific membrane protein with a wide distribution in neuronal and neurosecretory tissue. J. Cell Biol. *91*, 257–269.

Maycox, P.R., Link, E., Reetz, A., Morris, S.A., and Jahn, R. (1992). Clathrin-coated vesicles in nervous tissue are involved primarily in synaptic vesicle recycling. J. Cell Biol *118*, 1379–1388.

McDonald, K. (2007). Cryopreparation methods for electron microscopy of selected model systems. Methods Cell Biol. *79*, 23–56.

McDonald, K., Schwarz, H., Müller-Reichert, T., Webb, R., Buser, C., and Morphew, M. (2010). "Tips and tricks" for high-pressure freezing of model systems. Methods Cell Biol. *96*, 671–693.

McDonald, K.L., Morphew, M., Verkade, P., and Müller-Reichert, T. (2007). Recent advances in high-pressure freezing: equipment- and specimen-loading methods. Methods Mol. Biol. *369*, 143–173.

McDonald, K.L., and Webb, R.I. (2011). Freeze substitution in 3 hours or less. J Microsc *243*, 227–233.

McKinney, R.A., Capogna, M., Dürr, R., Gähwiler, B.H., and Thompson, and S.M. (1999). Miniature synaptic events maintain dendritic spines via AMPA receptor activation. Nature Neuroscience *2*, 44–49.

Milburn, T., Matsubara, N., Billington, A.P., Udgaonkar, J.B., Walker, J.W., Carpenter, B.K., Webb, W.W., Marque, J., Denk, W., and McCray, J.A. (1989). Synthesis, photochemistry, and biological activity of a caged photolabile acetylcholine receptor ligand. Biochemistry *28*, 49–55.

Miller, T.M., and Heuser, J.E. (1984). Endocytosis of synaptic vesicle membrane at the frog neuromuscular junction. J. Cell Biol *98*, 685–698.

Moor, H. (1987). Theory and practice of high pressure freezing. In Cryotechiniques in Biological Electron Microscopy, (Berlin: Springer-Verlag), pp. 175–191.

Moor, H., and Riehle, U. (1968). Snap-freezing under high pressure: A new fixation technique for freeze-etching. pp. 33–34.

Mueller-Reichert, T. (2010). Electron Microscopy of Model Systems, Volume 96 (Academic Press).

Müller-Reichert, T., Mäntler, J., Srayko, M., and O'Toole, E. (2008). Electron microscopy of the early Caenorhabditis elegans embryo. Journal of Microscopy *230*, 297–307.

Murphy, T.H., Blatter, L.A., Bhat, R.V., Fiore, R.S., Wier, W.G., and Baraban, J.M. (1994). Differential regulation of calcium/calmodulin-dependent protein kinase II and p42 MAP kinase activity by synaptic transmission. J. Neurosci. *14*, 1320–1331.

Nagel, G., Brauner, M., Liewald, J.F., Adeishvili, N., Bamberg, E., and Gottschalk, A. (2005a). Light activation of channelrhodopsin-2 in excitable cells of Caenorhabditis elegans triggers rapid behavioral responses. Curr. Biol. *15*, 2279–2284.

Nagel, G., Brauner, M., Liewald, J.F., Adeishvili, N., Bamberg, E., and Gottschalk, A. (2005b). Light activation of channelrhodopsin-2 in excitable cells of Caenorhabditis elegans triggers rapid behavioral responses. Curr. Biol. *15*, 2279–2284.

Nagel, G., Ollig, D., Fuhrmann, M., Kateriya, S., Musti, A.M., Bamberg, E., and Hegemann, P. (2002). Channelrhodopsin-1: a light-gated proton channel in green algae. Science *296*, 2395–2398.

Nagel, G., Szellas, T., Huhn, W., Kateriya, S., Adeishvili, N., Berthold, P., Ollig, D., Hegemann, P., and Bamberg, E. (2003a). Channelrhodopsin-2, a directly light-gated cation-selective membrane channel. Proceedings of the National Academy of Sciences of the United States of America *100*, 13940 –13945.

Nagel, G., Szellas, T., Huhn, W., Kateriya, S., Adeishvili, N., Berthold, P., Ollig, D., Hegemann, P., and Bamberg, E. (2003b). Channelrhodopsin-2, a directly light-gated cation-selective membrane channel. Proc. Natl. Acad. Sci. U.S.A. *100*, 13940–13945.

Neill, P.J., Smith, J.H., Doughty, B.L., and Kemp, M. (1988). The ultrastructure of the Schistosoma mansoni egg. Am. J. Trop. Med. Hyg. *39*, 52–65.

Otsu, Y., and Murphy, T.H. (2003). Miniature transmitter release: accident of nature or careful design? Sci. STKE *2003*, pe54.

Paillart, C., Li, J., Matthews, G., and Sterling, P. (2003). Endocytosis and vesicle recycling at a ribbon synapse. J. Neurosci *23*, 4092–4099.

Palay, S.L., and Palade, G.E. (1955). The fine structure of neurons. J Biophys Biochem Cytol *1*, 69–88.

Perin, M.S., Brose, N., Jahn, R., and Südhof, T.C. (1991). Domain structure of synaptotagmin (p65). J. Biol. Chem. *266*, 623–629.

Pyle, J.L., Kavalali, E.T., Piedras-Rentería, E.S., and Tsien, R.W. (2000). Rapid reuse of readily releasable pool vesicles at hippocampal synapses. Neuron *28*, 221–231.

Rasmussen, D.H., Macaulay, M.N., and MacKenzie, A.P. (1975). Supercooling and nucleation of ice in single cells. Cryobiology *12*, 328–339.

Richards, D.A., Bai, J., and Chapman, E.R. (2005). Two modes of exocytosis at hippocampal synapses revealed by rate of FM1-43 efflux from individual vesicles. J. Cell Biol *168*, 929–939.

Richards, D.A., Guatimosim, C., and Betz, W.J. (2000). Two Endocytic Recycling Routes Selectively Fill Two Vesicle Pools in Frog Motor Nerve Terminals. Neuron *27*, 551–559.

Rizzoli, S.O., and Betz, W.J. (2002). Effects of 2-(4-morpholinyl)-8-phenyl-4H-1-benzopyran-4-one on synaptic vesicle cycling at the frog neuromuscular junction. J. Neurosci. *22*, 10680–10689.

Rizzoli, S.O., and Betz, W.J. (2005). Synaptic vesicle pools. Nat. Rev. Neurosci *6*, 57–69.

de Robertis, E.D., and Bennett, H.S. (1954). A submicroscopic vesicular component of Schwann cells and nerve satellite cells. Exp. Cell Res. *6*, 543–545.

de Robertis, E.D., and Bennett, H.S. (1955). Some features of the submicroscopic morphology of synapses in frog and earthworm. J Biophys Biochem Cytol *1*, 47–58.

Rosenmund, C., and Stevens, C.F. (1996). Definition of the readily releasable pool of vesicles at hippocampal synapses. Neuron *16*, 1197–1207.

Rosenmund, C., and Stevens, C.F. (1997). The rate of aldehyde fixation of the exocytotic machinery in ultured hippocampal synapses. Journal of Neuroscience Methods *76*, 1–5.

Rostaing, P., Weimer, R.M., Jorgensen, E.M., Triller, A., and Bessereau, J.-L. (2004). Preservation of immunoreactivity and fine structure of adult C. elegans tissues using high-pressure freezing. J. Histochem. Cytochem *52*, 1–12.

Royle, S.J., and Lagnado, L. (2003). Endocytosis at the synaptic terminal. J. Physiol. (Lond.) *553*, 345–355.

Sara, Y., Virmani, T., Deák, F., Liu, X., and Kavalali, E.T. (2005). An isolated pool of vesicles recycles at rest and drives spontaneous neurotransmission. Neuron *45*, 563–573.

Sato, K., Ernstrom, G., Watanabe, S., Weimer, R., Chen, C., Sato, M., Siddiqui, A., Jorgensen, E., and Grant, B. (2009). Differential requirements for clathrin in receptor-mediated endocytosis and maintenance of synaptic vesicle pools. Proceedings of the National Academy of Sciences *106*, 1139.

Schikorski, T., and Stevens, C.F. (1997). Quantitative ultrastructural analysis of hippocampal excitatory synapses. J. Neurosci *17*, 5858–5867.

Schikorski, T., and Stevens, C.F. (2001). Morphological correlates of functionally defined synaptic vesicle populations. Nat. Neurosci *4*, 391–395.

Schobert, B., and Lanyi, J.K. (1982). Halorhodopsin is a light-driven chloride pump. J. Biol. Chem. *257*, 10306–10313.

Sineshchekov, O.A., Jung, K.-H., and Spudich, J.L. (2002). Two rhodopsins mediate phototaxis to low- and high-intensity light in Chlamydomonas reinhardtii. Proc. Natl. Acad. Sci. U.S.A. *99*, 8689–8694.

Smith, J.E., and Reese, T.S. (1980). Use of aldehyde fixatives to determine the rate of synaptic transmitter release. J. Exp. Biol. *89*, 19–29.

Stevens, C.F., and Tsujimoto, T. (1995). Estimates for the pool size of releasable quanta at a single central synapse and for the time required to refill the pool. Proc. Natl. Acad. Sci. U.S.A *92*, 846–849.

Sun, J.-Y., Wu, X.-S., and Wu, L.-G. (2002). Single and multiple vesicle fusion induce different rates of endocytosis at a central synapse. Nature *417*, 555–559.

Sutton, M.A., Wall, N.R., Aakalu, G.N., and Schuman, E.M. (2004). Regulation of dendritic protein synthesis by miniature synaptic events. Science *304*, 1979–1983.

Takei, K., Haucke, V., Slepnev, V., Farsad, K., Salazar, M., Chen, H., and De Camilli, P. (1998). Generation of coated intermediates of clathrin-mediated endocytosis on protein-free liposomes. Cell *94*, 131–141.

Teng, H., Lin, M.Y., and Wilkinson, R.S. (2007). Macroendocytosis and endosome processing in snake motor boutons. J. Physiol. (Lond.) *582*, 243–262.

Torri-Tarelli, F., Grohovaz, F., Fesce, R., and Ceccarelli, B. (1985). Temporal coincidence between synaptic vesicle fusion and quantal secretion of acetylcholine. J. Cell Biol *101*, 1386–1399.

Verhage, M., Maia, A.S., Plomp, J.J., Brussaard, A.B., Heeroma, J.H., Vermeer, H., Toonen, R.F., Hammer, R.E., Den, T.K. van, Berg, et al. (2000). Synaptic Assembly of the Brain in the Absence of Neurotransmitter Secretion. Science *287*, 864–869.

Verkade, P. (2008). Moving EM: the Rapid Transfer System as a new tool for correlative light and electron microscopy and high throughput for high-pressure freezing. J Microsc *230*, 317–328.

Walker, J.W., McCray, J.A., and Hess, G.P. (1986). Photolabile protecting groups for an acetylcholine receptor ligand. Synthesis and photochemistry of a new class of o-nitrobenzyl derivatives and their effects on receptor function. Biochemistry *25*, 1799–1805.

Whittaker, V.P. (1959). The isolation and characterization of acetylcholine-containing particles from brain. Biochem J. *72*, 694-706.

Wieboldt, R., Gee, K.R., Niu, L., Ramesh, D., Carpenter, B.K., and Hess, G.P. (1994). Photolabile precursors of glutamate: synthesis, photochemical properties, and activation of glutamate receptors on a microsecond time scale. Proc. Natl. Acad. Sci. U.S.A *91*, 8752–8756.

Wilhelm, B.G., Groemer, T.W., and Rizzoli, S.O. (2010). The same synaptic vesicles drive active and spontaneous release. Nat. Neurosci. *13*, 1454–1456.

Wu, W., and Wu, L.-G. (2007). Rapid bulk endocytosis and its kinetics of fission pore closure at a central synapse. Proc. Natl. Acad. Sci. U.S.A. *104*, 10234–10239.

Wu, W., Xu, J., Wu, X.-S., and Wu, L.-G. (2005). Activity-dependent acceleration of endocytosis at a central synapse. J. Neurosci. *25*, 11676–11683.

Wu, X.-S., and Wu, L.-G. (2009). Rapid endocytosis does not recycle vesicles within the readily releasable pool. J. Neurosci. *29*, 11038–11042.

Yamashita, T., Hige, T., and Takahashi, T. (2005). Vesicle endocytosis requires dynamin-dependent GTP hydrolysis at a fast CNS synapse. Science *307*, 124–127.

Yazawa, M., Sadaghiani, A.M., Hsueh, B., and Dolmetsch, R.E. (2009). Induction of protein-protein interactions in live cells using light. Nature Biotechnology *27*, 941–945.

Yizhar, O., Fenno, L.E., Davidson, T.J., Mogri, M., and Deisseroth, K. (2011). Optogenetics in neural systems. Neuron *71*, 9–34.

Zenisek, D., Steyer, J.A., and Almers, W. (2000). Transport, capture and exocytosis of single synaptic vesicles at active zones. Nature *406*, 849–854.

Zhang, F., Wang, L.-P., Brauner, M., Liewald, J.F., Kay, K., Watzke, N., Wood, P.G., Bamberg, E., Nagel, G., Gottschalk, A., et al. (2007a). Multimodal fast optical interrogation of neural circuitry. Nature *446*, 633–639.

Zhang, Q., Cao, Y.-Q., and Tsien, R.W. (2007b). Quantum dots provide an optical signal specific to full collapse fusion of synaptic vesicles. Proc. Natl. Acad. Sci. U.S.A *104*, 17843–17848.

Zhang, Q., Li, Y., and Tsien, R.W. (2009). The dynamic control of kiss-and-run and vesicular reuse probed with single nanoparticles. Science *323*, 1448–1453.

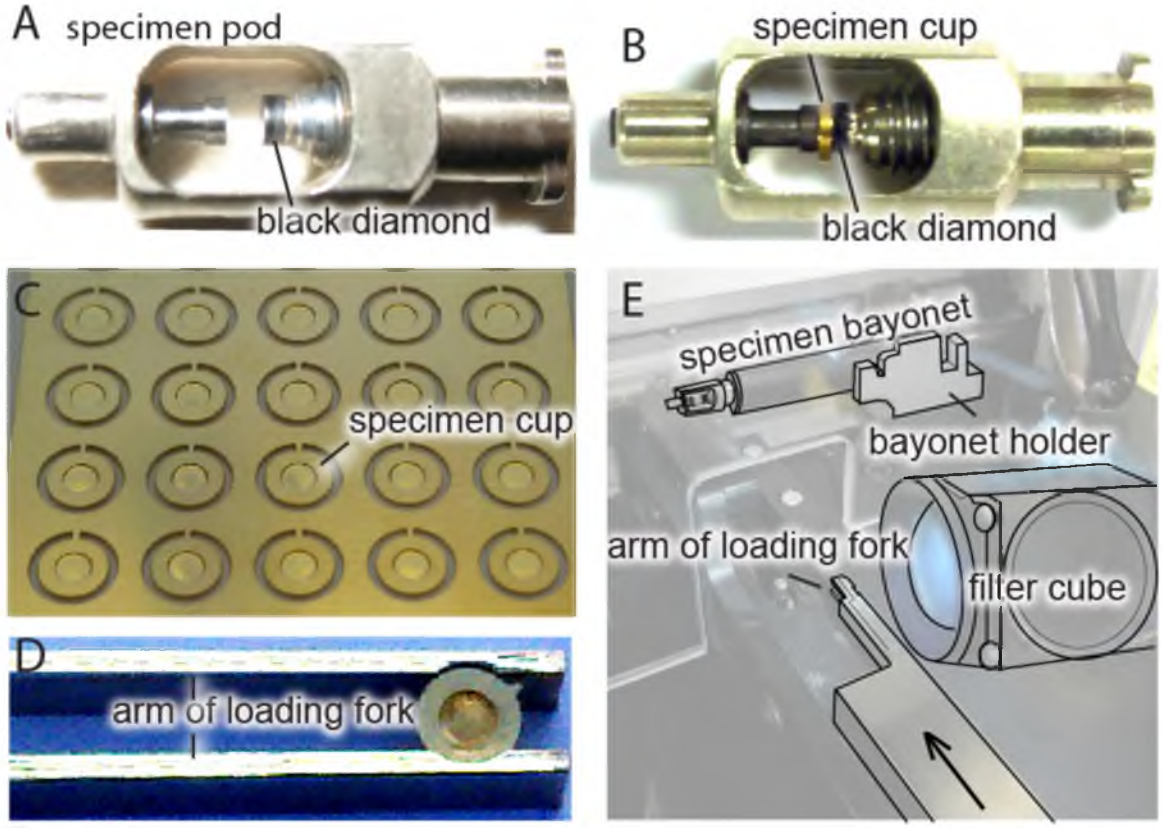

Fig. 2.1. Specimen mounting. (A) A specimen pod without the sample cup. (B) A specimen pod with a sample cup in place. Note that once the carrier is mounted in the pod, the specimens face the black diamond and cannot be exposed to light. (C) Sheet of 20 sample cups for the EM Pact2. Each cup can be detached from the surrounding metal by prying back and forth with forceps. Specimens are mounted into the depression of the sample cup (1.6 mm in diameter and 100 µm deep). (D) A sample cup is loaded into the arm of the loading fork. Note that the specimens are in an open cup and could potentially be exposed to light. (E) The experimental setup for light stimulation using the EM Pact2-RTS. A filter cube attached at the tip of an optical fiber can be placed next to the specimen loading path to shine light onto the specimen for up to two seconds before freezing. After stimulation, specimens are screwed into the specimen pod simply by sliding the loading device to the specimen pod (indicated by a black arrow on the loading device). Once the sample cup is screwed securely into the pod, the specimen bayonet is rapidly driven down a rail into the freezing chamber.

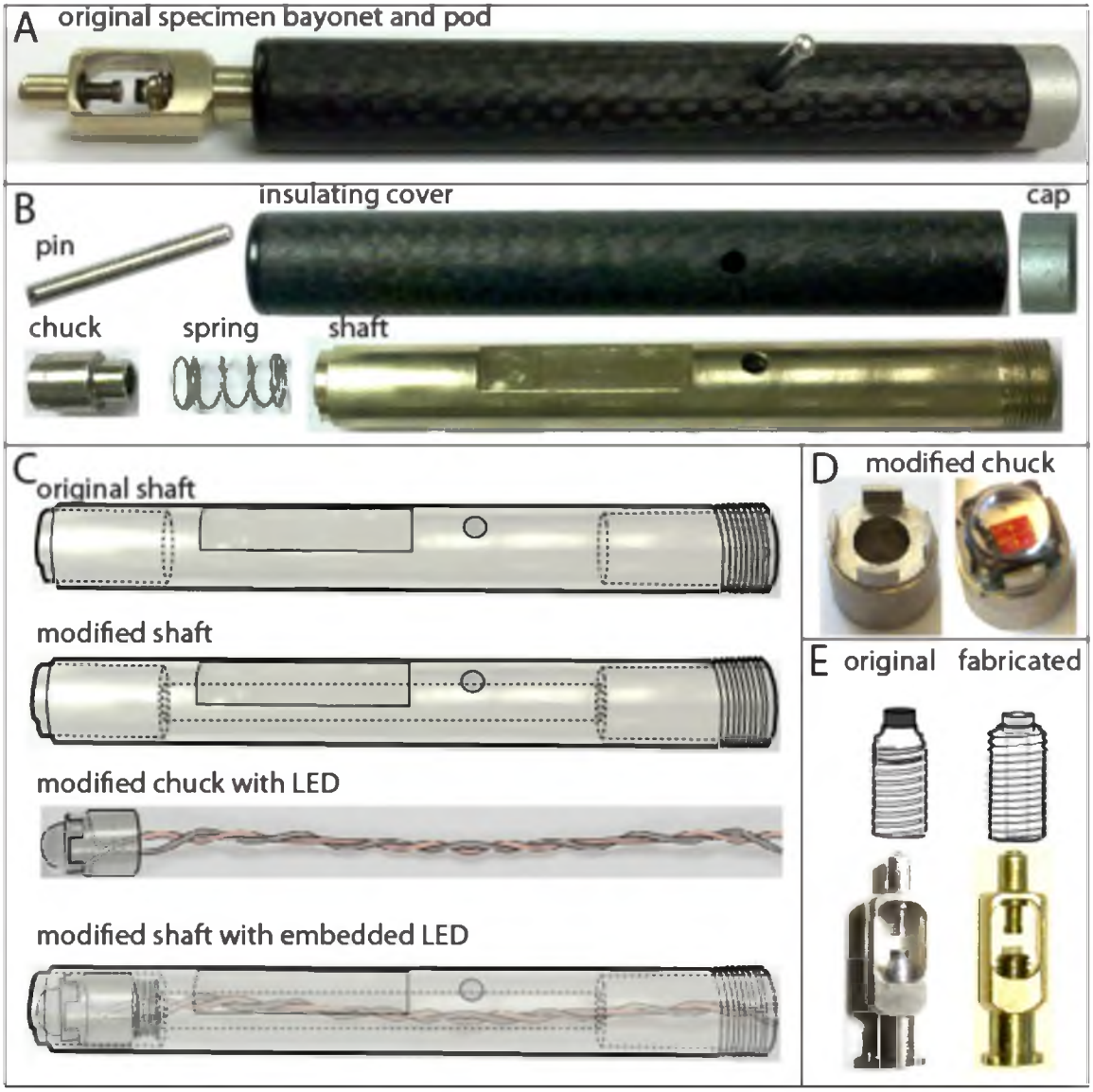

Fig. 2.2. Modifications of specimen bayonet and pod. (A) The original specimen bayonet and pod. (B) All six components of the specimen bayonet. (C) Schematic diagrams for bayonet modifications. The dotted lines represent the holes in the bayonet. We drilled a 2 mm hole in the middle as indicated in the modified shaft. We placed an LED onto the modified chuck. Finally, the modified pieces were assembled. (D) A modified chuck without (left) and with an LED (right). (E) Schematic diagrams (top) and photographs (bottom) showing the modified specimen pod. A screw with a 1.2 mm hole (dotted lines) was fabricated, and a sapphire anvil was glued into the countersink. These modifications allow for the application of light to the specimens milliseconds before freezing.

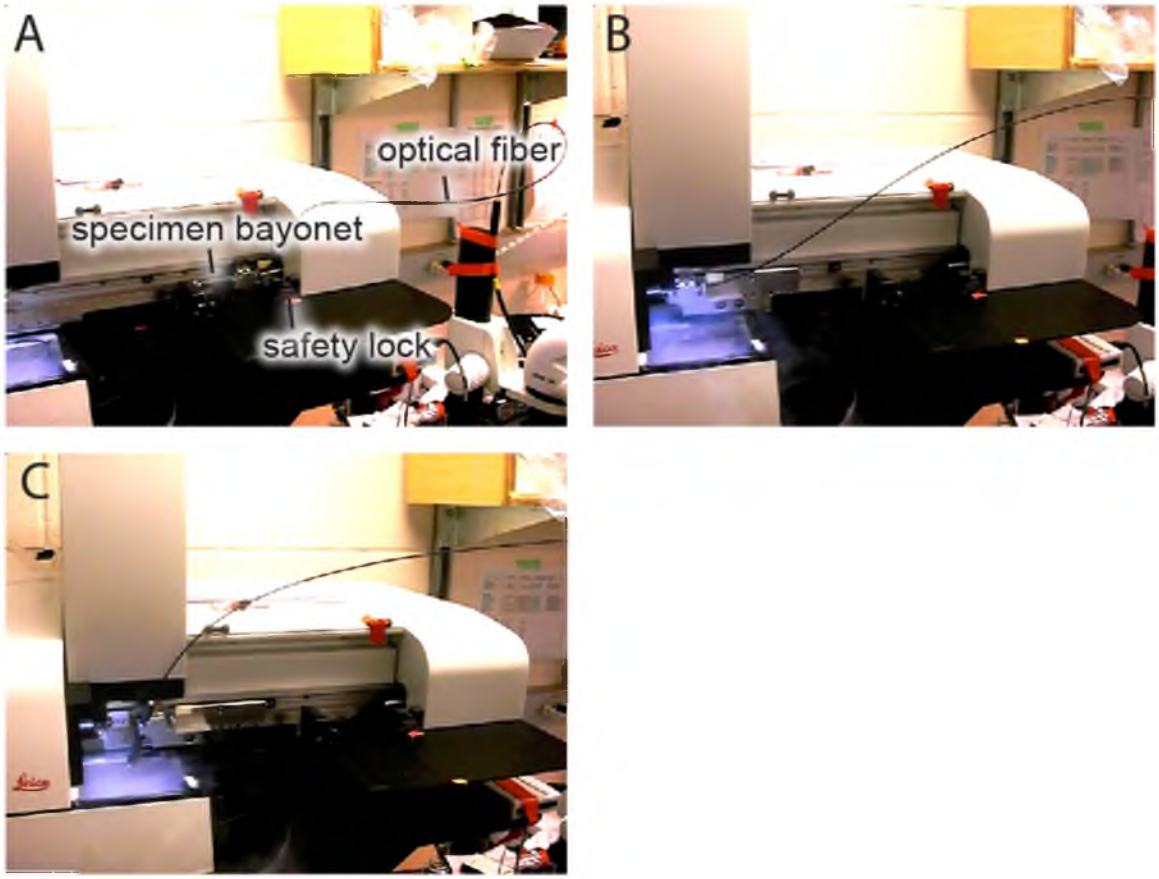

Fig. 2.3. Optional fiber optic configuration. (A) An optical fiber can be mounted into the modified bayonet. (B) A sample holder is driven into the freezing chamber. (C) The specimen bayonet is retracted from the freezing chamber, and the sample drops into the liquid nitrogen bath following high-pressure freezing.

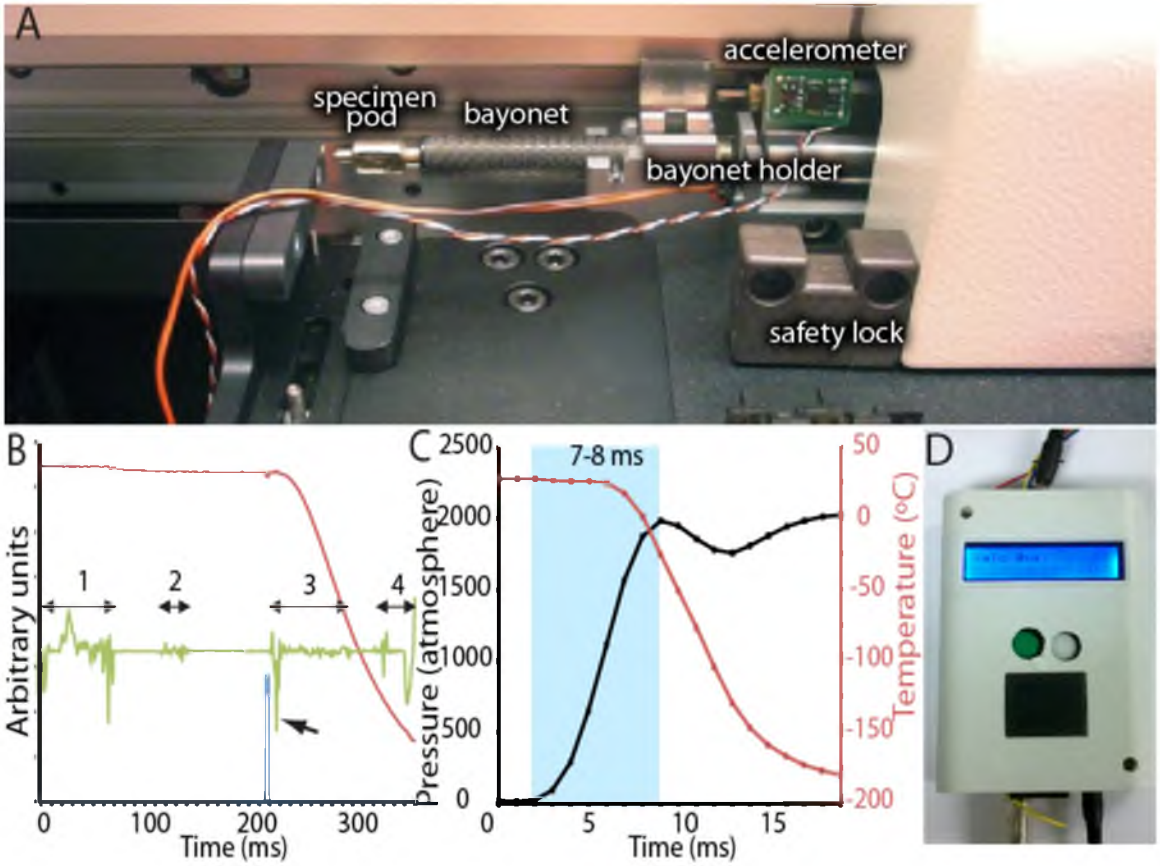

Fig. 2.4. Measuring the light flash to freezing interval. Temporal resolution for light stimulation is improved by implementing an accelerometer. (A) An accelerometer is attached to the bayonet holder. (B) A graph showing the readouts from a light stimulation device (blue), a thermistor (red), and an accelerometer (green). The outputs from the sensors were all recorded by a computer program. The readout from the accelerometer shows four intervals with multiple peaks. Interval 1 indicates the termination of the specimen bayonet movement along the rail as it enters the freezing chamber. The specimen bayonet is locked in place for freezing during interval 2. Pressure application occurs at the first downward deflection indicated by a black arrow in the interval 3. The specimen bayonet is retracted from the chamber during interval 4. (C) A graph showing the pressure and temperature readouts recorded by the high-pressure freezer. Pressure is indicated by the black line, and its value is found on the primary y-axis (black line). Temperature is indicated by the red line, and its value is found on the secondary y-axis (red line). There is a delay of about 7 to 8 ms from the application of pressure to the freezing of specimens below 0ºC. (D) The final light stimulation controller. The controller sends out signals to fire both the light stimulation and the freezer upon pressing the green button. The light stimulation protocols can be programmed using a computer, sent to the controller via a USB cable, and stored in a microSD card inserted into the controller. Different stimulation protocols can be selected by pressing the white button. The display shows the current protocol selected.

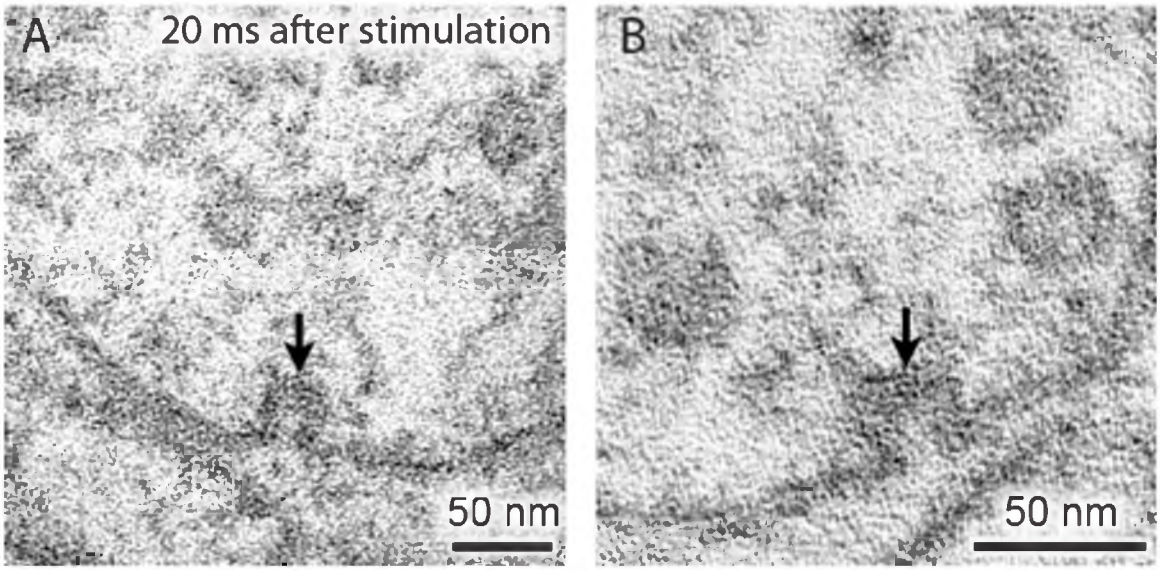

Fig. 2.5. Fusion intermediates are captured by freezing specimens 20 ms after light stimulation. (A, B) Electron micrographs of *C. elegans* motor neurons showing synaptic vesicle fusion intermediates. A single light pulse of 20 ms was applied to transgenic animals expressing ChIEF 20 ms before high-pressure freezing.

CHAPTER 3

PROTEIN LOCALIZATION IN ELECTRON MICROGRAPHS USING FLUORESNCE NANOSCOPY

Reprinted with permission from the Nature America, Inc.

Watanabe, et al., 2011. Originally published in Nature Methods. VOL. 1(8): 80-84

Protein localization in electron micrographs using fluorescence nanoscopy

Shigeki Watanabe[1], Annedore Punge[2], Gunther Hollopeter[1], Katrin I Willig[2], Robert John Hobson[1], M Wayne Davis[1], Stefan W Hell[2] & Erik M Jorgensen[1]

A complete portrait of a cell requires a detailed description of its molecular topography: proteins must be linked to particular organelles. Immunocytochemical electron microscopy can reveal locations of proteins with nanometer resolution but is limited by the quality of fixation, the paucity of antibodies and the inaccessibility of antigens. Here we describe correlative fluorescence electron microscopy for the nanoscopic localization of proteins in electron micrographs. We tagged proteins with the fluorescent proteins Citrine or tdEos and expressed them in *Caenorhabditis elegans*, fixed the worms and embedded them in plastic. We imaged the tagged proteins from ultrathin sections using stimulated emission depletion (STED) microscopy or photoactivated localization microscopy (PALM). Fluorescence correlated with organelles imaged in electron micrographs from the same sections. We used these methods to localize histones, a mitochondrial protein and a presynaptic dense projection protein in electron micrographs.

Proteins can be imaged in cells by tagging them with fluorescent proteins or antibodies. However, the resolution of conventional optical approaches is limited to about 200 nm by the diffraction of light and to even poorer resolutions in practice[1]. By contrast, typical proteins are about 4 nm in diameter and may be associated with organelles as small as 30 nm. Thus, localization of proteins to cellular structures using fluorescence methods is fairly crude. Recently, fluorescence techniques capable of nanometer-scale resolution ('nanoscopy')[2] have been developed, which permit separation of fluorophores closer than the diffraction limit[2].

In stimulated emission depletion (STED) microscopy[3], fluorescence is inhibited by a beam of light, called the STED beam. Patterned as a doughnut and overlaid with the excitation beam of a scanning microscope, this beam ensures that only fluorophores in a narrow region around the doughnut center are allowed to fluoresce; the other molecules illuminated by the excitation light remain dark[4]. Photoactivated localization microscopy (PALM) and similar techniques (fluorescence PALM (FPALM) and stochastic optical reconstruction microscopy (STORM))[5–7] use photoactivatable molecules whose fluorescence is activated by the absorption of a photon (usually ultraviolet). To separate features that are closer than the diffraction limit, only one fluorophore is randomly activated; the neighboring molecules remain dark. The position of the fluorophore is determined by calculating the centroid of the emission pattern. The registered molecules are subsequently turned off by bleaching, allowing adjacent molecules to be activated and become fluorescent. This sequence is continued until all molecules are registered.

Fluorescence nanoscopy can be used to localize proteins precisely[5], but the cellular context is limited in these images. Immunocytochemical electron microscopy (immuno-EM) can be used to localize proteins to organelles. However, this method is compromised by technical difficulties including the destruction of antigens, inaccessibility of antigens, the lack of suitable antibodies and nonspecific binding of antibodies[8–10]. Even when this method is used successfully, the size of antibodies (~19 nm long)[11] limits the ultimate resolution, particularly when secondary antibodies are used.

The advantage of fluorescence microscopy is that all proteins can potentially be tagged with a fluorophore. The advantage of electron microscopy is its exquisite depiction of subcellular structure. As their strengths are complementary, these two methods can be very effective if combined[12,13]. PALM has been performed on cryo-sectioned material fixed with aldehydes[5]. However, subcellular details are obscure in cryo-sections because of poor tissue contrast. Morphology could be improved using traditional electron microscopy techniques, but fluorescent proteins are quenched by the acidic, dehydrated and oxidizing conditions required for fixation and polymer embedding of the specimen[14]. Ultimately, a compromise must be found between preservation of fluorescence and morphology. To develop a practical method for correlative fluorescence electron microscopy, here we optimized each step of sample preparation, balancing the requirements for fluorescence and ultrastructure. As our model system, we used the nematode *Caenorhabditis elegans* because fluorescently tagged proteins can be stably expressed[15,16] and methods for electron microscopy are well established for this organism[9]. We developed methods to use both STED microscopy and PALM on ultrathin sections of fixed tissues to localize proteins at the nanoscale and subsequently correlate protein localization with ultrastructural features revealed by electron microscopy.

[1]Department of Biology and Howard Hughes Medical Institute, University of Utah, Salt Lake City, Utah, USA. [2]Department of NanoBiophotonics, Max Planck Institute for Biophysical Chemistry, Gottingen, Germany. Correspondence should be addressed to E.M.J. (jorgensen@biology.utah.edu).

RECEIVED 3 JUNE; ACCEPTED 20 OCTOBER; PUBLISHED ONLINE 21 NOVEMBER 2010; DOI:10.1038/NMETH.1537

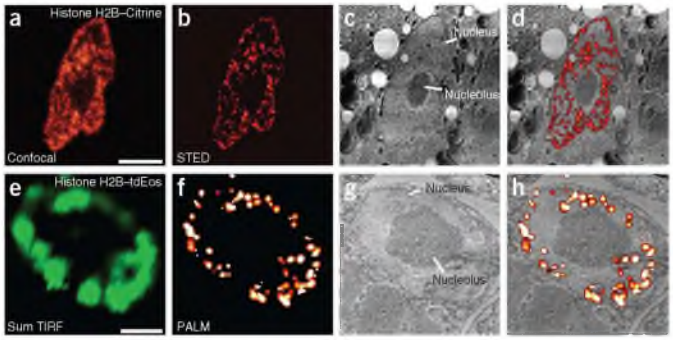

Figure 1 | Correlative fluorescence and electron microscopy using histone H2B fusion proteins. (**a**–**c**) Confocal image (**a**), STED image (**b**) and electron micrograph (**c**) from the same thin GMA section (120 nm) from a worm expressing histone H2B–Citrine. (**d**) Correlative STED microscopy and electron micrographs showing histone H2B–Citrine (overlay of the images in **b** and **c**). The images in **a**–**d** show an intestinal cell nucleus. (**e**–**g**) Sum TIRF image (**e**; represents all the photons detected by the camera during the experiment), PALM image (**f**) and electron micrograph (**g**) from a thin GMA section (70 nm) from a worm expressing histone H2B–tdEos. (**h**) Correlative PALM and electron micrographs showing histone H2B–tdEos (overlay of the images in **f** and **g**). The images in **e**–**h** show a muscle cell nucleus. Scale bars, 3 μm (**a**–**d**) and 1 μm (**e**–**h**).

RESULTS

Choice of target proteins

To evaluate fluorescence localization in electron micrographs, we tagged three proteins with well-described localization: histone H2B (encoded by *his-11*), translocase of outer mitochondrial membrane–20 (TOM20; encoded by *tomm-20*) and α-liprin (encoded by *syd-2*). Histones are localized to the nucleus. The nucleus can be easily visualized using a conventional light microscope, and the use of histone H2B is ideal for rapid optimization of preservation of fluorescence (**Fig. 1**). TOM20 is a 20-kDa mitochondrial outer membrane protein. A cross-section of mitochondria can be as narrow as 150 nm in diameter, which is below the diffraction limit, and thus TOM20 localization is a good test of super-resolution methodologies (**Fig. 2**). α-liprin is localized to the presynaptic dense projection[17]. Neurons in *C. elegans* are the most sensitive tissue to fixation and α-liprin localization required us to fully optimize our protocol (**Fig. 3**).

Optimization of fixatives

Fixatives cross-link cellular structures and protect the tissue from distortions caused by dehydration and embedding in plastic. Aldehyde-based fixatives, especially glutaraldehyde, cross-link proteins very effectively. Metallic oxide fixatives, such as osmium tetroxide, cross-link unsaturated lipids in membranes[18]. As osmium tetroxide scatters electrons, it also acts as a contrast enhancer for membranes. These fixatives also have disadvantages for fluorescence microscopy. Glutaraldehyde induces autofluorescence in fixed tissues[19]. Osmium tetroxide is a very strong oxidizing agent and can break peptide bonds, and GFP fluorescence is quenched by oxidation[14]. Thus, to evaluate the preservation of both fluorescence and morphology, we tested multiple combinations of fixatives at various concentrations.

We processed transgenic worms expressing Citrine or tandem dimer (td)Eos fused to histone H2B. For each treatment, we evaluated worms on a compound microscope before polymerization of the plastic to gauge the amount of fluorescence loss owing to the fixation. We evaluated morphology from ultrathin sections of neurons because of their sensitivity to fixation. As anticipated, fixation with aldehyde-based fixatives (paraformaldehyde, glutaraldehyde and acrolein) resulted in induction of autofluorescence. Autofluorescence could be quenched by 1% sodium borohydride[19], but cell membranes were not well preserved by aldehyde-based fixatives (**Supplementary Fig. 1a,b**). A low concentration of osmium tetroxide (0.1%) preserved membrane morphology effectively, but fluorescence was reduced to less than 10% after fixation and embedding in plastic (**Supplementary Fig. 1c,d**). If we applied osmium tetroxide at concentrations of less than 0.1%, we observed substantial degradation in tissue morphology. Another lipid cross-linking agent, potassium permanganate[9] (0.1%) preserved membrane morphology well (**Supplementary Fig. 1e**). Despite the fact that potassium permanganate is also an oxidizing agent, the fluorescence was about 30-fold brighter than with 0.1% osmium tetroxide (**Supplementary Fig. 1f**). However, synaptic vesicles appeared to be missing from the synaptic terminals (**Supplementary Fig. 1e**). To optimize membrane morphology, we added 0.001% osmium tetroxide to 0.1% potassium permanganate. With this cocktail, the morphology of neurons was better than with

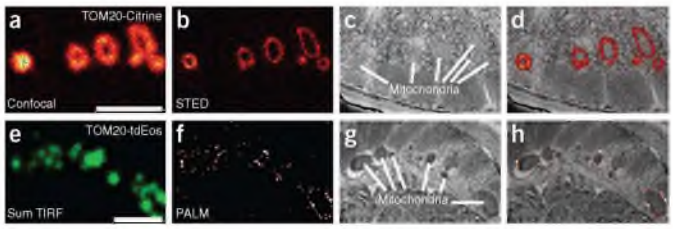

Figure 2 | Correlative fluorescence and electron microscopy using TOM20 fusion proteins. (**a**–**c**) Confocal image (**a**), STED image (**b**) and electron micrograph (**c**) from the same GMA thin section (120 nm) of a worm expressing TOM20–Citrine. (**d**) Correlative STED and electron micrographs showing TOM20–Citrine (overlay of the images in **b** and **c**). (**e**–**g**) Sum TIRF image (**e**), PALM image (**f**) and electron micrograph (**g**) from a thin LR White section (70 nm) of a worm expressing TOM20–tdEos. (**h**) Correlative PALM and electron micrographs showing TOM20–tdEos (overlay of the images in **f** and **g**). PALM images of sections from a worm expressing TOM20–tdEos are from tissue embedded in LR White; all other samples were embedded in GMA. Scale bars, 1 μm (**a**–**d**) and 2 μm (**e**–**h**).

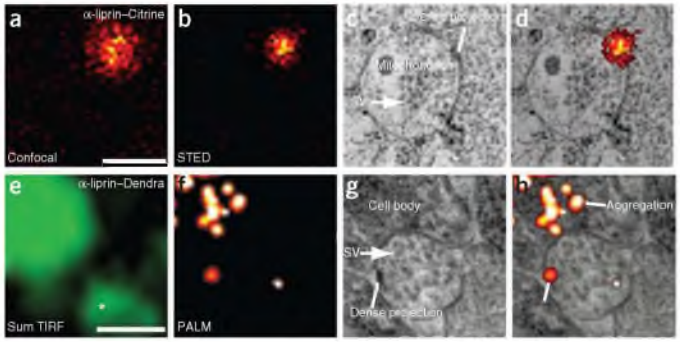

Figure 3 | Correlative fluorescence and electron microscopy using α-liprin fusion proteins. (**a**–**c**) Confocal image (**a**), STED image (**b**) and electron micrograph (**c**) of the same thin GMA section (70 nm) from a worm expressing α-liprin–Citrine. (**d**) Correlative STED microscopy and electron micrographs showing α-liprin–Citrine (overlay of the images in **b** and **c**). (**e**–**g**) Sum TIRF image (**e**), PALM image (**f**) and electron micrograph (**g**) from a thin section (70 nm) of a section of a worm expressing α-liprin–Dendra. Asterisk in **e** marks a region of predominant background signal, which was discarded by emission time threshold. (**h**) Correlative PALM and electron micrographs showing α-liprin–Dendra (overlay of the images in **f** and **g**). SV, synaptic vesicle. Scale bars, 500 nm.

either fixative alone at these concentrations (**Supplementary Fig. 1g**). Fluorescence was almost as bright as with 0.1% potassium permanganate alone (fluorescence was 40% of that for untreated worms; **Supplementary Fig. 1h**), and we observed strong fluorescence for both Citrine and tdEos after sectioning (**Fig. 1a,e**).

Optimization of plastic

After fixation, we embedded tissue samples in plastic resin for ultrathin sectioning. Polymerization typically requires dehydration and heat, which tend to denature proteins, including fluorophores. We processed worms expressing Citrine or tdEos fused to histone H2B (*Phsp-16.41::fluor::his-11::unc-54 3′UTR*) as described above and embedded them in the following hydrophilic resins capable of low-temperature polymerization: Lowicryl K4M (from EMS), LR Gold (from EMS), LR White (from EMS) and glycol methacrylate (GMA; from SPI). Additionally, we included 2–5% water in each resin. After polymerization, we assessed fluorescence preservation and sectioning quality.

Lowicryl K4M, the most hydrophilic resin, can reportedly tolerate up to 10% water by weight[20]. However, in our hands, inclusion of 5% water reduced the sectioning quality of the tissues beyond an acceptable level owing to poor polymerization.

LR Gold and LR White are very similar in their formula and chemistry; however, slightly different problems arose with polymerization. LR Gold polymerized rapidly but did not penetrate the tissue. The pH of LR White was too acidic for most fluorescent proteins; the pH with 2–5% water was quite low (~5.5). Neutralizing the pH of the plastic using ethanolamine preserved fluorescence (**Supplementary Fig. 1**) and resulted in good morphology (**Supplementary Fig. 1g**). However, batch-to-batch variability in pH and water capacity of LR White resulted in irregular polymerization.

GMA, by contrast, requires 3% water for polymerization at pH 8, fulfilling both the hydration and alkalinity requirements of the fluorophores. Fluorescence was slightly brighter in GMA-embedded samples compared to those in LR White. Moreover, application of water to ultrathin sections collected from worms embedded in GMA immediately increased fluorescence intensity by 30%. This restoration of fluorescence suggests that a large fraction of the fluorescent proteins are maintained in a nonfluorescent, dehydrated state and that about 70% of the fluorescence observed before fixation can be preserved. Ultrathin sections were difficult to cut because GMA does not cross-link to the cuticle like epoxy resin, and thus the tissue usually breaks loose from the surrounding resin if sectioned below 70 nm. However, we could resolve ultrastructure even on thicker sections by using low accelerating voltage and collecting back-scattered electrons on the scanning electron microscope.

Correlative fluorescence nanoscopy and electron microscopy

We imaged proteins tagged with Citrine using STED microscopy (**Figs. 1a,b**, **2a,b** and **3a,b**). We embedded transgenic strains expressing Citrine-tagged proteins in GMA and cut ~100-nm-thick sections to ensure sufficient signal strength. In confocal mode, fluorescence was diffuse, but resolution greatly improved when we applied STED microscopy. Resolution of STED fluorescence in these images was 60–80 nm by full-width half-maximum analysis of point-like emitters. It was difficult to assign histone H2B fluorescence to a particular structure in the nucleus (**Fig. 1b**), but it was clearly restricted to profiles with a shape similar to that of the nucleus. STED images of samples containing tagged TOM20 revealed circular rings (**Fig. 2b**). A single fluorescent spot in the confocal image of a sample containing tagged α-liprin, resolved into a smaller circle in the STED image but did not reveal a recognizable structure as expected for this very small organelle (**Fig. 3b**). We acquired corresponding scanning electron micrographs from the same sections used for STED imaging. Then we aligned the STED images to the electron micrographs using fluorescent silica beads as fiduciary marks, which we applied onto the sections before fluorescence imaging (**Supplementary Fig. 2**). The beads are fluorescent in UV light (excitation, 354 nm and emission, 450 nm), and we detected them in an additional imaging scan after recording the STED data. Silica beads become charged and reflect electrons, which resulted in black circles of 1 μm in diameter in electron micrographs. The organization of labeled histone H2B molecules into chromatin aligned on top of the profile of a nucleus (**Fig. 1c,d**). The rings of TOM20–Citrine seen in the STED image align with the outer membranes of mitochondria (**Fig. 2c,d**). The α-liprin–Citrine spots observed in the STED images localized to a presynaptic dense projection observed in electron micrographs (**Fig. 3c,d** and **Supplementary Fig. 3a,b**).

For PALM, we fused the target proteins to tdEos or Dendra and fixed the transgenic worms under the same conditions as above. Resolution in PALM depends on the number of photons collected from each fluorescent protein, and the localization precision is determined as a function of molecular photon statistics,

background noise and pixilation[21]. Given the signal-to-noise ratio achieved using Dendra and tdEos, we calculated a localization precision of 12 nm (Online Methods). Section thickness for PALM was about two-thirds of that used for STED microscopy, and the fluorescence signals were correspondingly reduced compared to STED microscopy. Fluorescence localization was as expected: histone H2B fluorescence corresponded to the size of the nucleus and appeared as circles several micrometers in diameter (**Fig. 1f**). TOM20 signals were confined to rings but were considerably less intense than those observed in the STED image (**Fig. 2f**). α-liprin signals were rare and uninterpretable in the absence of ultrastructural information (**Fig. 3f**). We correlated PALM fluorescence to the electron micrographs using 100-nm gold nanoparticles as fiduciary markers (**Supplementary Fig. 4**). Gold nanoparticles are fluorescent[22]; we excited the particles with a 561-nm laser and collected emission at 580 nm to mark the fluorescence micrographs. Gold particles also reflect the electron beam in the scanning electron microscope and mark the micrograph. In the alignments, tagged histones localized to the nucleus but not the nucleolus (**Fig. 1g,h**). The distribution of histone H2B in the nucleus of a muscle cell was confined to the rim of the inner membrane compared to the distribution of histone H2B in the intestinal cell, but these differences are likely due to the cell type rather than the technique (**Supplementary Fig. 5**). TOM20 molecules were localized to the outer membrane of mitochondria (**Fig. 2g,h**). Tagged α-liprin was expressed from multicopy arrays for both STED microscopy and PALM. Overexpression of liprin resulted in aggregations of the protein in the cell body adjacent to the nucleus (**Fig. 3h** and **Supplementary Fig. 3c,d**). α-liprin-tdEos signals at the synapse were localized to the presynaptic dense projection (**Fig. 3g,h**).

DISCUSSION

For correlative fluorescence electron microscopy, scanning electron microscopy has several advantages over transmission electron microscopy. First, sections for scanning electron microscopy can be mounted on a coverglass, which allows hundreds of sections in long ribbons to be examined for fluorescence, which can later be assembled for array tomography[13]. Moreover, PALM is performed in the total internal reflection fluorescence (TIRF) configuration, which requires mounting on a coverglass. Second, thick sections can be imaged with high resolution in scanning but not transmission electron microscopy. Sections must be relatively thick (70–100 nm) because they must be deep enough to produce an adequate fluorescence signal and it is difficult to cut acrylic resins thinner than 70 nm. Although thick sections obscure ultrastructure in transmission electron microscopy, in scanning electron microscopy, low accelerating voltages can be used so that only the top 30 nm reflect electrons[23].

In contrast, the images from the scanning electron microscope are not as crisp as those from a transmission electron microscope. Transmission electron microscopes can achieve a resolution of less than 1 nm. However, the beam diameter for a scanning electron microscope is 4.5 nm when it is operated at 5 keV[23]. Second, the production of back-scattered electrons requires stains with high atomic number such as osmium and uranium, but such staining quenches fluorescence and could not be used in our protocols before fluorescence imaging. Staining with uranyl acetate after fluorescence imaging enhances the membrane contrast considerably but still does not produce crisp images of internal membranes such as the lipid bilayers of synaptic vesicles. One potential solution would be to apply electron tomography, which might compensate for the poor staining.

Correlative fluorescence electron microscopy results in an improvement of sensitivity over immuno-EM. In many cases antibodies that work on plastic sections are not available. Although antibodies can penetrate somewhat into resins such as LR White, access to antigens remains limited in immuno-EM[5]. As correlative microscopy does not rely on immunocytochemistry, antibody availability is not a concern, and fluorescent proteins deep in the plastic section can be localized. In contrast, not all proteins tolerate fluorescent protein tags. In this case, if antibodies are available, they can be used for nanoscopic imaging of sections and could even be adapted for array tomography[11]. Despite the sensitivity of correlative fluorescence electron microscopy, at this point the method is not quantitative. Under our conditions, ~30% of the fluorescence was lost owing to the oxidizing fixatives required for membrane preservation. Truly quantitative methods await the development of more robust fluorescent proteins.

The resolution of a conventional fluorescence microscope is limited to 200 nm. In practice, multiple fluorescence sources scatter the signal at high magnification into a large and blurry blob. Under optimal conditions, STED microscopy or PALM resolve a fluorescent source to 30 nm or 20 nm[3,5], respectively. At these resolutions we can localize proteins to substructures of organelles in two dimensions. Correlative microscopy can also achieve higher axial resolution than current methods in nanoscopy. *Z*-dimension resolution in fluorescence microscopy is 700 nm, 2–3 times worse than in the *x*-*y* dimensions[24]. Axial resolution can be improved by using two objective lenses in the 4Pi microscope[23], isometric STED microscopy[25] and interferometric PALM[26], but these arrangements have their own limitations. By sectioning the tissue into 70-nm serial sections, subdiffraction resolution is imposed on the signal simply by section thickness. Super-resolution in three dimensions can be achieved by reconstructing the volume of the tissue[13,27].

STED microscopy and PALM each have advantages and disadvantages relative to sensitivity and resolution, and a choice must be made depending on the application. STED microscopy is robust because Citrine is bright, and this fluorophore survives sample preparation well. STED microscopy is preferable if protein levels are low and as a consequence the signal is highly sensitive to oxidation. We observed that PALM generates weaker signals because sensitivity of the photoconvertible fluorophores to oxidation and higher background fluorescence than STED microscopy. The background signals in PALM, however, can be reduced by prebleaching the sample with intensive 561-nm laser and imposing a threshold for the emission period. PALM provided high-resolution fluorescence signals and will be arguably more useful when imaging small and crowded structures like those within the synapse.

METHODS

Methods and any associated references are available in the online version of the paper at http://www.nature.com/naturemethods/.

Note: Supplementary information is available on the Nature Methods website.

ACKNOWLEDGMENTS

We thank H. Hess and E. Betzig (Janelia Farm) for access to the PALM microscope for proof-of-principle experiments; R. Fetter for sharing protocols, reagents and

encouragement; M. Davidson (Florida State University), G. Seydoux (Johns Hopkins Univeristy), S. Eimer (European Neuroscience Institute), R. Leube (Universitat Aachen), K. Nehrke (University of Rochester), C. Frøkjær-Jensen (Utah), A. Ada-Nguema (Utah) and M. Hammarlund (Yale University) for DNA constructs. We thank Marine Biological Laboratory for equipment and funding for pilot experiments and Carl Zeiss Inc. for providing access to a beta version of the PAL-M. This research was supported by the US National Institutes of Health (NS034307), National Science Foundation (0920069) and Marine Biology Laboratory fellowship. (The Dart Neuroscience Scholars Program in Learning and Memory).

AUTHOR CONTRIBUTIONS

S.W. and E.M.J. conceived and designed experiments. G.H., R.J.H. and M.W.D. provided strains and advice. S.W. optimized the methods, prepared the samples and performed PALM imaging. A.P. and K.I.W. performed STED imaging. S.W., S.W.H. and E.M.J. wrote the manuscript. S.W.H. and E.M.J. provided funding.

COMPETING FINANCIAL INTERESTS

The authors declare no competing financial interests.

Published online at http://www.nature.com/naturemethods/. Reprints and permissions information is available online at http://npg.nature.com/reprintsandpermissions/.

1. Cox, G. & Sheppard, C.J. Practical limits of resolution in confocal and non-linear microscopy. *Microsc. Res. Tech.* **63**, 18–22 (2004).
2. Hell, S.W. Far-field optical nanoscopy. *Science* **316**, 1153–1158 (2007).
3. Hell, S.W. & Wichmann, J. Breaking the diffraction resolution limit by stimulated emission: stimulated-emission-depletion fluorescence microscopy. *Opt. Lett.* **19**, 780–782 (1994).
4. Klar, T.A., Jakobs, S., Dyba, M., Egner, A. & Hell, S.W. Fluorescence microscopy with diffraction resolution barrier broken by stimulated emission. *Proc. Natl. Acad. Sci. USA* **97**, 8206–8210 (2000).
5. Betzig, E. *et al.* Imaging intracellular fluorescent proteins at nanometer resolution. *Science* **313**, 1642–1645 (2006).
6. Rust, M.J., Bates, M. & Zhuang, X. Sub-diffraction-limit imaging by stochastic optical reconstruction microscopy (STORM). *Nat. Methods* **3**, 793–795 (2006).
7. Hess, S.T., Girirajan, T.P.K. & Mason, M.D. Ultra-high resolution imaging by fluorescence photoactivation localization microscopy. *Biophys. J.* **91**, 4258–4272 (2006).
8. Roth, J., Bendayan, M., Carlemalm, E., Villiger, W. & Garavito, M. Enhancement of structural preservation and immunocytochemical staining in low temperature embedded pancreatic tissue. *J. Histochem. Cytochem.* **29**, 663–671 (1981).
9. Rostaing, P., Weimer, R.M., Jorgensen, E.M., Triller, A. & Bessereau, J. Preservation of immunoreactivity and fine structure of adult *C. elegans* tissues using high-pressure freezing. *J. Histochem. Cytochem.* **52**, 1–12 (2004).
10. Morphew, M.K. 3D immunolocalization with plastic sections. *Methods Cell Biol.* **79**, 493–513 (2007).
11. Murphy, R.M. *et al.* Size and structure of antigen-antibody complexes. Electron microscopy and light scattering studies. *Biophys. J.* **54**, 45–56 (1988).
12. Sims, P.A. & Hardin, J.D. Fluorescence-integrated transmission electron microscopy images: integrating fluorescence microscopy with transmission electron microscopy. *Methods Mol. Biol.* **369**, 291–308 (2007).
13. Micheva, K. & Smith, S. Array tomography: a new tool for imaging the molecular architecture and ultrastructure of neural circuits. *Neuron* **55**, 25–36 (2007).
14. Tsien, R. The green fluorescent protein. *Annu. Rev. Biochem.* **67**, 509–544 (1998).
15. Mello, C.C., Kramer, J.M., Stinchcomb, D. & Ambros, V. Efficient gene transfer in *C. elegans*: extrachromosomal maintenance and integration of transforming sequences. *EMBO J.* **10**, 3959–3970 (1991).
16. Frøkjaer-Jensen, C. *et al.* Single-copy insertion of transgenes in *Caenorhabditis elegans*. *Nat. Genet.* **40**, 1375–1383 (2008).
17. Yeh, E., Kawano, T., Weimer, R.M., Bessereau, J. & Zhen, M. Identification of genes involved in synaptogenesis using a fluorescent active zone marker in *Caenorhabditis elegans*. *J. Neurosci.* **25**, 3833–3841 (2005).
18. Riemersma, J.C. Osmium tetroxide fixation of lipids for electron microscopy. A possible reaction mechanism. *Biochim. Biophys. Acta* **152**, 718–727 (1968).
19. Clancy, B. & Cauller, L.J. Reduction of background autofluorescence in brain sections following immersion in sodium borohydride. *J. Neurosci. Methods* **83**, 97–102 (1998).
20. Newman, G.R. & Hobot, J.A. *Resin Microscopy and On-Section Immunocytochemistry* (Springer-Verlag, Berlin, 1993).
21. Thompson, R. Precise nanometer localization analysis for individual fluorescent probes. *Biophys. J.* **82**, 2775–2783 (2002).
22. Yguerabide, J. & Yguerabide, E.E. Light-scattering submicroscopic particles as highly fluorescent analogs and their use as tracer labels in clinical and biological applications: II. Experimental characterization. *Anal. Biochem.* **262**, 157–176 (1998).
23. Goldstein, J. *et al. Scanning Electron Microscopy and X-Ray Microanalysis* (Springer Science and Business Media, LLS, New York, 2003).
24. Hell, S.W., Lindek, S., Cremer, C. & Stelzer, E.H.K. Measurement of the 4Pi-confocal point spread function proves 75 nm axial resolution. *Appl. Phys. Lett.* **64**, 1335–1337 (1994).
25. Schmidt, R. *et al.* Mitochondrial cristae revealed with focused light. *Nano Lett.* **9**, 2508–2510 (2009).
26. Shtengel, G. *et al.* Interferometric fluorescent super-resolution microscopy resolves 3D cellular ultrastructure. *Proc. Natl. Acad. Sci. USA* **106**, 3125–3130 (2009).
27. Punge, A. *et al.* 3D reconstruction of high-resolution STED microscope images. *Microsc. Res. Tech.* **71**, 644–650 (2008).

ONLINE METHODS

Strains and oligonucleotides. Strains we used are listed in **Supplementary Note 1**. Oligonucleotides we used are listed in **Supplementary Table 1**.

Fluorescent labels of organelles. DNA constructs were assembled using the Multisite Gateway (Invitrogen) recombination technology adapted from bacteriophage lambda integration. DNA fragments were moved into entry clones; promoters were cloned into slot 1 clones flanked by *attL4* and *attR1* sites '(4-1)', coding regions are flanked by *attL1* and *attL2* sites '(1-2)', and 3′ untranslated regions (UTRs) flanked by *attR2* and *attL3* sites '(2-3)'. Entry vectors can be recombined into destination vectors containing the promoter, coding region and 3′ UTR of choice. For histone H2B, a minigene encoding Citrine with worm-optimized codons and three artificial introns (S. Eimer) was amplified by PCR using the primers oGH55 and oMPD6. This amplification introduced flanking *attB* recombination sites and the resulting product was recombined with pDONR 221 (Invitrogen) using BP Clonase II (Invitrogen) to produce the *attL1–attL2*–containing entry clone *(1-2)Citrine* (pGH114). A similar strategy with primers oGH95 and EOS_rev was used to clone *tdEos* (M. Davidson), resulting in *(1-2)tdEos* (pGH270).

The open reading frame (ORF) of encoding worm histone H2B (*his-11*) was released from the plasmid *Ppie-1::GFP::HIS-11::pie-1 3′UTR* (pJH4.52; G. Seydoux) by restriction digest with SpeI and ligated into the multiple cloning site in front of the *unc-54* 3′ UTR in pMH472 (M. Hammarlund). The resulting *attR2–attL3*–containing entry clone (pGH42) translationally fuses a histone onto the carboxy terminus of ORFs of fluorescent proteins in '(1-2)' entry clones when recombined in a Multisite Gateway LR reaction (Invitrogen). The heatshock promoter (*Phsp-16.41*) in an *attL4–attR1*–containing entry clone (pCM1.57, G. Seydoux) was used to drive expression of the fluorescent protein-tagged histone H2B in an inducible manner. To enable directed insertion of the transgenes into the *C. elegans* genome, the recombination reactions were performed using the *att*R4–*att*R3–containing destination vector (pCFJ150; C. Frøkjær-Jensen) that includes genomic fragments flanking a *Mos1* transposon insertion (*ttTi5605* II) for targeting, along with the *unc-119* gene from *C. briggsae* for selection. Recombination of pCM1.57, pGH114, pGH42 and pCFJ150 using LR Clonase II Plus (Invitrogen) generated *Phsp-16.41:: Citrine::HIS-11::unc-54 3′UTR* (pGH201), and recombination of pCM1.57, pGH270, pGH42 and pCFJ150 generated *Phsp-16.41:: tdEos::HIS-11::unc-54 3′UTR* (pGH154).

The expression constructs were integrated using *Mos1*-mediated single-copy insertion (MosSCI) as described previously[16]. Briefly, *unc-119(ed3)* III mutants containing *ttTi5605* II (EG4322) were injected with a mixture of plasmids containing the *Mos1* transposase to mobilize the transposon, the targeting vector to provide a repair template for the resulting chromosomal break and red fluorescent markers expressed in muscles and neurons to mark extrachromosomal arrays. Offspring of the injected worms were selected 2–4 generations later for homozygous *unc-119* rescue and the appearance of fluorescent nuclei following heatshock. MosSCI of pGH201 generated the strain EG5582 *oxSi282*(*Phsp-16.41::Citrine::his-11::unc-54 3′UTR*) II; *unc-119(ed3)* III and MosSCI of pGH154 generated the strain EG5576 *oxSi283*(*Phsp-16.41:: tdEos::his-11::unc-54 3′UTR*) II ; *unc-119(ed3)* III.

For TOM20, to generate '(2-3)' entry clones that would encode a protein with fused fluorescent tags onto the C terminus of proteins encoded by '(1-2)' entry vectors, *Citrine* was amplified with oGH76 and oGH57, and *tdEos* was amplified with oGH96 and oGH94. These PCR products were each inserted between the *attR2* and *let-858 3′UTR* of pADA-126 (A. Ada-Nguema) by amplifying this '(2-3)' entry vector with oGH38 and oGH39 and using In-Fusion PCR Cloning (Clontech) to produce *(2-3)Citrine::let-858 3′UTR* (pGH113) and *(2-3)tdEos:: let-858 3′UTR* (pGH271).

The sequence encoding the first 54 amino acids of the *C. elegans* TOM20 ortholog (*tomm-20*) of the outer mitochondrial membrane translocase was BP cloned to produce the '(1-2)' entry clone pMH496 (M. Hammarlund). This protein sequence is sufficient for protein targeting to the outer membrane of mitochodria[28]. The *myo-3* promoter in a '(4-1)' entry vector was from Open Biosystems (p_K12F2.1_93). LR recombination of *(4-1)Pmyo-3*, pMH496, pGH113 and the destination vector pDEST R4-R3 (Invitrogen) generated *Pmyo-3::TOMM-20(N-term)::Citrine:: let-858 3′UTR* (pGH194), and recombination of *(4-1)Pmyo-3*, pMH496, pGH271 and pCFJ150 produced *Pmyo-3::TOMM-20(N-term)::tdEos::let-858 3′UTR* (pGH158).

EG5515 *lin-15(n765ts)* X ; *oxEx1329* (*Pmyo-3::TOMM-20(N-term)::Citrine::let-858 3′UTR lin-15(+)* LITMUS 38i) was made by injecting MT1642 *lin-15(n765ts)* with 33 ng μl^{-1} each of pGH194, *lin-15* rescuing plasmid pL15EK[29] and LITMUS 38i (NEB). MosSCI of pGH158 resulted in EG5998 *oxSi203* (*Pmyo-3::TOMM-20(N-term)::tdEos::let-858 3′UTR unc-119(+)*) II; *unc-119(ed3)* III.

To tag α-liprin, the gene for the *C. elegans* ortholog (encoded by *syd-2*) was amplified with oRJH19 and oRJH20 from genomic DNA. The resulting PCR product was BP cloned into pDONR 221 (Invitrogen) to generate *(1-2)syd-2* (pRH247, R. Hobson). To generate '(2-3)' entry clones that would fuse fluorescent tags onto the C terminus of proteins encoded by '(1-2)' entry vectors, pDendra2 was amplified from *Prab-3::TBA-1::Dendra2::unc-54 3′ UTR* (pWD264) with oRJH21 and oRJH22. This PCR product was then cloned into pGH38 as BamHI-SpeI fragment. To drive expression in the nervous system, the promoter of *snt-1* was amplified with oRJH23 and oRJH24 from genomic DNA. The resulting PCR product was BP cloned into pDONR P4-P1R (Invitrogen) to produce *(4-1)Psnt-1* (pCFJ284; C. Frøkjær-Jensen). LR recombination of pCFJ284 pRH247 and pCFJ150 with either pGH113 or pWD240 resulted in *Psnt-1::SYD-2::Citrine:: let-858 3′UTR* (pRH409) and *Psnt-1::SYD-2::Dendra2::let-858 3′UTR* (pRH419).

EG6190 *ttTi5605; unc-119; oxEx1490*(*Psnt-1::SYD-2:: citrine; unc-119(+) lin-15(+)*) was made by injecting EG4322 *ttTi5605; unc-119(ed3)* with 25 ng μl^{-1} of pRH409 and 75 ng μl^{-1} pL15EK. EG6191 *ttTi4348; unc-119; oxEx1491*(*Psnt-1:: SYD-2::Dendra2; unc-119(+) lin-15(+)*) was made by injecting EG5299 *ttTi4348; unc-119(ed3)* with 25 ng μl^{-1} of pRH409 and 75 ng μl^{-1} pL15EK. All constructs were designed using the plasmid editor APE (http://www.biology.utah.edu/jorgensen/wayned/ape/).

Choice of fluorescent proteins. We chose Citrine for STED microscopy and tdEos or Dendra for PALM based on their characteristics and expression in *C. elegans* (**Supplementary Note 2**).

Sample preparations for correlative microscopy. The sample preparation for electron microscopy comprised rapid freezing, acetone substitution, fixation, staining, infiltrating with plastic and polymerizing the plastic (**Supplementary Note 3**).

High-pressure freezing and freeze substitution. The fixatives and freeze-substitution media, 95% anhydrous acetone (EMS, glass distilled) and 5% MilliQ water were mixed in the cryogenic vials (Nalgene) (see **Supplementary Note 4** for use of 5% water) and frozen in liquid nitrogen before use. Acetone was used as the organic solvent in all fixations. In contrast to acetone, ethanol extracted membranes from neuronal tissues. This result was consistent with the idea that acetone acts as a fixative during the freeze substitution[30].

The fixatives used here were 0.1–2% paraformaldehyde (EMS), 0.1–1% glutaraldehyde (EMS), a combination of paraformaldehyde and glutaraldehyde, 0.1% acrolein (Sigma-Aldrich), 0.001–0.5% osmium tetroxide (EMS, crystals), 0.1% potassium permanganate (EMS), and a combination of osmium tetroxide and potassium permanganate.

Worms expressing fluorescently tagged proteins were placed onto a 100-μm deep, type-A specimen carrier, filled with bacteria (OP50 or HB101) and were instantaneously frozen in a BAL-TEC HPM 010 high-pressure freezer (BAL-TEC). The specimens were transferred into a cryogenic vial containing freeze-substitution media and fixatives. The cryogenic vials are then transferred into an automatic freeze-substitution unit (Leica, AFS 2), and the specimen was freeze substituted with the following program: 30 h at −90 °C, 5 °C per hour to −20 °C and 2 h at −20 °C.

Infiltration. Acetone and fixatives were completely washed out from tissues using 95% ethanol before infiltration because the residual acetone causes improper polymerization owing to its action as a free-radical scavenger. Infiltration (30% for 5 h, 70% for 6 h and 95–98% for overnight) was carried out at −20 °C in cryogenic vials. After the removal of fixatives, the specimens were washed with 95% ethanol six times over a period of 2 h. Ethanol was prepared by adding 5% MilliQ water to anhydrous ethanol (Sigma-Aldrich). The solutions for infiltration were prepared by mixing 100% stock plastic solutions with 95% ethanol in glass scintillation vials (EMS). Mixing the solutions in plastic vials will cause incomplete polymerization. We tested the resins Lowicryl K4M (EMS), LR Gold (EMS), LR White (EMS) and glycol methacrylate (GMA). The components for these resins are listed in **Supplementary Note 5**. The formulas for 100% stock solutions are as follows. For K4M, 17.3 g methacrylic and acrylic esters, 2.7 g triethyleneglycol-di-methacrylate, 10 g benzoin-methyl-ether and 5% water were mixed. LR Gold was mixed with 5% water. Ten grams of catalyst, benzoyl peroxide, was mixed in 500 ml LR White one day before use. pH of LR White with 2–5% water tended to be low (~5.5), which was too acidic for most fluorescent proteins. Therefore, we neutralized the pH using ethanolamine as follows. The catalyzed LR White was mixed with 2–5% water depending on the batch and neutralized with ethanolamine (5 μl in 20 ml of catalyzed LR White). Fully neutralized LR White (pH 7–7.4) could not be completely polymerized, and the sections were torn or destroyed upon sectioning. We determined the amount of ethanolamine compatible with full polymerization to be 0.025% (5 μl in 20 ml of LR White), which increased the pH to 6.5. The pH of the catalyzed LR White dropped as the storage duration increased, and thus we only used catalyzed LR White that was less than 1 month old. For GMA, 67 ml glycol methacrylate, 30 ml butyl methacrylate, 3 ml water and 0.6 g benzoyl peroxide were mixed and used for all infiltration steps.

Polymerization. The worms were dissociated from bacteria, which was the space filler for high-pressure freezing. Because acrylic resins do not cross-link to tissues, in particular the cuticle, the tissues needs to be surrounded by the plastic as much as possible. Otherwise the tissue can break away from the matrix and experience distortion. The worms were then embedded in a cap of a polypropylene BEEM capsule (EBSciences, TC). Polypropylene capsules were used because LR White does not polymerize completely in a polyethylene capsule. A disc of aclar film (EMS) was placed in the bottom of the BEEM capsule, prepared by 3/8-inch paper punches (Ted Pella; Disc Punches). A few worms from each condition were mounted on the glass slide before polymerization, and the fluorescence was observed on a Zeiss Axioskop with a 63× plan-Apochromat (numerical apterture (NA) = 1.40) objective and imaged using a digital camera (Diagnostic Instruments). ImageJ was used to measure the photon intensity in each case.

For K4M and GMA polymerization, 1 ml of K4M or GMA was mixed with 1.5 μl *N,N*-dimethyl-*p*-toluidine (Sigma-Aldrich) and dispensed into the embedding cap containing the specimen. For LR Gold polymerization, 0.1% benzoyl peroxide was mixed into LR Gold, and the catalyzed LR Gold was applied to the specimens in the embedding cap. For LR White polymerization, LR White accelerator (Ted Pella) was added at 1.5 μl per 1 ml of catalyzed LR White. The embedded specimens were filled with this mixture. In each case, the embedding caps were covered with another layer of aclar film to block oxygen and thus allow polymerization of the plastic. The polymerization was carried out for 24 h. The polymerized blocks were stored in nitrogen-filled, vacuumed bags in the freezer at −20 °C if not sectioned immediately. We collected 70–500 nm sections on coverslips using an ultramicrotome (Leica, UC6) and imaged using a Zeiss Axioskop. For STED and PALM imaging, 70–100 nm ultrathin sections were collected from each strain mounted on the precleaned coverslips (#1.5, 18 mm × 18 mm for STED and #1.5, 25 mm diameter for PALM).

Fluorescence quantification. Loss of fluorescence intensity was monitored using ImageJ through all procedures from postinfiltration to sectioning. Using a point-selection tool, the intensity of 3–4 fluorescent spots from 2–3 worms in each condition was measured. The obtained values were averaged and compared.

Coverslip cleaning. Coverslips for PALM imaging were incubated in the Piranha solution (3 parts sulfuric acid: 1 part hydrogen peroxide) for an hour to reduce background fluorescence. The Piranha solution was then washed off thoroughly six times with MilliQ water. The coverslips were then sonicated for half an hour. The water was washed off again six times. The coverslips were dipped into 100% methanol to make the surface hydrophobic, which allows easy pick-up of sections. The coverslips were then air dried.

doi:10.1038/nmeth.1537

Storage and shipment of specimens. Although fluorophores can be preserved effectively through electron microscopy preparation, we found the fluorescence to be very sensitive to storage conditions, specifically ambient air and temperature. Fluorescence is quenched if the samples are left out in the air at room temperature for a few days. We found that storing the samples at −20 °C in a bag that was filled with nitrogen gas and then evacuated can preserve fluorescence. Likewise, shipping the samples overseas requires similar conditions: nitrogen-filled, vacuumed and cold. Additionally, cutting sections of 100 nm thickness instead of 70 nm preserved the fluorescence more reliably during the shipment. Extra caution needs to be paid during the summer when the samples can be exposed to very high temperatures.

STED imaging. For STED, a solution of silica nanoparticles (Sicasta BlueF, 1 µm, NH_2 functionalized, Micromod) was diluted to 1/10,000 with MilliQ water. For LR White sections, about 10 µl of this solution were applied to each coverglass. For GMA sections, the same silica nanoparticles were used but diluted to 1/500. 10 µl of the solution were applied to each coverslip and washed off after 5 min of incubation. The samples were kept in nitrogen until the water had evaporated. All coverslips were mounted onto single concave microscope slides (SailingBoat Lab Co.), where the concave depression was filled with MilliQ water. The samples were placed into a custom-designed STED microscope as previously described[27]. In brief, Citrine was excited at 490 nm by a diffraction-limited spot which was overlaid with a doughnut-shaped STED spot (at 590 nm) featuring zero intensity in the center. The STED spot prevents fluorescence by instantly driving excited molecules back to the ground state, except in proximity of the doughnut center. Therefore fluorescence is reduced to a volume smaller than the diffraction limit. For focusing we used high-numerical-aperture objective lenses (1.4 NA Plan Apochromat, 100×, oil or 1.3 NA Plan Apochromat, 63×, glycerol; Leica). The epifluorescence was filtered via a 525/60 nm band-pass filter and detected by an avalanche photodiode. The silica nanoparticles were excited at 405 nm and detected with a second detector channel at 450/60 nm. After STED imaging, the coverslips were removed from the microscope slides, dried and sent back to Utah for electron microscopy.

PALM imaging. The gold nanoparticles solution (Micospheres-Nanospheres, 100 nm or 250 nm) was diluted to 1/10 with MilliQ water, which was filtered with a 0.22 µm syringe filter (Millipore). The solution was applied to the coverslips, and after 4 min of incubation, the solution was washed off with the filtered MilliQ water. The coverslips were placed in the coverslip holder for Zeiss PAL-M microscope (Carl Zeiss, PAL-M Prototype serial number 2701000005) equipped with a 100× plan-apochromat (NA = 1.46) objective lens (Carl Zeiss). The vacuum grease was applied on the rim of the coverslip holder to minimize the drift. The region of the interest was located in the bright field and then prebleached using the intensive 561 nm laser illumination (5 mW) for 2–5 min until the autofluorescence was quenched. We acquired 10,000–20,000 frames at a rate of 20–30 frames s^{-1} using an Andor iXon DU-897D EMCCD camera (Andor Technology Plc) while photoconvertible 405 nm laser at 1–5 µW and readout 561 nm lasers at 1–5 mW were applied simultaneously. The intensity of 405 nm laser was set so that it only activated a few molecules in each frame. The centroid of the molecules was calculated and mapped using Zeiss Zen PAL-M program with the drift correction applied. Localization precision was calculated using the equation:

$$\left\langle (\Delta x)^2 \right\rangle = \frac{\left(s^2 + a^2/12\right)}{N} + \frac{8\pi s^4 b^2}{a^2 N^2}$$

where Δx is the error in localization, s is the s.d., N is the number of photons collected, a is the size of the pixel and b is the background noise[21]. Generally, the brighter the signal, the better the localization because the brightest spot within a single fluorescent molecule can be refined to one pixel or only a few pixels in each fluorescence mass, whereas a dark dim spot will have many more pixels with the same intensity. Thus knowing the center of the fluorescent molecule is more precise if the signal-to-noise ratio is better. One must keep in mind that each dot in the PALM image is not actually observed fluorescence but rather a calculated location of each fluorophore; because the dot size is controlled by the user, it is important not to set the dot size below the experimentally defined resolution. Background fluorescence leads to ambiguity in the protein localization but can be removed from the final image. Emission from fluorescent proteins such as tdEos and Dendra typically lasts for 500 ms or less, whereas the emission from the background signals lasts longer than 500 ms. By selecting molecules that were fluorescent for less than 500 ms, most of the background fluorescence was removed.

Scanning electron microscopy imaging. The sections on coverslips were stained for 4 min with 2.5% uranyl acetate in water to improve membrane contrast. The sections were carbon coated and then imaged under high vacuum in a FEI Nova Nano scanning electron microscope. Electrons were collected using a back-scatter detector (vCD, FEI). The immersion mode was applied to the field. The stage was negatively biased (the landing energy was set to 3 keV) to allow acceleration of back-scattered electrons toward the detector. The accelerating voltage and the beam current were set at 5 keV and 0.11 nA, respectively. The grayscale of the image is then inverted to resemble TEM images, and thus, electron reflective structures appear black instead of white. The contrast was enhanced using Adobe Photoshop.

Alignment of fluorescence and electron micrographs. A fluorescence image and an electron micrograph of the same section were overlaid based on the silica bead or gold fiduciary markers, which appear electron dense in electron micrographs (**Supplementary Figs. 2a** and **4a**). First, the image of fiduciary markers was aligned on the micrographs using Adobe Photoshop (**Supplementary Figs. 2b** and **4b**). Autofluorescence from the tissue owing to the UV-light illumination can be also used to refine the alignment. Based on the translation values we obtained from the fiduciary markers, the STED or PALM images were aligned to the corresponding electron micrographs (**Supplementary Figs. 2c** and **4c**). For α-liprin, the alignment could also be corrected at high magnification based on the perinuclear aggregation of α-liprin in the electron micrograph and strong fluorescence from such aggregations in the fluorescent image. This was useful in the STED image because the beads

sometimes moved and because the charging of the beads led to flare on the electron micrograph (**Supplementary Fig. 2a,b**).

For the merged panels, we applied a gradient transparency to the STED or PALM images using Adobe Photoshop so that the black background did not obscure the micrograph in the figures (**Supplementary Figs. 2d** and **4d**). The transparency of black pixels was set to 20%.

28. Kanaji, S., Iwahashi, J., Kida, Y., Sakaguchi, M. & Mihara, K. Characterization of the signal that directs Tom20 to the mitochondrial outer membrane. *J. Cell Biol.* **151**, 277–288 (2000).
29. Clark, S.G., Lu, X. & Horvitz, H.R. The *Caenorhabditis elegans* locus Lin-15, a negative regulator of a tyrosine kinase signaling pathway, encodes two different proteins. *Genetics* **137**, 987–997 (1994).
30. Weibull, C. & Christiansson, A. Extraction of proteins and membrane lipids during low temperature embedding of biological material for electron microscopy. *J. Microsc.* **142**, 79–86 (1986).

doi:10.1038/nmeth.1537

Nature Methods

Protein localization in electron micrographs using fluorescence nanoscopy

Shigeki Watanabe, Annedore Punge, Gunther Hollopeter, Katrin I Willig, Robert John Hobson, M Wayne Davis, Stefan W Hell & Erik M Jorgensen

Nature Methods: doi:10.1038/nmeth.1537

Supplementary Figure 1

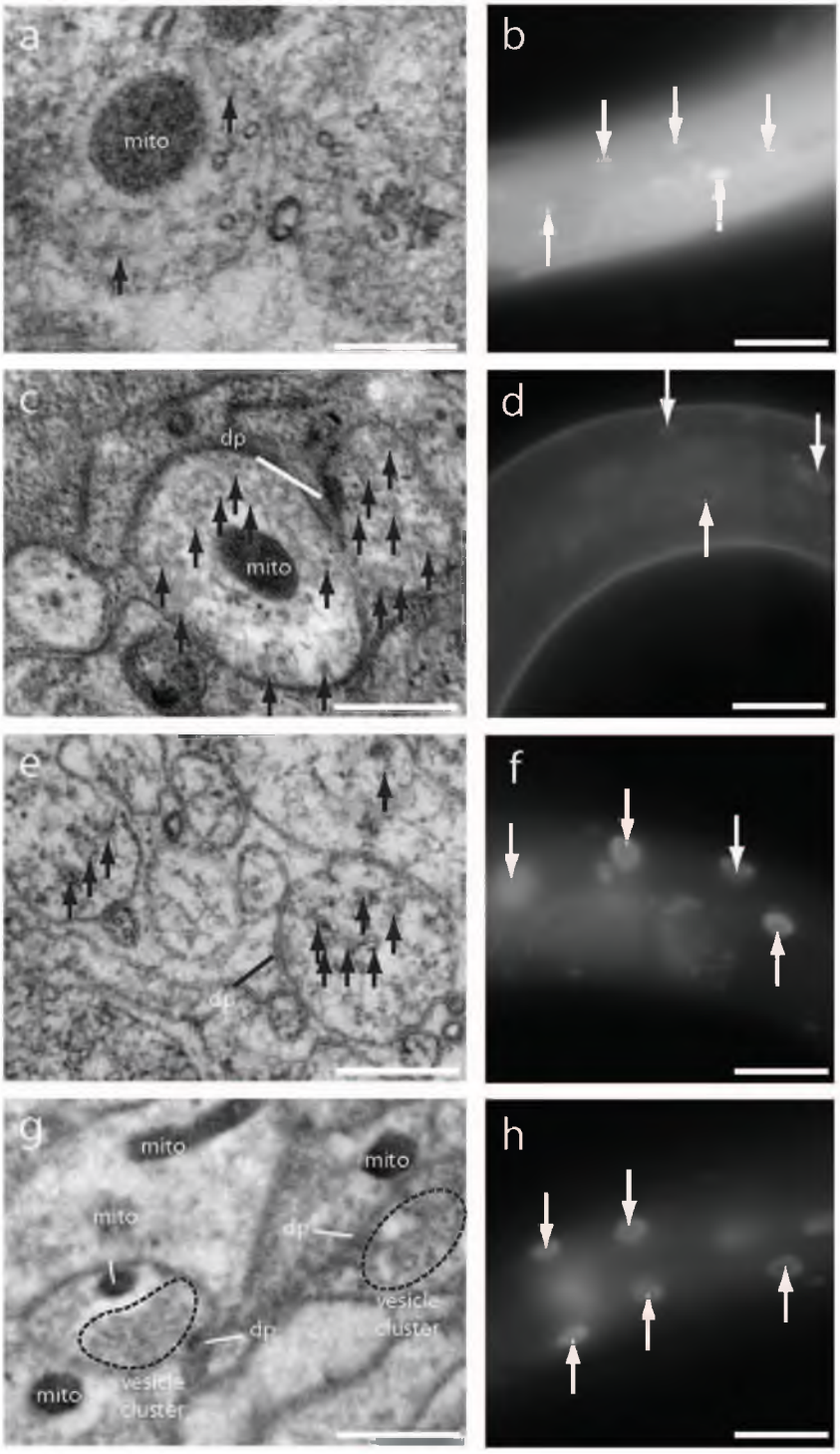

Nature Methods: doi:10.1038/nmeth.1537

Supplementary Figure 1: Preservation of morphology and fluorescence by different fixatives. (**a**) A TEM image of ventral nerve cord (VNC) fixed with 1% glutaraldehyde. (**b**) fluorescence micrograph of intestinal nuclei fixed with 1% glutaraldehyde. (**c**) A TEM image of VNC fixed with 0.1% osmium tetroxide. (**d**) A fluorescence micrograph of intestinal nuclei fixed with 0.1% osmium tetroxide. (**e**) A TEM image of ventral nerve cord (VNC) fixed with 0.1% potassium permanganate. (**f**) A fluorescence micrograph of intestinal nuclei fixed with 0.1% potassium permanganate preserves fluorescence well. (**g**) TEM image of the nerve ring fixed with 0.1% potassium permanganate + 0.001% osmium tetroxide. (**h**) A fluorescence micrograph of intestinal nuclei fixed with 0.1% potassium permanganate + 0.001% osmium tetroxide. Fluorescence images were acquired prior to plastic polymerization. Electron micrographs were acquired using a TEM. Transgenic animals (Citrine-Histone) were used to obtain the fluorescence images (b, d, f, and h) and electron micrographs of (**e**) and (**g**). Transgenic animals (P*myo-2::GFP*) were used to obtain electron micrographs of (**a**) and (**c**). The gain and exposure time of the camera were the same for (**b**,**f**,**h**), but for (**d**), the gain was increased 4x, and the exposure time was increased from 430 ms to 1000 ms to visualize the signal. Arrowheads indicate fluorescent signals in nuclei. In all images, resin was LR White with 5% water, pH 6.5. Black arrowheads indicate each synaptic vesicle in the electron micrographs. 'mito', mitochondria; 'dp', dense projection. Scale bars, 300 nm (**a**,**c**,**e**,**g**) and 30 μm (**b**,**d**,**f**,**h**).

Nature Methods: doi:10.1038/nmeth.1537

Supplementary Figure 2

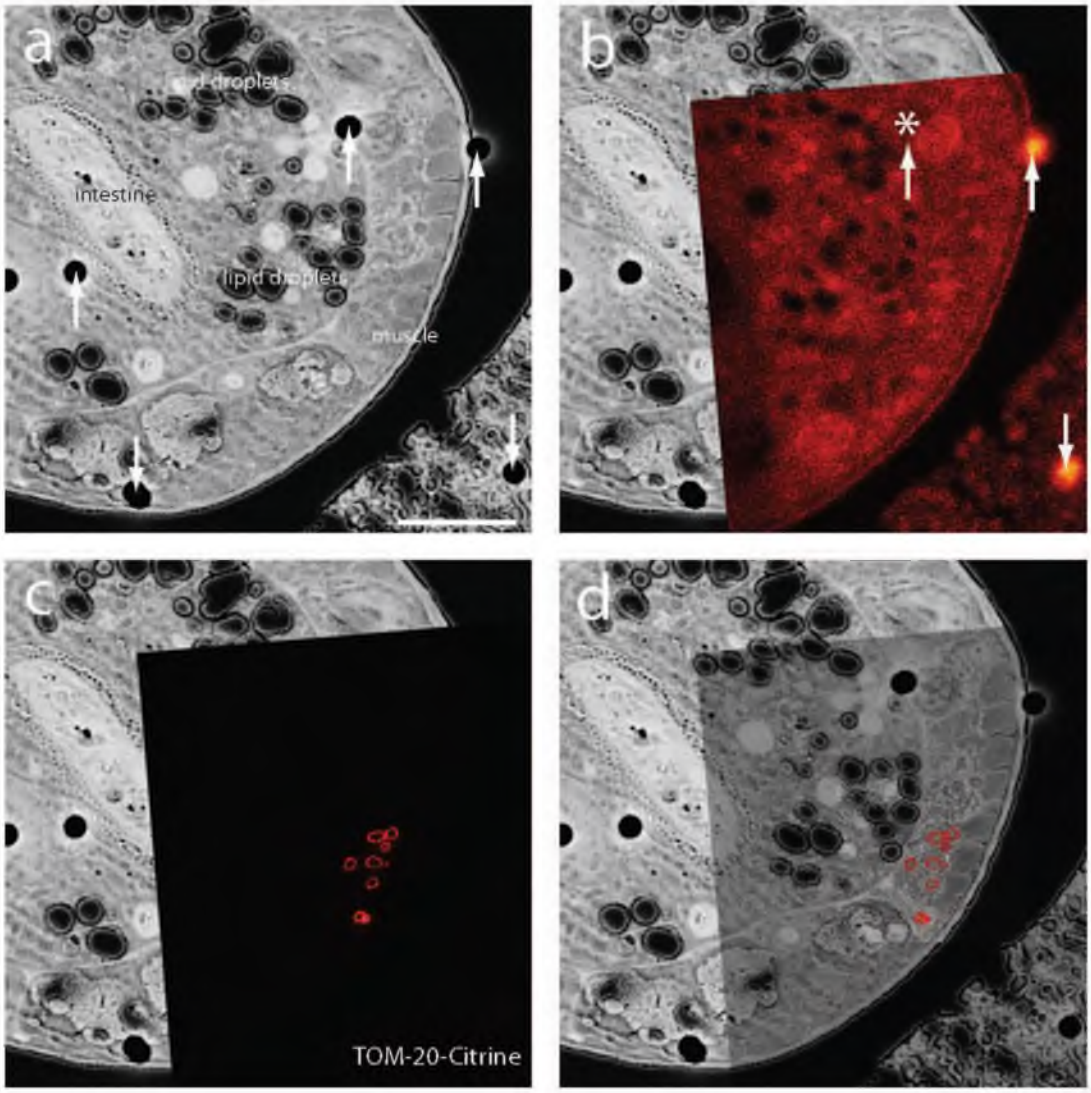

Nature Methods: doi:10.1038/nmeth.1537

Supplementary Figure 2: Silica beads were used to align fluorescence and electron micrographs. (**a**) A low magnification electron micrograph (5000x) from a cross section of *C. elegans* expressing TOM-20-Citrine. Black circles, indicated by white arrowheads, are the fiduciary marks from silica beads applied prior to STED imaging. (**b**) An image of fiduciary markers is aligned onto an electron micrograph based on the location of the fiduciary marks. * indicates a silica bead that was not present during the STED recording. Presumably the bead moved during the post-staining with uranyl acetate just prior to SEM imaging. (**c**) The STED image is then rotated and translated based on the values obtained in (**b**). (**d**) A gradient transparency is applied to the STED image so that the transparency of the background is reduced to 20% while that of citrine fluorescence remains at 100%. Scale bars, 5 μm (**a-d**).

Nature Methods: doi:10.1038/nmeth.1537

Supplementary Figure 3

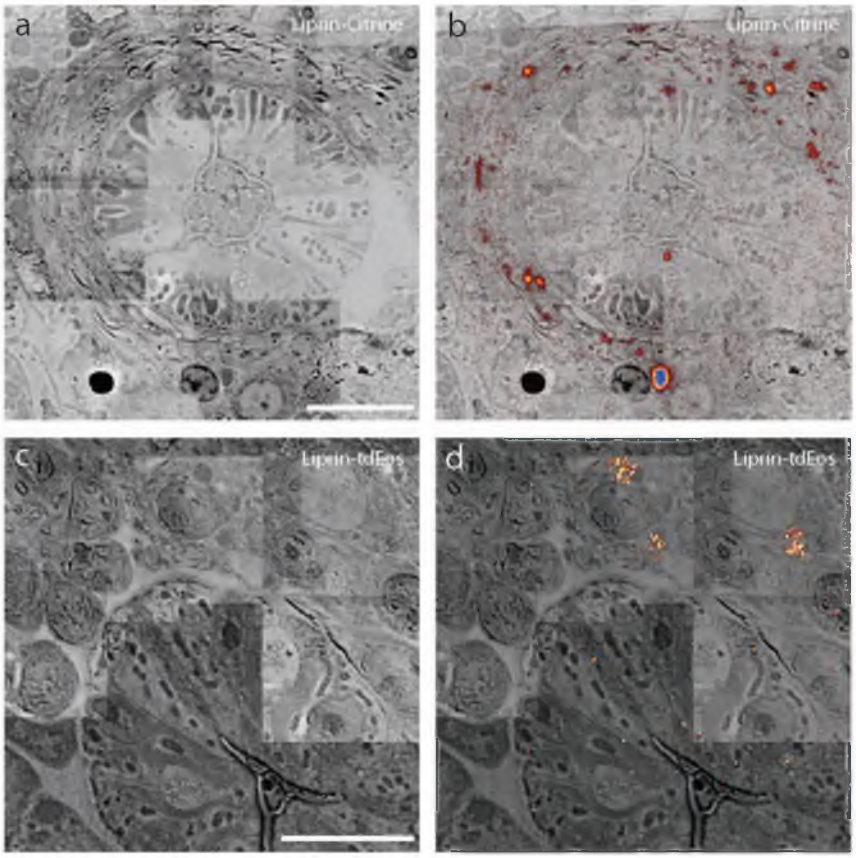

Supplementary Figure 3: Liprin localization at low magnification. High magnification electron micrographs of neurons are tiled on top of low magnification micrographs to depict morphology and protein localization in the nerve ring and head ganglia. (**a**) Electron micrograph of nerve ring of a Liprin-Citrine expressing strain, (**b**) Correlative STED and electron micrograph of Liprin-Citrine. Note large aggregate of liprin adjacent to the nucleus of a neuron cell body at the bottom of the micrograph. (**c**) Electron micrograph of head ganglion. (**d**) Correlative PALM and electron micrograph of Liprin-Dendra. Note the aggregations of liprin in the cell bodies adjacent to the nuclei. Scale bars, 5 μm (**a-d**).

Nature Methods: doi:10.1038/nmeth.1537

Supplementary Figure 4

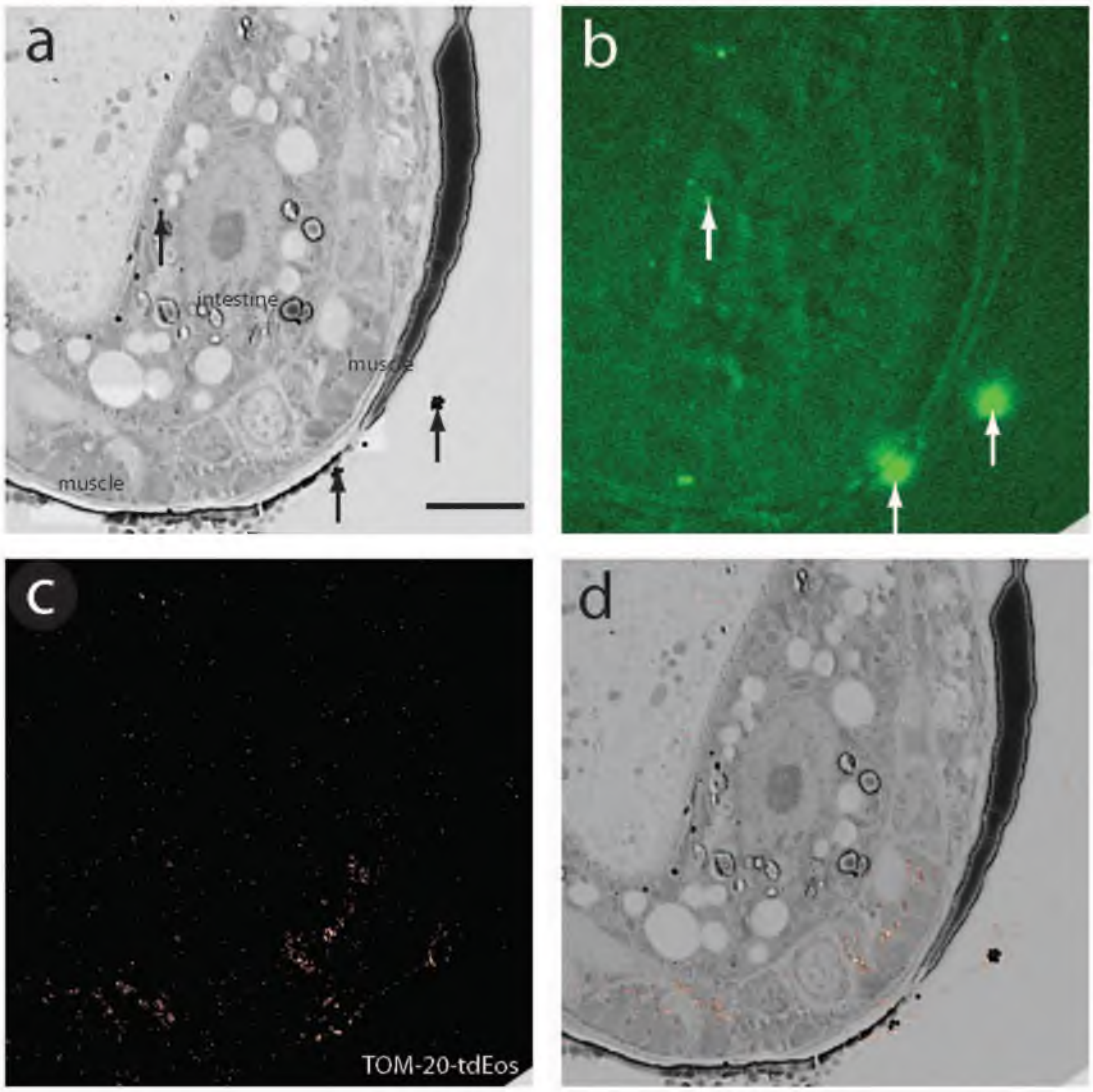

Nature Methods: doi:10.1038/nmeth.1537

Supplementary Figure 4: Gold nanoparticles were used to align fluorescence and electron micrographs. (**a**) A low magnification electron micrograph from a cross section of *C. elegans* expressing TOM-20::tdEos. Black dots are the fiduciary marks from 100 nm gold nanoparticles applied prior to PALM imaging. (**b**) An image of fiduciary markers is aligned onto an electron micrograph based on the location of the fiduciary marks. Note that the two bright spots on the lower right arise from clusters of gold particles. (**c**) A PALM image is then rotated and translated based on the values obtained in (**b**). (**d**) A gradient transparency is applied to the PALM image so that the transparency of the background is reduced to 20% while that of tdEos fluorescence remains at 100%. Scale bars, 5 μm (**a-d**).

Nature Methods: doi:10.1038/nmeth.1537

Supplementary Figure 5

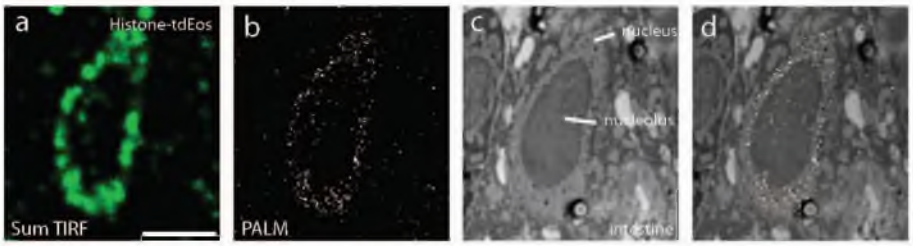

Nature Methods: doi:10.1038/nmeth.1537

Supplementary Figure 5: Histone localization in an intestinal nucleus is similar by correlative PALM-EM to what was observed using correlative STED-EM. (**a**) Sum TIRF image of Histone-tdEos acquired from a thin section (70 nm). Sum TIRF image represents all the photons detected by the camera during the experimental time course. (**b**) Corresponding PALM image of Histone-tdEos. (**c**) Electron micrograph of an intestinal cell nucleus acquired from the same section. (**d**) Correlative PALM and electron microscopy of Histone-tdEos. The fluorescent signals are tightly localized to the nucleus. The sample was embedded in LR White. Scale bars, 3 μm (**a-d**).

Nature Methods: doi:10.1038/nmeth.1537

Supplementary Note 1: Strains
The wild type is Bristol N2.
EG5582 *oxSi282*[P*hsp-16.41::Citrine::HIS-11::unc-54 3'UTR*] II; *unc-119(ed3)* III
EG5576 *oxSi283*[P*hsp-16.41:: tdEos::HIS-11::unc-54 3'UTR*] II ; *unc-119(ed3)* III.
EG5515 *lin-15(n765ts)* X ; *oxEx1329* [P*myo-3::TOM-20(N-term)::Citrine::let-858 3'UTR lin-15(+)* LITMUS 38i]
EG5998 *oxSi203* [P*myo-3::TOM-20(N-term)::tdEos::let-858 3'UTR unc-119(+)*] II ; *unc-119(ed3)* III
EG6190 *ttTi5605; unc-119; oxEx1490*[P*snt-1::SYD-2::citrine*; *unc-119(+) lin-15(+)*]
EG6191 *ttTi4348; unc-119; oxEx1491*[P*snt-1::SYD-2::Dendra2*; *unc-119(+) lin-15(+)*]

Supplementary Note 2: Choice of fluorescent proteins
For STED microscopy, fluorescent proteins must possess a high photostability. eYFP and Citrine have been shown to be well-suited for STED[1]. We choose Citrine as the fluorophore for STED because the quantum yield is slightly higher, and the transgenes (Citrine-Histone, TOM-20-Citrine, and liprin-Citrine) were expressed well in *C. elegans* animals.

For PALM, the fluorescent protein must be capable of conversion from a fluorescence inhibited (inactivated) to a non-inhibited (activated) state. Here, we focused on photo-convertible rather than simply photo-activatable fluorescent proteins since the preservation of fluorescence can be visualized and assessed before photoconversion. For example, Dendra and EosFP emit green light before photo-conversion, and red light after photo-conversion.

We evaluated potential photo-convertible fluorescent proteins based on the following characteristics: appropriate expression pattern in *C. elegans*, high photo-conversion efficiency, and bright fluorescence after photo-conversion. We examined mOrange, Dendra, mEosFP, mEosFP2, and tdEos for reliable expression in *C. elegans*. Fusion of mEosFP2 to TOM-20 caused perinuclear aggregations of the fluorescence in muscle cells, suggesting that the tag was causing proteins to aggregate. mOrange, Dendra, mEosFP, and tdEos fusions to TOM-20 appeared to be expressed in the expected locations in the cell.

Genes for different fluorescent proteins were fused to the open reading frame for histone H2B under the control of the heatshock promoter. The constructs were inserted into the genome using *Mos1*-mediated single copy insertion (MosSCI)[2]. Following a heat shock, the photo-conversion of each fluorophore was tested in whole animals by exposing them to 405 nm light (or 488 nm for mOrange[3]). Only mOrange was not detectably photo-converted. The transgenic strains expressing Dendra, mEosFP, or tdEos were fixed using 0.1% potassium permanganate and embedded in LR White. We prepared 100 nm slices from each and compared the photon intensity after the photo-conversion on a Zeiss PAL-M microscope.

Supplementary Note 3: Steps for sample preparation
The sample preparation for electron microscopy consists of six steps. Rapid freezing under high pressure immobilizes water molecules without generating ice crystals[4]. The vitreous water is then replaced by a fixative dissolved in organic solvents such as acetone. Fixation of rapidly frozen tissue can preserve morphology better than

Nature Methods: doi:10.1038/nmeth.1537

conventional fixation in which cells are immersed in fixatives. Plastic resin is then infiltrated into the fixed and dehydrated tissues and polymerized into a plastic block. Finally, the hardened block is sliced into ultra-thin sections of 30-70 nm and mounted. Each of these steps could potentially quench fluorophores and had to be optimized.

Supplementary Note 4: Freezing and solvents

To determine if freezing under high pressure reduced fluorescence, we simply froze animals expressing GFP in the pharyngeal muscles (*Pmyo-2::GFP*) and thawed them to room temperature without any further treatment. The fluorescence level in the frozen animals was comparable to animals that were not frozen. By contrast, organic solvents quenched fluorescence. The same transgenic strain was frozen and processed through the freeze-substitution either with 100% acetone or 95% acetone plus 5% water in the absence of fixatives. The fluorescence in the animals treated with 100% acetone was completely quenched while there was no reduction in fluorescence in animals processed with 95% acetone, compared with non-treated animals. The presence of water at all steps was essential for the maintenance of fluorescence[5]. Each of the remaining steps also perturbs fluorescence significantly; to maintain fluorescence signals certain fluorescent proteins, fixatives and resins were required.

Supplementary Note 4: Components of each plastic

Lowicryl K4M is a combination of triethyleneglycol-di-methacrylate and benzoin-methyl-ether with acrylic and methacrylic esters.

LR Gold is consisted of 80% Polyhydroxy substituted bisphenol A dimethacrylate resin, 19.6% C12 methacrylate ester, and 0.4% dimethyl para toluidine.

LR White is consisted of 80% Polyhydroxy substituted bisphenol A dimethacrylate resin,19.6% C12 methacrylate ester, and 0.9% benzoyl peroxide.

References for Supplemenary Notes

1. Nägerl, U.V., Willig, K.I., Hein, B., Hell, S.W. & Bonhoeffer, T. Live-cell imaging of dendritic spines by STED microscopy. *Proc. Natl. Acad. Sci. U.S.A* **105**, 18982-18987 (2008).
2. Frøkjaer-Jensen, C. et al. Single-copy insertion of transgenes in Caenorhabditis elegans. *Nat. Genet* **40**, 1375-1383 (2008).
3. Kremers, G., Hazelwood, K.L., Murphy, C.S., Davidson, M.W. & Piston, D.W. Photoconversion in orange and red fluorescent proteins. *Nat Methods* **6**, 355-358 (2009).
4. McDonald, K. Cryopreparation methods for electron microscopy of selected model systems. *Methods Cell Biol* **79**, 23-56 (2007).
5. Micheva, K. & Smith, S. Array tomography: a new tool for imaging the molecular architecture and ultrastructure of neural circuits. *Neuron* **55**, 25-36 (2007).

Nature Methods: doi:10.1038/nmeth.1537

CHAPTER 4

NANO-FEM: VISUALIZING PROTEINS IN ELECTRON MICROGRAPHS AT NANO-RESOLUTION

Reprinted with permission from the Elsevier, Inc.

Watanabe, et al., 2011. Originally published in Methods in Cell Biology.

VOL. 111: 283-306

CHAPTER 15

Visualizing Proteins in Electron Micrographs at Nanometer Resolution

Shigeki Watanabe and Erik M. Jorgensen

Howard Hughes Medical Institute and Department of Biology, University of Utah, Salt Lake City, UT 84112-0840

METHODS IN CELL BIOLOGY, VOL 111

0091-679X
http://dx.doi.org/10.1016/B978-0-12-416026-2.00015-7

Abstract

To understand protein function, we need a detailed description of the molecular topography of the cell. The subcellular localization of proteins can be revealed using genetically encoded fluorescent proteins or immunofluorescence. However, the precise localization of proteins cannot be resolved due to the diffraction limit of light. Recently, the diffraction barrier has been overcome by employing several microscopy techniques. Using super-resolution fluorescence microscopy, one can pinpoint the location of proteins at a resolution of 20 nm or even less. However, the cellular context is often absent in these images. Recently, we developed a method for visualizing the subcellular structures in super-resolution images. Here we describe the method with two technical improvements. First, we optimize the method to preserve more fluorescence without compromising the morphology. Second, we implement ground-state depletion and single-molecule return (GSDIM) imaging, which does not rely on photoactivatable fluorescent proteins. These improvements extend the utility of nano-resolution fluorescence electron microscopy (nano-fEM).

I. Introduction

First described by Robert Hooke in 1665 (Hooke, 1665), a cell is the fundamental unit of life. Since then, light-based microscopes have been used extensively to identify structures such as the nucleus, mitochondria, and Golgi apparatus within a cell. Further technological improvements, such as dark field, phase contrast, differential interference contrast (DIC), and fluorescence imaging (Murphy, 2001), have expanded our ability to probe the structure of a cell. However, due to the diffraction limit of light, structures cannot be pinpointed in a cell (McCutchen, 1967). Thus, although Golgi staining was used to reveal the basic anatomy of neurons (Cajal, 1894, 1899, 1903), neither the synaptic connections between neurons nor subcellular structures, such as synaptic vesicles, have yet been directly observed by light microscopy.

To overcome the resolution limit of light microscopy, electron microscopy was developed in 1931 (Knoll & Ruska, 1932). With the shorter wavelength of electrons, resolution was improved to less than 1 nm, allowing for a complete depiction of subcellular structures. However, proteins important for cellular functions cannot be easily identified in electron micrographs. An immunocytochemical approach on plastic sections has been the best method available to identify the location of a protein at the ultrastructural level. However, this approach is difficult. The proteins lose antigenicity or are inaccessible due the fixation and plastic embedding. Thus, although electron microscopy has tremendous resolution advantages over light microscopy, its use has been limited in biology.

Despite the resolution limit imposed by the diffraction of light, fluorescence microscopy has become the most popular imaging technique in cell biology since the turn of the twenty-first century. There are two types of fundamental innovations that continue to extend the utility of fluorescence microscopy in cell biology: first, the discovery and synthesis of new fluorescent probes and second, developments in microscopy techniques. The most important innovation was the discovery and adaptation of genetically encoded fluorophores, the first of which was green fluorescent protein (GFP) (Chalfie, Tu, Euskirchen, Ward, & Prasher, 1994; Shimomura, 2009). Subsequently, fluorophores with many different excitation and emission spectra have been developed (Tsien, 1998; Zhang, Campbell, Ting, & Tsien, 2002). Using different sets of fluorescent probes, the spatial relationships of multiple proteins in a cell have been studied. Furthermore, microscopy techniques that allow three-dimensional visualization of proteins have been developed. The first step in three-dimensional fluorescence imaging was the invention of confocal microscopy. In confocal microscopy, specimens are scanned in x–y dimensions while out-of-focus fluorescence is blocked by an aperture. Only in-focus fluorescence is detected for the reconstruction of an image. However, these techniques are light based and hence the resolution is still limited to ~200 nm. Recently, groundbreaking improvements in microscopy techniques have extended resolution beyond the diffraction limit of light.

Super-resolution fluorescence microscopy overcomes the diffraction barrier by isolating fluorescence from each molecule spatially and temporally (Hell, 2007). For example, stimulated emission depletion (STED) microscopy allows the emission of fluorescence from an area smaller than the diffraction limit (Hell & Wichmann, 1994). STED is similar to confocal microscopy in that all fluorescent proteins in a diffraction-limited spot are excited by a scanning laser. However, a doughnut-shaped de-excitation beam that immediately follows the excitation beam brings the excited molecules back to the ground state without allowing the emission of fluorescence. Thus, fluorescence is only collected from the center of the doughnut, which is smaller than the diffraction limit. This subdiffraction spot is scanned across a specimen to generate an image. A resolution of ~30 nm can be achieved using this technique (Harke *et al.*, 2008).

Another super-resolution fluorescence technique is photoactivated localization microscopy, PALM (Betzig *et al.*, 2006), and its related techniques: fluorescence photoactivation localization microscopy, fPALM (Hess, Girirajan, & Mason, 2006); ground-state depletion with single-molecule return, GSDIM (Fölling *et al.*, 2008); stochastic optical reconstruction microscopy, STORM (Rust, Bates, & Zhuang, 2006); and direct stochastic optical reconstruction microscopy, dSTORM (Heilemann *et al.*, 2008). In these techniques, each molecule is present one at a time by changing the fluorescence state of individual fluorophores. For example, in PALM and STORM, fluorophores can be photoactivated from a nonresponsive state to a responsive state one at a time (Fig. 7(A); Gurskaya *et al.*, 2006; Patterson & Lippincott-Schwartz, 2002; Wiedenmann *et al.*, 2004). Alternatively in GSDIM, fluorophores can be driven into a dark state, from which they return to the ground state in a stochastic manner (Fig. 8(A); Fölling *et al.*, 2008; Heilemann *et al.*, 2008). By taking advantage of such responses, each molecule is isolated stochastically in space and time. By acquiring multiple images and calculating

the centroid of each fluorescent spot, all the molecules in the field are mapped to produce the final image. Using these techniques, resolution can be improved to ~20 nm (Betzig *et al.*, 2006; Hess *et al.*, 2006; Rust *et al.*, 2006; Shtengel *et al.*, 2009).

Irrespective of the technique used, all super-resolution fluorescence imaging has the disadvantage that cellular context is missing from the images. To overcome this problem, attempts have been made to combine fluorescence microscopy with electron microscopy.

Methods for correlating protein localization in light and electron micrographs can be separated into three approaches: preembedding fluorescence microscopy, preembedding diaminobenzidine (DAB) imaging, and postembedding fluorescence electron microscopy (fEM). Preembedding fluorescence microscopy is the simplest: the whole cell is imaged using normal fluorescence techniques first to localize the protein and the specimen is then processed for electron microscopy (Müller–Reichert, Srayko, Hyman, O'Toole, & McDonald, 2007; Oberti, Kirschmann, & Hahnloser, 2010; Polishchuk *et al.*, 2000; Verkade, 2008). This approach makes fluorescence imaging simple; however, precisely locating the same region of interest in the electron microscope is difficult and it does not localize proteins with high-definition. The DAB precipitation method uses photooxidation (Grabenbauer *et al.*, 2005; Shu *et al.*, 2011; Sosinsky, Giepmans, Deerinck, Gaietta, & Ellisman, 2007) or enzymatic oxidation (Schikorski, 2010) of DAB, which forms precipitation that can be observed via both light and electron microscopy. This method can be useful when the proteins of interest are not abundant in the cell. However, the electron-dense precipitation of DAB molecules may obscure the fine details of electron micrographs, especially when the proteins are abundant. Moreover, this technique is only compatible with conventional chemical fixation, and thus fixation artifacts caused by dehydration (McDonald, 2007) are inevitable. Correlative fEM preserves fluorescence in plastic sections and images fluorescence and electron-dense structures from the same sections (Kukulski *et al.*, 2011; Micheva & Smith, 2007; Nixon *et al.*, 2009; Schwarz & Humbel, 2007; Sims & Hardin, 2007;). Fluorescence signals can be overlaid on electron micrographs using this approach, but the disparity between diffraction-limited fluorescence imaging and ultrastructure means that the proteins cannot be precisely localized, and the preservation of fluorescence and morphology is often compromised. Recently, we have developed a method, called nano-fEM, that preserves 60–70% fluorescence while retaining good ultrastructure (Watanabe *et al.*, 2011). By applying super-resolution imaging techniques, proteins can be localized to subcellular structures with ~20 nm resolution. Here we will describe our improved methods for protein localization in electron micrographs and discuss the current issues and future directions of this approach.

II. Rationale

To fully characterize the functions of a protein, the location of the protein relative to the subcellular structures must be revealed. A fluorescence-tagging approach is

a very robust method to localize proteins at a subcellular level. If super-resolution fluorescence imaging is applied, the resolution of fluorescence images can be comparable to that of electron micrographs (Hell, 2007). However, the lack of cellular context in fluorescence images limits the ability to localize proteins to subcellular structures. On the other hand, immuno-electron microscopy has high resolution, but it is limited by the poor quality of fixation and availability of antibodies (Morphew, 2007; Rostaing, Weimer, Jorgensen, Triller, & Bessereau, 2004; Roth, Bendayan, Carlemalm, Villiger, & Garavito, 1981). A combination of these two techniques can merge the robustness of fluorescence imaging with the ultrastructures depicted by electron microscopy and potentially reveal protein localization at its maximum resolution. Therefore, we sought fixation conditions that preserve both fluorescence and morphology in the plastic sections.

We recently published a paper describing methods for correlating STED or PALM images with electron micrographs (Watanabe *et al.*, 2011). With 60–70% preservation of fluorescence after fixation and plastic embedding, signals appeared very bright using STED microscopy. This result was partly due to the brightness and the superior quantum efficiency of Citrine (Heikal, Hess, Baird, Tsien, & Webb, 2000) used for STED. However, the resolution of STED was ~50–70 nm (Watanabe *et al.*, 2011). On the other hand, the average localization precision of PALM images, that is, a standard error of mean of a localization, was ~12 nm (Watanabe *et al.*, 2011). However, photoconvertible fluorescent proteins appeared more sensitive to the sample preparation. Moreover, PALM imaging is often restricted to a single color. Therefore, we sought to improve fEM technique in two ways. First, we have been refining the protocol to preserve more photoconvertible fluorescent proteins without compromising the morphology. In this chapter, we will present a new protocol that preserves ~90% of fluorescence with the same quality of ultrastructure. Second, since Citrine is very bright and has shown to be compatible for GSDIM (Lalkens, Testa, Willig, & Hell, 2011), we also tested GSDIM imaging using Citrine. Fluorescent proteins compatible for multicolor PALM imaging are rare; thus, if this approach is successful, GSDIM imaging will allow the use of specimens that have already been tagged with fluorescent proteins for confocal microscopy.

III. Methods

To perform postembedding fluorescence imaging, fluorescent proteins must be functional in plastic sections. The retention of fluorescence through the fixation and plastic embedding processes is extremely difficult because of the oxidizing, acidic, and dehydrated conditions required for sample preparation. Fluorescent proteins require a hydrated environment with alkaline pH for their best performance (Tsien, 1998). Thus, we optimized the protocol to balance the preservation of morphology and fluorescence. Protein localization using correlative nano-fEM consists of the following seven steps: high-pressure freezing, freeze-substitution, plastic embedding, sectioning, super-resolution imaging, electron microscopy imaging, and image alignment (Fig. 1).

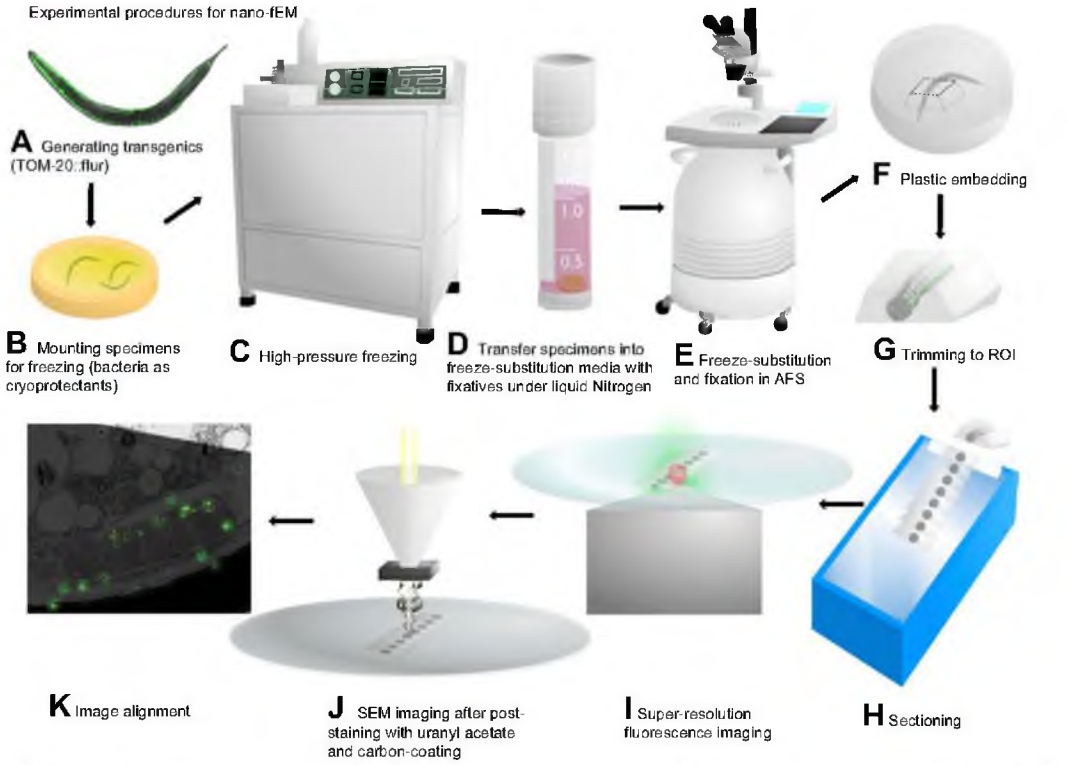

Fig. 1 Schematic diagram showing the procedure for nano-fEM. Transgenic animals (A) are subject to high-pressure freezing (B, C). The cellular water is substituted with acetone, while tissues are fixed with 0.1% potassium permanganate and 0.001% osmium tetroxide (D, E). The specimens are embedded into GMA plastic (F). The plastic block is trimmed to the region of interest (G), and thin slices (~80 nm thick) of tissues are cut using a diamond knife (H). Sections are imaged first with super-resolution fluorescence microscopy (I) and second with SEM (J). The correlative image is then aligned based on the fiducial markers (K).

A. High-Pressure Freezing

High-pressure freezing is the first step required for preserving both fluorescence and morphology. The high-pressure freezing and freeze-substitution techniques allow near-instantaneous immobilization of specimens, prevent fixation and dehydration of artifacts such as protein aggregations (Payne, 1973), and also prevent membrane shrinkage (McDonald, 2007) often observed using the conventional method. The preparation can be carried out in the way recommended for the specimens of choice (McDonald *et al.*, 2010; Müller-Reichert, 2010). For *Caenorhabditis elegans*, transgenic animals expressing photoconvertible fluorescent proteins are raised in an opaque box to minimize their exposure to ultraviolet light. Raising them in darkness prevents spontaneous photoconversion of fluorescent proteins. Once animals are raised to the desired developmental stage, typically to adulthood, they are subjected to freezing. For Baltec HPM 10, two types of specimen carriers are used: type A and type B. Type A has two chambers. One is

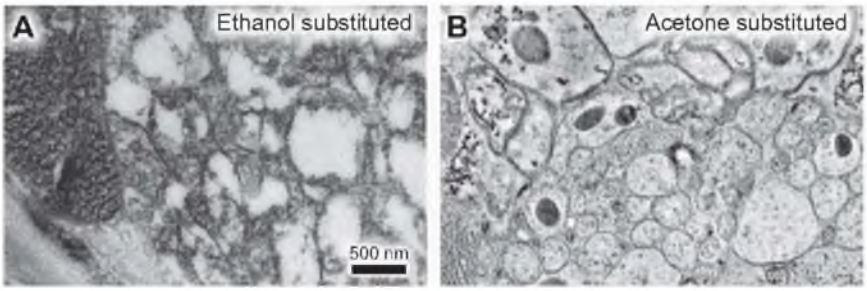

Fig. 2 Preservation of morphology by different freeze-substitution media. Transgenic animals expressing TOM-20–tdEos were freeze-substituted in ethanol (A) or acetone (B). The ventral nerve cord in an adult *C. elegans* is shown in each case. Note that ethanol washed out the tissues. 0.1% potassium permanganate and 0.001% osmium tetroxide was used as the fixative in both cases. The membrane contrast was enhanced by both *en bloc* staining and section staining using uranyl acetate.

100 μm deep and the other is 200 μm deep. Type B has a 300 μm-deep well on one side and a flat surface on the other side. Hexadecane should be applied to the 100 μm-deep well of type A and the flat side of type B. Hexadecane should be removed from the wells by blotting the carriers against a piece of filter paper. Since the diameter of an adult *C. elegans* is about ~70 μm, we mount animals into the 100 μm-deep side of a type A specimen carrier. We add animals and bacteria to the specimen carrier by scooping animals from the lawn of bacteria (*Escherichia coli*) with a paintbrush. The bacteria serve as cryoprotectants. This configuration allows us to separate the animals easily from the bacteria during the plastic embedding step. Alternatively, 20% BSA in M9 solution can be used (McDonald, Morphew, Verkade, & Müller-Reichert, 2007). However, it is harder to dissociate the animals from the BSA solution. The chamber should be slightly overfilled to avoid trapping air bubbles in the chamber when it is capped with the flat side of the type B specimen carrier. We then freeze the specimens as instructed by the manufacturer.

B. Freeze-Substitution

Following high-pressure freezing, the vitrified water is replaced with organic solvents such as acetone so that the water does not recrystallize when the specimens are brought back to higher temperatures for plastic embedding. In addition, fixation of tissues is carried out simultaneously to stabilize the subcellular structures and enhance the contrast of tissues.

Prior to the freeze-substitution, cryovials containing 0.1% potassium permanganate and 0.001% osmium tetroxide in 95% acetone (a mix of anhydrous acetone with milliQ water) are frozen in liquid nitrogen. The use of acetone as a freeze-substitution medium is critical for preserving ultrastructure because acetone cross-links with membrane (Weibull & Christiansson, 1986; Fig. 2). The automated freeze-substitution (AFS) unit should also be prepared as instructed by the manufacturer. The program should be set as summarized in Table I. The duration at –90°C can be shortened or lengthened to accommodate one's schedule.

Table I
Freeze-substitution programs for AFS 1 and 2.

AFS 1	AFS 2
–90°C for 5–36 h	–90°C for 30–36 h
5°C/h to –50°C	5°C/h to –50°C
–50°C for 2 h	Pause
5°C/h to –30°C	Unpause after acetone wash
–30°C for 72 h	5°C/h to –30°C
Stop the program and initiate another program after plastic embedding	Pause
–30°C for 0 h	Unpause after plastic embedding
10°C/h to –20°C	10°C/h to –20°C
–20°C for 24 h	–20°C for 24 h

The frozen samples are transferred into the cryovials containing the fixative under liquid nitrogen. Only the specimen carrier containing specimens (typically type A) is transferred into the cryovials. The cryovials are capped and placed in the AFS, which is held at –90°C. To ensure the homogeneity of the fixative and to accelerate the diffusion of chemicals, the cryovials are shaken periodically (at least twice a day). When the temperature reaches –60°C, a glass vial containing 95% acetone is placed in the AFS chamber. As soon as the temperature reaches –50°C, the fixative is replaced with 95% acetone. To ensure the complete removal of the fixative, this step is repeated five times with 20 min intervals. In the meantime, 0.1% uranyl acetate in 95% acetone is prepared and precooled to –50°C. At the last washing step, 95% acetone is replaced with the uranyl acetate solution. Uranyl acetate stains phospholipids and nucleic acids and does not affect fluorescence (Kukulski *et al.*, 2011). Uranyl acetate is often included in the fixative; however, we have observed improved morphology when uranyl acetate is applied after fixation. It is possible that the uranyl acetate interferes with osmium cross-linking the membranes. The AFS program should be resumed if paused. The vials containing 95% ethanol (anhydrous ethanol + 5% milliQ water) are placed in the chamber so that the solution is precooled. When the program reaches the –30°C step, the uranyl acetate solution is replaced with 95% ethanol. Again, this step is repeated five times over a period of 2 h. Although ethanol can extract lipids (Weibull & Christiansson, 1986), switching from acetone to ethanol is necessary to make the specimen competent for acrylic resin embedding, since acetone interferes with plastic polymerization by scavenging free radicals (Newman & Hobot, 1993). About 90% of fluorescence can be preserved using this protocol (Fig. 3). If significant reduction in fluorescence level is observed using this protocol, one may need to alter the duration of uranyl acetate application because some batches of uranyl acetate is highly acidic and quenches fluorescence. One hour of incubation is sufficient for enhancing the contrast of tissues.

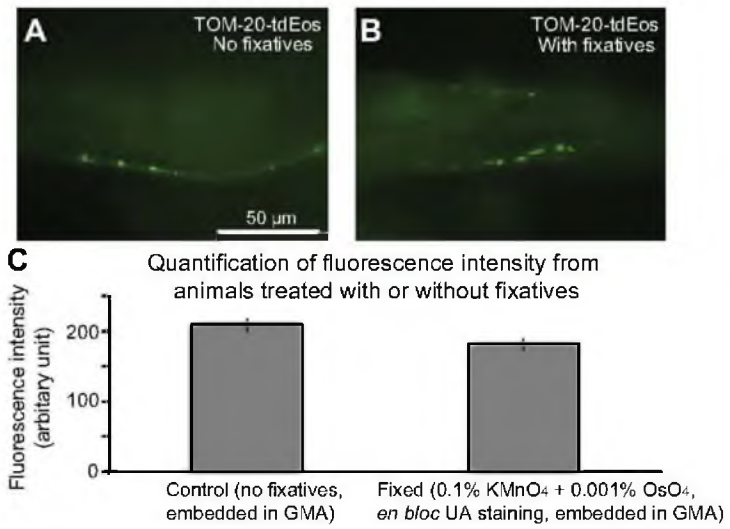

Fig. 3 Preservation of fluorescence after fixation and plastic infiltration. (A) Fluorescent mitochondria in an unfixed adult worm. Transgenic animals expressing the mitochondrial marker TOM-20–tdEos were freeze-substituted with 95% acetone in the absence of fixatives. Mitochondria in the muscles of an adult worm are visible. 100% of fluorescence is preserved when compared to unfixed animals (not shown). (B) Fluorescent mitochondria in a fixed adult worm. Transgenic animals expressing TOM-20–tdEos were freeze-substituted with 95% acetone in the presence of fixatives (0.1% $KMnO_4$ + 0.001% OsO_4) and *en bloc* stained with uranyl acetate. (C) Fluorescence intensity of TOM-20–tdEos was measured from the control and the fixed animals and quantified. A 10% reduction in the fluorescence level was observed when animals were treated with fixatives and staining solution. (See color plate.)

C. Plastic Embedding

After freeze-substitution, specimens are infiltrated with glycol methacrylate (GMA). The infiltration is carried out in a stepwise fashion (30%, 70%, and 100%) at –30°C. The stock solution of GMA can be prepared by mixing 22.7 ml of GMA, 10 ml of butyl methacrylate, 1 ml of milliQ water, and 200 mg of benzoyl peroxide in a 50 ml conical tube. Dissolving benzoyl peroxide may require a few minutes, and thus it is best to leave the tube on the nutator in a cold room. Once the benzoyl peroxide is fully dissolved, the stock solution is transferred into 20 ml scintillation vials and stored at –20°C until use. To prepare the infiltration media, we mix the GMA stock solution media with 95% ethanol. The infiltration media is then placed in the AFS chamber. This step should be carried out concurrently with the ethanol-washing step of freeze-substitution so that the medium is cooled down to –30°C before use. Each step of the infiltration process can be spaced to accommodate one's schedule. Specimens are typically incubated with the 30% solution for 2–4 h, the 70% solution for 3–5 h, and the 100% solution overnight.

The next day, the specimens are transferred into the cap from a polypropylene BEEM capsule. An Aclar disk, prepared by a 3/8× punch, should be placed at the bottom of the cap. The disk makes the surface of the plastic smooth which makes trimming of the block easier. An Aclar disk must be placed on the top surface of the resin

as well if you are using LR White, since oxygen will prevent the polymerization of the acrylic resin. Specimens are placed on the top of the Aclar disk, and thus the Aclar disk blocks oxygen at the base of the cap. The media is exchanged twice more, with a 2 h interval. Animals are separated from the bacteria so that individual nematodes are exposed to plastic without being surrounded by bacteria or other animals. Acrylic resin does not cross-link with tissues; thus, when sectioned, specimens can dissociate from the surrounding plastic, resulting in distortion of the plastic and discontinuity of the ribbon of sections (Fig. 4(A)). If individual animals that are completely surrounded by the plastic are sectioned one at a time, the distortion of the plastic will be minimal, improving the sectioning result (Fig. 4(B)). Therefore, the removal of the cryoprotectants is critical. At the final step, a catalyst, *n,n*-dimethy-*p*-toluidine, is added to the GMA stock solution at a concentration of 1.5 µl catalyst per 1 ml GMA stock. The reaction is highly exothermic and can be complete within 30 min of the addition of the catalyst at room temperature, so the catalyst should be added while the GMA stock solution is held in the AFS chamber. The specimens should be left in the chamber overnight to ensure completion of the process. Specimens are stored in nitrogen-gas-filled vacuum bags (Ziploc) at –20°C to reduce oxidation of the fluorescent protein.

D. Sectioning

Once the plastic has polymerized, the specimens can be manipulated at room temperature. A room with bright sunlight or even bright room light should be avoided at all times. To find a region of interest before sectioning, the specimens can be exposed briefly (~1 s) to blue light. Once the area of interest has been located under the stereomicroscope, a knife mark is left near this area, and the block is trimmed to the knife mark using a razor blade. Sectioning of GMA plastic can be challenging because of the hydrophilic nature of the plastic. If further trimming of the block with a glass knife is necessary, water in the boat should be underfilled. If water gets on the block face, the section submerges rather than floats on the surface and cannot be retrieved.

Ultrathin sectioning can be carried out in a manner similar to that used for epoxy resins. However, sectioning quality of GMA is inconsistent. Cutting even the same block on a different day may result in poor appearance of morphology (Fig. 4(C and D)). Occasionally, folding of a tissue due to sectioning can also be observed (Fig. 4(E)). In addition, structures such as lipid droplet in gut can also dissociate while sectioning (Fig. 4(F)). Sectioning thickness and cutting speed can be adjusted to minimize the sectioning artifacts—we often cut 80 nm thick sections with the cutting speed of 1.6 mm/s.

If sections are imaged on a TIRF microscope, the sections must be mounted directly on a coverglass; otherwise, sections can be mounted on a transmission electron microscopy (TEM) grid. For PALM imaging, autofluorescence from dust particles can also be detected because of the high sensitivity of the EMCCD camera. Therefore, coverglasses should be cleaned using piranha solution. The piranha solution can be prepared by mixing three parts of sulfuric acid and one part hydrogen peroxide. The coverglasses are left in the piranha solution for 1 h, washed thoroughly with milliQ water six times, sonicated for half an hour, and washed again with milliQ water six times. This treatment

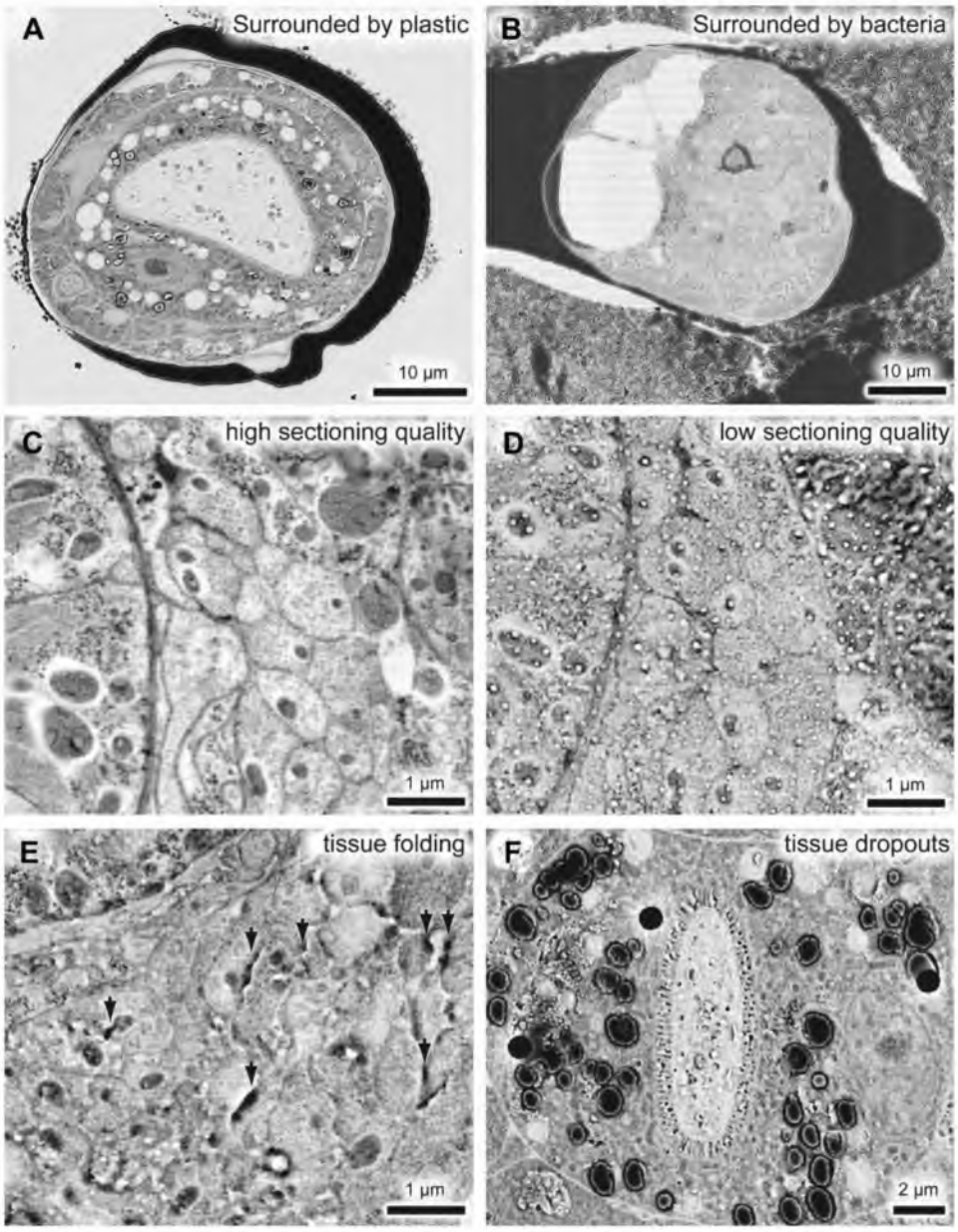

Fig. 4 Problems associated with GMA sectioning. (A, B) Low magnification electron micrographs, showing the dissociation of worms from the surrounding media. The section is more distorted in a specimen that is surrounded by the cryoprotecting bacteria (B) than when the specimen is surrounded by plastic (A). The bacterial cryoprotectant in the gallette should be dissected away from the fixed sample before plastic embedding. (C, D) Electron micrographs of neurons from the same specimen, sectioned on different dates. The preservation of tissues is superb on one day (C), but such morphology is obscured by the inconsistent sectioning quality (D). (E) Electron micrograph of nerve ring, showing folding of sections due to the incomplete polymerization of plastic (black arrows). (F) Electron micrograph of intestine, showing dropouts of tissues (black circles).

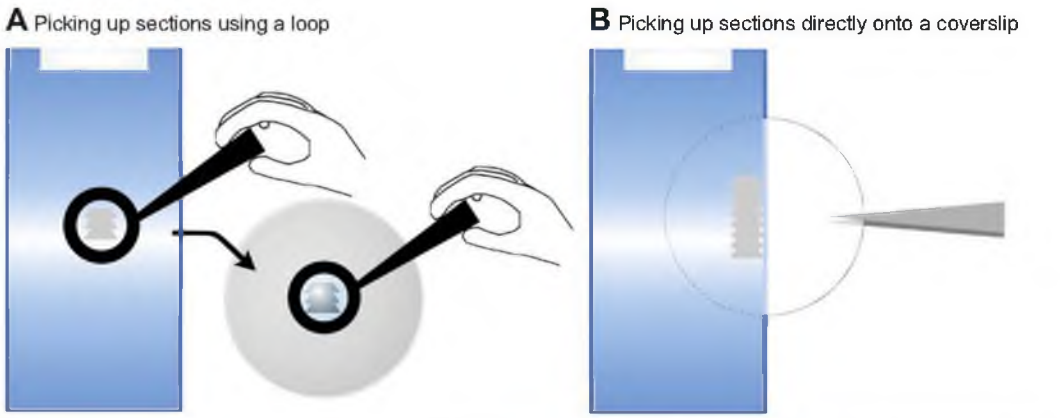

Fig. 5 Schematic diagrams showing two methods for mounting sections onto a coverslip. Sections can be picked up using a loop (A) or by simply immersing a coverslip in the boat of a diamond knife (B). A longer ribbon of sections can be mounted by immersing a coverslip. (See color plate.)

leaves the surface of the coverglasses hydrophilic, which is not ideal for picking up sections. The addition of a few drop of hexamethyldisilazane (HMDS) in a sealed jar containing the coverglasses creates the hydrophobic surface.

There are two ways to mount sections on a coverglass (Fig. 5). First, sections can be picked up using a perfect loop (Electron Microscopy Scieneces) or something similar and placed on a coverglass (Fig. 5(A)). A problem with this approach is that sections may dissociate from the ribbon in the process. The loop should be cleaned using ethanol prior to use so that dust particles are not transferred with the sections. The use of a Kimwipe or filter paper to remove water from the loop also leaves dust on the sections, so the drop of water containing sections should be blown off to a coverglass from the loop. Once the water evaporates, sections will adhere to the surface of the coverglass. The second method is to use a diamond knife with a large boat so that a coverglass can be submerged in the water to pick up sections, just as they are on a TEM grid (Fig. 5(B)). Mounting sections in the middle of the coverglass is technically more challenging because sections become invisible in the concave water surface created from submerging the coverglass in water. A longer ribbon can be mounted on a coverglass using this method, whereas the dimension of the ribbon is restricted by the size of the loop in the former case. Ideally, sectioning should be carried out in a darkened room. Once sections from the region of interest are collected, the coverglass should be covered with aluminum foil and stored at –20°C until further processing.

E. Fluorescence Imaging

Prior to fluorescence imaging, a solution containing gold nanoparticles should be applied to the sections for 1 min. The sections are then soaked in milliQ water for 2 min. The 100 nm gold nanoparticles emit red fluorescence when excited by green light due to surface plasmon resonance (Link & El-Sayed, 1999) and reflect electrons when imaged

under an electron microscope. Therefore, they can mark both fluorescence images and electron micrographs and serve as alignment markers for the image correlation. The solution containing gold nanoparticles with a concentration at 1.2×10^{10} particles/ml is applied to the specimen for ~30 s to 1 min and then removed by blowing the solution off to the side of the coverslip and blotting it using a Kimwipe or filter paper. Next, a drop of water is applied to the sections. The water restores the function of fluorescent proteins. After fixation and plastic embedding, some of the fluorescent proteins are preserved in a nonfluorescent state (Watanabe *et al.*, 2011). We found that the addition of water prior to imaging increases the fluorescence intensity 30-fold (Watanabe *et al.*, 2011). However, autofluorescence in GMA resin also increases after hydration. This increase is detected by an EM-CCD camera, with which the PALM scope is equipped. Therefore, PALM imaging cannot be carried out while immersing the samples in water. Water is only applied to specimens for 2 min and is removed just prior to imaging. The use of a Kimwipe or filter paper to draw the solution off directly from the specimen would introduce dust particles into the sections and induce autofluorescence, so the solution must be blown to the edge of the coverslip and then absorbed onto a Kimwipe or filter paper.

For PALM imaging, the microscope should be set up as recommended by the manufacturer. The frame rate should be set at 20 Hz or less. Bright field illumination should be used to locate specimens. A low-intensity 488 nm laser can be employed to localize proteins in the region of interest if necessary but should be avoided if possible. Once the region of interest is set, 561 nm laser light at the highest intensity should be applied for ~2 min to the specimen to bleach the autofluorescence. To collect images, the activation laser and readout laser should be set at their lowest and maximum intensities, respectively. We usually collect ~ 6000 frames per section; this is sufficient to sample the distribution of fluorophores. However, if every molecule in the region must be localized, the frame number should be increased accordingly. If the activated molecules in a given space are sparse, the activation energy can be gradually increased. It is important to note that the computer calculates the centroid of each fluorescent spot; thus, if two molecules emit fluorescence in a given diffraction-limited spot at the same time, only one dot would be placed in the middle of these two molecules, resulting in a false negative. PALM images should be acquired from each section on the coverslip. The sections become dehydrated during a long imaging session, so they are rehydrated with a drop of milliQ water approximately every half-hour. Again, the milliQ water should be blown to the side before absorbing it onto a Kimwipe or filter paper to avoid contamination.

For GSDIM imaging, fluorescent proteins must be driven into the dark state in the absence of oxygen (Fölling *et al.*, 2008). Plastic seems to serve as a diffusion barrier for oxygen; thus, a solution containing oxygen scavengers or a chamber filled with nitrogen gas may not be necessary. Following the gold particle application and hydration described in the previous section, 488 nm laser at 5 mW/mm^2 intensity is applied to induce the state shift of fluorescent proteins from the ground to the dark state (Fig. 8(B and C)). About 5000 images are collected at a frame rate of 20/s while applying a continuous 488 nm laser at 1 mW/mm^2.

After their acquisition, images should be processed for PALM (Fig. 7(B and C) or GSDIM (Fig. 8(D and E). Since some background fluorescence is inevitable when

imaging plastic sections, it should be filtered out in the final fluorescence image. For background subtraction, we impose two thresholds: fluorescence lifetime and brightness. The emission from tdEos molecules typically lasts for ~500 ms or less before they become bleached when 5 mW/mm^2 laser is applied. A threshold of 500 ms is set so that any molecules that fluoresce for longer than 500 ms do not appear in the final image. Additionally, low-intensity background autofluorescence can be subtracted by visualizing the molecules with high-localization precision. Localization precision depends on the number of photons collected at each spot. Fluorescence from tdEos or Citrine molecules often appears brighter than background fluorescence; hence, by imposing a threshold for localization precision, low-intensity noise can be filtered.

F. SEM Imaging

To observe the ultrastructure of biological specimens under a scanning electron microscopy (SEM), tissues must first be post-stained with uranyl acetate, and then coated with carbon. Although uranyl acetate is applied to the specimens during the cryosubstitution process, the contrast is insufficient for SEM imaging. To post-stain the sections, a solution containing 2.5% uranyl acetate in milliQ water should be prepared. Filtering the solution using a 0.2 μm syringe filter is highly recommended. A drop of the solution is applied directly to the top of the sections, and after 4 min, it is washed off by gently running filtered milliQ water thoroughly over the specimens. The sections should be air dried rather than blotted with filter paper.

Plastic sections and coverglasses are not electron-conductive materials. Thus, the surfaces of such specimens will be charged when placed under the electron beam. To prevent charging, specimens must be coated with carbon. Using a carbon sputter, a layer of carbon is applied to the specimen so that the glass slides appear dark brown. The surface of the specimen is then grounded by applying one end of a piece of carbon tape to the edge of the glass and attaching the other end to the base of the specimen stub. The electrons that accumulate on the glass surface will now run to the ground.

After preprocessing and the routine alignment of the microscope, the samples can be imaged. Backscattered electrons should be collected. The FEI Nova Nano has two features that make it more sensitive to backscattered electrons. First, a magnetic field can be applied between the pole piece and the specimen so that backscattered electrons do not leave the beam path. The stage can also be negatively biased so that backscattered electrons can be accelerated toward the detector. A combination of the magnetic field and stage bias thus enhances detection efficiency. Typically, the specimen current is set at 0.11 nA, the accelerating voltage at 5 keV, and the landing energy at 3 keV. "Immersion mode" should be turned on. Typically, two sets of images are generated: low magnification and high magnification. A fluorescence image is aligned to the low magnification image. The higher magnification image is then used to observe the distribution of signals relative to the subcellular structures. The grayscale of the image should be inverted to resemble a transmission electron micrograph.

G. Image Alignment

A fluorescence image and an electron micrograph are aligned based on gold fiducial markers. This is possible because the 100 nm gold nanoparticles emit fluorescence in red and reflect electrons, marking both fluorescence and electron micrographs (Fig. 6(A and B). To align the images, a new window of 5000 × 5000 pixels with a resolution at 300 pixels/in. should be opened in Photoshop. The low magnification electron micrograph is then copied and pasted to the window and transformed ("command" + "t" for Mac) so that the image occupies about 80% of the space. The aspect ratio of the image should not be changed when the image is transformed (holding down the "shift" key while scaling the image will keep the ratio). The sum TIRF image is copied to a new layer and transformed (scaling, translation, and rotation) so that the fluorescence from the gold particles lies on top of particles visualized in the electron micrographs (Fig. 6(B)). For alignment, although some gold particles are visible in a PALM image, a sum TIRF image should be used because fluorescence from gold particles is more distinctive from the background noise in the sum TIRF image. Nonlinear transformations may be necessary to align the images perfectly because electron beams can distort the specimens (Newman & Hobot, 1993). The fluorescence image is then copied to another layer and aligned on the top of the sum TIRF image using the same transformational value (Fig. 6(C)).

For presentation purposes, a gradient transparency in the fluorescence image may be applied so that only the background pixels become transparent. First, the transformed fluorescence image should be duplicated so that the original file is not manipulated. Using "color range" under the "select" dropdown menu, select the background "black pixel" and invert the selection (the "invert" option should be clicked). The fuzziness should be adjusted so the black pixels surrounding the signals are not selected. Only now the signals should be selected. The signals are then cut and pasted to a new layer. This action leaves blanks in the locations where the signals were in the manipulated

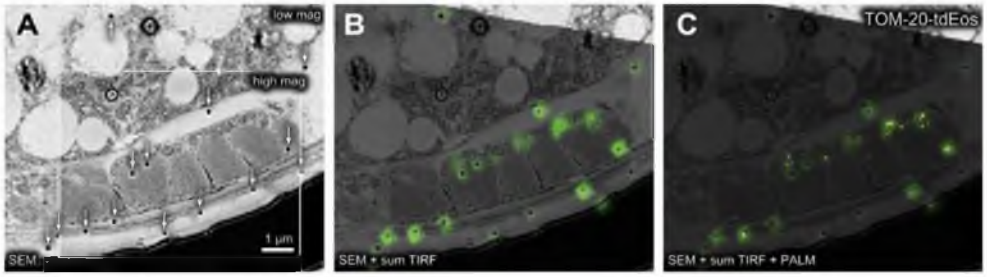

Fig.6 Gold nanoparticles are used as fiducial markers to align fluorescence and electron micrographs. Image is a cross section of a *C. elegans* adult expressing TOM-20–tdEos. (A) A low magnification SEM image is used to orient and place the high magnification SEM image. The low magnification image (5000×) is opened in photoshop first. A higher magnification electron micrograph (50,000×) is aligned on top of the low magnification image. High magnification image is outlined with a white line. Black dots, indicated by arrows, are the fiducial marks from 100 nm gold nanoparticles applied prior to PALM imaging. (B) A sum TIRF image is aligned onto an electron micrograph based on fluorescence from the gold fiducials. A "sum TIRF" image represents all of the fluorescence obtained during the length of the imaging session. (C) A PALM image is then rotated and translated based on the values obtained in (B). (See color plate.)

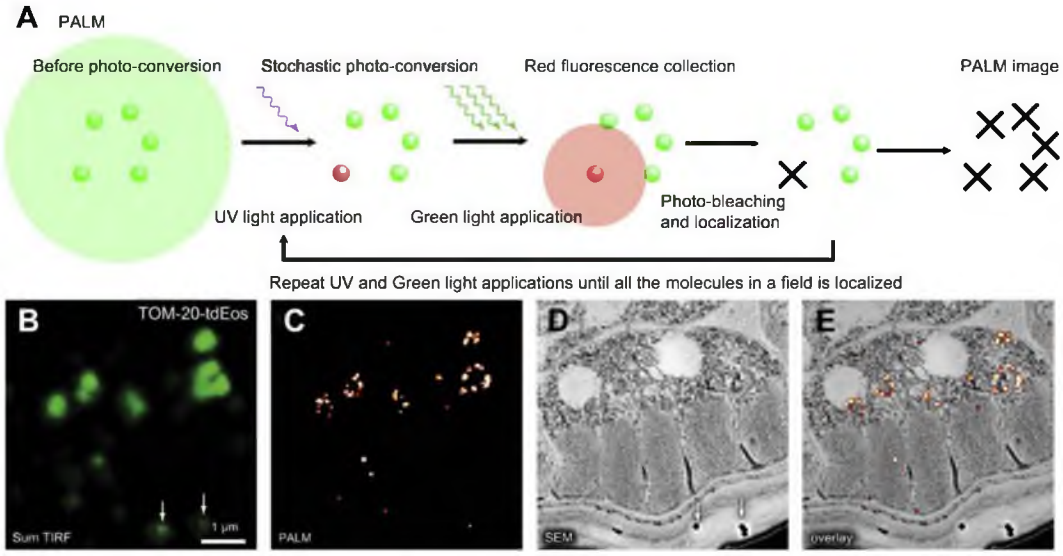

Fig. 7 Nano-fEM using photoactivation localization microscopy (PALM). (A) Schematic diagram showing the concept of PALM. Molecules are activated stochastically, imaged, and photobleached. The centroid of each fluorescence spot is then calculated and reconstructed in a final image. (B) Sum TIRF image of TOM-20–tdEos acquired from a thin section (80 nm) of a GMA-embedded sample. White arrow indicates fluorescence emitted from gold particles. (C) Corresponding PALM image of TOM-20–tdEos. (D) Electron micrograph of a body muscle acquired from the same section. (E) Nano-fEM of TOM-20–tdEos. The fluorescent signals are localized to the outer membrane of the mitochondria. (See color plate.)

layer—this layer thus contains only the background pixels. The transparency should be set to 10% in the background layer. Now the signals are distinctive from the background, and can be overlaid on the electron micrograph. The representative images for correlative microscopy using PALM (Fig. 7(B–E)) or GSDIM (Fig. 8(D–G)) from the transgenic animals expressing TOM-20::tdEos or TOM-20::Citrine, respectively, showed similar distribution of proteins on the outer membrane of mitochondria.

IV. Instrumentations and Materials

A. High-Pressure Freezing

1. High-pressure freezer (HPM010, Baltec)
2. Specimen carriers type A (#241-200, TechnoTrade)
3. Specimen carriers type B (#242-200, TechnoTrade)
4. Hexadecene (#H2131-100 ML, Sigma-Aldrich)
5. Albumin from bovine serum (A2153-10G, Sigma-Aldrich)
6. Worm buffer M9 (22 mM KH_2PO_4, 19 mM NH_4Cl, 48 mM Na_2HPO_4, and 9 mM NaCl)
7. Forceps (insulated; #16LZ01873KN, Leica Microsystem)

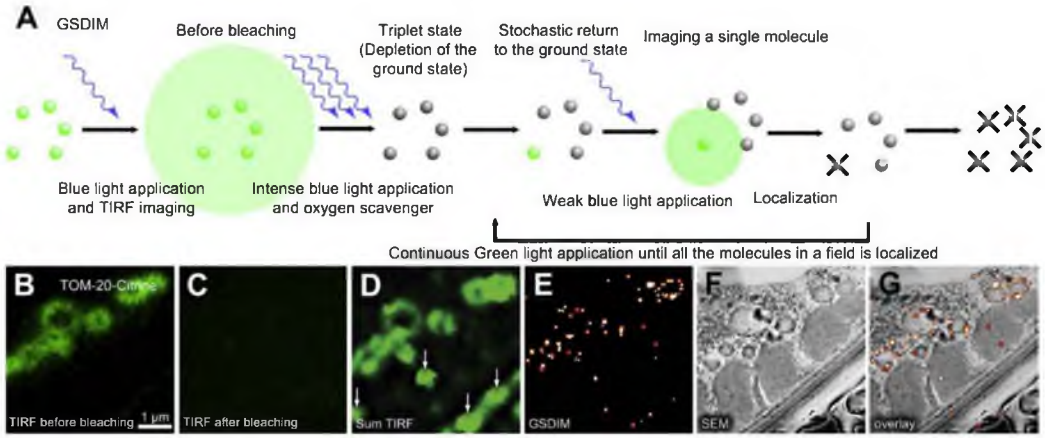

Fig. 8 Nano-fEM using ground-state depletion (GSDIM). (A) Schematic diagram showing the concept of GSDIM. Fluorescent proteins, Citrine, are excited and driven into a dark state with intense laser in the presence of an oxygen scavenger. Fluorophores return to the ground state stochastically and are imaged. The centroid of each fluorescent spot is calculated and localized in a similar manner as PALM to reconstruct a final image. (B) TIRF image of TOM-20–Citrine acquired from a thin section (80 nm). Fluorescence signals are diffraction limited because all molecules fluoresce at the same time. (C) TIRF image of the same region imaged in (B). All the molecules are driven into a dark state (the triplet state) by intense 488 nm laser, and thus no signals are observed. (D) Sum TIRF image reconstructed from all the fluorescence spots detected by the camera. Background fluorescence is typically higher using GSDIM because sections cannot be prebleached using the readout laser. (E) Corresponding GSDIM image of TOM-20–Citrine. (F) Electron micrograph of a body wall muscle acquired from the same section. (G) Correlative GSDIM and electron microscopy of TOM-20–Citrine. The fluorescent signals are localized to the outer membrane of the mitochondria. (See color plate.)

8. Paintbrush #00 (7/16 inch)
9. Whatman filter paper (#09-810D, Fisher)
10. Isopropanol (#19030-4L, Sigma-Aldrich)
11. Liquid nitrogen

B. Freeze-Substitution

1. Automated freeze-substitution unit (AFS 2, Leica microsystem)
2. Cyrovials (#D9912, Nalgene)
3. 50 ml screw cap conical tubes (#62.547.004, Starstedt)
4. 15 ml screw cap conical tubes (#62.554.002 PP, Starstedt)
5. Acetone (RT10016, EMS)
6. Ethanol (#459844-1L, Sigma-Aldrich)
7. Osmium tetroxide (crystals, 1/10g; RT19134, EMS)
8. Potassium permanganate (RT20200, EMS)
9. Uranyl acetate (#21447-252, Polysciences)
10. Disposable transfer pipette (#14670-201, VWR)
11. Disposable pasteur pipette (Borosilicate glass; #13-678-20A, Fisher)
12. Pipetman and tips (P1000, P200, and P20)

C. Plastic Embedding

1. GMA kit (low acid and TEM grade; #02630-AA, SPI)
2. *N,N*-Dimethyl-*p*-toluidine (#D9912, Sigma-Aldrich)
3. Scintillation vials (20 ml; #72632, EMS)
4. Aclar film (#50425-10, EMS)
5. BEEM capsule (polypropylene; #TC, EBSciences)
6. 3/8" disk punches (#54741, Ted Pella)
7. 25 ml serological pipette (#13-678-11, Fisher)
8. 10 ml serological pipette (#13-678-11 E, Fisher)
9. Petri dish (35 × 10 mm; #351008, Fisher)

D. Coverslip Cleaning

1. Coverslip (#1.5, round; #40300, Warner Instruments)
2. Sulfuric acid (#320501-2.5L, Sigma-Aldrich)
3. Hydrogen peroxide (#216763-500ML, Sigma-Aldrich)
4. Coverslips rack (Teflon; C-14784, Invitrogen)
5. Sonicator

E. Sectioning

1. Ultramicrotome (UC6, Leica microsystem)
2. Diamond knife (Ultra jumbo, 45°, 4.0 mm; DiATOME)
3. Glass strips (#8030, Ted Pella)
4. Glass knife boats (#123-3, Ted Pella)
5. Nail polish (clear)
6. Perfect loop (#70944, EMS)
7. Hair tool for manipulation of plastic sections
8. Razor blade (Double edge; #72000, EMS)
9. High profile microtome blades (#818, Leica microsystem)

F. PALM Imaging

1. Zeiss PAL-M (ELYRA P.1, Zeiss)
2. Gold nanoparticles (call for 2× concentrated solution; #790122-010, microspheres-nanospheres.com)
3. Canned air
4. Attofluor cell chamber for microscopy (#A7816, Invitrogen)

G. Staining

1. Uranyl acetate (#21447-252, Polysciences)
2. Syringe (10 ml)
3. Syringe filter (0.22 μm; SLGP033RB, Millipore)

H. SEM Imaging

1. FEI Nova Nano
2. Backscattered electron detector (vCD, FEI)
3. Carbon fiber cord (#4539, EMS)
4. SEM pin stub (#16111, Ted Pella)
5. Carbon conductive tape (double coated; #16084-7, Ted Pella)

I. Image alignment

1. Photoshop (CS5, Adobe)

V. Discussion

Super-resolution fluorescence microscopy allows one to precisely pinpoint the location of a single molecule in a cell (Betzig *et al.*, 2006; Hell & Wichmann, 1994; Hess *et al.*, 2006; Rust *et al.*, 2006). However, precise localization in a field of black is not useful. Where is that protein in the context of cellular structure? Where are previously described organelles in relationship to this protein? Here, we demonstrate that fluorescently tagged proteins can be correlated with ultrastructure in electron micrographs to identify the cellular location of a protein. Five issues in particular bear discussion: fixation, plastic, imaging, alignment, and quantification.

A. Fixation

Here we use a combination of potassium permanganate and osmium tetroxide followed by *en bloc* uranyl acetate staining to balance the fluorescence and morphology preservation at synapses. Neuronal tissues are the most sensitive to the fixation condition (Watanabe *et al.*, 2011), and thus the use of lipid cross-linkers, such as osmium tetroxide and potassium tetroxide, is essential. One drawback is that these cross-linkers are also oxidizing agents; consequently, fluorescent proteins may not be functional after fixation. These chemicals are less reactive at lower temperatures, so the aforementioned cryomethods are required for preserving fluorescence during sample preparation. On the other hand, fixation may not be necessary if the tissue of interest has a naturally high contrast in electron microscopy and thereby requires no additional fixation and staining with uranyl acetate. In this case, cryosectioning (Betzig *et al.*, 2006) can be employed. However, such high-contrast tissues or subcellular structures are rare, and thus reaction with electron dense fixatives is required to elucidate the subcellular details in tissues. Recently, the use of uranyl acetate alone in the cryosubstitution medium has shown to enhance the contrast of membranes while preserving almost 100% of the fluorescence level in yeast cells and cell cultures (Kukulski *et al.*, 2011). Therefore, fixation conditions can be altered according to need.

B. Plastic

The choice of resin media is critical for the functionality of fluorescent proteins and the quality of sectioning. Fluorescent proteins require a hydrated environment that is neutral or alkaline in pH. There are two types of resins often used in electron microscopy: epoxy and acrylic. Epoxy-based resins have a superior sectioning quality because they can cross link with tissues; however, they are very hydrophobic, making them incompatible with fluorescent proteins. Moreover, they require a temperature of 60°C for polymerization. Fluorescent proteins are denatured at such a temperature. Acrylic resins, on the other hand, are hydrophilic, fulfilling the requirement for a hydrated environment, and can be polymerized at low temperatures by either UV light or chemicals (Newman & Hobot, 1993). However, most acrylic resins have a low pH—fluorescent proteins are quenched in such a condition. Here we chose GMA because it fulfilled the hydrated and alkaline requirements of fluorescent proteins. However, since GMA does not cross link with tissues, dropouts of tissues are often observed. Ultimately, a plastic with good features of both types of resins should be developed.

C. Super-Resolution Fluorescence Imaging

To understand the functions of proteins, the relationship of one protein to another and to subcellular structures must be revealed. Photoactivated localization microscopy can pinpoint the location of proteins at nanometer resolution, but the applications have been somewhat limited due to the lack of fluorescent proteins compatible for multicolor imaging. Here we show that fEM can provide the structural information in the PALM image. The method described here also introduces the possibility for multiple colors to be imaged by using GSDIM. Potentially, a large number of preexisting transgenic lines, expressing GFP, for example, can be imaged at the single-molecule level using GSDIM instead of requiring the construction of strains using photoactivatable tags such as Eos for PALM imaging. Although Citrine is unique, and other fluorescent proteins such as GFP are not compatible with GSDIM imaging, other super-resolution fluorescence imaging modalities, such as structured illumination microscopy, might be employed to localize fluorescence in sections before electron microscopy. Moreover, depending on the application, diffraction-limited fluorescence spots may provide enough information so that simple correlative fEM is sufficient for one's imaging needs. For example, the subtype of neurons in a neuropil can be identified simply by overlaying the diffraction-limited fluorescence images on the electron micrographs (Micheva & Smith, 2007). Thus, the choice of fluorescent proteins should be made based on the application. One must also remember that fEM without super-resolution imaging still produces subdiffraction fluorescence images because the axial resolution is determined by the thickness of the section, which is typically about 50 nm, rather than the actual point-spread function of the fluorescence, which is over 700 nm (Micheva and Smith, 2007).

D. Electron Microscopy Imaging

For fEM, we have been using a SEM extensively, but TEM can also be used. However, two factors should be considered before using TEM. First, sections must

be ultrathin for TEM imaging. Typically, 50- to 70 nm-thick sections are imaged by TEM. If specimens are very darkly stained with osmium tetroxide, contrast can still be obtained using a typical accelerating voltage of 100 keV. However, because the primary fixative used here is potassium permanganate, the tissue contrast is low with such a high accelerating voltage. A lower voltage can be used to enhance the contrast, but in this case, the sections must be even thinner, but obtaining such thin sections with GMA-embedded specimens can be challenging. Moderately high-resolution images (~5 nm resolution) can be achieved from the surface of the specimens in SEM with a low accelerating voltage (~5 keV), and thus the thickness of sections is not an issue. Second, a grid with lateral dimensions of 2 mm × 1 mm must be used for TEM imaging. Therefore, one must manipulate many ribbons of sections without losing sections or losing the order of the sections, whereas with SEM, long ribbons of sections can be mounted on the coverglass. Therefore, unless resolution better than 5 nm is necessary to capture cellular details, SEM offers advantages over TEM.

E. Alignment

A fluorescence image and an electron micrograph are aligned based on gold fiducial markers, but the alignment may not be precise for two reasons. First, gold particles emit fluorescence constantly. Because each particle is not stochastically activated, the fluorescence signals from a few neighboring gold particles appear as one fluorescent spot due to the diffraction limit of light. On the other hand, electron microscopy depicts the actual dimensions of the particles. The disparity in the resolution results in some ambiguity in the alignment. Second, electron beams can distort the specimen even though the sections are mounted on a solid glass surface. The distortion is usually more severe in acrylic resins such as GMA. Aligning a portion of the image or applying nonlinear transformations could help overcome this distortion problem.

F. Quantification

Counting the number of fluorescent molecules in PALM images is very tempting, but one must consider three factors that affect the number of molecules present in each spot of an image. First, fluorescence is lost during sample preparation. We reported above that most of the fluorescence is preserved when measured in our specimens at the beginning and end of the fixation and embedding procedure, but we may be overestimating fluorescence because of mechanical damage to the fluorophores during sectioning and oxidation after sectioning has not been quantified. Second, the stochastic nature of photoactivatable fluorescent proteins affects quantification. Each molecule must be activated separately in space and time and must be permanently bleached after emitting fluorescence for calculating the precise number of molecules. However, fluorophores can be easily undercounted or overcounted. The fluorophores can emit too little light and fail to be counted. Alternatively, they may return from the triplet dark state instead of becoming bleached and be counted twice. This uncertainty is compounded in GSDIM, in which overcounting is routine and thus this method is not quantitative. Third, tagged proteins are typically not expressed at the endogenous level. Therefore, quantification cannot be precise.

VI. Perspective

Nano-resolution fEM (nano-fEM) using super-resolution fluorescence microscopy can reveal the precise location of proteins within a cell. Unlike immuno-EM, protein localization is limited only by the ability to tag the protein of interest with fluorophores. This method can thus reveal the localization of proteins more quantitatively and at very high resolution. In the future, a few improvements could greatly extend the utility of this method. These improvements include the development of hydrophilic plastics that cross link with tissues, fluorophores that are osmium resistant, photoactivatable fluorescent proteins that can be imaged simultaneously in two color spectra, and a method to combine three-dimensional PALM imaging with electron tomography.

Acknowledgments

We thank Harald Hess and Eric Betzig for access to the PALM microscope for proof-of-principle experiments; Rick Fetter for sharing fixation protocols, reagents, and encouragement; Michael Davidson, Geraldine Seydoux, Stefan Eimer, Rudolf Leube, Keith Nehrke, Christian Frøkjær-Jensen, Aude Ada-Nguema, and Marc Hammarlund for DNA constructs; Gunther Hollopeter for generating transgenic lines used in these experiments; Jackson Richards for a critical reading of the manuscript; and Carl Zeiss Inc. for providing access to the beta version of the Elyra PALM microscope.

References

Betzig, E., Patterson, G. H., Sougrat, R., Lindwasser, O. W., Olenych, S., Bonifacino, J. S., *et al.* (2006). Imaging intracellular fluorescent proteins at nanometer resolution. *Science, 313*, 1642–1645.

Cajal, S.R.Y. (1894). Die Retina der Wirbelthiere: Untersuchungen mit der Golgi-Cajal'schen Chromsilbermethode und der Ehrlich'schen Methylenblaufärbung (Wisbaden, Bergmann).

Cajal, S.R.Y. (1899). Comparative study of the sensory areas of the human cortex. Worcester: Clark University.

Cajal, S.R.Y. (1903). Studien über die Hirnrinde des Menschen (Johann Ambrosius Barth).

Chalfie, M., Tu, Y., Euskirchen, G., Ward, W. W., & Prasher, D. C. (1994). Green fluorescent protein as a marker for gene expression. *Science, 263*, 802–805.

Folling, J., Bossi, M., Bock, H., Medda, R., Wurm, C. A., Hein, B., *et al.* (2008). Fluorescence nanoscopy by ground-state depletion and single-molecule return. *Nature Methods, 5*, 943–945.

Grabenbauer, M., Geerts, W. J. C., Fernadez-Rodriguez, J., Hoenger, A., Koster, A. J., & Nilsson, T. (2005). Correlative microscopy and electron tomography of GFP through photooxidation. *Nature Methods, 2*, 857–862.

Gurskaya, N. G., Verkhusha, V. V., Shcheglov, A. S., Staroverov, D. B., Chepurnykh, T. V., Fradkov, A. F., *et al.* (2006). Engineering of a monomeric green-to-red photoactivatable fluorescent protein induced by blue light. *Nature Biotechnology, 24*, 461–465.

Harke, B., Keller, J., Ullal, C. K., Westphal, V., Schönle, A., & Hell, S. W. (2008). Resolution scaling in STED microscopy. *Optics Express, 16*, 4154–4162.

Heikal, A. A., Hess, S. T., Baird, G. S., Tsien, R. Y., & Webb, W. W. (2000). Molecular spectroscopy and dynamics of intrinsically fluorescent proteins: coral red (dsRed) and yellow (Citrine). *Proceedings of the National Academy of Sciences of the United States of America, 97*, 11996–12001.

Heilemann, M., van de Linde, S., Schüttpelz, M., Kasper, R., Seefeldt, B., Mukherjee, A., *et al.* (2008). Subdiffraction–resolution fluorescence imaging with conventional fluorescent probes. *Angewandte Chemie International Edition*, *47*, 6172–6176.

Hell, S. W., & Wichmann, J. (1994). Breaking the diffraction resolution limit by stimulated emission: stimulated-emission-depletion fluorescence microscopy. *Optics Letters*, *19*, 780–782.

Hell, S. W. (2007). Far-field optical nanoscopy. *Science*, *316*, 1153–1158.

Hess, S. T., Girirajan, T. P. K., & Mason, M. D. (2006). Ultra-high resolution imaging by fluorescence photoactivation localization microscopy. *Biophysical Journal*, *91*, 4258–4272.

Hooke, R. (1665). *Micrographia: Or some physiological descriptions of minute bodies made by magnifying glasses with observations and inquiries thereupon Jo. Matryn and Ja. Allestry*. London: The Royal Society.

Knoll, M., & Ruska, E. (1932). Elektronenmikroskop. *Zeitschrift Physikalische*, *78*, 318–339.

Kukulski, W., Schorb, M., Welsch, S., Picco, A., Kaksonen, M., & Briggs, J. A. G. (2011). Correlated fluorescence and 3D electron microscopy with high sensitivity and spatial precision. *The Journal of Cell Biology*, *192*, 111–119.

Lalkens, B., Testa, I., Willig, K. I., & Hell, S. W. (2012). MRT letter: nanoscopy of protein colocalization in living cells by STED and GSDIM. *Microscopy Research and Technique*, *75*, 1–6.

Link, S., & El-Sayed, M. A. (1999). Spectral properties and relaxation dynamics of surface plasmon electronic oscillations in gold and silver nanodots and nanorods. *The Journal of Physical Chemistry B*, *103*, 8410–8426.

McCutchen, C. W. (1967). Superresolution in microscopy and the Abbe resolution limit. *Journal of the Optical Society of America*, *57*, 1190–1192.

McDonald, K. L., Morphew, M., Verkade, P., & Müller-Reichert, T. (2007). Recent advances in high-pressure freezing: equipment- and specimen-loading methods. *Methods in Molecular Biology*, *369*, 143–173.

McDonald, K., Schwarz, H., Müller-Reichert, T., Webb, R., Buser, C., & Morphew, M. (2010). "Tips and tricks" for high-pressure freezing of model systems. *Methods in Cell Biology*, *96*, 671–693.

McDonald, K. (2007). Cryopreparation methods for electron microscopy of selected model systems. *Methods in Cell Biology*, *79*, 23–56.

Micheva, K., & Smith, S. (2007). Array tomography: a new tool for imaging the molecular architecture and ultrastructure of neural circuits. *Neuron*, *55*, 25–36.

Morphew, M. K. (2007). 3D immunolocalization with plastic sections. *Methods in Cell Biology*, *79*, 493–513.

Müller-Reichert, T., Srayko, M., Hyman, A., O'Toole, E. T., & McDonald, K. (2007). *Correlative light and electron microscopy of early Caenorhabditis elegans embryos in mitosis. In cellular electron microscopy*. Oxford, Elsvier. pp. 101–119).

Müller-Reichert, T. (2010). (1st ed.). *Electron microscopy of model systems*. (Vol. 96). New York: Academic Press.

Murphy, D. B. (2001). *Fundamentals of light microscopy and electronic imaging*. Hoboken, NJ: John Wiley and Sons.

Newman, G. R., & Hobot, J. A. (1993). *Resin microscopy and on-section immuno-cytochemistry*. Berlin, Germany: Springer-Verlag.

Nixon, S. J., Webb, R. I., Floetenmeyer, M., Schieber, N., Lo, H. P., & Parton, R. G. (2009). A single method for cryofixation and correlative light, electron microscopy and tomography of zebrafish embryos. *Traffic*, *10*, 131–136.

Oberti, D., Kirschmann, M. A., & Hahnloser, R. H.R. (2010). Correlative microscopy of densely labeled projection neurons using neural tracers. *Frontiers in Neuroanatomy*, *4*, 24.

Patterson, G. H., & Lippincott-Schwartz, J. (2002). A photoactivatable GFP for selective photolabeling of proteins and cells. *Science*, *297*, 1873–1877.

Payne, J. W. (1973). Polymerization of proteins with glutaraldehyde. Soluble molecular-weight markers. *Journal of Biochemistry*, *135*, 867–873.

Polishchuk, R. S., Polishchuk, E. V., Marra, P., Alberti, S., Buccione, R., Luini, A., *et al.* (2000). Correlative light-electron microscopy reveals the tubular-saccular ultrastructure of carriers operating between Golgi apparatus and plasma membrane. *The Journal of Cell Biology*, *148*, 45–58.

Rostaing, P., Weimer, R. M., Jorgensen, E. M., Triller, A., & Bessereau, J.-L. (2004). Preservation of immunoreactivity and fine structure of adult *C. elegans* tissues using high-pressure freezing. *The Journal of Histochemistry and Cytochemistry, 52*, 1–12.

Roth, J., Bendayan, M., Carlemalm, E., Villiger, W., & Garavito, M. (1981). Enhancement of structural preservation and immunocytochemical staining in low temperature embedded pancreatic tissue. *The Journal of Histochemistry and Cytochemistry, 29*, 663–671.

Rust, M. J., Bates, M., & Zhuang, X. (2006). Sub-diffraction-limit imaging by stochastic optical reconstruction microscopy (STORM). *Nature Methods, 3*, 793–795.

Schikorski, T. (2010). Horseradish peroxidase as a reporter gene and as a cell-organelle-specific marker in correlative light-electron microscopy. In S. D. Schwartzbach, & T. Osafune (Eds.), *Immunoelectron microscopy* (pp. 315–327). Totowa, NJ:: Humana Press.

Schwarz, H., & Humbel, B. M. (2007). Correlative light and electron microscopy using immunolabeled resin sections. *Methods in Molecular Biology, 369*, 229–256.

Shimomura, O. (2009). Discovery of green fluorescent protein (GFP) (Nobel Lecture). *Angewandte Chemie International Edition in English, 48*, 5590–5602.

Shtengel, G., Galbraith, J. A., Galbraith, C. G., Lippincott-Schwartz, J., Gillette, J. M., Manley, S., *et al.* (2009). Interferometric fluorescent super-resolution microscopy resolves 3D cellular ultrastructure. *Proceedings of the National Academy of Sciences, 106*, 3125–3130.

Shu, X., Lev-Ram, V., Deerinck, T. J., Qi, Y., Ramko, E. B., Davidson, M. W., *et al.* (2011). A genetically encoded tag for correlated light and electron microscopy of intact cells, tissues, and organisms. *PLoS Biology, 9*, e1001041.

Sims, P. A., & Hardin, J. D. (2007). Fluorescence-integrated transmission electron microscopy images: integrating fluorescence microscopy with transmission electron microscopy. *Methods in Molecular Biology, 369*, 291–308.

Sosinsky, G. E., Giepmans, B. N.G., Deerinck, T. J., Gaietta, G. M., & Ellisman, M. H. (2007). Markers for correlated light and electron microscopy. *Methods in Cell Biology, 79*, 575–591.

Tsien, R. (1998). The green fluorescent protein. *Annual Review of Biochemistry, 67*, 509–544.

Verkade, P. (2008). Moving EM: the rapid transfer system as a new tool for correlative light and electron microscopy and high throughput for high–pressure freezing. *Journal of Microscopy, 230*, 317–328.

Watanabe, S., Punge, A., Hollopeter, G., Willig, K. I., Hobson, R. J., Davis, M. W., *et al.* (2011). Protein localization in electron micrographs using fluorescence nanoscopy. *Nature Methods, 8*, 80–84.

Weibull, C., & Christiansson, A. (1986). Extraction of proteins and membrane lipids during low temperature embedding of biological material for electron microscopy. *Journal of Microscopy, 142*, 79–86.

Wiedenmann, J., Ivanchenko, S., Oswald, F., Schmitt, F., Röcker, C., Salih, A., *et al.* (2004). EosFP, a fluorescent marker protein with UV-inducible green-to-red fluorescence conversion. *Proceedings of the National Academy of Sciences of the United States of America, 101*, 15905–15910.

Zhang, J., Campbell, R. E., Ting, A. Y., & Tsien, R. Y. (2002). Creating new fluorescent probes for cell biology. *Nature Reviews. Molecular Cell Biology, 3*, 906–918.

CHAPTER 5

NANO-FEM: PROTEIN LOCALIZATION USING PHOTO-ACTIVATED LOCALIZATION MICROSCOPY AND ELECTRON MICROSCOPY

Reprinted with permission from the Journal of Visualized Experiments

Watanabe, et al., 2012. Journal of Visualized Experiments. (*In press*)

jove Journal of Visualized Experiments www.jove.com

Video Article

Nano-fEM: Protein Localization Using Photo-activated Localization Microscopy and Electron Microscopy

Shigeki Watanabe, Jackson Richards, Gunther Hollopeter, Robert J. Hobson, Wayne M. Davis, Erik M. Jorgensen
Department of Biology, Howard Hughes Medical Institute, University of Utah

Correspondence to: Erik M. Jorgensen at jorgensen@biology.utah.edu

URL: http://www.jove.com/video/3995
DOI: doi:10.3791/3995

Keywords: Molecular Biology, Issue 70, Cellular Biology, Genetics, Proteomics, Proteins, Protein localization, super-resolution fluorescence microscopy, fluorescence, electron microscopy, nano-fEM, EM, SEM, electron micrograph, imaging

Date Published: 12/3/2012

Citation: Watanabe, S., Richards, J., Hollopeter, G., Hobson, R.J., Davis, W.M., Jorgensen, E.M. Nano-fEM: Protein Localization Using Photo-activated Localization Microscopy and Electron Microscopy. *J. Vis. Exp.* (70), e3995, doi:10.3791/3995 (2012).

Abstract

Mapping the distribution of proteins is essential for understanding the function of proteins in a cell. Fluorescence microscopy is extensively used for protein localization, but subcellular context is often absent in fluorescence images. Immuno-electron microscopy, on the other hand, can localize proteins, but the technique is limited by a lack of compatible antibodies, poor preservation of morphology and because most antigens are not exposed to the specimen surface. Correlative approaches can acquire the fluorescence image from a whole cell first, either from immuno-fluorescence or genetically tagged proteins. The sample is then fixed and embedded for electron microscopy, and the images are correlated [1-3]. However, the low-resolution fluorescence image and the lack of fiducial markers preclude the precise localization of proteins.

Alternatively, fluorescence imaging can be done after preserving the specimen in plastic. In this approach, the block is sectioned, and fluorescence images and electron micrographs of the same section are correlated [4-7]. However, the diffraction limit of light in the correlated image obscures the locations of individual molecules, and the fluorescence often extends beyond the boundary of the cell.

Nano-resolution fluorescence electron microscopy (nano-fEM) is designed to localize proteins at nano-scale by imaging the same sections using photo-activated localization microscopy (PALM) and electron microscopy. PALM overcomes the diffraction limit by imaging individual fluorescent proteins and subsequently mapping the centroid of each fluorescent spot [8-10].

We outline the nano-fEM technique in five steps. First, the sample is fixed and embedded using conditions that preserve the fluorescence of tagged proteins. Second, the resin blocks are sectioned into ultrathin segments (70-80 nm) that are mounted on a cover glass. Third, fluorescence is imaged in these sections using the Zeiss PALM microscope. Fourth, electron dense structures are imaged in these same sections using a scanning electron microscope. Fifth, the fluorescence and electron micrographs are aligned using gold particles as fiducial markers. In summary, the subcellular localization of fluorescently tagged proteins can be determined at nanometer resolution in approximately one week.

Video Link

The video component of this article can be found at http://www.jove.com/video/3995/

Protocol

1. High-pressure Freezing

1. Prepare the cryo-protectant by adding 0.2 g of BSA into 1 ml of an appropriate medium for your specimen (for example, culture medium for cell cultures, M9 for *C. elegans*). Incubate the tube in a 37 °C water bath until all BSA is dissolved.
2. Prior to freezing, fill the automated freeze-substitution device (Leica AFS) with liquid nitrogen
3. Set the AFS program: -90 °C for 5-30 hr*, 5 °C/hr to -60 °C, -60 °C for 2 hr (or select "pause" option if you are using Leica AFS 2), 5 °C/hr to -30 °C and -30 °C for 72 hr. If the AFS machine is capable of having more than five steps, the -30 °C step should be replaced with a "pause" option set to 0 hr, and two further steps should be added: 10 °C/hr to -20 °C and 24 hr at -20 °C. If the machine is limited to five steps, set up another program in a different memory slot as follows: 10 °C/hr to -20 °C and 24 hr at -20 °C.

   *The time here can be adjusted so that the -60 °C step starts in the early morning.
4. Prepare 1% osmium tetroxide stock solution by mixing 0.1 g osmium tetroxide crystals (EMS, RT19134) with 10 ml of anhydrous acetone (EMS, # RT10016). Prepare the fixatives in a 50 ml conical tube as follows. First, add 1 ml of milliQ water, and then dissolve in it 0.02 g of potassium permanganate (EMS, RT20200). Add 19 ml of acetone and mix it well. Finally, add 20 µl of 1% osmium stock solution into the tube. Acetone is a free-radical scavenger[11] and thus prevents polymerization of plastic, but the use of acetone as a freeze-substitution

medium is necessary for preserving morphology because of its interaction with lipids. Acetone will be substituted with ethanol prior to plastic infiltration. Aliquot 1 ml to each cryovial and keep the fixatives frozen by storing the tubes in liquid nitrogen.
5. Fill a specimen carrier with 20% BSA or bacteria. Both 20% BSA and bacteria serve as cryo-protectants. The choice for the type of the specimen carrier depends on the specimen. For *C. elegans*, use a 100 µm well.
6. Place the specimen in the carrier and freeze it using a high-pressure freezer.
7. After freezing and under liquid nitrogen, transfer the specimen into the cryotube containing fixatives. Make sure the specimen stays under the liquid at all times.
8. Repeat 1.5) - 1.7) until all the specimens are frozen.
9. Transfer all the cryotubes into the AFS unit, and resume the program.

2. Freeze-substitution

1. When the temperature reaches -60 °C, place vials containing 20 ml of 95% acetone into the AFS.
2. When the temperature reaches -50 °C, replace the fixatives with 95% acetone six times over the period of 2 hr.
3. Place a vial containing 20 ml of 0.1% uranyl acetate (Polysciences, #21447-25) in 95% acetone into the chamber and pre-cool it to -50 °C.
4. At the end of the washing step, add ~1 ml of uranyl acetate solution to each vial. Unpause the program if necessary.
5. When the temperature reaches -30 °C, replace the uranyl acetate with 95% ethanol six times over the period of 2 hr.
6. In the meantime, make up 97% glycol methacrylate resin (GMA, SPI Supplies/Structure Probe, Inc., #02630-AA) by mixing 22.3 ml GMA, 10ml n-Butyl Methacrylate, 1 ml milliQ water, and 0.2 g benzoyl peroxide (catalyst). Store it in glass vials (EMS, #72632) and prepare 30% GMA by mixing it with 95% ethanol. **Do not store GMA media in plastic tubes** because the quality of polymerization degrades with the long-term storage in polyethylene-based plastics. Pre-cool the GMA solution to -30 °C.

   Traditional epoxy resins such as Araldite and Epon cannot be used in the protocol since they are anhydrous and acidic which quenches fluorescent proteins. Acrylic resins, such as LR White, can tolerate a small amount of water and can preserve the fluorescent protein, but its acidic pH tends to quench the fluorophore [12]. GMA tolerates, in fact requires, a small amount of water and is alkaline (pH8)[12]. GMA is unfortunately somewhat brittle. Moreover, GMA does not cross-link with tissues like traditional epoxy resins do. These characteristics of GMA cause inconsistency in sectioning quality especially when sectioned thinner than 80 nm.

   Although the shelf life of GMA is about a year, GMA should be used within 3 months of the purchase to ensure its quality.

3. Infiltration and Polymerization

Steps 3.1-3.3 are carried out in the same cryovials used for freeze-substitution. Infiltration and polymerization are carried out at -30 °C in the AFS to preserve the fluorescent protein.

1. Prepare infiltration media by mixing the GMA stock solution with 95% ethanol. Incubate specimens in 30% GMA for 3-5 hr.
2. Incubate specimens in 70% GMA for 4-6 hr.
3. Incubate specimens in 97% GMA overnight.
4. On the next day, make up fresh 97% GMA.
5. Transfer the samples to an embedding mold (EBSciences, #TC). Prepare a disk of ACLAR film (EMS, #50425-10) by using a 3/8" DISC Punch (Ted Pella Inc.) and place the disk in the bottom of the BEEM capsule.
6. Exchange the 97% GMA three times over 6 hr at -30 °C.
7. After the third exchange, add the initiator N,N-dimethyl-p-toluidine (Sigma-Aldrich, #D9912) to GMA at a concentration of 1.5 µl/1 ml GMA and apply this solution to each specimen mold. Immediately position the specimen in the embedding mold in the AFS.

   Note that benzoyl peroxide is the catalyst and is present during all infiltration steps so stirring is not necessary. Benzoyl peroxide does not polymerize the plastic until it is exposed to the chemical initiator N,N,-dimethyl-p-toluidine. The initiator activates polymerization immediately and will polymerize the resin even in tissues within 1 hr. Nevertheless, tissue dropouts may result in deep tissues due to the incomplete polymerization. Moreover, GMA does not crosslink the specimen to the block well, so separate the specimen from the cryoprotectant by tapping on the matrix of bacteria.

   If polymerization is performed outside of an AFS, the embedding mold must be covered with an aclar disk to block exposure to oxygen. GMA does not polymerize completely when exposed to oxygen.
8. Allow the plastic to cure overnight even though it polymerizes within 1 hr.
9. Store the specimen in a nitrogen gas-filled vacuum bag (Ziploc) in the freezer (-20 °C) until further processing so that fluorescent proteins are not exposed to oxygen.

4. Sectioning

1. Sectioning of GMA-embedded specimens can be carried out in a manner similar to that for epon-embedded specimens. Extra caution should be taken not to wet the sectioning surface because GMA is very hydrophilic and the ribbons will be driven into the water bath if they are wetted on both sides.
2. Collect ribbons of sections (50-80 nm) on a glass coverslip if a TIRF microscope is being used for localization. Otherwise, use a grid made for transmission electron microscopy. The cutting speed should be set at1.6 mm/s or higher. Otherwise, a ribbon may not form.
3. Store sections at -20 °C if not imaged immediately. Protect the fluorophores from UV light by covering section holders with aluminum foil.

5. PALM Imaging

1. Set up the PALM microscope according to manufacturer recommendations. The temperature of an EMCCD camera should be set to -70 °C or below.
2. Apply gold particles (#790122-010 - 2x concentrated, microspheres-nanospheres.com) in solution (approximately 50 µl) to the sample to be imaged. Allow the solution to sit for 30 seconds on the coverslip while under a black cover case.
3. Remove the gold solution by blowing it to the edge of the coverslip and absorbing it with a kimwipe.
4. Insert the coverslip into a circular coverslip holder. If needed, apply vacuum grease to the rim to keep the coverslip in place.
5. Apply immersion oil to the underside of the coverslip, directly below the samples.
6. Insert the sample holder into the slot on the stage of the microscope. Take special care not to touch the objectives.
7. Adjust the holder so it is tight and centers the sections above the objective.
8. Locate the sections using a 10x objective lens.
9. Change to the 100x objective lens.
10. Focus on the specimen.
11. Locate a region of interest by observing the strength of the fluorescence signals. Use the 488 nm laser and increase the intensity in the Channels menu to 10%. Focus on the areas of brightest fluorescence. Note that this step is not necessary if the region of interest can be identified in the bright field by eye.
12. Switch the laser to 561 nm and increase the intensity to 100% to bleach out the background autofluorescence. Bleach the sample for ~2 min.
13. If the focus changes during bleaching, allow 5 min to elapse before adjusting the focus and capturing images. This pause allows the temperature to stabilize. If the PALM scope is equipped with an incubation chamber, set the temperature to 20 °C and wait for ~2 hr to stabilize the temperatures in the chamber.
14. When bleaching is complete, activate the 405 nm laser and set it to the lowest intensity.
15. Start collecting the images at 20 frames per second. We typically collect 5,000-6,000 frames per experiment, but the number of frames should be adjusted depending on the goal of the experiment. For example, if all proteins in a region of interest must be imaged, the frame number should be increased.
16. If the signals are sparse or faint, slowly increase the 405 nm laser intensity.
17. During the acquisition process, be sure to keep the samples in focus by carefully adjusting the knob as necessary.
18. When images are collected, the PALM analysis should be performed. For tdEos, we filter out any signals that fluoresce longer than 500 msec because those signals are likely due to autofluorescence.

6. SEM Imaging

1. Prior to SEM imaging, stain the sections using 2.5% uranyl acetate (in water) for 4 min. Wash off the uranyl acetate thoroughly with filtered milliQ water.
2. After the sections are dried, carbon-coat the coverslip using a carbon sputter until the coverslip becomes fairly dark. Apply one end of carbon conductive tape at the edge of the coverslip and the other end on the metal stub so that electrons that accumulate on the surface of the coverslip are grounded.
3. Mount the specimen into the SEM chamber (FEI Nova Nano).
4. Insert the vCD detector.
5. Close the chamber and pump it using the high vacuum setting.
6. Once evacuated, open the column valve so that electron beam is applied to a specimen.
7. Perform a routine alignment of electron beam.
8. Locate the specimen.
9. Once the focus is adjusted, link the specimen stage and bring up the stage to 5 mm below the pole piece.
10. Take a low magnification image of the specimen (~5,000x).
11. Zoom into the region of the interest and obtain high magnification (50,000x) images.
12. Move to the next section, and repeat step 6.10) and 6.11) until all the sections are imaged.

7. Aligning PALM and EM Images

1. Open Photoshop and the acquired SEM images.
2. Create a new window with dimensions of 5,000 x 5,000 pixels and 300 pixels/inch resolution.
3. Copy the low magnification SEM image into the new window (**Figure 1A**).
4. Scale the image so that it fills up the entire window by using the transform manipulation (Command + T for a Mac).
5. Copy the higher magnification SEM images and scale them as necessary.
6. Flip the sum TIRF image horizontally by selecting image rotation from the image drop-down menu bar.
7. Copy and paste the sum TIRF image (from PALM) into a new layer.
8. Scale the image using the transform manipulation and then rotate as necessary to match the fluorescence of the gold particles (white arrows in **Figure 1A**) with the corresponding structures visualized in SEM (**Figure 1B**).
9. Copy the PALM image into a new layer and apply the same transformation (**Figure 1C**). A higher magnification image can be extracted from this image (**Figure 2**).
10. For presentation, copy the transformed PALM image into a new layer. Select the PALM signals but not background by using "color range" in the "select" drop-down menu. Make sure to select a background pixel as a reference pixel and turn on the "invert" option.
11. Cut the desired PALM signals and paste them to a new layer.
12. Apply transparency to the background layer, and set it to 10%. This allows for visualization of the PALM signals by making the background transparent without compromising their intensity (**Figure 2D**).

8. Representative Results

Histone tagged with tdEos can be stably expressed in the nematode *C. elegans*, and the transgenic animals were processed using the protocol described above. The PALM and electron micrographs were acquired from the same section (**Figure 1**). To align the images, the sum TIRF image, which sums the fluorescence over the entire time course, is overlaid on the electron micrograph. The gold nanoparticles appear in both the fluorescence and electron micrographs and can be used to align the two images using the 'transform' function in Photoshop (**Figure 1A and B**). Then, the same 'transform' value was applied to the PALM image (**Figure 1C**). At this magnification, structural detail cannot be distinguished, so we zoomed into a region near the top end of the micrograph (**Figure 2**). In the high magnification image, subcellular details such as a nucleus, a nucleolus, nuclear pores, and endoplasmic reticulum could be observed. Moreover, the tagged Histone molecules are exclusively localized to the nucleus but not to the nucleolus, as expected. The correlative PALM and electron microscopy thus allows for protein localization at the highest resolution.

Five problems can compromise the quality of the images. First, ice crystal damage can distort ultrastructure (**Figure 3A and B**). Placing specimens in a cryo-protectant such as bacteria, which reduces the propagation of ice crystals, can reduce this damage. Nevertheless, one must still screen specimens by electron microscopy and discard those with freezing artifacts. Second, GMA does not cross-link to tissues like epoxy resins, and thus specimens often break loose from the surrounding plastic and stretch, shrink or even fall out of the section (**Figure 3C and D**). Dissection of the sample away from the bacteria or other cryo-protectant before embedding provides for greater adhesion of the plastic to the specimen (**Figure 3C**). Similarly, structures such as lipid droplets in the gut often dissociate from the tissues due to the absence of cross-linking (**Figure 3E**). Third, the incomplete polymerization of plastic causes stretching or folding of tissues (**Figure 3F**); the presence of oxygen in the sample also impedes the polymerization of GMA. Fourth, the poor sectioning quality of GMA often results in an inconsistent morphology (**Figure 3G and H**). GMA sections should be cut at 70 nm or thicker and at a speed of around 1.6 mm/s to minimize sectioning artifacts. Fifth, background autofluorescence from dust on the coverslip or section is inevitable. Autofluorescence from dust can be minimized by using pre-cleaned coverslips and by avoiding dust contamination from kimwipes and filter paper as described in the protocol. The PALM analysis program can edit out signals from the specimen or plastic that fluoresce longer than typical signals from fluorescent proteins (**Figure 2 A and B**). The final image will therefore be free of such artifacts.

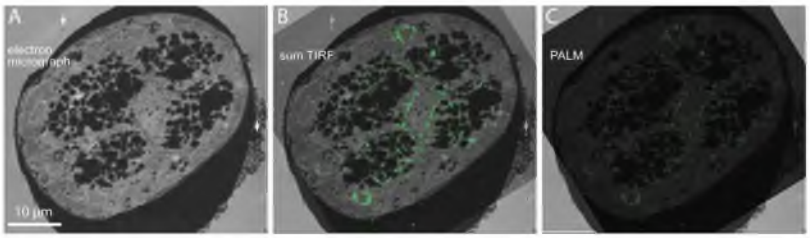

Figure 1. Aligning fluorescence and electron micrographs using gold nanoparticles. (A) A low magnification electron micrograph from a cross section of *C. elegans* expressing the tagged histone tdEos::HIS-11. White arrows indicate 100 nm electron-dense gold nanoparticles applied prior to PALM imaging that serve as fiducial marks. (B) The gold beads fluoresce upon exposure to ~580 nm light and create fiducial marks in the fluorescence image. The sum TIRF image is aligned onto an electron micrograph based on the location of the fiducial marks. The sum TIRF image represents all the photons detected by the camera during the experimental time course. Note that the bright spots on the upper left (white arrow) arise from the clusters of gold particles. (C) A PALM image is then added to the electron micrograph and rotated and translated based on the values determined from the alignment of the sum TIRF image in (**B**). Click here to view larger figure.

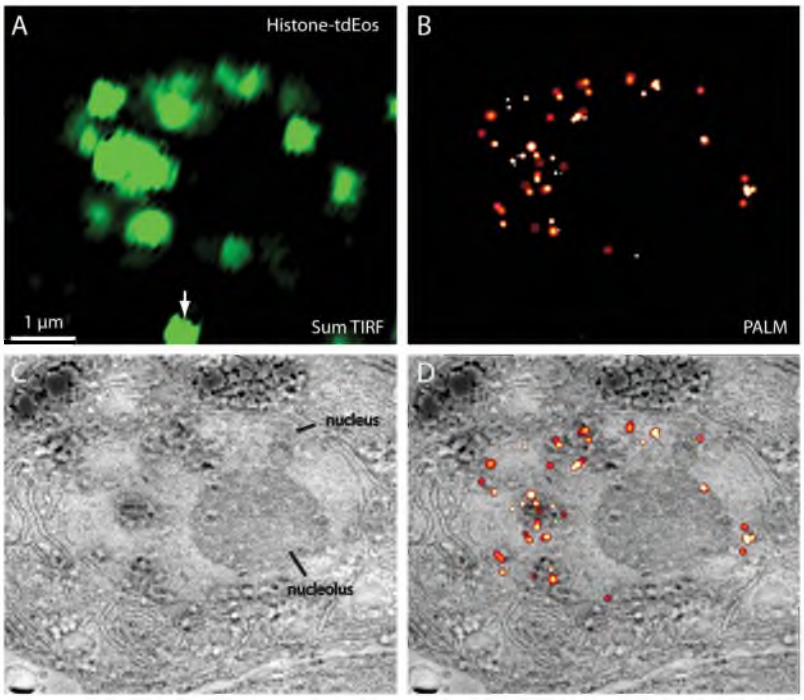

Figure 2. Correlative nano-fEM using Histone fusion proteins. (A) Sum TIRF image of tdEos::HIS-11 acquired from a thin section (70nm). (B) Corresponding PALM image of tdEos::HIS-11. Autofluorescence (white arrow) lasting longer than 500 msec was filtered out by the PALM program. (C) Electron micrograph of a nucleus acquired from the same section. (D) Correlative PALM image and electron micrograph of tdEos::HIS-11. Fluorescence is tightly localized to the chromatin in the nucleus.

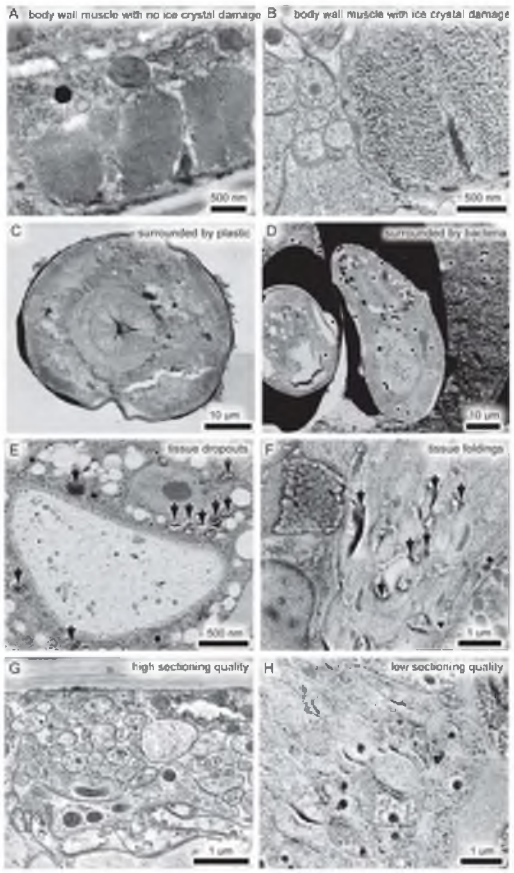

Figure 3. Problems associated with nano fEM. (A) Electron micrograph of a *C. elegans* body muscle without ice crystal damage. (B) Electron micrograph of a body muscle with ice crystal damage. Instead of discrete cross-sections, actin and myosin filaments are collapsed into aggregates due to the formation of ice crystals. (C, D) Low magnification electron micrographs, showing the dissociation of worms from the surrounding media. The section is more distorted in a specimen that is surrounded by the cryo-protecting bacteria (D) than when the specimen is surrounded by plastic (C). The bacterial cryo-protectant in the gallette should be dissected away from the fixed sample before plastic embedding. Note that the animal on the right in (D) was sectioned obliquely, and thus the shape is not due to the distortion of tissues. (E) Electron micrograph of intestine, showing dropouts of tissues (black arrows). (F) Electron micrograph of nerve ring, showing folding of sections due to the incomplete polymerization of plastic (black arrows). (G, H) Electron micrographs of neurons from the same specimen, sectioned on different dates. The preservation of tissues is superb on one day (G), but such morphology is obscured by the inconsistent sectioning quality (H). Click here to view larger figure.

Discussion

Here we describe how to preserve fluorescent proteins in plastic, localize the fluorescent proteins in sections, and image the ultrastructure using electron microscopy. Proteins were localized below the diffraction limit using PALM microscopy to nanometer resolution. To adapt this protocol to particular specimens, the following parameters should be considered: fluorophore, quantification, and alignment.

The choice of fluorescent protein or organic fluorophore depends on the application and the model system. We have tested a variety of fluorescent proteins, including EGFP, YFP, Citrine, mEosFP, mEos2, tdEos, mOrange, PA-mCherry, and Dendra[12]. The preservation of fluorescence from each fluorophore was similar, suggesting that all fluorescent proteins can be preserved using the described method. We chose tdEos because it expressed well in *C. elegans*, proteins remained functional when fused to tdEos, and because its photo-activation characteristics were optimal for PALM microscopy. However, aggregation or failed expression of tdEos has been occasionally observed[12].

Depending on the application, a different fluorophore may be better suited. In many cases, it is not necessary to use a photo-activated fluorescent protein. Simple correlative fluorescence electron microscopy does not require photo-activated fluorescent protein. GFP or organic dyes can be used to image fluorescence from tagged proteins in sections above the diffraction limit. For example, one can image an axon in a

neuropil using fluorescence microscopy and correlate the fluorescence signal with a particular axon in an electron micrograph by imaging the fluorescence on a fluorescence microscope. Other super-resolution techniques, such as stimulated emission depletion microscopy (STED)[12], ground state depletion microscopy followed by individual molecule return (GSDIM)[13], and structured illumination microscopy (SIM)[14], do not require photo-activated fluorescent proteins. Moreover, super-resolution imaging techniques that use organic dyes[9,15,16] or the intrinsic property of fluorescent probes[17] are readily applicable.

In PALM, the number of molecules can be quantified because fluorescence of each molecule is separated spatially and temporally. However, quantification may be misleading for four reasons: oxidation, undercounting, overcounting, and overexpression. First, a fraction of the fluorescent proteins can be denatured or oxidized during sample processing[5,12]. Although ~90% of the fluorescence signal was preserved through fixation and embedding in our protocol, oxidation of the fluorescent protein may occur after the specimen has been sectioned and the surface exposed to oxygen. Second, the activation of photo-activatable proteins is stochastic, and thus multiple molecules can be activated in a given diffraction limited spot[8]. Fluorescence from the multiple molecules will appear as one spot, and thus the total number of proteins will be undercounted. Third, a similar problem can lead to overcounting. In PALM, each fluorescent protein is localized and then "erased" by bleaching. However, fluorescent proteins can return from the dark state without being permanently bleached[18]. Such molecules will then be counted multiple times. Fourth, tagged proteins are expressed as transgenes and are often present in multiple copies, which can lead to overexpression. Therefore, quantification from PALM can be used to estimate but not precisely determine the number of molecules in a given location.

The alignment of a PALM image with an electron micrograph can also be challenging because of the resolution difference in light and electron microscopy and distortion caused by the electron beam. Gold particles serve as tightly localized fiducial markers in electron micrographs. However, fluoresecence from gold particles is not photo-activated, and appears as a large diffraction-limited spot. Thus, the placement of a fluorescence image over an electron micrograph is an estimate. Distortions can also arise from interactions of electrons with the plastic section. Acrylic resins such as GMA are less stable under the electron beam, and the dimensions of the plastic can be altered. Under these circumstances, aligning the fluorescence with ultrastructure may require non-linear transformation of the fiducial markers.

Disclosures

Production and Free Access to this article is sponsored by Carl Zeiss, Inc.

Acknowledgements

We thank Harald Hess and Eric Betzig for access to the PALM microscope for proof-of-principle experiments, Richard Fetter for sharing fixation protocols, reagents and encouragement. We thank Michael Davidson, Geraldine Seydoux, Stefan Eimer, Rudolf Leube, Keith Nehrke, Christian Frøkjr-Jensen, Aude Ada-Nguema and Marc Hammarlund for DNA constructs. We also thank Carl Zeiss Inc. for providing access to the Zeiss PAL-M, a beta version of the Zeiss Elyra P.1 PALM microscope.

References

1. Polishchuk, R.S., *et al.* Correlative light-electron microscopy reveals the tubular-saccular ultrastructure of carriers operating between Golgi apparatus and plasma membrane. *J. Cell Biol.* **148**, 45-58 (2000).
2. Oberti, D., Kirschmann, M.A., & Hahnloser, R.H.R. Correlative microscopy of densely labeled projection neurons using neural tracers. *Front. Neuroanat.* **4**, 24 (2010).
3. Bishop, D., *et al.* Near-infrared branding efficiently correlates light and electron microscopy. *Nat. Meth.* **8**, 568-570 (2011).
4. Sims, P.A. & Hardin, J.D. Fluorescence-integrated transmission electron microscopy images: integrating fluorescence microscopy with transmission electron microscopy. *Methods Mol. Biol.* **369**, 291-308 (2007).
5. Micheva, K. & Smith, S. Array tomography: a new tool for imaging the molecular architecture and ultrastructure of neural circuits. *Neuron.* **55**, 25-36 (2007).
6. Nixon, S.J., *et al.* A single method for cryofixation and correlative light, electron microscopy and tomography of zebrafish embryos. *Traffic.* **10**, 131-136 (2009).
7. Kukulski, W., *et al.* Correlated fluorescence and 3D electron microscopy with high sensitivity and spatial precision. *J. Cell Biol.* **192**, 111-119 (2011).
8. Betzig, E., *et al.* Imaging Intracellular Fluorescent Proteins at Nanometer Resolution. *Science.* **313**, 1642-1645 (2006).
9. Rust, M.J., Bates, M., & Zhuang, X. Sub-diffraction-limit imaging by stochastic optical reconstruction microscopy (STORM). *Nat. Methods.* **3**, 793-795 (2006).
10. Hess, S.T., Girirajan, T.P.K., & Mason, M.D. Ultra-high resolution imaging by fluorescence photoactivation localization microscopy. *Biophys. J.* **91**, 4258-4272 (2006).
11. Weibull, C. & Christiansson, A. Extraction of proteins and membrane lipids during low temperature embedding of biological material for electron microscopy. *J. Microsc.* **142**, 79-86 (1986).
12. Watanabe, S., *et al.* Protein localization in electron micrographs using fluorescence nanoscopy. *Nat. Methods.* **8**, 80-84 (2011).
13. F lling, J., *et al.* Fluorescence nanoscopy by ground-state depletion and single-molecule return. *Nat. Methods.* **5**, 943-945 (2008).
14. Gustafsson, M.G. Surpassing the lateral resolution limit by a factor of two using structured illumination microscopy. *J. Microsc.* **198**, 82-87 (2000).
15. Wombacher, R., *et al.* Live-cell super-resolution imaging with trimethoprim conjugates. *Nature Methods.* **7**, 717-719 (2010).
16. Dertinger, T., Colyer, R., Iyer, G., Weiss, S., & Enderlein, J. Fast, background-free, 3D super-resolution optical fluctuation imaging (SOFI). *PNAS.* **106**, 22287-22292 (2009).

17. Burnette, D. T., Sengupta, P., Dai, Y., Lippincott-Schwartz, J., & Kachar, B. Bleaching/blinking assisted localization microscopy for superresolution imaging using standard fluorescent molecules. *PNAS*. doi:10.1073/pnas.1117430109 (2011).
18. Annibale, P., Vanni, S., Scarselli, M., Rothlisberger, U., & Radenovic, A. Identification of clustering artifacts in photoactivated localization microscopy. *Nat. Meth.* **8**, 527-528 (2011).

CHAPTER 6

NANOMETER-RESOLUTION FLUORESCENCE ELECTRON MICROSCOPY (NANO-FEM) IN CULTURED CELLS

Summary

Nano-resolution fluorescence electron microscopy (nano-fEM) pinpoints the location of individual proteins in electron micrographs. Plastic sections are first imaged using a super-resolution fluorescence microscope and then imaged on an electron microscope. The two images are superimposed to correlate the position of labeled proteins relative to subcellular structures. Here, we describe the method in detail and present five technical advancements: the use of uranyl acetate during the freeze-substitution to enhance the contrast of tissues and reduce the loss of fluorescence, the use of ground-state depletion instead of photoactivation for temporal control of fluorescence, the use of organic fluorophores instead of fluorescent proteins to obtain brighter fluorescence signals, the use of tissue culture cells to broaden the utility of the method, and the use of a transmission electron microscope to achieve sharper images of ultrastructure.

Introduction

Proteins play essential roles in cellular functions; to fully understand their roles we must know where they are localized relative to subcellular structures. Previously, there have been two methods for localizing proteins to subcellular structures: immuno-electron microscopy and fluorescence microscopy. Immuno-electron microscopy localizes proteins at an ultrastructural level using gold-labeled antibodies (FELDHERR and MARSHALL, 1962; Duc-Nguyen and Rosenblum, 1967; Faulk and Taylor, 1971; Rostaing et al., 2004; Morphew, 2007). However, it has many drawbacks, including a reliance on antibodies that can work on plastic sections, poor survival of epitopes, poor preservation of morphology, high non-specific background, and a spatial displacement of up to 38 nm (the molecular length of two antibodies) (Roth et al., 1981; Rostaing et al., 2004; Morphew, 2007). Moreover, only a minority of the proteins are labeled due to the inaccessibility of antigens in the plastic.

Fluorescence microscopy, on the other hand, has become the method of choice for protein localization. In particular, genetic tagging of proteins with green fluorescent protein (GFP) (Chalfie et al., 1994; Tsien, 1998; Shimomura, 2009) is very useful because every protein is labeled and can be imaged in living cells. However, two drawbacks limit its ability to locate proteins in a cell: resolution and cellular context. The light from a fluorescent protein can be only focused to a 450 nm spot on a camera. If there were only two proteins in an image, they could theoretically be distinguished if they were separated by greater than 250 nm, but typically many proteins are labeled and the image is really no

more than an incoherent micron-sized ghost at high magnification. Thus the diffraction limit means that proteins, typically on the order of 4 nm in diameter (the diameter of GFP), cannot be associated with cellular organelles, that are on the order of 40 nm in diameter (such as synaptic vesicles or Golgi cisternae). In the last few years, several super-resolution techniques have been developed that can resolve fluorescence at resolutions below the diffraction limit (Hell and Wichmann, 1994; Gustafsson, 2000; Betzig et al., 2006; Hess et al., 2006; Rust et al., 2006; Fölling et al., 2008; Heilemann et al., 2008). Single molecule-based techniques include photoactivated localization microscopy (PALM) (Betzig et al., 2006), fluorescence photoactivation localization microscopy (fPALM) (Hess et al., 2006), stochastic optical reconstruction microscopy (STORM) (Rust et al., 2006), direct stochastic optical reconstruction microscopy (dSTORM) (Heilemann et al., 2008) and ground-state depletion microscopy followed by individual molecule return (GSDIM) (Fölling et al., 2008). Despite the variations in acronyms, these techniques overcome the diffraction barrier by imaging single molecules one at a time (Galbraith and Galbraith, 2011). The location of individual molecules is then calculated and mapped to reconstruct an image. In this chapter, we will use the terms PALM, for imaging individual fluorescent proteins, and dSTORM, for imaging organic fluorophores using ground-state depletion (*see* **Note 1**). These imaging techniques break the diffraction limit of conventional fluorescence microscopy, and can localize a protein with a precision of 10 nm (SEM) (Hell, 2007; Shtengel et al., 2009) (*see* **Note 2**).

The second drawback with fluorescence microscopy is that it lacks cellular context. A precisely localized pinpoint of fluorescence in a black background is not useful. Combining these new subdiffraction fluorescence methods with electron microscopy merges the protein localization advantages of fluorescence microscopy with the structural definition of electron microscopy (Watanabe et al., 2011).

To localize GFP in ultrathin sections one must maintain GFP fluorescence during the harsh osmium fixation steps, the dehydration steps, and incubation and polymerization in acidic resins. Recently, we developed a method to preserve fluorescence by reducing fixative concentrations, maintaining hydration, and compromising on ideal polymerization conditions (Watanabe et al., 2011). In short, transgenic worms expressing proteins tagged with fluorescent proteins are subject to high-pressure freezing and freeze-substitution. These animals are embedded into glycol methacrylate resin at -20ºC. Ultrathin sections are cut using a microtome and collected onto pre-cleaned cover glasses. These sections are first imaged on a super-resolution light microscope, then post-stained with uranyl acetate and imaged using back-scattered electrons on a scanning electron microscope (SEM). Using this approach, we successfully localized histones, mitochondrial membrane proteins, and liprin-alpha to their proper organelles in a cell (Watanabe et al., 2011). However, several improvements can be implemented to increase the sensitivity and the utility of our methods.

There are five problems associated with the original protocol we published. First, ~40% of fluorescent proteins were lost during the fixation. Second, photoactivatable fluorescent proteins suitable for PALM imaging are not ideal. EosFP and its variants are the most reliable fluorophores for PALM. However, they emit green fluorescence before photo-conversion and red fluorescence after photo-conversion, covering two large spectra of visible light. Thus, multicolor imaging is extremely difficult. Third, the number of photons collected from each EosFP molecule before bleaching is very low (~300), reducing the calculated precision of the protein location by the computer. Fourth, the protocol was originally developed using the nematode *Caenorhabditis elegans*, optimal conditions for other biological samples such as cultured cells were not known. Fifth, despite the well-preserved morphology, the resolution of images generated by collecting back-scatter electrons in a scanning electron microscope is limited by the size of the electron beam scanning the sample and leads to blurry images at high magnification (Fig. 6.1A, C).

Therefore, since the original publication, we have improved our methods to solve these five problems. First, we fine-tuned our protocol to preserve up to 90% of the fluorescence without compromising the fixation quality (Watanabe and Jorgensen, 2012). Second, to overcome the paucity of suitable fluorescent proteins with PALM imaging and demonstrate the potential for the method to localize multiple proteins at a time, we imaged the fluorescent protein, Citrine, that is not photoactivatable or photoconvertible using a ground-state depletion scheme (Watanabe and Jorgensen, 2012). Third, we labeled with an organic

fluorophore, Alexa-647, capable of generating many more photons and hence higher precision, and imaged using a dSTORM scheme although this approach is not quantitative (*see* **Note 3**) (Fig. 6.2A, B). Fourth, we demonstrated that this method could be readily applied to specimens other than *C. elegans* using the protocol (Fig. 6.2). Fifth, we developed a method to image using a transmission electron microscopy to provide higher-resolution details of ultrastructure (Fig. 6.1 and Fig. 6.2). Here, we describe the improved protocol in detail.

Materials

2.1 High-pressure freezing for *C. elegans*

1. High-pressure freezer (Baltec HPM010, ABRA/Boeckeler Instruments Inc., Tucson, AZ, U.S.A.; *see* **Note 4**)
2. Specimen carriers type A (catalog number 241-200, Technotrade International, Manchester, NH, U.S.A.)
3. Specimen carriers type B (catalog number 242-200, Technotrade International, Manchester, NH, U.S.A.)
4. Hexadecene (catalog number H2131-100ML, Sigma-Aldrich, St. Louis, MO, U.S.A.)
5. Forceps (catalog number 16LZ01873KN, Leica Microsystems, Wetzlar, Germany)
6. Paintbrush #00
7. Whatman filter paper (catalog number 09-810D, Fisher Scientific, Pittsburgh, PA, U.S.A.)
8. Liquid Nitrogen (160L)

2.2 High-pressure freezing for cell cultures

1. High-pressure freezer (HPM100, Leica Microsystems, Wetzlar, Germany; *see* **Note 5**)
2. Sapphire disks (6mm diameter, catalog number 616-100, Wohlwend GambH, Sennwald, Switzerland)
3. Specimen carriers Type A (6 mm diameter, catalog number 16770181, Leica Microsystems, Wetzlar, Germany)
4. Culture media: DMEM medium (90% DMEM, 10% FCS, 10 µg/ml Penicillin, and 1 µg/ml Streptomycin), FUDR stock solution (19.94 mg 5-fluoro-2'-deoxyuridine, 49.82 mg Uridine, and 10 ml DMEM), and NBA medium (97% NBA, 2% B27, 1% Glutamax, 10 µg/ml Penicillin, and 1 µg/ml Streptomycin).
5. Recording media: BASE +(140mM NaCl, 2.4mM KCl, 10mM Hepes, 10mM Glucose, 2mM $CaCl_2$, 4mM $MgCl_2$; pH adjusted to 7.5-7.6; osmolarity adjusted to ~300 mOsm)
6. Transferrin from Human Serum, Alexa Fluor 647 Conjugate (catalog number T-23366, Invitrogen, Grand Island, NY, U.S.A.)
7. Sapphire disk holder middle plate (6 mm diameter, catalog number 16770160, Leica Microsystems, Wetzlar, Germany)
8. Sample holder half cylinder (6 mm diameter, catalog number 16770139, Leica Microsystems, Wetzlar, Germany)
9. Forceps (insulated, catalog number 16LZ01873KN, Leica Microsystems, Wetzlar, Germany)

10. Ethanol (absolute, catalog number 459844-1L, Sigma-Aldrich, St. Louis, MO, U.S.A.)
11. Liquid nitrogen
12. Whatman filter paper (catalog number 09-810D, Fisher Scientific, Pittsburgh, PA, U.S.A.)

2.3 Freeze-substitution

1. Automated freeze-substitution unit (AFS 2, Leica Microsystems, Wetzlar, Germany)
2. Cryovials (catalog number 033377D, Thermo Scientific, Rochester, NY, U.S.A.)
3. 50 ml screw cap conical tubes (catalog number 62.547.004, Starstedt, Newton, NC, U.S.A.)
4. 15 ml screw cap conical tubes (catalog number 62.554.002, Starstedt, Newton, NC, U.S.A.)
5. Acetone (glass distilled, catalog number RT10016, Electron Microscopy Sciences, Hartfield, PA, U.S.A.)
6. Ethanol (absolute, catalog number 459844-1L, Sigma-Aldrich, St. Louis, MO, U.S.A.)
7. Osmium tetroxide (crystals, 1/10g, catalog number RT19134, Electron Microscopy Sciences, Hartfield, PA, U.S.A.)
8. Potassium permanganate (catalog number RT20200, Electron Microscopy Sciences, Hartfield, PA, U.S.A.)

9. Uranyl acetate (catalog number 21447-252, Polysciences, Warrington, PA, U.S.A.; *see* **Note 6**)
10. Disposable transfer pipette (7.5 ml, catalog number 14670-201, VWR, Randor, PA, U.S.A.)
11. Disposable transfer pipette (1.5 ml, catalog number 14670-364, VWR, Randor, PA, U.S.A.)
12. Disposable Pasteur pipette (Borosilicate glass, catalog number 13-678-20A, Fisher Scientific, Pittsburgh, PA, U.S.A.)
13. Pipetman and tips (P1000, P200, P20)

2.4 Plastic embedding

1. Glycol methacrylate kit (GMA, 2-Hydroxyethyl methacrylate, low acid and TEM grade, catalog number 02630-AA, SPI, West Chester, PA, U.S.A.)
2. *N,N*-Dimethyl-*p*-toluidine (catalog number 8220400005, EMD Chemicals, Philadelphia, PA, U.S.A.)
3. Scintillation vials with screw caps (20 ml, catalog number 72632, Electron Microscopy Sciences, Hartfield, PA, U.S.A.)
4. ACLAR film (catalog number 50425-10, Electron Microscopy Sciences, Hartfield, PA, U.S.A.)
5. BEEM capsule (polypropylene, catalog number TC, EBSciences, East Granby, CT, U.S.A.; *see* **Note 7**)
6. 3/8" disk punches (catalog number 54741, Ted Pella Inc., Redding, CA, U.S.A.)

7. 25 ml serological pipette (catalog number 13-678-11, Fisher Scientific, Pittsburgh, PA, U.S.A.)
8. 10 ml serological pipette (catalog number 13-678-11E, Fisher Scientific, Pittsburgh, PA, U.S.A.)
9. Petri dish (35 x 10 mm, catalog number 351008, Fisher Scientific, Pittsburgh, PA, U.S.A.)

2.5 Cover glass cleaning

1. Cover glass (#1.5, round, catalog number 40300, Warner Instruments, Hamden, CT, U.S.A.)
2. Sulfuric acid (catalog number 320501-2.5L, Sigma-Aldrich, St. Louis, MO, U.S.A.)
3. Hydrogen peroxide (catalog number 216763-500ML, Sigma-Aldrich, St. Louis, MO, U.S.A.)
4. Cover glass rack (Teflon; C-141784, Invitrogen, Grand Island, NY, U.S.A.)
5. Sonicator
6. Glass beaker (500 ml)

2.6 Cover glass coating

1. Microarray high-speed centrifuge (catalog number MHC110V, ArrayIt, by Microarray Technology, Sunnyvale, CA, U.S.A.; *see* **Note 8**)
2. Pioloform (catalog number 19244, Ted Pella Inc., Redding, CA, U.S.A.)

3. Chloroform (catalog number 372978-100ML, Sigma-Aldrich, St. Louis, MO, U.S.A.)
4. Wax

2.7 Sectioning

1. Ultramicrotome (UC6, Leica Microsystems, Wetzlar, Germany)
2. Diamond knife (Ultra jumbo, 45º, 4.0 mm; DiATOME, Hartfield, PA, U.S.A.)
3. Glass strips (catalog number 8030, Ted Pella Inc., Redding, CA, U.S.A.)
4. Glass knife boats (catalog number 123-3, Ted Pella Inc., Redding, CA, U.S.A.)
5. Nail polish (clear)
6. Perfect loop (catalog number 70944, Electron microscopy sciences, Hartfield, PA, U.S.A.)
7. Hair tool for manipulation of plastic sections
8. Razor blade (Double edge; catalog number 72000, Electron microscopy sciences, Hartfield, PA, U.S.A.)
9. High profile microtome blades (catalog number 818, Leica Microsystems, Wetzlar, Germany)

2.8 PALM imaging

1. Zeiss PALM microscope (ELYRA P.1, Zeiss, Jena, Germany; *see* **Note 9**)
2. Gold nanoparticles (Call for 2x concentrated solution; catalog number 790122-010, Microspheres-Nanospheres Inc., Cold Spring, NY, U.S.A.)

3. Canned air
4. Attofluor cell chamber for microscopy (catalog number A7816, Invitrogen, Grand Island, NY, U.S.A.)

2.9 Cover glass mounting for dSTORM imaging

1. Twinsil (two-component silicone-glue, catalog number 13001000, Picodent, Wipperfürth, Germany)
2. Concave blank microscope slides (catalog number 44417, Celestron, Torrance, CA, U.S.A.)
3. Imaging buffer (Cysteamine, Glucose, Catalase, Glucose oxidase, and PBS)

2.10 dSTORM imaging

1. Zeiss PALM microscope (ELYRA P.1, Zeiss, Jena, Germany; *see* **Note 9**)
2. TetraSpeck fluorescent microspheres (0.1 µm diameter, catalog number T7270, Invitrogen, Grand Island, NY, U.S.A.)

2.11 Staining

1. Uranyl acetate (catalog number 21447-252, Polysciences, Warrington, PA, U.S.A.)
2. Syringe (10 ml)
3. Syringe filter (0.22µm; catalog number SLGP033RB, Millipore, Billerica, MA, U.S.A.)

2.12 Retrieval of sections from cover glass

1. Hydrofluoric acid (catalog number 339261-100ML, Sigma-Aldrich, St. Louis, MO, U.S.A.)
2. Parafilm

2.13 SEM imaging

1. FEI Nova Nano (FEI, Hillsboro, OR, U.S.A.; *see* **Note 10**)
2. Backscattered electron detector (vCD, FEI, Hillsboro, OR, U.S.A.)
3. Carbon fiber cord (catalog number 4539, Electron microscopy sciences, Hartfield, PA, U.S.A.)
4. Carbon sputter device (SCD005, Baltec; *see* **Note 11**)
5. SEM pin stub (catalog number 16111, Ted Pella Inc., Redding, CA, U.S.A.)
6. Carbon conductive tape (double coated; catalog number 16084-7, Ted Pella Inc., Redding, CA, U.S.A.)

2.14 Image alignment

1. Photoshop (CS6, Adobe, San Jose, CA, U.S.A.)

Methods

3.1 Preparing sapphire disks for culturing cells

1. Wash the disks in ethanol (absolute) and let them dry in air.
2. Apply a thin layer (10-30 nm) of carbon coat using a carbon sputter *(Hess et al., 2000; Sawaguchi et al., 2002)*. The sapphire disk should be fairly dark. Note that cells will be cultured on the carbon-coated surface.
3. To keep a track of the carbon-coated surface during the subsequent manipulation, mark the carbon-coated surface by scratching out an asymmetrical letter such as "F" or "G" *(McDonald et al., 2010)*. If finding particular cells (for example, fluorescence-positive cells) is required, a finder grid (catalog number 16770162, Leica Microsystems) can be placed on top of the sapphire disk to generate a specific pattern on the surface when carbon-coating (Fig. 6.3A, B).
4. Bake the disks in an oven (120ºC) overnight.
5. Place sapphire disks into a 12-well culture plate (we typically place two in each well), apply poly-L-lysine for 5 min, and let it dry for an hour.
6. Apply ultraviolet light for 20 min.
7. The sapphire disks are now ready for culturing. For culturing neuronal cells, we followed a protocol described in Pyott and Rosenmund (2002) *(Pyott and Rosenmund, 2002)*. Follow the appropriate protocol for your particular cell type (Fig. 6.3C).

3.2 Transferrin-647 uptake

1. To prepare transferrin conjugates, we followed a protocol provided by Invitrogen (http://tools.invitrogen.com/content/sfs/manuals/mp02871.pdf). In short, we mixed 5 mg transferrin-647 with 1 ml deionized water.
2. Dilute the transferrin-647 solution to 5 ng/ml by adding 1 µl of the solution into 1 ml of recording media (BASE +).
3. Apply the diluted solution to cell cultures for two hours.
4. Wash cells with recording media several times.

3.3 High-pressure freezing

1. Prepare the automated freeze-substitution device (Leica AFS2) by filling the tank with liquid nitrogen, programming the freeze-substitution protocol as shown in Fig. 6.4, and initiating the program. Note that the program must be paused while the chamber is cooled down to -90ºC and unpaused when all the samples are loaded into the chamber.
2. Prepare the fixatives (20 ml) by adding 1 ml milliQ water, 20 mg potassium permanganate, and 20 ml osmium tetroxide (1% in anhydrous acetone; *see* **Note 11**) into a 50 ml conical tube and filled with anhydrous acetone (*see* **Note 12**) up to the 20 ml mark. Aliquot 1 ml of this solution into each cryovial, and submerge the cryovials into liquid nitrogen immediately. Store the vials under liquid nitrogen until use.
3. Mount the specimens for high-pressure freezing (HPM 100; for other high-pressure freezers, *see* **Note 13**). For *C. elegans*, fill a 100 µm well of a type

A specimen carrier (3 mm diameter; Fig. 6.5A) with bacteria using a paint brush (Fig. 6.5B), and place transgenic animals on top of the bacteria (Fig. 6.5C). Make sure the well is slightly overfilled. Cap the well with the flat side of a type B specimen carrier (3 mm diameter; Fig. 6.5C, D). For cell cultures, mount a sapphire disk (6 mm diameter) directly onto a sapphire disk holder middle plate (Fig. 6.3D, E). Make sure the surface that cells are cultured on faces up. Dip a 100 μm well side of a type A specimen carrier into the recording solution so that the well is filled (overfilled) with the solution (Fig. 6.3F). Place the specimen carrier gently onto the sapphire disk (Fig. 6.3F, G). Now, specimens are ready for freezing (Fig. 6.3G and Fig. 6.5D).

4. Freeze specimen according to the instructions provided by the instrument's manufacturer.

3.4 Freeze-substitution and plastic embedding

1. Once frozen, transfer specimens into a cryovial containing fixatives under liquid nitrogen.
2. Place the cryovials in the chamber of AFS.
3. Unpause the program.
4. When the temperature reaches -60ºC, place a scintillation vial containing 95% acetone (made up of 5% milliQ water and anhydrous acetone) into the chamber.
5. When the temperature reaches -50ºC, remove the solutions from each vial and add pre-cooled 95% acetone using a precooled glass pipette. Repeat

the process five more times with each spaced by 15 min. Place a scintillation vial containing 0.1% uranyl acetate in 95% acetone to pre-cool the solution.

6. At the end of step 5, replace acetone in the vials with 1 ml of pre-cooled 0.1% uranyl acetate solution. Place a scintillation vial containing 95% ethanol (made up of 5% milliQ water and anhydrous acetone).
7. After 1 hour incubation with uranyl acetate, replace the solution and wash specimens with 95% ethanol (*see* **Note 12**) for six times over 2 hours. Note that step 8 – 10 should be carried out concurrently with this step.
8. Prepare GMA media for infiltration by mixing 22.3 ml glycol methacrylate, 10 ml butyl methacrylate, 1 ml milliQ water, and 0.2 g benzoyl peroxide (*see* **Note 14**). Do not pre-polymerize the GMA media as instructed by the manufacturer. These components are simply mixed, and no further processing is required before use.
9. Prepare 30% and 70% GMA media by mixing GMA media with 95% ethanol.
10. Place a scintillation vial containing 30% GMA media in the chamber of AFS at least one hour before use.
11. At the last step of ethanol washing (step 7), replace ethanol with pre-cooled 30% GMA media. Incubate the specimens in 30% media for 3-5 hours (*see* **Note 15**). Place a scintillation vial containing 70% GMA media in the chamber of AFS.
12. Replace 30% media with 70% media, and incubate specimens for 4-6 hours (*see* **Note 15**). Place a scintillation vial containing 100% GMA media in the chamber of AFS.

13. Replace 70% media with 100% media and incubate specimens overnight.
14. On the next day, transfer specimens into caps of BEEM capsules (*see* **Note 16**). Fill the embedding cap with 100% media immediately after the transfer.
15. Replace the media two additional times with each change spaced at 2 hours.
16. To polymerize GMA media, add N,N-dimethyl-*p*-toluidine into the GMA media at 1.5 µl/1 ml GMA media (*see* **Note 17**). Replace the GMA media in the embedding cap with the GMA media with N,N-dimethyl-*p*-toluidine.
17. Allow the plastic to polymerize overnight, even though reaction is complete within 30 min (*see* **Note 18**).
18. If not processed immediately, samples should be wrapped in foil and stored in a vacuum bag at -20ºC.

3.5 Cover glass cleaning and coating

1. Immerse cover glasses in piranha solution (3 parts sulfuric acid and 1 part hydrogen peroxide) for 1 hour (*see* **Note 19**).
2. Rinse cover glasses with milliQ water for 6 times.
3. Sonicate cover glasses for 30 min.
4. Rinse cover glasses with milliQ water for 6 times.
5. Dry cover glasses in air.
6. To coat a cover glass with a film compatible with transmission electron microscopy imaging, mount a cover glass in a desktop centrifuge as shown in Fig. 6.6 A-C.

7. Apply 250 µl of 0.7% Pioloform solution (in chloroform) to a cover glass (Fig. 6.6D), and spin it off immediately (Fig. 6.6E). This treatment leaves a thin layer of Pioloform on top of the cover glass (Fig. 6.6F). The film along with sections can be retrieved after the super-resolution imaging (Fig. 6.7).

3.6 Sectioning

1. Sectioning is carried out at room temperature. Extra cautions should be paid not to expose the specimens to sunlight or bright room light. Locate a region of interest (*see* **Note 20**), and trim the block so that the sectioning surface is in a trapezoid shape with a dimension of less than 100 µm high and 1 mm long.
2. Set up the microtome as instructed by the manufacturer. Mount the specimens on the microtome.
3. After aligning the specimen with a diamond knife, start cutting 50-70 nm thick sections with the cutting speed set at 1.6 mm/s.
4. After cutting a sufficient number of sections, collect sections onto a cover glass with or without the Pioloform film by immersing the cover glass into a water bath, touching the edges of sections to the center of the cover glass, and sliding the cover glass gently out of the water bath.
5. Place the cover glass in a dark place, and allow it to air dry. Once dried, store the cover glasses at -20ºC in a vacuum bag until further processing.

3.7 PALM imaging of tdEos

1. Place a small drop (~50 µl) of 100 nm gold nanospheres solution (1.2×10^{10} particles/ ml; *see* **Note 21**) directly on top of the sections. After 30-60 s, blow the drop to the edge of the cover glass and blot with a Kimwipe. Gold nanospheres serve as fiducial markers for aligning fluorescence and electron micrographs and can also be used to correct sample drift during image acquisition.
2. Hydrate the sections for 2 min by placing a small drop of milliQ water directly on top of the sections, then blow to the edge of the cover glass and blot.
3. Start PALM microscope and associated software. 561 nm, 488 and 405 nm lasers should be turned to standby mode.
4. Load cover glass into a cover glass holder (cell chamber), sections facing up, and place on microscope stage over the low-power objective. If no cover glass holder is available, the cover glass can be fixed to a microscope slide by a few spots of nail polish. The sections should be sandwiched between the cover glass and the slide, and the assembly placed into the microscope so the cover glass is towards the objective. Apply immersion oil on the cover glass.
5. Using wide-field illumination and a low-power objective, locate the sections.
6. Switch to the high-power TIRF objective. Low power 488 nm laser light can be used to locate a region of interest, but this should be performed only briefly and only if necessary, as it will reduce the available fluorescence signal during image acquisition.

7. Using maximum intensity 561 nm light, illuminate the region of interest for ~2 min to bleach the autofluorescence.
8. For image acquisition, use minimum intensity 405 nm illumination to activate fluorophores, and maximum intensity 561 nm illumination for readout. The frame rate should be set to 20 Hz or greater. We typically collect 6000 frames for each region, but this number can be adjusted to suit the specifics of the experiment. For example, if recording of every molecule in the region is required, more frames may be necessary.
9. If the activated molecules are sparse, increase the intensity of 405 nm laser (*see* **Note 22**).
10. Collect images for each section on the cover glass. During long imaging sessions, the sections may become dehydrated resulting in weakened signal; rehydrate as in step 2 every ~30 min.
11. After acquisition, images should be processed by PALM software. Both sum TIRF (a collection of all the fluorescence signals acquired) and PALM images should be created. The sample shift during image acquisition is corrected based on the locations of gold particles in the first image. To eliminate background fluorescence, which is typically long-lived, we filter out molecules that are active for > 500 ms; tdEos usually bleaches before 500 ms under these illumination conditions. The final image only shows molecules with high localization precision (below 35 nm) to filter out background fluorescence because background fluorescence is typically dim and localization precision is directly related to the quantity of photons received.

3.8 dSTORM imaging

1. Place a small drop of 100 nm TetraSpeck fluorescent microspheres (9.0×10^9 particles/ ml; *see* **Note 21**) directly on top of the sections. Blow the solution off to the edge of the cover glass and absorb it with a Kimwipe. TetraSpeck fluorescence microspheres also serve as fiducials for image alignment and sample drift (Fig. 6.2B, C).
2. Prepare dSTORM imaging buffer: 50 mM Tris (pH8.0), 10 mM NaCl, 0.5mg/ml glucose oxidase, 40 µg/ml catalase, 10% (w/v) glucose, and 10 mM MEA (*see* **Note 23**) (Dempsey et al., 2011).
3. Mount the cover glass onto a microscope slide with a concave surface. First, fill the concave surface with the imaging buffer, and then apply a few drops of the imaging buffer onto the cover glass containing sections. Carefully flip the cover glass and mount it onto the microscope slide so that there is no air bubbles trapped in the chamber. Wipe out the excess buffer using a Kimwipe. To fix the cover glass onto the microscope slide and seal solutions from the air, apply Twinsil to the edges of cover glass and let it dry for ~5 min after mixing the two components of Twinsil solution, (*see* **Note 24**).
4. For dSTORM imaging, turn on the microscope and associated software. Turn on 405 nm and 641 nm lasers to stand-by mode.
5. Locate the sections and regions of interest using a low power objective lens and a bright-field illumination.
6. Switch to a high-power objective lens. Turn on the 641 nm laser at its lowest power and locate the region of interest.

7. Collect ~10,000 frames at 30 ms/frame with 641 nm laser set at its maximum power. Turn on the 405 nm laser as necessary (*see* **Note 25**).
8. Process the images with the PALM/STORM software (quickPALM; Henriques et al., 2010) was used to process dSTORM images in this chapter). Because fluorescence from Alexa-647 dyes is much brighter than tdEos fluorescence, signals are highly distinctive from the background fluorescence, and thus subtraction of background as described in 3.7.11 is not necessary. For sample drift correction using quickPALM (Fig. 6.2B, C), *see* **Note 26**.

3.9 SEM imaging

1. Prior to SEM imaging, the sections must first be post-stained with uranyl acetate to increase contrast. With 2.5% uranyl acetate in milliQ water passed through a 0.2 μm filter, place a drop directly on top of the sections. After 4 min, thoroughly but gently rinse the sections with filtered milliQ water. Allow to air dry.
2. To prevent charging by the electron beam, the sections should be carbon coated. Use a carbon sputter to deposit a thin layer of carbon, until the surface of the cover glass becomes dark brown. Use a piece of carbon tape to ground the surface of the cover glass by affixing one end to the carbon-coated surface and contacting the base of the metal specimen stub with the other end.
3. Electron micrographs of the sections can now be obtained from back-scattered electrons. We typically image with specimen current set at 0.11 nA,

the accelerating voltage at 5 keV, the landing energy at 3 keV, and the immersion mode "on" (*see* **Note 27**).

4. Collect both low magnification and high magnification images for each section. The low magnification images will be used as a guide for alignment with the fluorescence micrographs, and the high magnification to define the fine ultrastructure. Invert the grayscale to achieve a look similar to a TEM micrograph.

3.10 TEM imaging

1. Following fluorescence imaging, sections should be post-stained with uranyl acetate as described in 3.9.1.
2. The sections then must be retrieved from the cover glass for a TEM imaging. To retrieve sections, first cut a square around the sections using a razor blade (Fig. 6.7A). Second, apply 1% hydrofluoric acid to the cover glass (Fig. 6.5B, C). Once the glass is etched a little bit, the Pioloform film and sections will float on top of the hydrofluoric solution (Fig. 6.7B, C). Immerse the cover glass into a water bath so that the film containing sections are floated on the surface of water (Fig. 6.7D, E). Place a single-slot TEM grid on top of the film so that the sections appear in the middle of the slot window (Fig. 6.7F). Finally, retrieve the grid by gently laying a strip of Parafilm on top of the grid and Pioloform, followed by carefully withdrawing the Parafilm strip from the water surface in a rolling motion. The grid and surrounding excess Pioloform will come with the Parafilm. Once dry, separate the grid from the excess

Pioloform by carefully poking the film at the edge of the grid with the tips of a pair of forceps. The grid can then be cleanly removed from the excess Pioloform film.

3. After the grid is dried, regular TEM imaging can be performed on these plastic sections. Both low magnification and high magnification images should be collected.

3.11 Image alignment

1. In Adobe Photoshop, open a new 5000 x 5000 pixel window with 300 pixel/in.
2. Paste the low magnification electron micrograph into the window and transform to fill ~80% of the window. Be certain to maintain the aspect ratio during transformation (hold down the "shift" key in Windows or Mac).
3. Paste the high magnification electron micrograph into a new layer and transform to align with the low magnification micrograph.
4. Paste the sum TIRF micrograph into a new layer and scale, rotate, and transform to align the fiducials. Gold nanospheres should appear as fluorescence in the sum TIRF and as electron density in the electron micrograph. Nonlinear transformations may be necessary (*see* **Note 28**).
5. Paste the PALM image into a new layer. Align perfectly with the sum TIRF by applying identical transformation values.
6. For presentation, it is desirable to apply a transparency to the black background of the sum TIRF and PALM images. In a duplicate file (to avoid manipulation of the original), select "Color range" from the "Select" menu.

Select a black background pixel and invert selection. Adjust the fuzziness so that the black pixels surrounding the signal are not selected.

7. Cut and paste the selection into a new layer. This new layer thus contains only the signal, and the previous layer now contains only black background, with blank spots where the signal has been cut out.
8. Apply a 10% transparency to the background layer.

Notes

1. Because of the fluorophores used in the original publications, the acronym PALM is usually associated with imaging fluorescent proteins, whereas STORM is associated with organic fluorophores usually attached to antibodies. All these methods are based on localizing individual molecules. Imaging single molecules requires the spatio-temporal separation of individual molecules in a densely labeled sample. There are two schemes for separating molecules. PALM, fPALM, and STORM rely on the stochastic activation of fluorophores from a nonresponsive state to a responsive state. On the other hand, dSTORM and GSDIM drive fluorescent molecules into a dark state ('ground-state depletion') and image single molecules that stochastically return to a ground state.
2. There are two important concepts in super-resolution microscopy: resolution and precisioin. 'Resolution' in fluorescence microscopy reflects the ability to determine that the light collected in a field arises from two separate objects. For example, astronomers must resolve two stars in the sky. Biologists must

determine that the fluorescence in a cell arises from two adjacent proteins, instead of one. Our ability to distinguish the presence of two labeled proteins is restricted by the diffraction limit: light from a point source can only be focused on a camera to a spot with a diameter of about 450 nm. Two spots cannot be separated once they are closer than about half the wavelength of light – around 200 nm. There are various ways to estimate this distance depending on the wavelength of light and the optics of the microscope; two commonly cited methods are the Abbé limit and the Rayleigh limit. However, PALM and STORM microscopy bypass the diffraction limit by separating the detection of the fluorescent sources in time. Determining that light coming from a spot is composed of two sources is obvious, since they appear at different times. Counting proteins, unlike stars, can be made to be quite easy.

Resolution is however important when trying to determine the shape and size of an organelle: for example, to distinguish the stacks in a Golgi. For these applications one must 'paint' the organelle with dense enough labeling to know that they comprise a single structure, and have a fine enough resolution to know that these molecules do not belong to the adjacent structure. Resolution of current super-resolution microscopes has been reported to be ~20 nm (Hell, 2007; Shtengel et al., 2009).

'Precision' reflects one's confidence that a protein is actually located at the calculated position. Precision is important when one is trying to determine if two different proteins are located at the same position, by imaging in two colors. Precision is also very important in nano-fEM, since the location of a

protein will be correlated with a structure observed in an electron micrograph. Precision relies on fitting a Gaussian distribution to the photons collected on the camera face from a particular tagged protein. The more photons collected, the more accurate the calculation. Localization precision of proteins in PALM images using fluorescent proteins is about ~12-15 nm (Watanabe et al., 2011).

3. There are two factors that make STORM and dSTORM imaging not quantitative: antibody labeling density and organic fluorophores. First, antibodies are large and binding occludes access to neighboring antigens (van de Linde et al., 2010; Lakadamyali et al., 2012), and typically not all proteins are bound to an antibody. Second, unlike fluorescent proteins (*however* ***see*** van de Linde, Wolter, and Heliemann (2010) and Lakadamyali, Babcock, and Bates (2012)), organic fluorophores blink several times before quenching, and thus the same molecules are sampled multiple times (Rust et al., 2006; Heilemann et al., 2008; Huang et al., 2008).
4. Baltec is now a part of Leica Microsystems. The HPM010, however, can only be purchased from ABRA.
5. We used HPM100 for freezing cell cultures, but other high-pressure freezers or freezing methods such as self-pressurized freezing (Leunissen and Yi, 2009) can be used. The HPM100 holds samples as large as 6 mm in diameter, allowing more cells to be examined.
6. The pH of uranyl acetate solution is usually highly acidic (pH 2-5), and fluorescence proteins will be quenched in such conditions. If the pH of the

uranyl acetate is low, shorten the incubation duration with uranyl acetate solution in the step 3.4.6. Uranyl acetate from Polysciences seems to have higher pH (around 6).

7. Unfortunately, polypropylene BEEM capsules have been discontinued. We have not been able to find a replacement source. Although the use of polyethylene is not recommended for glycol methacrylate, we have been successfully polymerized GMA in polyethylene BEEM capsules by placing a layer of ACLAR film (*see* **Note 15**) (Watanabe et al., 2011; Watanabe and Jorgensen, 2012) or a sapphire disk at the bottom of the polyethylene BEEM capsule cap.
8. Any desktop centrifuge that is equipped with a microscope slide holder is likely adequate for removing the excess Pioloform solution off of the cover glass, but this particular desktop centrifuge is capable of reaching its maximum speed rapidly, resulting in the very uniform thin layer of film coated on the cover glass.
9. As discussed in the Introduction, single molecule based super-resolution imaging can be performed on any microscope equipped with an EMCCD camera and appropriate laser lines and filter sets. For dSTORM imaging in this chapter, we used a custom-built microscope in the laboratory of Dr. Schmoranzer at Leibniz-Institut für Molekulare Pharmakologie im Forschungsverbund in Berlin, Germany (for details of the microscope setup, *see* (Lampe et al., 2012)). Free software for analysis is available from NIH (http://code.google.com/p/quickpalm/ and http://code.google.com/p/palm3d/)

(Henriques et al., 2010; York et al., 2011). Currently, three commercial PALM/STORM microscopes are available for purchase: Zeiss Elyra, Nikon N-STORM, and Vutara SR-200.

10. Although most microscopes are capable of imaging back-scattered electrons, a scanning electron microscope with a field emission gun and a sensitive back-scattered electrons detector should be used for the best resolution.
11. We prepare 1% osmium tetroxide stock solution by mixing 0.1 g osmium crystals with 10 ml anhydrous acetone. We then aliquot it into cryovials and store them in a liquid nitrogen storage tank until use.
12. We found that the use of acetone is required to preserve membrane morphology (Watanabe et al., 2011; Watanabe and Jorgensen, 2012) presumably due to its ability to interact with lipids (Weibull and Christiansson, 1986). However, acetone acts as free radical scavenger and blocks proper polymerization of plastic resins (Webster, 2007). Therefore, we substitute specimens with ethanol prior to plastic infiltration.
13. Here, we are describing the protocol for Leica HPM 100. For other high-pressure freezers, please refer to Watanabe and Jorgensen (2012) (Watanabe and Jorgensen, 2012) and McDonald (2007 and 2010) (McDonald, 2007; McDonald et al., 2010).
14. To dissolve benzoyl peroxide, use a Nutator in a cold room (4ºC) or place the tube on ice while mixing. Otherwise, the solution becomes cloudy. It requires ~5-10 min.

15. The incubation duration can be altered depending on the size of specimens or your schedule.
16. For cell cultures, make sure the side that the side with cells faces up after transferring. For *C. elegans*, place a disk of ACLAR film at the bottom of the cap so that specimens do not contact the BEEM capsule directly.
17. Once the catalyst, N,N-dimethyl-*p*-toluidine, is added to GMA media, polymerization reaction initiates immediately, and is completed within 30 min. Work as quickly as possible while replacing solutions.
18. If the resin is polymerized outside the AFS chamber, the embedding cap should be sealed with ACLAR film. Otherwise, oxygen will block complete polymerization of the plastic. The AFS chamber is filled with nitrogen gas, and thus the resin can polymerize without the ACLAR film.
19. Piranha solution makes the glass surface hydrophilic, making it difficult to retrieve sections in step 3.6.4. To create a hydrophobic surface, cover glasses should be rinsed in methanol or should be incubated with hexamethyldisilazane (HMDS) gas in a sealed glass beaker.
20. A region of interest in *C. elegans* is located based on the morphology visualized using a stereomicroscope. For example, if we are interested in imaging a nerve ring, we locate the region by the morphology of pharynx in the animal. If there are no distinctive morphological features, we locate the region of interest by fluorescence. If animals are expressing tdEos, we briefly expose animals to blue light (less than 1 s) and leave a knife mark close to where fluorescence is expressed. For cell cultures, locating a cell of interest

would be most reliably performed by marking a sapphire disk with a finder grid pattern (*see* **Methods 3.2.3**). Before performing a high-pressure freezing, locate the cells of interest using a light microscope and remember the position of the cells in the sapphire disks. The carbon layer is transferred into a plastic block along with the cells, and thus the specific pattern generated by the finder grid helps locate the cells of interest in a plastic block after embedding.

21. Gold nanospheres emit fluorescence due to surface plasmon resonance (Link and El-Sayed, 1999). The 100 nm gold particles absorb green light and emit red light. Its emission spectra overlaps with that of tdEos after photo-conversion and thus can be used to correct the specimen drift during fluorescence imaging. Because gold scatters electrons, the gold particles also mark the electron micrographs and can be used as fiducial marks for aligning the fluorescence and electron micrographs. TetraSpeck beads can be excited at four different wavelengths: 365 nm (UV), 505 nm (green), 560 nm (orange), and 660 nm (red). Because the emission spectra of Alexa-647 overlaps with that of TetraSpeck beads, we used TetraSpeck beads in our dSTORM imaging as fiducial markers. Because these beads are made of nonelectron conductive polystyrene, electrons accumulate on the beads, causing incoming electrons to be repelled when imaged under an electron microscope. Thus these beads also mark electron micrographs. Note that polystyrene beads do not stick to plastic sections nor the glass surface in the absence of buffer, so we dilute the original solution with PBS to 1:200. We

obtained 3-5 beads in each imaging frame at this concentration when applied to the specimens for 1 min.

22. During acquisition, the intensity of the activation (405 nm) laser can be adjusted to deliver an appropriate level of fluorophore activation. If the activated signal is meager, increase the power. Note, however, that if activation is too dense and fluorescence spots overlap, the computer will incorrectly calculate the centroid and produce erroneous data.
23. MEA should be stored as a solid at 4ºC and prepared freshly each day as a 1 M stock solution in water. The pH of the solution should be adjusted to ~8 with 1 M HCl.
24. Twinsil is the same silicon material used to create impression molds or dental molds. Its use for mounting coverslips was introduced by Leica Microsystems as an alternative to a nail polish since nail polish contains organic solvents that interfere with dSTORM imaging (http://www.leica-microsystems.com/science-lab/sample-preparation-for-gsdim-protocols-and-tips/).
25. The 405 nm laser increases the rate of blinking but also increases background fluorescence level. Thus, its intensity should be determined experimentally.
26. To account for sample drift using quickPALM, a square box with a size larger than the displacement of a particle during the image acquisition is drawn around three individual particles. These squares are saved as a region of interest (ROI) in ImageJ. The drift is calculated based on the displacement of

the particles. The corrected locations of the particles are saved as a tif file, reloaded into imageJ, and reconstructed to obtain the final image. For more details, refer to the quickPALM wiki page (http://code.google.com/p/quickpalm/wiki/Welcome).

27. There are two features in the FEI NovaNano that make it sensitive to back-scattered electrons. First, it is capable of introducing a negative bias to the stage, which accelerates back-scattered electrons towards the detector and thus improves signal. Second, an electromagnetic field (immersion mode "on") can be applied between the pole piece and the specimen so that electrons scattered by the specimens do not leave the field and thus are collected by the detectors.
28. Aligning the images can be accomplished in Fiji by using TrakEM2 and selecting the fiducials in each image as alignment targets.

Acknowledgements

We thank Harald Hess and Eric Betzig for access to the PALM microscope for proof-of-principle experiments. We thank Michael Davidson and Stefan Eimer for DNA constructs. We thank Gunther Hollopeter for generating transgenic lines used in these experiments. We thank Agnieszka Münster-Wandowski for access to a transmission electron microscope. We also thank Manasa Gudheti and Vutara Microscopes for sharing their imaging buffer protocol. We also thank Carl Zeiss Inc. for providing access to the beta version of the Elyra PALM microscope.

References

Betzig, E., Patterson, G.H., Sougrat, R., Lindwasser, O.W., Olenych, S., Bonifacino, J.S., Davidson, M.W., Lippincott-Schwartz, J., and Hess, H.F. (2006). Imaging intracellular fluorescent proteins at nanometer resolution. Science *313*, 1642–1645.

Burnette, D.T., Sengupta, P., Dai, Y., Lippincott-Schwartz, J., and Kachar, B. (2011). Bleaching/blinking assisted localization microscopy for superresolution imaging using standard fluorescent molecules. Proc. Natl. Acad. Sci. U.S.A. *108*, 21081–21086.

Chalfie, M., Tu, Y., Euskirchen, G., Ward, W.W., and Prasher, D.C. (1994). Green fluorescent protein as a marker for gene expression. Science *263*, 802–805.

Dempsey, G.T., Vaughan, J.C., Chen, K.H., Bates, M., and Zhuang, X. (2011). Evaluation of fluorophores for optimal performance in localization-based super-resolution imaging. Nat. Methods *8*, 1027–1036.

Duc-Nguyen, H., and Rosenblum, E.N. (1967). Immuno-electron microscopy of the morphogenesis of mumps virus. J. Virol. *1*, 415–429.

Faulk, W.P., and Taylor, G.M. (1971). An immunocolloid method for the electron microscope. Immunochemistry *8*, 1081–1083.

FELDHERR, C.M., and MARSHALL, J.M., Jr (1962). The use of colloidal gold for studies of intracellular exchanges in the ameba Chaos chaos. J. Cell Biol. *12*, 640–645.

Fölling, J., Bossi, M., Bock, H., Medda, R., Wurm, C.A., Hein, B., Jakobs, S., Eggeling, C., and Hell, S.W. (2008). Fluorescence nanoscopy by ground-state depletion and single-molecule return. Nat. Methods *5*, 943–945.

Galbraith, C.G., and Galbraith, J.A. (2011). Super-resolution microscopy at a glance. J Cell Sci *124*, 1607–1611.

Gustafsson, M.G. (2000). Surpassing the lateral resolution limit by a factor of two using structured illumination microscopy. J Microsc *198*, 82–87.

Heilemann, M., van de Linde, S., Schüttpelz, M., Kasper, R., Seefeldt, B., Mukherjee, A., Tinnefeld, P., and Sauer, M. (2008). Subdiffraction-resolution fluorescence imaging with conventional fluorescent probes. Angewandte Chemie International Edition *47*, 6172–6176.

Hell, S.W. (2007). Far-field optical nanoscopy. Science *316*, 1153–1158.

Hell, S.W., and Wichmann, J. (1994). Breaking the diffraction resolution limit by stimulated emission: stimulated-emission-depletion fluorescence microscopy. Opt. Lett. *19*, 780–782.

Henriques, R., Lelek, M., Fornasiero, E.F., Valtorta, F., Zimmer, C., and Mhlanga, M.M. (2010). QuickPALM: 3D real-time photoactivation nanoscopy image processing in ImageJ. Nature Methods *7*, 339–340.

Hess, M.W., Müller, M., Debbage, P.L., Vetterlein, M., and Pavelka, M. (2000). Cryopreparation provides new insight into the effects of brefeldin A on the structure of the HepG2 Golgi apparatus. J. Struct. Biol. *130*, 63–72.

Hess, S.T., Girirajan, T.P.K., and Mason, M.D. (2006). Ultra-high resolution imaging by fluorescence photoactivation localization microscopy. Biophys. J *91*, 4258–4272.

Huang, B., Wang, W., Bates, M., and Zhuang, X. (2008). Three-dimensional super-resolution imaging by stochastic optical reconstruction microscopy. Science *319*, 810–813.

Lakadamyali, M., Babcock, H., Bates, M., Zhuang, X., and Lichtman, J. (2012). 3D Multicolor Super-Resolution Imaging Offers Improved Accuracy in Neuron Tracing. PLoS ONE *7*, e30826.

Lampe, A., Haucke, V., Sigrist, S.J., Heilemann, M., and Schmoranzer, J. (2012). Multi-colour direct STORM with red emitting carbocyanines. Biol. Cell *104*, 229–237.

Lee, S.-H., Shin, J.Y., Lee, A., and Bustamante, C. (2012). Counting single photoactivatable fluorescent molecules by photoactivated localization microscopy (PALM). Proc. Natl. Acad. Sci. U.S.A. *109*, 17436–17441.

Leunissen, J.L.M., and Yi, H. (2009). Self-pressurized rapid freezing (SPRF): a novel cryofixation method for specimen preparation in electron microscopy. J Microsc *235*, 25–35.

van de Linde, S., Wolter, S., Heilemann, M., and Sauer, M. (2010). The effect of photoswitching kinetics and labeling densities on super-resolution fluorescence imaging. J. Biotechnol. *149*, 260–266.

Link, S., and El-Sayed, M.A. (1999). Spectral properties and relaxation dynamics of surface plasmon electronic oscillations in gold and silver nanodots and nanorods. J. Phys. Chem. B *103*, 8410–8426.

McDonald, K. (2007). Cryopreparation methods for electron microscopy of selected model systems. Methods Cell Biol *79*, 23–56.

McDonald, K., Schwarz, H., Müller-Reichert, T., Webb, R., Buser, C., and Morphew, M. (2010). "Tips and tricks" for high-pressure freezing of model systems. Methods Cell Biol. *96*, 671–693.

Morphew, M.K. (2007). 3D immunolocalization with plastic sections. Methods Cell Biol *79*, 493–513.

Pyott, S.J., and Rosenmund, C. (2002). The effects of temperature on vesicular supply and release in autaptic cultures of rat and mouse hippocampal neurons. J Physiol *539*, 523–535.

Rostaing, P., Weimer, R.M., Jorgensen, E.M., Triller, A., and Bessereau, J.-L. (2004). Preservation of immunoreactivity and fine structure of adult C. elegans tissues using high-pressure freezing. J. Histochem. Cytochem *52*, 1–12.

Roth, J., Bendayan, M., Carlemalm, E., Villiger, W., and Garavito, M. (1981). Enhancement of structural preservation and immunocytochemical staining in low temperature embedded pancreatic tissue. J. Histochem. Cytochem *29*, 663–671.

Rust, M.J., Bates, M., and Zhuang, X. (2006). Sub-diffraction-limit imaging by stochastic optical reconstruction microscopy (STORM). Nat. Methods *3*, 793–795.

Sawaguchi, A., Mcdonald, K.L., Karvar, S., and Forte, J.G. (2002). A new approach for high-pressure freezing of primary culture cells: the fine structure and stimulation-associated transformation of cultured rabbit gastric parietal cells. Journal of Microscopy *208*, 158–166.

Shimomura, O. (2009). Discovery of green fluorescent protein (GFP) (Nobel Lecture). Angew. Chem. Int. Ed. Engl. *48*, 5590–5602.

Shtengel, G., Galbraith, J.A., Galbraith, C.G., Lippincott-Schwartz, J., Gillette, J.M., Manley, S., Sougrat, R., Waterman, C.M., Kanchanawong, P., Davidson, M.W., et al. (2009). Interferometric fluorescent super-resolution microscopy resolves 3D cellular ultrastructure. Proceedings of the National Academy of Sciences *106*, 3125–3130.

Tsien, R. (1998). The green fluorescent protein. Annual Review of Biochemistry *67*, 509–544.

Watanabe, S., and Jorgensen, E.M. (2012). Visualizing proteins in electron micrographs at nanometer resolution. Methods Cell Biol. *111*, 283–306.

Watanabe, S., Punge, A., Hollopeter, G., Willig, K.I., Hobson, R.J., Davis, M.W., Hell, S.W., and Jorgensen, E.M. (2011). Protein localization in electron micrographs using fluorescence nanoscopy. Nat. Methods *8*, 80–84.

Webster, P. (2007). Microwave-Assisted Processing and Embedding for Transmission Electron Microscopy. In Electron Microscopy, J. Kuo, ed. (Humana Press), pp. 47–65.

Weibull, C., and Christiansson, A. (1986). Extraction of proteins and membrane lipids during low temperature embedding of biological material for electron microscopy. J Microsc *142*, 79–86.

York, A.G., Ghitani, A., Vaziri, A., Davidson, M.W., and Shroff, H. (2011). Confined activation and subdiffractive localization enables whole-cell PALM with genetically expressed probes. Nat Methods *8*, 327–333.

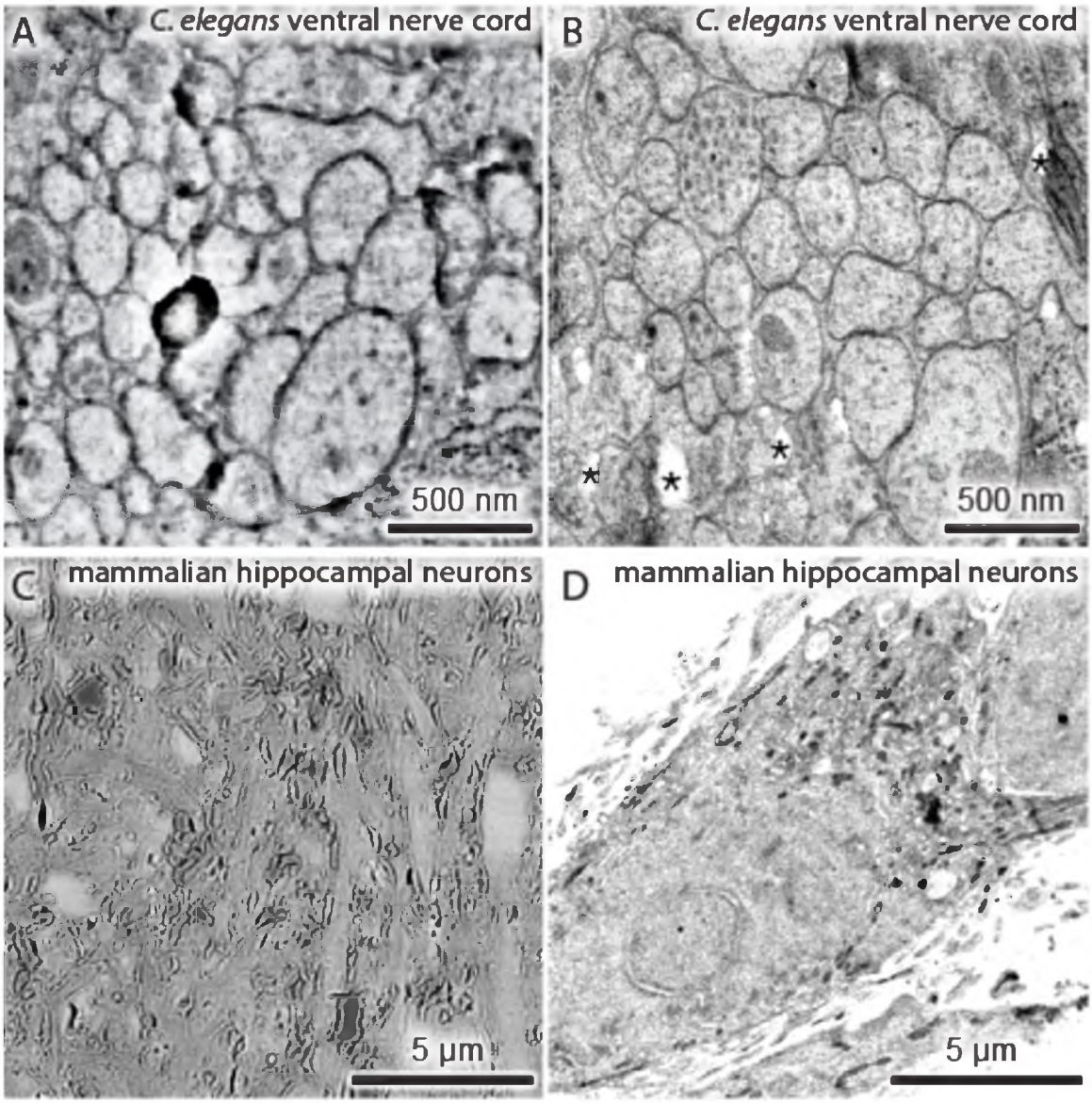

Fig. 6.1. Comparisons between SEM and TEM images. A nematode expressing a fluorescently labeled transgene was processed for nano-fEM, and the adjacent sections were imaged using SEM (A) and TEM (B). Mouse hippocampal neurons were labeled with Alexa-647 transferrin. Labeled transferrin binds transferrin receptors and is endocytosed. Cells were processed for nano-fEM and imaged using SEM (C) and TEM (D). The subcellular details are clearly visible in the TEM images. * indicates holes in a section created during sectioning due to incomplete infiltration or polymerization of the GMA resin. For the complete list of artifacts observed with GMA plastic, please refer to Watanabe and Jorgensen (2012).

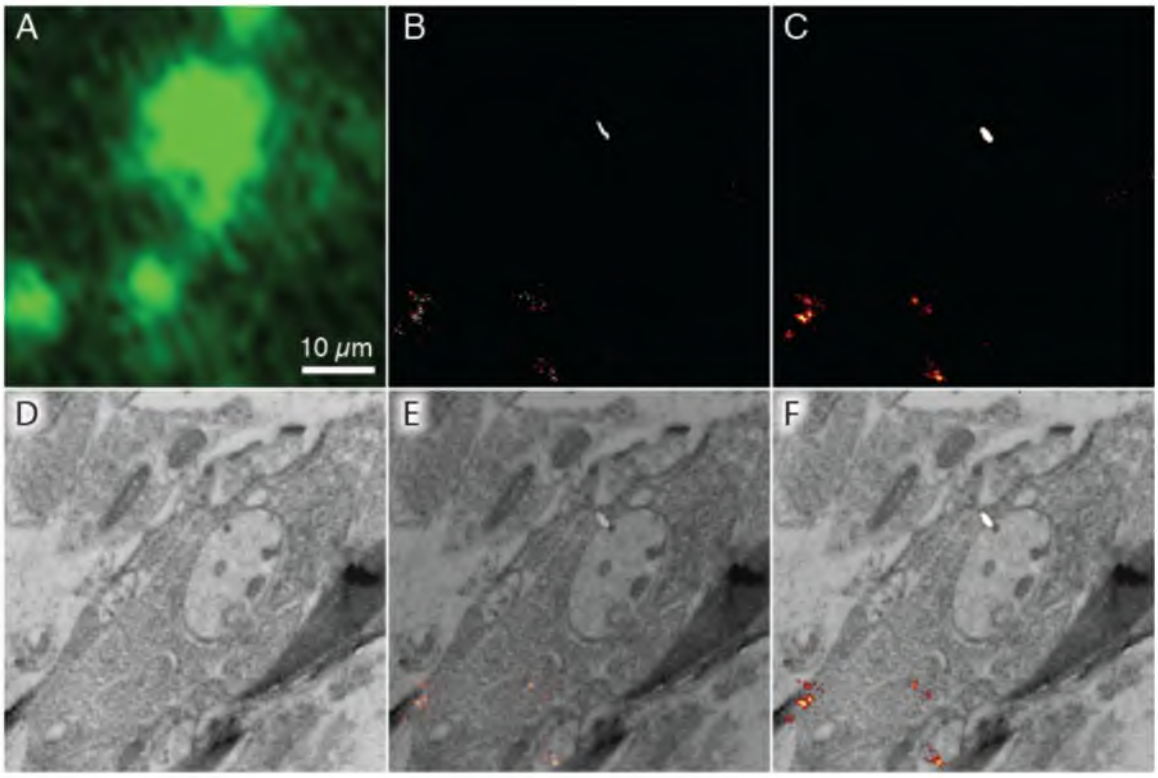

Fig. 6.2. dSTORM images of plastic sections of cultured mouse primary hippocampal cells with fluorescently labeled transferrin. Wide-field fluorescence image (A), dSTORM image without drift correction (B), dSTORM image with drift correction (C), TEM image (D) from the same GMA thin section (50 nm) of cell cultures incubated with Alexa647-labeled transferrin. The sample drift during imaging was corrected based on the positions of TetraSpeck beads in the first image of the acquired series. (E, F) Correlative dSTORM – TEM image showing transferrin localization. The transparency was applied to the whole STORM image in (E) whereas the transparency was applied only to the background black pixels in the STORM image in (F). Note that the STORM signal intensity is not compromised using a gradient transparency in (F). The section was incubated in imaging buffer containing oxygen scavengers and imaged using a fluorescence microscope equipped with an EMCCD camera and appropriate laser lines and filter sets. For the dSTORM image, a total of 10,000 frames (30ms/frame) were collected and processed using ImageJ with the quickPALM plugin (Henriques et al., 2010).

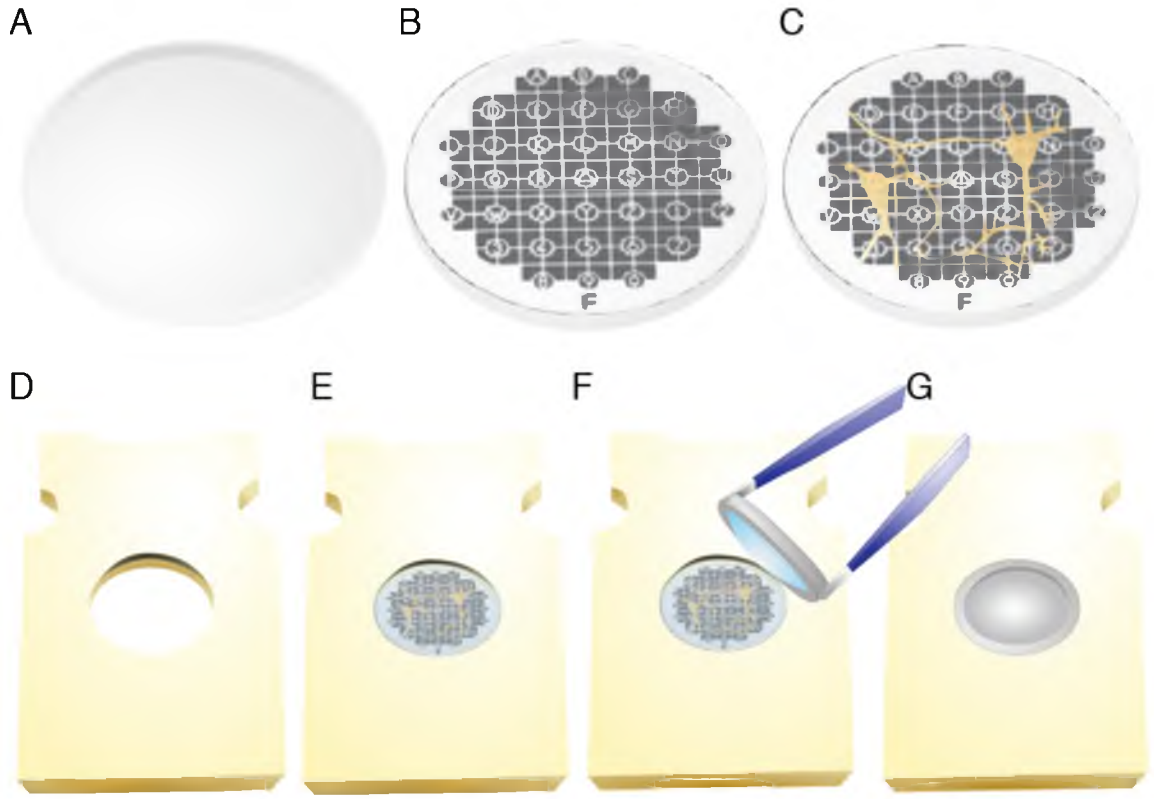

Fig. 6.3. Preparing cell cultures for high-pressure freezing. (A) 6-mm diameter sapphire disks are rinsed in ethanol before use. (B) A carbon-coated sapphire disk with a finder grid pattern. A finder grid was placed on top of a sapphire disk before carbon coating. (C) Mouse hippocampal neurons cultured on a coated sapphire disk after the treatment with poly-L-lysine. Cells can grow as well on sapphire disks as on a cover glass. (D) A middle plate for the HPM100 that can hold a sapphire disk. (E) A sapphire disk mounted directly in the plate. Note that the countersink holds the sapphire disk in place. (F) A type-A specimen carrier, over-filled with culture media, placed on top of the sapphire disk. Make sure there are no air bubbles trapped in the chamber of the specimen carrier. (G) A sample holder ready for freezing.

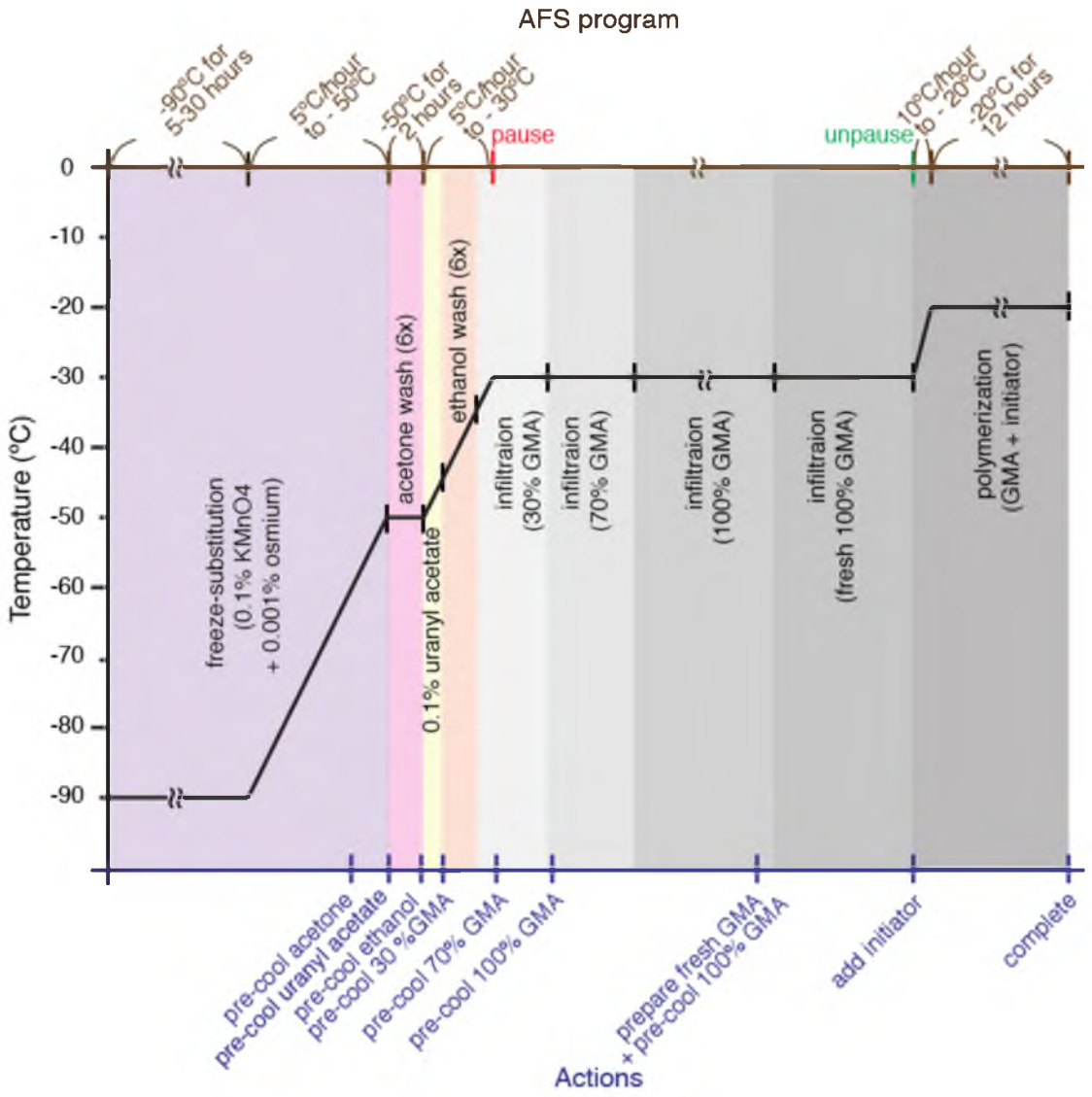

Fig. 6.4. An overview of freeze-substitution and plastic embedding incubations for the AFS program. The y-axis of the graph shows temperature. The black line in the graph indicates the temperature change through the freeze-substitution and plastic embedding procedures. The graph is shaded with colors to indicate different solutions used in the particular steps: purple, 0.1% KMnO4 + 0.001% osmium tetroxide + 5% water + anhydrous acetone; pink, 95% acetone; yellow, 0.1% uranyl acetate in 95% acetone; orange, 95% ethanol; and gray, GMA solutions. The brown-colored x-axis at the top shows how to program the AFS (-90ºC for 5-30 hours, 5ºC/hour to -50ºC, -50ºC for 2 hours, 5ºC/hour to -30ºC, pause/unpause at -30ºC, 10ºC/hour to -20ºC, and -20ºC for 12 hours). The blue-colored x-axis at the bottom indicates the actions one should take at a particular time point in the program.

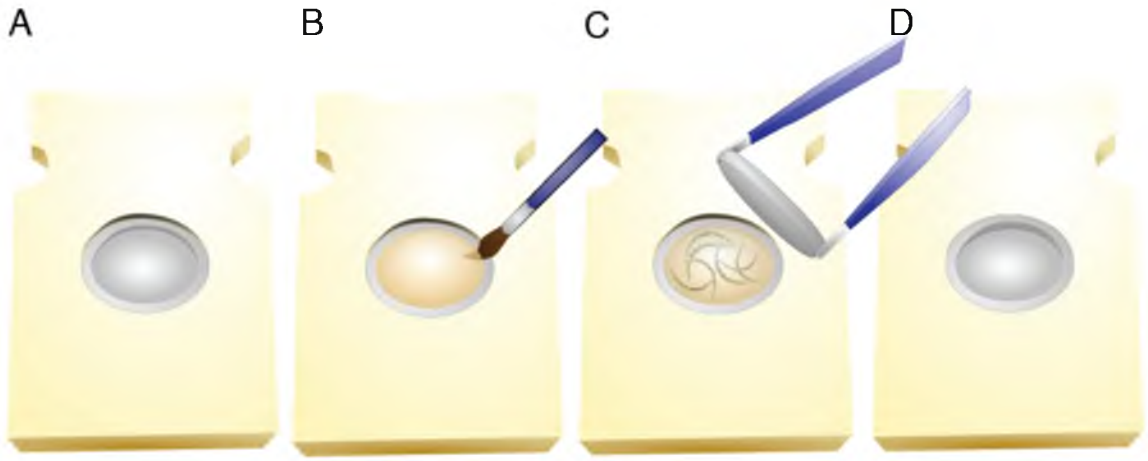

Fig. 6.5. Preparing *C. elegans* for high-pressure freezing. (A) A type-A specimen carrier (3 mm diameter) mounted in the middle plate for the HPM100 freezer with its 100 µm well facing up. (B) A 100 µm well of a specimen carrier filled with bacteria using a paint brush. Note that the well is slightly overfilled. (C) The specimen carrier capped with a flat side of a type-B specimen carrier after placing the worms in the well. (D) A sample holder ready for freezing.

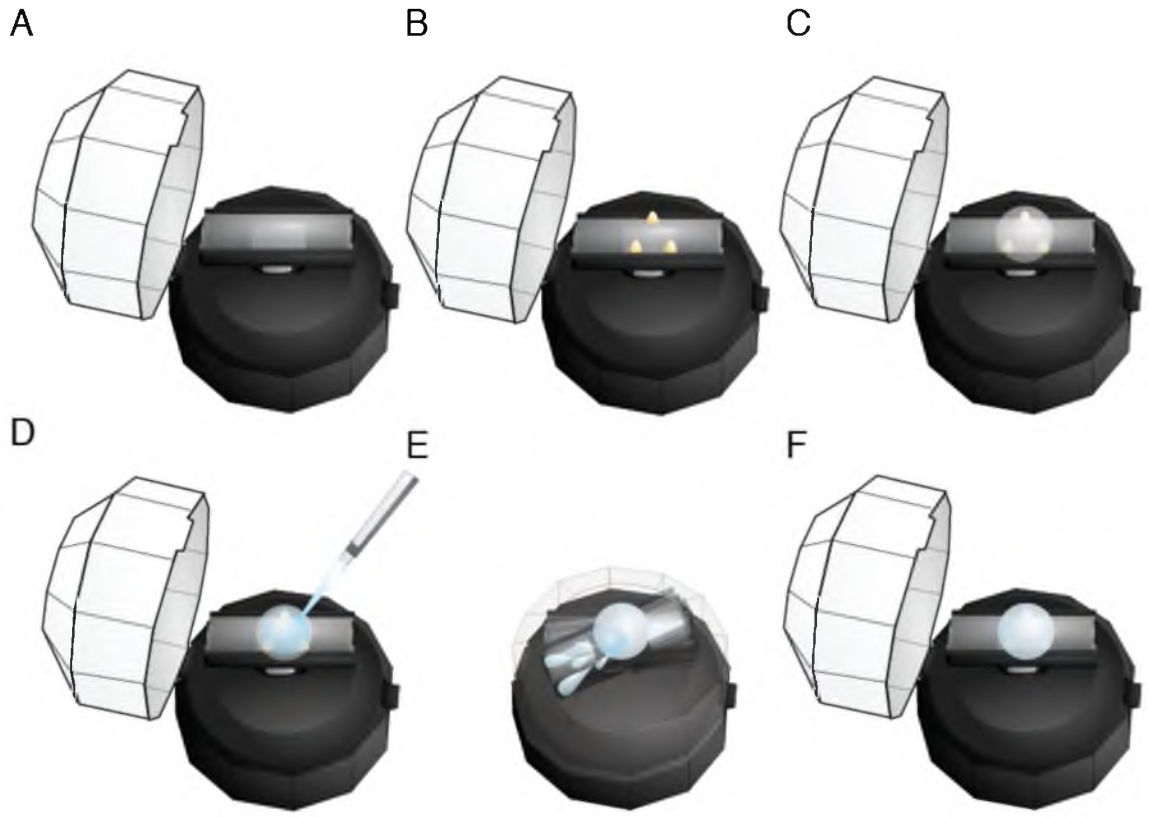

Fig. 6.6. Coating a cover glass with TEM-compatible film (Pioloform). (A) A microscope slide inserted into a desktop centrifuge. (B) Three wax cones placed on a cover glass to serve as a mount for the cover glass. Note that the wax cones are placed so that the center of the cover glass does not touch the wax. (C) A round cover glass placed on top of the wax cones. (D) 0.5% Pioloform solution (250 ml) applied on a coverslip. (E) Pioloform solution spun off by closing the lid immediately after the application of Pioloform solution. (F) A cover glass coated with a thin layer of Pioloform.

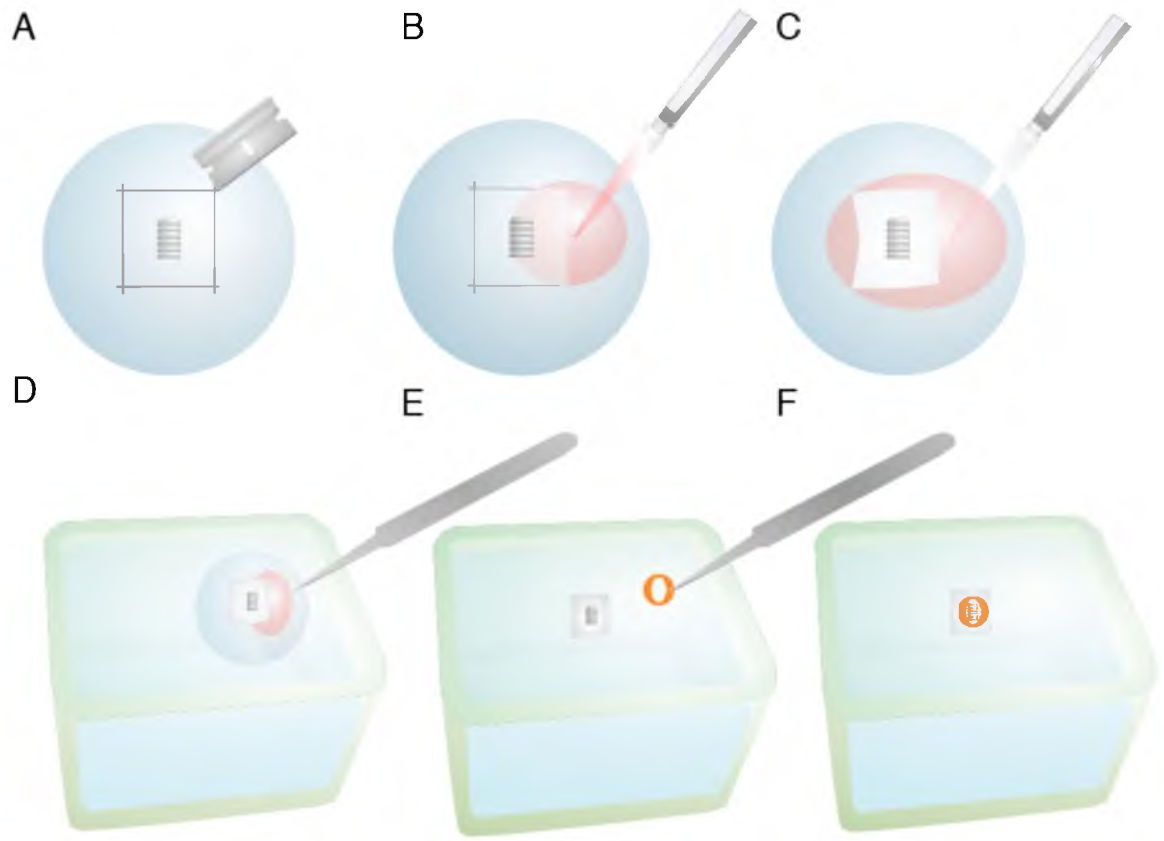

Fig. 6.7. Retrieving sections from a cover glass for TEM imaging. (A) A Pioloform film scored using a razor blade. The cuts should be made far from where the sections are located. (B) 1% hydrofluoric acid applied to the cover glass. Note that the solution is applied gently from the side of the cover glass. The glass will be etched slightly as soon as the solution is applied, causing the film to float onto the solution. (C) A film containing sections fully detached from the cover glass and floated on top of the solution. (D) A cover glass submerged into a water bath. (E) The film floating on top of the water surface. (F) A single slot grid placed on top of the film so that the sections appear inside the window of the grid.

CHAPTER 7

TWO MODES OF FAST ENDOCYTOSIS AT SYNAPSES

Summary

Synaptic vesicles can be released at neuromuscular junctions at extremely high rates, up to 100 Hz, which places an extraordinary demand on the recycling machinery. Classic studies by Heuser and Reese suggested that recovery of synaptic vesicles is via a clathrin-mediated mechanism and is slow. By contrast, studies from the Ceccarelli group suggested that synaptic vesicles simply reverse the fusion pore to rapidly regenerate a synaptic vesicle. Both of these studies were conducted in dissected preparations, and used intense stimulation to maximize the probability of capturing events in electron micrographs. Here, a single stimulus was applied to motor neurons in intact nematodes using channelrhodopsin, and the animals were rapidly frozen. We found that docked vesicles fuse along the face of a broad active zone, and are replenished with a time constant of about 2 s. Endocytosis takes place at two sites: at the dense projection and at adherens junctions. Endocytosis is ultrafast at the dense projection (<50 ms) and is fast at the adherens junction (<1 s). Dynamin is found at these sites, and endocytic structures are trapped at these sites in dynamin mutants. The mechanism is not consistent with kiss-and-run endocytosis because the sites of endocytosis and exocytosis do not coincide and

the amount of membrane invaginated is larger than a synaptic vesicle. Nor are the data consistent with clathrin-mediated endocytosis since endocytosis is rapid and the invaginations lack clathrin coats. Thus, endocytosis at *C. elegans* neuromuscular junctions is extremely fast and is unlikely to conform to current models for endocytosis.

Introduction

Synaptic transmission is quantal – postsynaptic responses have a uniform minimal size (Fatt and Katz, 1952). Katz hypothesized that fusion of synaptic vesicles with the plasma membrane accounted for the release of fixed amounts of neurotransmitter (del Castillo and Katz, 1956). To test the "vesicle hypothesis", frog motor neurons were stimulated and examined by electron microscopy (Ceccarelli et al., 1972, 1973; Heuser and Reese, 1973). Heuser and Reese found that vesicles fused and collapsed into the plasma membrane and thereby provided proof of the vesicle hypothesis (Heuser and Reese, 1981). Furthermore, Torri-Tarelli *et al*. demonstrated that the timing of vesicle fusion coincided precisely with that of transmitter release (Torri-Tarelli et al., 1985).

Ultrastructural studies further suggested that synaptic vesicles are recycled at synapses. Recycling was originally inferred from standard fixations based on the presence of coated vesicles on the plasma membrane (Heuser and Reese, 1973) and the uptake of peroxidase after stimulation (Ceccarelli et al., 1972). Heuser and Reese improved the temporal resolution of their analysis by building a 'freeze slammer' capable of instantaneously freezing a sample at

arbitrary time points after stimulation (Heuser et al., 1979). Invaginations were most abundant 30 s after stimulation and were observed in membrane domains lateral to the active zone in freeze fracture studies (Miller and Heuser, 1984). Based on the presence of coated pits in traditional fixations (Heuser and Reese, 1973), it was proposed that recycling of synaptic vesicles was mediated via the clathrin coat protein that had been recently described (Pearse, 1976).

Since the publication of the morphological data, both biochemical and functional experiments support a model in which synaptic vesicles are recycled via a clathrin-mediated mechanism (Dittman and Ryan, 2009). Reconstitution experiments demonstrate that clathrin and its adaptors are sufficient for budding membranes prepared from brain (Takei et al., 1998). Purification of vesicles from brain demonstrated that synaptic vesicle proteins (and not just membrane) are found in clathrin-coated vesicles (Maycox et al., 1992). Moreover, in the absence of functional dynamin, clathrin-coated pits accumulate at terminals (Koenig and Ikeda, 1989; Shupliakov et al., 1997). Disruption of clathrin function by peptide injections, siRNA application, or photoinactivation all slow the rate of endocytosis (Jockusch et al., 2005; Granseth et al., 2006; Heerssen et al., 2008; Kasprowicz et al., 2008). Moreover, synaptic vesicle proteins tagged with pHluorin are recovered with a time course similar to the recovery of membrane observed in morphological experiments (Granseth et al., 2006; Balaji and Ryan, 2007).

Clathrin-mediated endocytosis, however, may not constitute the sole pathway for synaptic vesicle endocytosis. The prodigious speed of exocytosis at some synapses may exceed the rate of clathrin-mediated endocytosis. For

example, during locomotion, lumbar motor neurons in the mouse can fire at ~100 Hz (Maeno-Hikichi et al., 2011). Moreover, in some central synapses such as the Calyx of Held, firing rates can reach up to 500 Hz (Kopp-Scheinpflug et al., 2008; Lorteije et al., 2009). Calculations suggest that at the Calyx of Held each vesicle is reused every 13 s, assuming that all the vesicles in the terminal are mobile (Neher, 2010). This rate of reuse is faster than the 15 to 20 s required to recover vesicles by clathrin-mediated endocytosis at synapses (Miller and Heuser, 1984; Cocucci et al., 2012), and would overwhelm the capacity to recycle vesicles. Furthermore, experiments using FM dyes suggest that only 5-20% of vesicles in the terminal are cycling during physiological activity (Harata et al., 2001; Rizzoli and Betz, 2005). Therefore, even fewer vesicles may be available to sustain high release rates, placing an even greater demand on the endocytic machinery (de Lange et al., 2003; Yamashita et al., 2005).

An alternative mechanism for synaptic vesicle endocytosis, now called 'kiss-and-run' (Fesce et al., 1994), was proposed by Bruno Ceccarelli based on experiments nearly identical to those of Heuser and Reese. When frog neuromuscular junctions were stimulated at low frequency, vesicles with fusion pores lacking clathrin coats were observed in the active zone (Ceccarelli et al., 1972). The fusion pores are unstable, lasting about 1 s (Wu and Wu, 2009; Zhang et al., 2009). Some experiments using optical tracers including FM dyes, pH-sensitive fluorescent proteins, and quantum dots support a fast pathway (Richards et al., 2000; Aravanis et al., 2003; Harata et al., 2006; Zhang et al., 2007b, 2009; Zhu et al., 2009; Park et al., 2012). This has led to a model in

which exocytosis and endocytosis are coupled via a transient fusion pore. The key aspects of kiss-and-run endocytosis is that first, the vesicles are recycled at the site of release in the active zone; second, they are recovered quickly (in less than 1 s), and third, the vesicles remain intact and retain their protein and membrane complement, rather than fully collapsing into the membrane.

Another clathrin-independent mechanism that may contribute to vesicle recycling is bulk endocytosis (Smith et al., 2008; Cousin, 2009). Under repetitive, intense stimulation, the increase in membrane surface area causes the plasma membrane to invaginate into the cell. These large invaginations are pinched off by dynamin, and synaptic vesicles are then regenerated at endosomes (Miller and Heuser, 1984; Cousin, 2009). Such large invaginations of membrane have been observed following intense stimulation in the active zone of frog neuromuscular junctions (Miller and Heuser, 1984; Richards et al., 2000; Gaffield et al., 2011), retinal bipolar cells (Holt et al., 2003), and mammalian central synapses (Clayton et al., 2010).

Ultrastructural analysis of stimulated neurons has provided the basis for models of synaptic vesicle endocytosis. However, in each of these studies, non-physiological or intense sustained stimulation was used in dissected preparations to trigger cycling of synaptic vesicles. For example, in studies of cross sections, Heuser and Reese applied stimulation at 10 Hz for 1 min (1973), and Ceccarelli employed 2 Hz stimulation for 2 hours (1972). For freeze-fracture studies, Heuser and Miller delivered a single stimulus in the presence of 4-aminopyridine and 10 mM calcium; these images provide the best temporal analysis of

endocytosis but the nature of the invaginations was not examined in cross sections. Here, we stimulated motor neurons in vivo with a single activation pulse by using the light-sensitive ion channel ChIEF (Lin et al., 2009). Samples were rapidly frozen using a high-pressure freezer, and the ultrastructure was examined using transmission electron microscopy. We found that endocytosis occurs rapidly at two sites, adjacent to the dense projection at the center of the synapse and at adherens junctions flanking the synapse. These two regions represent the edges of the active zone, and endocytosis is complete within 50 ms and 1.4 s, respectively, after stimulation.

Results

Stimulation of neurons at millisecond temporal resolution

Capturing membrane dynamics in an intact organism requires rapid freezing of tissue. Heuser and Reese used a freeze-slammer to capture membrane dynamics after synchronous neurotransmitter release (1979 and 1981). However, freeze-slamming cannot preserve morphology deeper than 10 mm from the cell surface without ice crystal damage, whereas the diameter of an adult worm is about 70 mm. We employed high-pressure freezing because it can freeze a sample as thick as 200 μm within 25 ms with reduced ice crystal formation (Moor and Riehle, 1968; Moor, 1987).

The second requirement for an ultrastructural analysis of vesicle dynamics is that the synapse must be stimulated at a precise time relative to freezing. Previously, we demonstrated that channelrhodopsin-2 and halorhodopsin (Nagel

et al., 2003; Zhang et al., 2007a) can be expressed in *C. elegans* motor neurons to stimulate or inhibit neurotransmission with pulses of light (Liu et al., 2009). Here, we expressed ChIEF, a variant of channelrhodopsin that is less prone to desensitization (Lin et al., 2009), to depolarize the acetylcholine motor neurons to stimulate exocytosis (Fig. 7.1A), and expressed halorhodopsin to hyperpolarize these motor neurons and thus inhibit exocytosis at neuromuscular junctions (Fig. 7.1B).

Finally, we created a light path to the specimen by drilling a hole through the bayonet specimen holder for the Leica EMpact2 high-pressure freezer and replacing the black diamond anvil with a transparent sapphire anvil. We mounted a 3 mm LED at the tip of the bayonet (Fig. 7.1C); the measured light intensity at the sample was ~20 mW/mm^2. We constructed a programmable circuit with a temporal resolution of ~5 ms or less. The minimal interval between stimulation and freezing was ~20 ms due to the mechanics of the freezing device (see **Experimental Procedures**). The motor neurons were hyperpolarized or depolarized by a light pulse and rapidly frozen under high pressure at fixed time points.

Tonic release takes place adjacent to the dense projection

The site of vesicle fusion is defined as the active zone (Couteaux and Pécot-Dechavassine, 1974; Landis, 1988). In order to examine the spatial relationship between exocytosis and endocytosis , we first determined the extent of the active zone at neuromuscular junctions in *C. elegans*. Nematode

neuromuscular junctions can exhibit two modes of neurotransmitter release: tonic and evoked. The high rate of tonic release in nematodes depends on a weakly polarized resting potential and voltage-gated calcium channels (Richmond et al., 1999; Liu et al., 2009). This high rate of tonic release can be blocked by hyperpolarization of membrane, and thus vesicles are expected to accumulate at release sites after activating halorhodopsin, a light-activated chloride pump (Zhang et al., 2007a). After light-induced hyperpolarization, the number of docked vesicles increased (Fig. 7.2A, C, D, and E; more example micrographs can be found in Fig. 7.S1). The number of tethered vesicles only increased slightly (Fig. 7.2B, F). The spatial distribution of the increase in docking was not uniform - docked vesicles accumulated adjacent to the dense projection ('0 nm pool'; Fig. 7.2G). We observed a significant increase in docked vesicles up to 100 nm from the dense projection (nonstimulated 9.3 ± 0.4; stimulated 13 ± 0.4; $p<0.0001$) (Fig. 7.2G), suggesting that the release site for tonic neurotransmission is near the dense projection.

Only docked vesicles are released by depolarization

Evoked release, by contrast, draws upon vesicles broadly distributed along the active zone. We applied a single pulse of blue light to animals expressing ChIEF in acetylcholine motor neurons while recording currents from the postsynaptic muscle cell. The amplitude of evoked responses triggered by ChIEF was similar to electrically stimulated responses, suggesting that ChIEF activation can cause the simultaneous fusion of about 100 synaptic vesicles per

muscle cell or approximately 4-10 synaptic vesicles per synapse (Fig. 7.1A). We froze animals 20 ms after stimulation and observed vesicles fusing with the plasma membrane (Fig. 7.3A-E); the diameter of these vesicles was 28.4 nm ± 0.3, the same size as a synaptic vesicle. The exocytic intermediates had a wide opening at their neck, suggesting that vesicles fully collapse to the membrane. The number of docked vesicles was reduced after the stimulus (Fig. 7.3F), whereas the number of tethered vesicles remained the same (Fig. 7.3G). These data suggest that the docked, but not tethered, vesicles fuse in response to depolarization and thus constitute the readily releasable pool (Zenisek et al., 2000).

Vesicles fuse across a broad surface of the synapse during evoked release

Fusing vesicles were found along the entire face of the synapse between the dense projection and the flanking cell junctions and thus defines a broad active zone for the *C. elegans* neuromuscular junction (Fig. 7.3B and H). On average, approximately four fusion intermediates were observed in profiles containing a dense projection; although this could be an underestimate given that neurotransmission is declining at this time point (Fig. 7.1A).

To estimate the total number of vesicle fusions per synapse, we froze animals 50 ms after stimulation when neurotransmission is complete (Fig. 7.4A and B). Fusion intermediates were no longer observed 50 ms after stimulation; however, docked vesicles were depleted from the terminals (Fig. 7.4A-E; more micrographs in Fig. 7.S2A and C). These results suggest that the vesicles had

fully collapsed at 50 ms but that the release sites had not been refilled. Therefore, we were able to estimate the total number of vesicle fusions by comparing docked vesicles before and after stimulation. In unstimulated neurons, there were about 11 docked vesicles in the active zone lateral to the dense projection. A single stimulus caused the release of about four to six vesicles from profiles containing a dense projection, or about one third of the docked vesicles in these sections. These synapse reconstructions are only partial. From full end-to-end reconstructions of synapses, we previously counted a mean of 34 docked vesicles per synapse (Hammarlund et al., 2007). Thus, a single neuromuscular junction may release up to 12-18 vesicles per stimulus, in agreement with the reconstruction at 20 ms (Fig. 7.3B).

To determine the location of release sites, we analyzed the distribution of docked vesicles along the plasma membrane relative to the presynaptic dense projection. Following a single 20 ms stimulus, docked vesicles were depleted along the entire face of the synapse (Fig. 7.4E). Some vesicles are docked in the perisynaptic zone beyond the adherens junctions at the far edge of the synapse, sometimes called “ectopic docking” (Zenisek et al., 2000; Lenzi et al., 2002; Matsui and Jahr, 2003; Hammarlund et al., 2007). These perisynaptic vesicles are not released after a stimulus (Fig. 7.4F). Together, these results suggest that the active zone extends on either side of the dense projection to the flanking cell-cell junctions (Fig. 7.4G).

Refilling the docked pool

If the pool of docked vesicles solely constitutes the readily-releasable pool, then the morphologically defined docked pool should be restored in parallel with the electrophysiologically defined readily-releasable pool. To determine the refilling rate of the readily releasable pool, we characterized paired-pulse depression at acetylcholine neuromuscular junctions. We applied two 10 ms light pulses to neuromuscular junctions of transgenic animals (*acr-16(ok789)*; P*unc-17::ChIEF::mCherry*) while patch-clamping a body wall muscle. Nicotine-sensitive acetylcholine receptors (encoded by *acr-16*) desensitize rapidly, so the paired-pulse recordings were performed in animals lacking nicotine-sensitive but retaining the levamisole-sensitive acetylcholine receptors. By varying the time of the application of the second pulse, the recovery rate from synaptic depression was measured (Fig. 7.5A). The time constant (τ) for the slow phase of recovery was 2.2 s, and required about 6 s for full recovery (Fig. 7.5B).

To determine the time course for the recovery of docking, we characterized the ultrastructure of synapses after single stimuli (Fig. 7.5C-F and Fig. 7.S2). Acetylcholine motor neurons were depolarized with a single light pulse, allowed to recover for 20 ms, 50 ms, 100 ms, 300 ms, 1 s, 3 s, and 10 s, and then frozen (Fig. 7.S2A-H). The number of docked vesicles was reduced from 3 to 1 immediately after the stimulus (20 ms-300 ms: Fig. 7.5D). Docked vesicles were not depleted in transgenic worms without trans-retinal (the second column in Fig. 7.5D and E), suggesting that the depletion of vesicles depended on the activation of channelrhodopsin. Docked vesicles in active zones recovered

with a time constant of 2.4 s (Fig. 7.5C), which corresponds well to the rate of electrophysiological recovery. The total number of vesicles, as well as tethered vesicles, decreased slightly after stimulation but recovered by 300 ms (Fig. 7.5E and F) and can be accounted for by the number of vesicles lost through fusion. This fluctuation may indicate that vesicles pass through a docking intermediate (Zenisek et al., 2000). Together, these results suggest that the docked vesicles are likely the morphological correlate of the readily releasable pool.

Invaginations adjacent to the dense projection 20 ms after stimulation

Following exocytosis, synaptic vesicle proteins and membranes need to be recycled locally at synapses. Kiss-and-run endocytosis does not require vesicles to collapse into the membrane, but instead the fusion pore reverses rapidly (within 1 s) to regenerate the vesicle. Clathrin-mediated endocytosis is thought to take place lateral to the active zone, by the relatively slow (~20 s) recruitment of clathrin machinery (Rizzoli and Jahn, 2007; Dittman and Ryan, 2009). Images from three different animals frozen at each time point were scored for endocytic structures blind (Fig. 7.6). At 20 ms after stimulation, about 50% of the synapses showed large (>35 nm) invaginations or vesicles next to the dense projection (Fig. 7.6D-H, and Fig. 7.S3). At least one large vesicle was found in each synapse at 50 ms, localized within ~100 nm of dense projection (Fig. 7.6B and C for quantification; Fig. 7.6E and F for representative micrographs; more examples in Fig. 7.S3E-H). These large vesicles near dense projections only appeared after stimulation (Fig. 7.6B), suggesting that the formation of large

vesicles was triggered by exocytosis. The average diameter of invaginations and large vesicles (42.8 nm) was significantly larger than synaptic vesicles (29.3 nm; p <0.0001) or vesicles captured in the act of fusing (28.4 nm; p <0.0001; Fig. 7.6A) and was bimodally distributed (Fig. 7.6I).

To test if endocytosis at the dense projection is triggered by exocytosis and not by calcium influx alone (Yamashita et al., 2005), we stimulated synapses in *unc-13(s69)* mutants (Figure S4). Exocytosis is almost completely absent in *unc-13* mutants (Richmond et al., 1999), presumably due to the lack of docked vesicles (Hammarlund et al., 2007). Therefore, the stimulation of the neuron in an *unc-13* mutant should cause an influx of calcium without the addition of membrane to the surface. There was no increase in the number of large vesicles next to the dense projection after stimulation (Fig. 7.6B), although occasionally a large vesicle was observed in unstimulated *unc-13* mutants. Thus, the formation of large vesicles at the dense projection requires exocytosis of synaptic vesicles.

Membrane invaginations at adherens junctions 300 ms after stimulation

After about 100 ms, invaginations appeared at the flanking adherens junctions (Fig. 7.7A, E, and G; more example micrographs in Fig. 7.S5A-C). At later time points, deeper invaginations (Fig. 7.7B; more example micrographs in Fig. 7.S5D-F) and large vesicles (Fig. 7.7C) were also observed at adherens junctions, suggesting that the shallow pits are likely endocytic intermediates. These invaginations lacked obvious clathrin coats, although clathrin-coated vesicles can be observed using this sample preparation (Fig. 7.7D and Fig.

7.S5G). The mean diameter of the deeper pits, as well as the large vesicles, was 44 nm, the equivalent of 2.3 synaptic vesicles (Fig. 7.S5H). The prevalence of shallow pits peaks at 300 ms (Fig. 7.7E) and decays exponentially with a time constant of 1.4 s (Fig. 7.7F). Large vesicles associated with the adherens junction (within 50 nm) peak at 3 s and decline, suggesting that shallow pits are precursors to large vesicles. After 10 s, the number of large vesicles declines to background levels, but vesicles in the center of the terminal peak at this time (dashed line in Fig. 7.7E), suggesting that the vesicles were transported to the center of the terminal. Endocytic pits did not appear in animals lacking trans-retinal or in *unc-13(s69)* mutants (Fig. 7.7F), thus the formation of shallow pits was triggered by the exocytosis of synaptic vesicles. Together, these results suggest that a second endocytosis pathway takes place at adherens junctions.

Dynamin is required for fast endocytosis

These two endocytic sites are associated with dynamin, a GTPase required for membrane scission. We generated transgenic animals expressing tagged dynamin in a dynamin null background (*dyn-1(ox447);* P*dyn-1::DYN-1::tdEos*). Tagged dynamin was imaged using nano-resolution fluorescence electron microscopy (nano-fEM) (Watanabe et al., 2011; Watanabe and Jorgensen, 2012). Clusters of tagged dynamin are observed at dense projections and adherens junctions (Fig. 7.8A-B; more examples in Fig. 7.S6), and there is an 8-10-fold increase in the density of dynamin at dense projections and adherens junctions compared with other regions of the synapse (Fig. 7.8C-D).

Dynamin is also required to resolve invaginations at these sites into vesicles. *dyn-1(ky51)* is a temperature-sensitive allele which is not functional at 30ºC (Clark et al., 1997). Worms were moved from the permissive temperature at 15°C to 30°C for 2 min and then frozen. Large vesicles were only observed adjacent to the dense projection and adherens junctions (Fig. 7.8E-G; more example micrographs Fig. 7.S7). These vesicles were often associated with a filament to the dense projection or membrane. Although necks were difficult to discern, prolonged incubation at the restrictive temperature (5 min) revealed the presence of membrane necks attached to the plasma membrane (Fig. 7.S7C). These data suggest that endocytosis takes place adjacent to the dense projection and the adherens junctions; these are locations close to, but not coincident with, the release sites.

Membrane retrieval is complete within 10 s after a single stimulus

Does fast endocytosis account for the number of vesicles that fuse during neurotransmission? We calculated the total amount of membrane exocytosed and endocytosed at 300 ms and 1 s after stimulation in our profiles (see **Experimental Procedures**). We estimate that a total of 88-132 synaptic vesicles fused to the plasma membrane for all 22 synapses analyzed at the 300 ms time point and a total of 111 synaptic vesicles were recycled. For the 1 s time point, a total of 92-138 synaptic vesicles were estimated to exocytose, and membrane area equivalent to roughly 144 synaptic vesicles was recovered. These data suggest that most vesicles that fuse during exocytosis are retrieved rapidly after

exocytosis; 43% are recovered at dense projections with a time constant of less than 50 ms and 57% are recovered at adherens junctions with a time constant for pit resolution of 1.4 s (Fig. 7.7F).

Discussion

Two models for synaptic vesicle endocytosis have emerged from studies of ultrastructure: clathrin-mediated endocytosis and kiss-and-run endocytosis. Clathrin-mediated endocytosis predicts that vesicles collapse into the membrane and are recovered slowly at a specialized site lateral to the active zone. Kiss-and-run predicts that vesicles fuse briefly to the membrane and are recovered at the site of release. A long-standing criticism of these morphological studies has been that they did not employ single physiological stimuli, but rather relied on either high-frequency stimulation or pharmacological methods to increase exocytosis. A brief review is warranted: Heuser and Reese (1973) stimulated neuromuscular junctions at 10 Hz for 1 min and then fixed the sample on ice. After this intense stimulation, vesicles were depleted and invaginations with distinct clathrin coats appeared on the plasma membrane. Miller and Heuser (1984) stimulated the nerve with a single stimulus in the presence of the K^+ channel blocker 4-aminopyridine and 10 mM calcium and froze the sample rapidly using a freeze-slammer. 20 s after this single stimulus, pits formed at the lateral edges of the active zone. Because these were freeze-fracture studies, the presence of clathrin coats could not be ascertained. However, because clathrin

coats had been observed in the 1973 study, they concluded that synaptic vesicle endocytosis is most likely mediated by clathrin.

Ceccarelli and colleagues (1972) stimulated at 2 Hz for 2 hours and fixed using glutaraldehyde on ice. Membrane invaginations with various neck sizes were observed: wide, narrow, and almost invisible. Horseradish peroxidase (Ceccarelli et al., 1972) and dextran (Ceccarelli et al., 1973) were taken up into these invaginations, suggesting that endocytosis takes place in the active zone. Given the presence of invaginations with a narrow neck, they speculated that exocytosis and endocytosis are coupled via the fusion pore. To support these conclusions with high temporal resolution images, they applied a single stimulus in the presence of 4-aminopyridine and 10 mM calcium and preserved structure using a freeze slammer (Torri-Tarelli et al., 1985). They did not observe an accumulation of exocytic figures from 2.5 ms to 10 ms as they expected based on the Heuser and Reese experiment, and concluded that vesicle fusion pores were reversing before collapse of the vesicles into the membrane (Torri-Tarelli et al., 1985).

These studies were performed in dissected preparations and K^+ channels were blocked to maximize the exocytosis. Here, we developed a method to visualize the ultrastructure of endocytosis after a single stimulus in an intact *C. elegans* nervous system. We found that synaptic vesicle exocytosis takes place along the entire membrane from the dense projection to the adherens junction. By contrast, endocytosis takes place at the edges of the active zone, either directly adjacent to the dense projection or laterally at the adherens junction.

Endocytosis adjacent to the dense projection is completed 50 ms after a stimulus, and endocytosis at the adherens junction is completed at about 3 s. Both of these events are rapid, and do not fully support either kiss-and-run or clathrin-mediated mechanisms.

Which vesicles are released?

A fraction of the vesicles, known as the readily releasable pool, can be stimulated to fuse by a single action potential (Rosenmund and Stevens, 1996; Schweizer and Ryan, 2006). Previously, live cell imaging of retinal bipolar cells using FM-dye and TIRF microscopy demonstrated that the vesicles in the evanescent field (within ~100 nm of the surface) fuse upon electrical stimulation (Zenisek et al., 2000). Our data in *C. elegans* suggest that vesicles that are in contact with the membrane ("docked") fuse with the plasma membrane. However, vesicles within 30nm of the membrane ("tethered") and those docked at "ectopic" sites in the perisynaptic zone on the distal side of the synapse do not fuse in response to a stimulus.

Physiological recordings from *C. elegans* reinforce the notion that docked vesicles comprise the readily releasable pool. Physiological recovery of the releasable vesicles occurs with a time constant of 2.2 s, and morphological recovery of docked vesicles occurs with a time constant of 2.4 s. These values are very similar to the refilling times of the release-ready vesicles at photoreceptors (~2 s; Zenisek et al., 2000) and are also comparable to the

physiological recovery of 4.3 s at synapses in cultured hippocampal cells (Pyott and Rosenmund, 2002).

Where are vesicles released?

The active zone is defined as the site of synaptic vesicle exocytosis at a synapse (Couteaux and Pécot-Dechavassine, 1974). This definition requires an ultrastructural characterization of synapses during stimulation. At frog neuromuscular junctions, the active zone is adjacent to the dense projection (Heuser et al., 1979; Szule et al., 2012). Similarly in *C. elegans,* vesicles fuse adjacent to the dense projection, in particular during tonic neurotransmission in the absence of external stimuli. Voltage-gated calcium channels are associated with the dense projection (Kittel et al., 2006; Gracheva et al., 2008), and it is likely that brief calcium channel openings lead to tonic vesicle fusions. By contrast, evoked stimuli in *C. elegans* cause the exocytosis of vesicles along the entire active zone, from the dense projection to the adherens junction. Thus, a more sustained opening of calcium channels causes an elevation of calcium across the entire active zone.

Are pits endocytic intermediates?

We observed shallow pits appearing next to dense projections and adherens junctions immediately following a stimulus. These pits are likely endocytic intermediates for three reasons: First, the pits are larger than the fusing vesicles (Fig. 7.6A). Second, the formation of pits is followed by the

appearance of large vesicles at these sites suggesting a precursor-product relationship. Third, endocytic structures at these sites are stabilized in temperature-sensitive dynamin mutants. This result is similar to a previous finding in the *Drosophila* retina: trapped endocytic structures were observed adjacent to the dense projection and at lateral sites in dynamin mutants (Koenig and Ikeda, 1996). Moreover, dynamin localizes to these sites, suggesting that dense projections and adherens junctions are normal sites for endocytosis in *C. elegans* neuromuscular junctions.

How fast is endocytosis?

Endocytosis at the dense projection occurs very rapidly. Endocytic pits adjacent to the dense projection appear at 20 ms and these have resolved into large endocytic structures in less than 50 ms. This rate is extremely fast compared to measures of kiss-and-run endocytosis (~1 s; Wu and Wu, 2007; Zhang et al., 2009)) and clathrin-mediated endocytosis (15-20 s; Miller and Heuser, 1984; Jockusch et al., 2005; Balaji and Ryan, 2007).

At the adherens junction endocytosis is not as fast as at the dense projection but is still fast. Shallow pits peak at 300 ms and most are resolved by 3 s. However, the presence of some pits even 10 s after stimulation suggests that a slower mechanism is at work here. The time constant for clathrin-mediated endocytosis is reported to be ~15-20 s (Miller and Heuser, 1984; Granseth et al., 2006; Balaji and Ryan, 2007), which is in the range of the events we observe adjacent to the adherens junction. This speed for endocytosis is still extremely

fast given the slow speed of clathrin assembly (Kirchhausen, 2009; Cocucci et al., 2012). It is possible that clathrin-mediated endocytosis at synapses is accelerated, possibly due to pre-formed clathrin cages at endocytic sites (Wienisch and Klingauf, 2006).

Clathrin-mediated or kiss-and run?

The distinguishing feature of clathrin-mediated endocytosis is that clathrin coats can be observed by electron microscopy. Coats are preserved when neurons are fixed with glutaraldehyde (Heuser and Reese, 1973; Koenig and Ikeda, 1989; Takei et al., 1998), and coated vesicles are preserved in the conditions used here. The absence of coats on endocytic pits is consistent with the absence of a genetic requirement for clathrin heavy chain at *C. elegans* neuromuscular junctions (Sato et al., 2009). However, these results do not exclude the possibility that clathrin is required at synapses after repetitive stimulation or that it acts later to regenerate synaptic vesicles from endosomes. In fact, synaptic vesicles are smaller in the temperature-sensitive allele of clathrin (Sato et al., 2009), suggesting that vesicles may pass through a clathrin-coated intermediate.

Kiss-and-run endocytosis is thought to occur within about 1 s of stimulation (Miller and Heuser, 1984; Wu and Wu, 2007; Zhang et al., 2009). The appearance of endocytic structures within 50 ms after stimulation at the *C. elegans* neuromuscular junction is consistent with kiss-and-run endocytosis. However, there are two morphological features that suggest kiss-and-run is

unlikely to account for endocytosis after stimulation at the *C. elegans* neuromuscular junction: position and size. Kiss-and-run is predicted to occur at the site of exocytosis: the vesicle forms a fusion pore, which reverses itself to regenerate an empty vesicle. All exocytic intermediates captured at 20 ms after stimulation at the *C. elegans* neuromuscular junction have wide necks, suggesting that synaptic vesicles are collapsing into the membrane. Moreover, vesicles fuse throughout the active zone, but endocytosis takes place at the edges of the active zone; thus, at least some membrane must translocate to endocytic sites.

The size of the endocytic structures also does not fit a classical model for kiss-and-run endocytosis. The kiss-and-run model predicts that synaptic vesicles retain their integrity, that is, the vesicle is recovered intact (Murthy and Stevens, 1998). Thus, endocytic vesicles should be 30 nm in diameter. In fact, some of the vesicles recovered at dense projections were only slightly larger than a single vesicle. However, about 30% of the endocytic structures adjacent to the dense projection are greater than twice the size of a synaptic vesicle. Moreover, the arrested endocytic structures in the dynamin mutants became even larger with prolonged synaptic activity. These enlarged endocytic structures suggest that vesicles collapse into the plasma membrane and are retrieved via a large endocytic structure.

Bulk endocytosis?

Bulk endocytosis is a compensatory membrane retrieval mechanism caused after high frequency stimulation or synaptic fatigue. When synapses are subjected to exhaustive stimulation, large membrane invaginations with no clathrin coats are observed in the active zone of frog neuromuscular junctions (Miller and Heuser, 1984), retinal bipolar cells (Holt et al., 2003), and mammalian central synapses (Clayton et al., 2010). These invaginations are severed from the surface by dynamin (Clayton et al., 2010). Synaptic vesicles are then regenerated from an endosomal-like compartment (Heuser and Reese, 1973; de Hoop et al., 1994; Voglmaier et al., 2006; Cousin, 2009; Hoopmann et al., 2010). This mechanism is thought to take place under conditions of intense stimulation when active mechanisms cannot keep up with the high rates of exocytosis (Holt et al., 2003; Cousin, 2009; Dittman and Ryan, 2009). The rapid endocytosis observed at the *C. elegans* neuromuscular junction shares features with bulk endocytosis: large endocytic invaginations are formed from the plasma membrane and these structures are resolved by dynamin but lack clathrin coats. Although the ultrafast endocytosis described here occurs after single stimuli rather than after fatigue, it is possible that the mechanisms for bulk endocytosis and ultrafast endocytosis are similar. It is possible that ultrafast endocytosis might require optogenetic methods to be observed: endocytosis is assayed in this preparation in an undissected animal. Neurons in intact nervous systems are bundled together, thereby imposing spatial constraints on the synapse and may promote membrane invagination. Thus, in intact nervous systems

compensatory mechanisms may accelerate synaptic vesicle endocytosis even during moderate activity.

Experimental Procedures

Strains

N2 Bristol was used as the wild type in all experiments. All strains were maintained at 22 ^{0}C on standard NGM media seeded with OP50 except for *dyn-1(ky51)*, which was kept at 15ºC. EG5793 *oxSi91[Punc-17::ChIEF::mCherry::unc-54UTR; unc-119*(+)] *II* was generated using a MosSCI direct insertion protocol (Frøkjaer-Jensen et al., 2008). Although MosSCI usually generates single copy inserts, the *oxSi91* transgene was a rare event specifically selected for high expression and is likely to be more than a single copy. pQL12 plasmid was injected into EG4322 *ttTi5605; unc-119(ed3)* worms. The injection mix consisted of 25 ng/ml targeting plasmid (pQL12), 10 ng/ml pCFJ103 (*Ppie-1::mosase::pie-1 UTR*), 5 ng/ml pGH8 (*Prab-3::mCherry*), 5 ng/ml pCFJ104 (*Pmyo-3::mCherry*) and 2.5 ng/ml pCFJ90 (*Pmyo-2::mCherry*). Injected worms were individually transferred to standard NGM plates at room temperature and allowed to exhaust the food source. Once starved, plates containing transgenic lines were screened for insertion events on a fluorescence dissection microscope based on wild-type movement but complete lack of fluorescent coinjection markers. Several independent lines were obtained and EG5793 was selected for its strong mCherry expression in the nervous system. The strong mCherry expression suggests that a multicopy transgene was inserted.

To generate a strain expressing DYN-1::tdEos, we injected pMPD38 (*Pdyn-1::dyn-1::tdEos*) into the homozygous knockout strain (EG6028) rescued by the extrachromosomal array *oxEx1473[dyn-1(+); unc-119; ccGFP])*. Plates containing transgenic lines were screened for the loss of *oxEx1473* and the rescue of *dyn-1(ox447)* lethality.

Other strains used in this study are:

EG5899 *acr-16(ok789) V;oxSi93[Punc-17::ChIEF::mCherry; unc-119+] II*

EG5183 *unc-13(s69) I; oxIs364[Punc-17::channelrhodopsin-2::mCherry; lin-15+; Litmus38i].*

CX51 *dyn-1(ky51ts) X.*

EG5278 *oxIs433[Punc-17::halorhodopsin::GFP; lin-15+; Litmus] V; lin-15(n765ts) X.*

EG5374 *unc-49(e407) III; oxIs433[Punc-17::halorhodopsin::GFP; lin-15+; Litmus] V; lin-15(n765ts) X.*

Retinal feeding

Transgenic worms were grown in the presence of all-trans retinal 16~48 hours before experiments. All trans-retinal (Sigma) was dissolved in ethanol to make 100 mM stock solution and stored at -20 ^{0}C in the dark. NGM plates were seeded with 4ul 100 mM retinal stock solution mixed with 250 µl OP50 per 50 mm plate. Seeded retinal plates were kept in the dark at 4 ^{0}C for up to a week. Young adult transgenic worms were transferred from regular plates to freshly seeded retinal plates in the dark at room temperature.

Electrophysiology

Young adult hermaphrodite animals were used for electrophysiological analysis. Tonic and evoked postsynaptic currents (mPSCs and ePSCs) at the neuromuscular junction were recorded as previously described (Richmond et al., 1999; Liu et al., 2009). Evoked responses are not observed in nontransgenic animals with exogenously added retinal or transgenic animals expressing channelrhodopsin in absence of trans-retinal (Nagel et al., 2005; Liewald et al., 2008). In brief, an animal was immobilized on a Sylgard-coated glass coverslip by applying a cyanoacrylate adhesive along the dorsal side. A longitudinal incision was made in the dorsolateral region. The cuticle flap was folded back and glued to the coverslip, exposing the ventral nerve cord and two adjacent muscle quadrants. An upright microscope (Axioskop; Carl Zeiss, Inc.) equipped with a 40x water immersion lens and 15x eyepieces was used for viewing the preparation. Borosilicate glass pipettes with a tip resistance of ~ 3–5 MΩ were used as electrodes for voltage clamping. The classical whole-cell configuration was obtained by rupturing the patch membrane of a gigaohm seal formed between the recording electrode and a right medial body muscle two cells anterior to the vulva. The cell was voltage clamped at -60 mV to record mPSCs and ePSCs. Postsynaptic currents were amplified (EPC10; HEKA) and acquired with Patchmaster software (HEKA). Data were sampled at a rate of 10 kHz after filtering at 2 kHz. The recording pipette solution contained the following: 120 mM KCl, 20 mM KOH, 5 mM TES, 0.25 mM $CaCl_2$, 4 mM $MgCl_2$, 36 mM sucrose, 5 mM EGTA, and 4 mM Na_2ATP; adjusted to pH 7.2 with KOH and osmolarity to

310–320 mOsm with sucrose. The standard external solution included the following: 150 mM NaCl, 5 mM KCl, 5 mM $CaCl_2$, 1 mM $MgCl_2$, 5 mM sucrose, 10 mM glucose, and 15 mM HEPES; adjusted to pH 7.35 with NaOH and an osmolarity of 330–340 mOsm. Amplitude and frequency of mPSCs were analyzed using MiniAnalysis (Synaptosoft). A detection threshold of 10 pA was used in initial automatic analysis, followed by visual inspections to include missed events (≥5 pA) and to exclude false events resulting from baseline fluctuations. Amplitudes of ePSCs were measured with Patchmaster (HEKA) and analyzed with Fitmaster. The amplitude of the largest peak of ePSCs from each experiment was used for statistical analysis. Data were imported into Origin, version 7.5 (OriginLab), for graphing and statistical analysis. Unpaired t-test was used for statistical comparisons. A P value of < 0.05 was considered statistically significant.

Illumination system for electrophysiology

The light source was an AttoArc 2 HBO 100W system (Zeiss) with a mercury arc bulb (Osram). A Zeiss bandpass filter set was used to excite channelrhodopsin (at 450-490 nm) or Halorhodopsin (at 540-552 nm). Light intensity was controlled by adjusting dialing the power supply. The light on/off switch was controlled by a Uniblitz VS25 shutter and a VCM-D1 driver (Uniblitz). Light-activated currents in ChIEF transgenic animals were evoked by shining light (10 mW/mm^2 unless specified) onto the dissected worm preparation on a Zeiss Axioskop microscope, equipped with a 40X water-immersion objective and

15X eyepieces. Rapid shutter opening and closing was triggered by TTL signals from the HEKA EPC-10 amplifier. A liquid light guide (Sutter) was installed between the Axioskop microscope and the shutter to avoid mechanical vibrations during repetitive stimulations. Light intensity was measured with a Coherent FieldMax II-TOP Laser Power/Energy Meter.

Paired-pulse protocol

A single 10 ms light pulse was followed by a second 10 ms pulse after a variable delay for each trial. These inter-pulse intervals ranged from 50 ms to 15 s. Between consecutive trials there was >30 s of darkness to allow for complete channel recovery. The ratios of the second current peak to the first current peak were calculated and plotted relative to the recovery intervals.

Modifications of the Leica EMpact2

Freezing was conducted using a Leica EMpact2 (Leica), which does not include the rapid transfer system (RTS) attachment. To create a light path, the specimen pod (Leica, #16707829) and the manual loading bayonet for the EMpact2 (Leica, #16707828) were modified. The anvil mounting screw in the specimen pod was drilled out and machined with a countersink on the top of the screw (Fig. 7.1C). The black diamond anvil was removed and replaced with a sapphire disk (SwissJewel, #E2.08) with a diameter of 2.08 mm and a thickness of 1 mm. The sapphire anvil was glued into the countersink of the screw using two-part epoxy (Devcon, #14250) (Fig. 7.1C).

A 2mm hole was drilled through the middle of the bayonet (Fig. 7.1C). A 3mm blue light-emitting diode (LED) was inserted into the bayonet just behind the specimen pod (Fig. 7.1C). For initial experiments, a power supply for the LED was constructed using a 9 V battery, a TIP110 transistor and a 200 kW current limiting resistor. This was connected to the LED using sub micro twisted servo wire (Radical RC, Dayton OH, www.radicalrc.com W3ST-34JR). The transistor base was connected to an analog output channel of a USB multifunction DAQ device (National Instruments, Austin TX, www.ni.com, NI-USB6008). The DAQ device was driven by a custom Labview program (available on request) which could monitor an accelerometer mounted to the bayonet holder and update the LED output level every 7-8 ms. In later experiments, we constructed a dedicated device based on an Arduino Uno microcontroller board (http://www.arduino.cc/) driven by custom firmware. For these experiments, we changed from the 3 mm LED to a 3.2 mm diameter high brightness LED (LED Engin, http://www.ledengin.com/ , LZ1-00B200), fitted into the bayonet with a custom-machined adapter. The LED is powered using a dedicated constant current LED power module (Luxdrive, www.luxdrive.com/, 7023-D-E-1000), which is controlled by the microcontroller. The microcontroller triggers the freezing of the sample by communicating with the EMpact-2 via an RS232 serial communication channel.

Stimulation and high-pressure freezing

For inducing neurotransmission, 10 young wild-type or *unc-13(s69)* animals expressing ChIEF in the acetylcholine neurons (*Punc-17::ChIEF::mCherry*) were mounted onto a membrane carrier with a depth of 100μm (Leica, #16707898) and stimulated with a single 20 ms pulse of blue light (488 nm). To maximize the absorbance of light by specimens, 20% BSA (Sigma-Aldrich, A3059-10G) was used as a cryoprotectant instead of bacteria. We set the light stimulation device so that a light pulse was triggered at 30 ms, 100 ms, 300 ms, 1 s, 3 s, and 10 s before freezing. The actual time when the light pulse was applied relative to freezing was calculated based on the movement recording from the accelerometer and the output of the light pulse recorded by the computer (see the next section).

Similarly, for depressing neurotransmission, 10 young adults expressing halorhodopsin were prepared as described above. Yellow light was then applied to the specimen continuously for 5 s. The light was left on during the freezing to ensure that halorhodopsin was continuously activated until the completion of the freeze.

Calculations for the interval between stimulation and freezing

The light stimulus was correlated post facto with the freeze. To calculate the actual interval between stimulation and freezing, we summed the time between light stimulation and pressure application and the time between pressure application and freezing. The interval between the pressure and

freezing can be determined based on values recorded by the high-pressure freezer, and it was consistently 8 ms. To calculate the interval between light and pressure, we needed to monitor when the application of pressure is initiated after sending the "start" signal to the high-pressure freezer. To measure when pressure is applied, we mounted an accelerometer on the specimen bayonet. The bayonet jolts when the pressure is applied to the specimen. We could then record the interval between the application of light and pressure.

We programmed our light device so that the desired interval between stimulation and freezing could be achieved by simply modifying the timing of the output signal to initiate the freezing process. Based on the accelerometer reading, the pressure increase occurs around 170 ms after sending out the "start" signal. The 170 ms delay is required for the operating system of the freezer to communicate with the pressure firing switch. Since the freezing initiates 8 ms after the pressure application, 178 ms is required for specimens to freeze after sending out the "start" signal. Thus, to freeze a sample 1 s after stimulation, one needs to activate the high pressure freezer 822 ms after the light stimulus; to freeze a sample 100 ms after stimulation, one needs to activate the high pressure freezer 78 ms *before* the light. However, in our experiments, we found that the 170 ms delay is not consistent – it varies by ±20 ms. Thus, the actual time between light stimulation and freezing was calculated post hoc from the accelerometer read-out versus when the light was stimulated. Unfortunately, for very short time points, the light was often flashed *after* the sample was frozen

because of fluctuations in the pressure time point. Because of this fluctuation, 30 ms time points were not obtained in the study.

Post-stimulation electron microscopy

After freezing, the specimens were transferred to the cryovial containing 2% glutaraldehyde (EMS, #16530) in anhydrous acetone (EMS, #RT10016) under liquid nitrogen. The use of glutaraldehyde as a primary fixative was necessary for preserving clathrin coats when cryo-methods are employed (Forostyan, Watanabe, Jorgensen, unpublished). The freeze-substitution was carried out in a Leica Automatic Freeze Substitution unit (Leica, AFS2) with the following program: 48 hours at -90 ºC, 5 ºC/hour to -60 ºC, 6 hours at -60 ºC, 5 ºC/hour to -20 ºC, 16 hours at -20 ºC, and 10 ºC/hour to 20 ºC. The glutaraldehyde was removed and the sample rinsed with acetone six times when the program reached -60 ºC. The fixative was then changed to 1% osmium tetroxide (EMS, #RT19130) + 0.1% uranyl acetate (EMS, #RT22400) at -60 ºC. The vials were swirled at least twice a day to promote the diffusion of fixatives into tissues. After the completion of the program, the fixative was removed using 6 acetone washes. The infiltration of plastic, araldite-epon (Ted Pella, #18028), was carried out on a nutator with a gradual change in the concentration of plastic (30%, 70%, and 90%). The next day, the specimen was transferred into the cap of a BEEM capsule (EMS, #70010-B) containing 100% fresh resin. Following three changes of resin over 6 hours, the plastic was polymerized at 60 ºC for 48 hours.

Electron microscopy

We imaged and analyzed three animals from each condition blind. 250-300 contiguous sections were cut using a microtome (Leica, UC6) from each condition and collected onto formvar–coated (EMS, #RT15820) grids (Ted Pella, #1GC12H). The sections were stained with 2.5% uranyl acetate in 70% methanol for 4 min prior to imaging. Sections were imaged on a Hitachi H-7100 electron microscope equipped with a Gatan digital camera (Gatan, Orius).

Electron tomography

For electron tomography imaging, grids were first coated with 0.5% pioloform, and then carbon was sputtered on top of the film for ~10 s. Using a microtome as described above, arrays of 200 nm thick sections were collected onto the carbon-coated grids. The sections were imaged on a FEI Tecnai G2 F20 fitted with an Eagle HR CCD camera. The accelerating voltage was set at 200 keV. A tilt series of ±65º was collected from each section. The tomograms were computed and reconstructed from the tilt series using IMOD.

Morphological analysis

We developed a macro for ImageJ and a Matlab program for morphological analysis of synapse (Watanabe, Davis, and Jorgensen, unpublished). From each axon profile, the locations of vesicles, plasma membrane, dense projection, and adherens junctions, as well as the diameters of vesicles, were annotated, and these values were exported as a text file. Vesicles

were categorized into three types depending on their appearance: synaptic vesicles, dense core vesicles, and large vesicles. Synaptic vesicles have a diameter of ~30 nm and are most abundant in the terminals. Synaptic vesicles that are in the physical contact with plasma membrane are categorized as docked vesicles. Other vesicles are close to the membrane (less than 30 nm) but are not in contact with the membrane. Such vesicles with a physical tether are categorized as "tethered", and such vesicles with no obvious tether are categorized as the "30 nm pool". Note that a combination of both pools was previously defined as the "tethered pool" (Broadie et al., 1995; Toonen et al., 2006; Hammarlund et al., 2007; Siksou et al., 2009; Gracheva et al., 2010). Dense core vesicle can be distinguished by the dark appearance of the vesicle core, and their diameter is typically around 40 nm. Large vesicles are clear-core vesicles that are larger than 35 nm in diameter. Then, these text files were imported into the Matlab analysis program. In this program, the distances from each vesicle to the nearest edge of dense projection, to the closest plasma membrane, and to the adherens junctions were calculated.

3D model generation

The structural features were segmented from serial section electron micrographs and a 200 nm tomogram using a pen tablet display (Wacom Cintiq 21UX) and Amira (version 4.1.2). Synaptic vesicles were created using the landmark tools. Plasma membrane was traced in a way that does not leave holes

and gaps between sections, thus the thickness of plasma membranes does not reflect the actual dimensions of bilayers.

Dynamin localization

Transgenic animals expressing dynamin::tdEos were frozen and processed for nano-resolution fluorescence electron microscopy (nano-fEM) as previously described (Watanabe et al., 2011). Serial 80-nm sections were cut from animals embedded in glycol methacrylate resin and collected onto cover glasses. Following the application of gold particles (100 nm) onto sections and rehydration, the animals were imaged using PALM (Zeiss Elyra P.1). 5000 frames were collected and analyzed using the Zen software (Zeiss). Localization precision better than 40 nm is shown in the PALM images. The same sections were stained with uranyl acetate and coated with carbon and then imaged using a scanning electron microscopy (FEI Nova Nano) under both low (~5,000x) and high magnification (50,000x to 100,000x). To overlay PALM signals onto electron micrographs, we aligned the fluorescence signals of the gold particles with their corresponding locations in electron micrographs using Photoshop (Adobe, CS5) and the black pixels in the PALM image were made transparent.

To quantify dynamin localization, we reconstructed nine synapses from five different motor neurons. We divided a synapse into 4 different regions: the dense projection, adherens junction, cytosol, and nonspecific membrane (Fig. 7.8C). To account for the localization errors by PALM, molecules within 50 nm of

the membrane and within 100 nm of the dense projection or adherens junctions were counted as associated molecules.

Membrane calculations

To calculate the total amount of recycled membrane, the following four assumptions were made. First, we assumed that our partial reconstructions would provide a reasonable sampling of exocytic and endocytic events at a synapse. Vesicles and endocytic figures were only analyzed in profiles containing a dense projection. These profiles are cross sections of a single synapse that include active zone membrane on two sides from the dense projection to the flanking adherens junctions. The dense projection spans approximately 4 sections (Hammarlund et al., 2007) and is encompassed by about one third of the vesicles found at a synapse. Thus, our reconstructions sample a significant fraction of vesicles at each synapse. On the other hand, it is likely that exocytic and endocytic events are occurring at the active zone in adjacent sections, leading to a systematic undercounting of recycling events per synapse. We confirmed the presence of pits in anterior or posterior sections not containing a dense projection. These were also strictly associated with adherens junctions but were not included in our calculations. Second, we assume that all endocytic events near the dense projections occur within 50 ms of stimulation and that the presence of large vesicles at later time points is due to the slow clearance of these vesicles from this area and not the generation of new large vesicles. This assumption is supported by the observation that pits are not observed forming at

dense projections 50 ms after stimulation – pit formation appears to occur in the first 50 ms. Third, we assume that shallow pits observed at the adherens junctions, across all time points, will be resolved as a large vesicle with a diameter of ~45 nm, which is the diameter of the deeper pits and large vesicles observed at later time points. Fourth, we assumed that the formation of deep pits from shallow pits takes longer than 1 s. For example, pit formation may be initiated by 300 ms but resolving these pits into large vesicles may require long periods of time. This idea is supported by the exponential decay in the number of shallow pits; they peak at 300 ms and declines with a time constant of 1.4 s. Thus, we compared the number of exocytic vesicles and endocytic structures at two time points - 300 ms and 1 s after stimulation.

Based on these assumptions, we calculated the total amount of membrane exocytosed from the 300 ms data set in profiles containing a dense projection. We analyzed a total of 22 synapses from 300 ms after stimulation. Since four to six vesicles are typically released per synapse, then the area from 88-132 vesicles (~110 SVs) was added to the surface. Given that the surface area of single synaptic vesicle of 29.3 nm is 2700 nm^2 ($4\pi r^2$), then the total amount of membrane will be 238,000 – 356,000 nm^2 (110 SV, 297,000 nm^2).

We then calculated the number of synaptic vesicle equivalents that we observed endocytosed at the 300 ms time points. At the 300 ms time point, there were 14 large vesicles at dense projections. Based on their time course, ~47% of the large vesicles (~12 large vesicles) would have diffused away from the dense projection by this time (Fig. 7.6B), so a total of ~26 large vesicles were likely

internalized at dense projections. The average diameter of 18 of these vesicles (70% of the vesicle at the dense projection) was ~ 37 nm (surface area = 4300 nm^2), and the remaining eight had an average diameter of 46 nm (surface area = 6600 nm^2) (Fig. 7.6I). Thus, the total surface area of membrane recovered at dense projections is 130,200 nm^2. We also observed 29 shallow pits at adherens junctions. Assuming that each endocytic structure resolves into a large vesicle with a diameter of 43.2 nm (surface area = 6000 nm^2) (Fig. 7.S5H), about 174,000 nm^2 of membrane was retrieved at adherens junctions. Thus, for 238,00 – 356,00 nm^2 released, 304,200 nm^2 were recovered or projected to recover based on the number of endocytic structures present 300 ms after stimulation. The total amount of membrane exocytosed and endocytosed is roughly equal, suggesting that all endocytic structures are likely present by 300 ms after stimulation.

Calculations from the 1 s time point yielded similar results. We analyzed a total of 23 synapses 1 s after stimulation. Since four to six vesicles are typically released per synapse, the area from 92-138 vesicles (250,000 – 370,000 nm^2) was added to the surface. At the 1 s time point, there were 25 large vesicles at dense projections. Based on the data from 50 ms, ~ 50% of the large vesicles (~ 25 large vesicles) would have diffused away from the dense projection by this time (Fig. 7.6B), so a total of ~50 large vesicles were likely internalized at dense projections. The diameter of 35 of these vesicles (70% of the vesicles at the dense projection) was ~ 37 nm (surface area = 4300 nm^2), and 15 had a diameter of 46 nm (surface area = 6600 nm^2). Thus, the total membrane

recovered at dense projections is 249,500 nm^2. We also observed 20 shallow pits and 4 large vesicles at adherens junctions. We assume that all of these will resolve into large vesicles of 43.2 nm in diameter like the deep pits observed at the adherens junctions later. Each of these vesicles removes 6000 nm^2 ($4\pi r^2$) from the surface, so the area recovered or projected to recover at adherens junctions is 140,000 nm^2. With a range of 250,000 – 370,000 nm^2, roughly 115 vesicles were exocytosed, and about 390,000 nm^2 or 144 vesicle equivalents were recycled, again suggesting that all endocytic structures are likely formed very rapidly – in less than 1 s.

Statistics

Serial sections containing a dense projection were considered as a synapse, typically about four sections. For statistical comparisons, we calculated p-values using the normalized numbers (the numbers of docked and tethered vesicles in each profile were normalized by the area of profiles or the area of active zones to account for a size difference across synapses). Distributions in Fig. 7.2 and 3 are not normalized but are absolute values. Large vesicles were averaged per profile or synapse. P values were determined in Mann-Whitney U tests because of the sample size and skewed distribution of the data. The confidence level was set at 95%. We applied the Bonferroni correction for multiple comparisons, and thus the confidence level is 0.007 for the P*unc-17:ChIEF* experiment in Fig. 7.5D-F. *p*-values are listed in the figure legends.

Acknowledgements

We would like to thank the Grass Foundation and the Marine Biological Laboratory at Woods Hole for providing us space and equipment necessary to perform the freezing experiments. We would like to thank Roger Y. Tsien for providing us a construct for ChIEF, Robert J. Hobson for critical reading of the manuscript, and Stefan Eimer for communicating results before publication. The research was supported by the US National Institutes of Health (NS034307), National Science Foundation (0920069) and the Marine Biological Laboratory (The Dart Scholars Program and the Grass Fellowship). E.M.J. is an Investigator of the Howard Hughes Medical Institute.

References

Aravanis, A.M., Pyle, J.L., and Tsien, R.W. (2003). Single synaptic vesicles fusing transiently and successively without loss of identity. Nature *423*, 643–647.

Balaji, J., and Ryan, T.A. (2007). Single-vesicle imaging reveals that synaptic vesicle exocytosis and endocytosis are coupled by a single stochastic mode. Proc. Natl. Acad. Sci. U.S.A *104*, 20576–20581.

Broadie, K., Prokop, A., Bellen, H.J., O'Kane, C.J., Schulze, K.L., and Sweeney, S.T. (1995). Syntaxin and synaptobrevin function downstream of vesicle docking in Drosophila. Neuron *15*, 663–673.

del Castillo, J., and Katz, B. (1956). Biophysical aspects of neuro-muscular transmission. Prog Biophys Biophys Chem *6*, 121–170.

Ceccarelli, B., Hurlbut, W.P., and Mauro, A. (1972). Depletion of vesicles from frog neuromuscular junctions by prolonged tetanic stimulation. J. Cell Biol *54*, 30–38.

Ceccarelli, B., Hurlbut, W.P., and Mauro, A. (1973). Turnover of transmitter and synaptic vesicles at the frog neuromuscular junction. J. Cell Biol. *57*, 499–524.

Clark, S.G., Shurland, D.L., Meyerowitz, E.M., Bargmann, C.I., and van der Bliek, A.M. (1997). A dynamin GTPase mutation causes a rapid and reversible

temperature-inducible locomotion defect in C. elegans. Proc. Natl. Acad. Sci. U.S.A *94*, 10438–10443.

Clayton, E.L., Sue, N., Smillie, K.J., O'Leary, T., Bache, N., Cheung, G., Cole, A.R., Wyllie, D.J., Sutherland, C., Robinson, P.J., et al. (2010). Dynamin I phosphorylation by GSK3 controls activity-dependent bulk endocytosis of synaptic vesicles. Nat. Neurosci *13*, 845–851.

Cocucci, E., Aguet, F., Boulant, S., and Kirchhausen, T. (2012). The first five seconds in the life of a clathrin-coated pit. Cell *150*, 495–507.

Cousin, M.A. (2009). Activity-dependent bulk synaptic vesicle endocytosis--a fast, high capacity membrane retrieval mechanism. Mol. Neurobiol *39*, 185–189.

Couteaux, R., and Pécot-Dechavassine, M. (1974). [Specialized areas of presynaptic membranes]. C.R. Hebd. Seances Acad. Sci., Ser. D, Sci. Nat. *278*, 291–293.

Dittman, J., and Ryan, T.A. (2009). Molecular circuitry of endocytosis at nerve terminals. Annu. Rev. Cell Dev. Biol *25*, 133–160.

Dworetzky, S.I., Boissard, C.G., Lum-Ragan, J.T., McKay, M.C., Post-Munson, D.J., Trojnacki, J.T., Chang, C.P., and Gribkoff, V.K. (1996). Phenotypic alteration of a human BK (hSlo) channel by hSlobeta subunit coexpression: changes in blocker sensitivity, activation/relaxation and inactivation kinetics, and protein kinase A modulation. J. Neurosci. *16*, 4543–4550.

Fatt, P., and Katz, B. (1952). Spontaneous subthreshold activity at motor nerve endings. J. Physiol. (Lond.) *117*, 109–128.

Fesce, R., Grohovaz, F., Valtorta, F., and Meldolesi, J. (1994). Neurotransmitter release: fusion or "kiss-and-run"? Trends Cell Biol. *4*, 1–4.

Frøkjaer-Jensen, C., Davis, M.W., Hopkins, C.E., Newman, B.J., Thummel, J.M., Olesen, S.-P., Grunnet, M., and Jorgensen, E.M. (2008). Single-copy insertion of transgenes in Caenorhabditis elegans. Nat. Genet *40*, 1375–1383.

Gaffield, M.A., Romberg, C.F., and Betz, W.J. (2011). Live imaging of bulk endocytosis in frog motor nerve terminals using FM dyes. J Neurophysiol.

Gracheva, E.O., Hadwiger, G., Nonet, M.L., and Richmond, J.E. (2008). Direct interactions between C. elegans RAB-3 and Rim provide a mechanism to target vesicles to the presynaptic density. Neurosci. Lett *444*, 137–142.

Gracheva, E.O., Maryon, E.B., Berthelot-Grosjean, M., and Richmond, J.E. (2010). Differential regulation of synaptic vesicle tethering and docking by UNC-18 and TOM-1. Front Synaptic Neurosci *2*, 141.

Granseth, B., Odermatt, B., Royle, S.J., and Lagnado, L. (2006). Clathrin-mediated endocytosis is the dominant mechanism of vesicle retrieval at hippocampal synapses. Neuron *51*, 773–786.

Hammarlund, M., Palfreyman, M.T., Watanabe, S., Olsen, S., and Jorgensen, E.M. (2007). Open syntaxin docks synaptic vesicles. PLoS Biol *5*, e198.

Harata, N., Ryan, T.A., Smith, S.J., Buchanan, J., and Tsien, R.W. (2001). Visualizing recycling synaptic vesicles in hippocampal neurons by FM 1-43 photoconversion. Proceedings of the National Academy of Sciences *98*, 12748 – 12753.

Harata, N.C., Choi, S., Pyle, J.L., Aravanis, A.M., and Tsien, R.W. (2006). Frequency-dependent kinetics and prevalence of kiss-and-run and reuse at hippocampal synapses studied with novel quenching methods. Neuron *49*, 243–256.

Heerssen, H., Fetter, R.D., and Davis, G.W. (2008). Clathrin dependence of synaptic-vesicle formation at the Drosophila neuromuscular junction. Curr. Biol. *18*, 401–409.

Heuser, J.E., and Reese, T.S. (1973). Evidence for recycling of synaptic vesicle membrane during transmitter release at the frog neuromuscular junction. J. Cell Biol *57*, 315–344.

Heuser, J.E., and Reese, T.S. (1981). Structural changes after transmitter release at the frog neuromuscular junction. J. Cell Biol *88*, 564–580.

Heuser, J.E., Reese, T.S., Dennis, M.J., Jan, Y., Jan, L., and Evans, L. (1979). Synaptic vesicle exocytosis captured by quick freezing and correlated with quantal transmitter release. J. Cell Biol *81*, 275–300.

Holt, M., Cooke, A., Wu, M.M., and Lagnado, L. (2003). Bulk membrane retrieval in the synaptic terminal of retinal bipolar cells. J. Neurosci *23*, 1329–1339.

de Hoop, M.J., Huber, L.A., Stenmark, H., Williamson, E., Zerial, M., Parton, R.G., and Dotti, C.G. (1994). The involvement of the small GTP-binding protein Rab5a in neuronal endocytosis. Neuron *13*, 11–22.

Hoopmann, P., Punge, A., Barysch, S.V., Westphal, V., Bückers, J., Opazo, F., Bethani, I., Lauterbach, M.A., Hell, S.W., and Rizzoli, S.O. (2010). Endosomal sorting of readily releasable synaptic vesicles. Proc. Natl. Acad. Sci. U.S.A *107*, 19055–19060.

Jockusch, W.J., Praefcke, G.J.K., McMahon, H.T., and Lagnado, L. (2005). Clathrin-dependent and clathrin-independent retrieval of synaptic vesicles in retinal bipolar cells. Neuron *46*, 869–878.

Kasprowicz, J., Kuenen, S., Miskiewicz, K., Habets, R.L.P., Smitz, L., and Verstreken, P. (2008). Inactivation of clathrin heavy chain inhibits synaptic recycling but allows bulk membrane uptake. J. Cell Biol *182*, 1007–1016.

Kirchhausen, T. (2009). Imaging endocytic clathrin structures in living cells. Trends Cell Biol. *19*, 596–605.

Kittel, R.J., Wichmann, C., Rasse, T.M., Fouquet, W., Schmidt, M., Schmid, A., Wagh, D.A., Pawlu, C., Kellner, R.R., Willig, K.I., et al. (2006). Bruchpilot promotes active zone assembly, Ca2+ channel clustering, and vesicle release. Science *312*, 1051–1054.

Koenig, J.H., and Ikeda, K. (1989). Disappearance and reformation of synaptic vesicle membrane upon transmitter release observed under reversible blockage of membrane retrieval. J. Neurosci *9*, 3844–3860.

Koenig, J.H., and Ikeda, K. (1996). Synaptic vesicles have two distinct recycling pathways. J. Cell Biol. *135*, 797–808.

Kopp-Scheinpflug, C., Tolnai, S., Malmierca, M.S., and Rübsamen, R. (2008). The medial nucleus of the trapezoid body: comparative physiology. Neuroscience *154*, 160–170.

Landis, D.M. (1988). Membrane and cytoplasmic structure at synaptic junctions in the mammalian central nervous system. J Electron Microsc Tech *10*, 129–151.

de Lange, R.P.J., de Roos, A.D.G., and Borst, J.G.G. (2003). Two modes of vesicle recycling in the rat Calyx of Held. The Journal of Neuroscience *23*, 10164 –10173.

Lenzi, D., Crum, J., Ellisman, M.H., and Roberts, W.M. (2002). Depolarization Redistributes Synaptic Membrane and Creates a Gradient of Vesicles on the Synaptic Body at a Ribbon Synapse. Neuron *36*, 649–659.

Liewald, J.F., Brauner, M., Stephens, G.J., Bouhours, M., Schultheis, C., Zhen, M., and Gottschalk, A. (2008). Optogenetic analysis of synaptic function. Nat. Methods *5*, 895–902.

Lin, J.Y., Lin, M.Z., Steinbach, P., and Tsien, R.Y. (2009). Characterization of Engineered Channelrhodopsin Variants with Improved Properties and Kinetics. Biophysical Journal *96*, 1803–1814.

Liu, Q., Hollopeter, G., and Jorgensen, E.M. (2009). Graded synaptic transmission at the Caenorhabditis elegans neuromuscular junction. Proceedings of the National Academy of Sciences *106*, 10823 –10828.

Lorteije, J.A.M., Rusu, S.I., Kushmerick, C., and Borst, J.G.G. (2009). Reliability and precision of the mouse calyx of Held synapse. J. Neurosci *29*, 13770–13784.

Maeno-Hikichi, Y., Polo-Parada, L., Kastanenka, K.V., and Landmesser, L.T. (2011). Frequency-dependent modes of synaptic vesicle endocytosis and exocytosis at adult mouse neuromuscular junctions. J. Neurosci *31*, 1093–1105.

Matsui, K., and Jahr, C.E. (2003). Ectopic release of synaptic vesicles. Neuron *40*, 1173–1183.

Maycox, P.R., Link, E., Reetz, A., Morris, S.A., and Jahn, R. (1992). Clathrin-coated vesicles in nervous tissue are involved primarily in synaptic vesicle recycling. J. Cell Biol *118*, 1379–1388.

Mike, A., Castro, N.G., and Albuquerque, E.X. (2000). Choline and acetylcholine have similar kinetic properties of activation and desensitization on the α7 nicotinic receptors in rat hippocampal neurons. Brain Research *882*, 155–168.

Miller, T.M., and Heuser, J.E. (1984). Endocytosis of synaptic vesicle membrane at the frog neuromuscular junction. J. Cell Biol *98*, 685–698.

Moor, H. (1987). Theory and practice of high pressure freezing. In Cryotechiniques in Biological Electron Microscopy, (Berlin: Springer-Verlag), pp. 175–191.

Moor, H., and Riehle, U. (1968). Snap-freezing under high pressure: A new fixation technique for freeze-etching. pp. 33–34.

Murthy, V.N., and Stevens, C.F. (1998). Synaptic vesicles retain their identity through the endocytic cycle. Nature *392*, 497–501.

Nagel, G., Brauner, M., Liewald, J.F., Adeishvili, N., Bamberg, E., and Gottschalk, A. (2005). Light activation of channelrhodopsin-2 in excitable cells of Caenorhabditis elegans triggers rapid behavioral responses. Curr. Biol. *15*, 2279–2284.

Nagel, G., Szellas, T., Huhn, W., Kateriya, S., Adeishvili, N., Berthold, P., Ollig, D., Hegemann, P., and Bamberg, E. (2003). Channelrhodopsin-2, a directly light-gated cation-selective membrane channel. Proceedings of the National Academy of Sciences of the United States of America *100*, 13940 –13945.

Neher, E. (2010). What is rate-limiting during sustained synaptic activity: Vesicle Supply or the Availability of Release Sites. Front Synaptic Neurosci *2*, 144.

Park, H., Li, Y., and Tsien, R.W. (2012). Influence of synaptic vesicle position on release probability and exocytotic fusion mode. Science *335*, 1362–1366.

Pyott, S.J., and Rosenmund, C. (2002). The effects of temperature on vesicular supply and release in autaptic cultures of rat and mouse hippocampal neurons. J Physiol *539*, 523–535.

Richards, D.A., Guatimosim, C., and Betz, W.J. (2000). Two endocytic recycling routes selectively fill two vesicle pools in frog motor nerve terminals. Neuron *27*, 551–559.

Richmond, J.E., Davis, W.S., and Jorgensen, E.M. (1999). UNC-13 is required for synaptic vesicle fusion in C. elegans. Nat. Neurosci *2*, 959–964.

Rizzoli, S.O., and Betz, W.J. (2005). Synaptic vesicle pools. Nat. Rev. Neurosci *6*, 57–69.

Rosenmund, C., and Stevens, C.F. (1996). Definition of the readily releasable pool of vesicles at hippocampal synapses. Neuron *16*, 1197–1207.

Sato, K., Ernstrom, G.G., Watanabe, S., Weimer, R.M., Chen, C.-H., Sato, M., Siddiqui, A., Jorgensen, E.M., and Grant, B.D. (2009). Differential requirements for clathrin in receptor-mediated endocytosis and maintenance of synaptic vesicle pools. Proc. Natl. Acad. Sci. U.S.A *106*, 1139–1144.

Schweizer, F.E., and Ryan, T.A. (2006). The synaptic vesicle: cycle of exocytosis and endocytosis. Curr. Opin. Neurobiol *16*, 298–304.

Shupliakov, O., Löw, P., Grabs, D., Gad, H., Chen, H., David, C., Takei, K., De Camilli, P., and Brodin, L. (1997). Synaptic Vesicle Endocytosis Impaired by Disruption of Dynamin-SH3 Domain Interactions. Science *276*, 259–263.

Siksou, L., Varoqueaux, F., Pascual, O., Triller, A., Brose, N., and Marty, S. (2009). A common molecular basis for membrane docking and functional priming of synaptic vesicles. Eur. J. Neurosci. *30*, 49–56.

Smith, S.M., Renden, R., and von Gersdorff, H. (2008). Synaptic vesicle endocytosis: fast and slow modes of membrane retrieval. Trends Neurosci. *31*, 559–568.

Szule, J.A., Harlow, M.L., Jung, J.H., De-Miguel, F.F., Marshall, R.M., and McMahan, U.J. (2012). Regulation of synaptic vesicle docking by different classes of macromolecules in active zone material. PLoS ONE *7*, e33333.

Takei, K., Haucke, V., Slepnev, V., Farsad, K., Salazar, M., Chen, H., and De Camilli, P. (1998). Generation of coated intermediates of clathrin-mediated endocytosis on protein-free liposomes. Cell *94*, 131–141.

Toonen, R.F., Kochubey, O., de Wit, H., Gulyas-Kovacs, A., Konijnenburg, B., Sørensen, J.B., Klingauf, J., and Verhage, M. (2006). Dissecting docking and tethering of secretory vesicles at the target membrane. EMBO J. *25*, 3725–3737.

Torri-Tarelli, F., Grohovaz, F., Fesce, R., and Ceccarelli, B. (1985). Temporal coincidence between synaptic vesicle fusion and quantal secretion of acetylcholine. J. Cell Biol *101*, 1386–1399.

Vergara, C., Latorre, R., Marrion, N.V., and Adelman, J.P. (1998). Calcium-activated potassium channels. Current Opinion in Neurobiology *8*, 321–329.

Voglmaier, S.M., Kam, K., Yang, H., Fortin, D.L., Hua, Z., Nicoll, R.A., and Edwards, R.H. (2006). Distinct endocytic pathways control the rate and extent of synaptic vesicle protein recycling. Neuron *51*, 71–84.

Watanabe, S., and Jorgensen, E.M. (2012). Visualizing proteins in electron micrographs at nanometer resolution. Methods Cell Biol. *111*, 283–306.

Watanabe, S., Punge, A., Hollopeter, G., Willig, K.I., Hobson, R.J., Davis, M.W., Hell, S.W., and Jorgensen, E.M. (2011). Protein localization in electron micrographs using fluorescence nanoscopy. Nat. Methods *8*, 80–84.

Wienisch, M., and Klingauf, J. (2006). Vesicular proteins exocytosed and subsequently retrieved by compensatory endocytosis are nonidentical. Nat. Neurosci *9*, 1019–1027.

Wu, W., and Wu, L.-G. (2007). Rapid bulk endocytosis and its kinetics of fission pore closure at a central synapse. Proc. Natl. Acad. Sci. U.S.A. *104*, 10234–10239.

Wu, X.-S., and Wu, L.-G. (2009). Rapid endocytosis does not recycle vesicles within the readily releasable pool. J. Neurosci. *29*, 11038–11042.

Yamashita, T., Hige, T., and Takahashi, T. (2005). Vesicle endocytosis requires dynamin-dependent GTP hydrolysis at a fast CNS synapse. Science *307*, 124–127.

Zenisek, D., Steyer, J.A., and Almers, W. (2000). Transport, capture and exocytosis of single synaptic vesicles at active zones. Nature *406*, 849–854.

Zhang, F., Wang, L.-P., Brauner, M., Liewald, J.F., Kay, K., Watzke, N., Wood, P.G., Bamberg, E., Nagel, G., Gottschalk, A., et al. (2007a). Multimodal fast optical interrogation of neural circuitry. Nature *446*, 633–639.

Zhang, Q., Cao, Y.-Q., and Tsien, R.W. (2007b). Quantum dots provide an optical signal specific to full collapse fusion of synaptic vesicles. Proc. Natl. Acad. Sci. U.S.A *104*, 17843–17848.

Zhang, Q., Li, Y., and Tsien, R.W. (2009). The dynamic control of kiss-and-run and vesicular reuse probed with single nanoparticles. Science *323*, 1448–1453.

Zhu, Y., Xu, J., and Heinemann, S.F. (2009). Two Pathways of Synaptic Vesicle Retrieval Revealed by Single-Vesicle Imaging. Neuron *61*, 397–411.

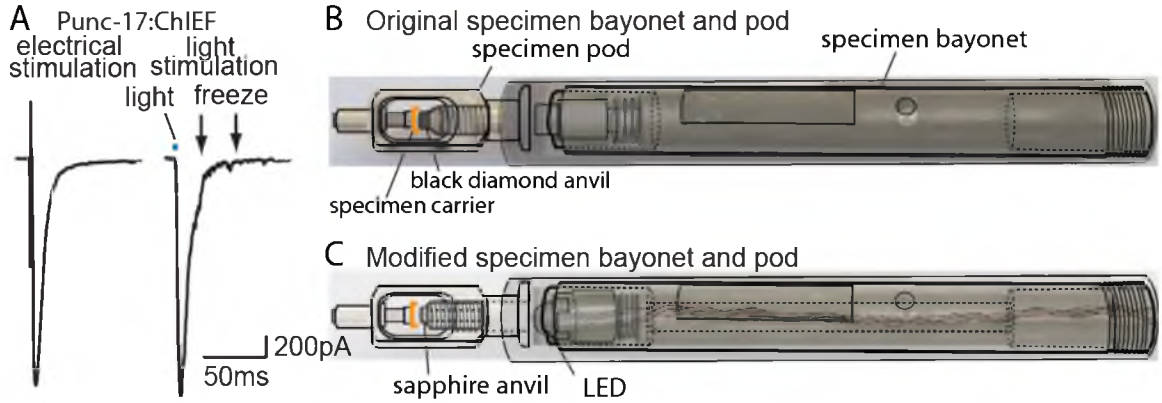

Figure 7.1. Optogenetics coupled with high-pressure freezing. (A) A sample trace of an excitatory postsynaptic current from the muscle of animals expressing ChIEF in acetylcholine neurons, evoked by an electrode (left) and by a 3 ms pulse of blue light (right). The blue line indicates the application of blue light. Arrows indicate freezing times at 20ms and 50ms. (B) A sample trace of endogenous tonic currents recorded from the muscle of an animal expressing halorhodopsin in acetylcholine neurons. This recording is from an animal lacking GABA receptors (unc-49), thus the trace only shows miniature currents from acetylcholine synapses. When yellow light is applied to the animal (indicated by the yellow line), tonic vesicle fusions are suppressed, although not completely eliminated. The black arrow indicates when samples were frozen for electron microscopy. (C) A schematic diagram of specimen bayonet and a pod. The bayonet was bored out (the dotted lines) to house the LED and wires. A sapphire end stone was mounted into the pod. Specimens in the cup of the specimen carrier face the sapphire anvil and LED.

Figure 7.2. Tonic release sites are in the proximity of the dense projection. Representative micrographs of (A) docked vesicles (in direct contact with the plasma membrane), and (B) tethered vesicles (within 30 nm of plasma membrane). Docked vesicles (black arrows) are in direct contact with the plasma membrane. Tethered vesicles (white arrows) are often connected by filaments and within 30 nm of plasma membrane. Representative micrographs of *C. elegans* acetylcholine neuromuscular junctions before (C) and after (D) activation of Halorhodopsin. (E) Absolute number of docked vesicles in the active zone per profile . The numbers are normalized by the size of active zones. A significant increase in docked vesicles was observed when acetylcholine motor neurons were hyperpolarized by activation of halorhodopsin (control 2.5 ± 0.1% SVs per profile; Halorhodopsin activated 3.8 ± 0.2 SV; $p < 0.0001$). (F) Percentage of total vesicles per profile tethered in the active zone. A slight increase in tethered vesicles was observed in acetylcholine neurons (unactivated 2.7 ± 0.2 SV; halorhodopsin-activated 3.1 ± 0.2 SV; $p = 0.4$). (G) Distance of docked vesicles along the plasma membrane relative to the dense projection in acetylcholine neurons. The first column along the x-axis labeled as 0 nm in this figure shows the number of docked vesicles that are touching the dense projection, and each column thereafter is binned by 33 nm. The inset illustrates how vesicles were binned according to their distance from the dense projection. The total number of synaptic vesicles did not differ between the control and halorhodopsin-activated animals (unactivated 25.9 ± 0.9 SV per reconstructed dense projection profiles; halorhodopsin-activated 25.8 ± 0.8 SV). Docked vesicles accumulate in proximity of the dense projection after activation of halorhodopsin (control 0.3 ± 0.1 SV per reconstructed dense projection profiles; halorhodopsin-activated 1.5 ± 0.3 SV; $p=0.02$). ***, **, * indicate p-values of <0.001, <0.01, and <0.05, respectively. n.s., 'not significant'. The standard error of the mean is shown in each graph.

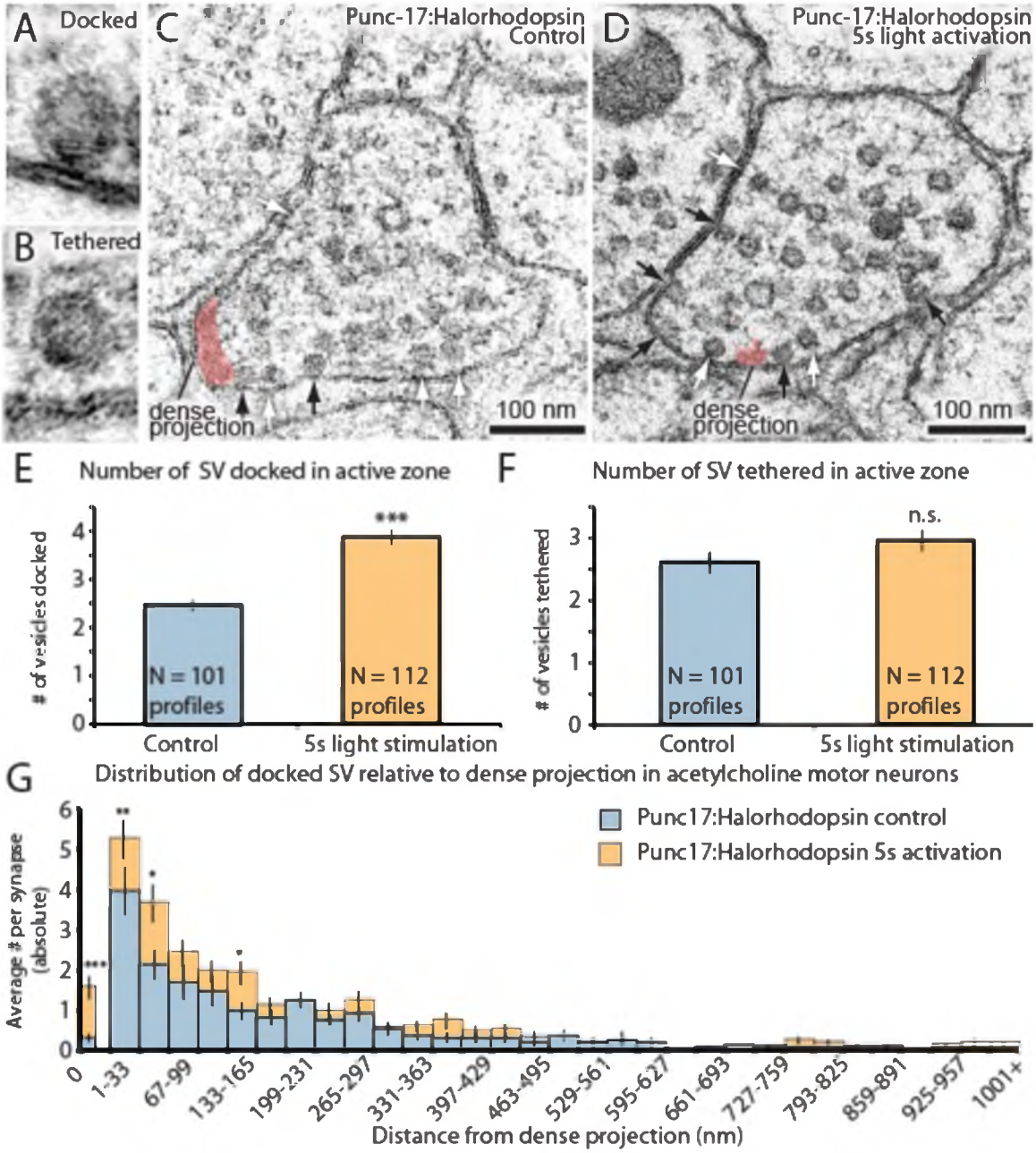
A Docked
B Tethered
C Punc-17:Halorhodopsin Control
D Punc-17:Halorhodopsin 5s light activation
dense projection
100 nm
E Number of SV docked in active zone
# of vesicles docked
N = 101 profiles
N = 112 profiles
***
Control
5s light stimulation
F Number of SV tethered in active zone
# of vesicles tethered
n.s.
G Distribution of docked SV relative to dense projection in acetylcholine motor neurons
Punc17:Halorhodopsin control
Punc17:Halorhodopsin 5s activation
Average # per synapse (absolute)
0
1-33
67-99
133-165
199-231
265-297
331-363
397-429
463-495
529-561
595-627
661-693
727-759
793-825
859-891
925-957
1001+
Distance from dense projection (nm)

Figure 7.3. Fusing vesicles are observed 20 ms after stimulation. (A, C-E) Sample electron micrographs of acetylcholine neuromuscular junctions 20 ms after depolarization by light stimulation of channelrhodopsin. Exocytic figures, indicated by the black arrow, with the size of a synaptic vesicle were present in the active zone, defined by the flanking adherens junctions. (B) An active zone was reconstructed from 27 serial sections for a total distance of ~900 nm. The reconstruction is cut open along the adherens junctions, and it shows the entire face of the active zone. Fusing vesicles are colored blue, docked vesicles are colored green. A large vesicle (orange) was observed above the dense projection (red) at this synapse. (C-E) Vesicle fusions in three different states show the possible sequence of events. The necks of these pits are wide, suggesting that vesicles are undergoing full collapse into the membrane. Average number of vesicles per profile docked (F) and tethered (G) in the active zone. The numbers were normalized the length of the active zone. Only the number of docked vesicles was reduced. (H) Distance of vesicle fusions to the dense projection in acetylcholine neurons. The absolute number is shown. Exocytic pits were observed across the entire length of the active zone. ***, **, * indicate p-values of <0.001, <0.01, and <0.05, respectively. n.s., 'not significant'. The standard error of the mean is shown in each graph.

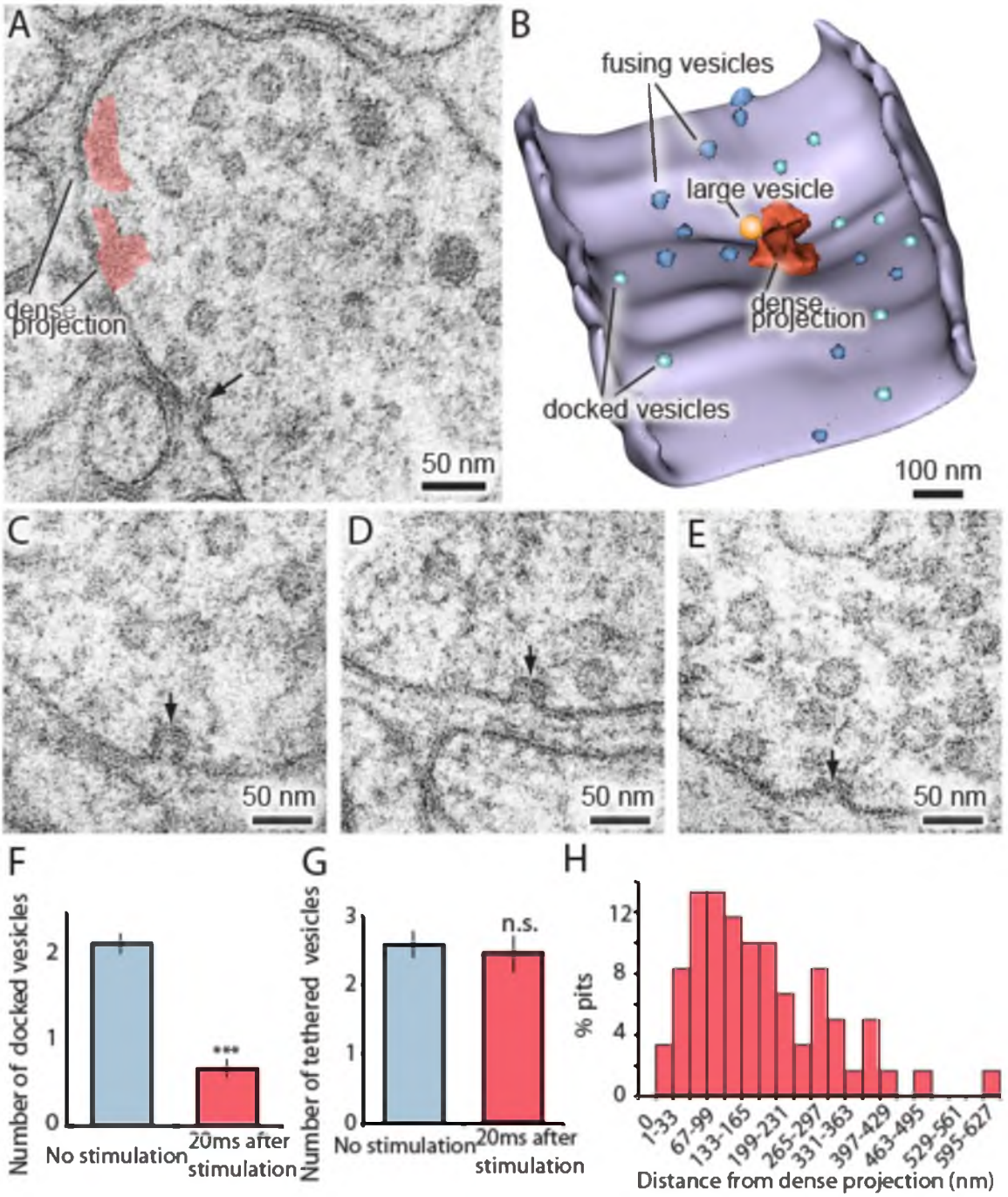
A
dense projection
50 nm
B
fusing vesicles
large vesicle
dense projection
docked vesicles
100 nm
C
50 nm
D
50 nm
E
50 nm
F
Number of docked vesicles
2
1
0
***
No stimulation
20ms after stimulation
G
Number of tethered vesicles
3
2
1
0
n.s.
No stimulation
20ms after stimulation
H
% pits
12
8
4
0
0
1-33
67-99
133-165
199-231
265-297
331-363
397-429
463-495
529-561
595-627
Distance from dense projection (nm)

Figure 7.4. The readily-releasable pool is solely constituted of docked vesicles. An electron micrograph of an unstimulated (A) and stimulated (B) acetylcholine motor neuron after depolarization by channelrhodopsin. Docked vesicles (black arrows) are present near the dense projection before the stimulation but are missing 50 ms after the stimulation. Tethered vesicles (white arrows) are present before and after stimulation. (C) Average number of vesicles per profile docked in active zones. The number is normalized by the size of active zones. A significant reduction in docked vesicles was observed in the active zone after depolarization (unstimulated 2.1± 0.1 SV per profile; stimulated 0.9 ± 0.1 SV; $p < 0.0001$). (D) Average number of vesicles per profile tethered in the active zone. The number is normalized by the size of active zones. No reduction in tethered vesicles was observed after depolarization (unstimulated 3.2 ± 0.2 SV per profile; stimulated 3.4 ± 0.3 SV; $p = 0.34$). (E) Distance of docked vesicles to dense projection in acetylcholine neurons. The absolute number is shown. Docked vesicles are released across the entire length of the active zone. (F) Average number of docked vesicles per profile in the perisynaptic zone before and after stimulation. The number is normalized by the size of perisynaptic zone. The docked vesicles in the perisynaptic zone were not released by a single stimulus ($p = 0.95$). (G) The active zone extends from the dense projection to the flanking adherens junctions at *C. elegans* neuromuscular junctions based on where synaptic vesicles fuse. Note that the side of the neuron that faces the muscle (bottom) can be very broad. ***, **, and * indicate p-values of <0.001, <0.01, and <0.05, respectively. n.s. stands for 'not significant'. The standard error of the mean is shown in all graphs.

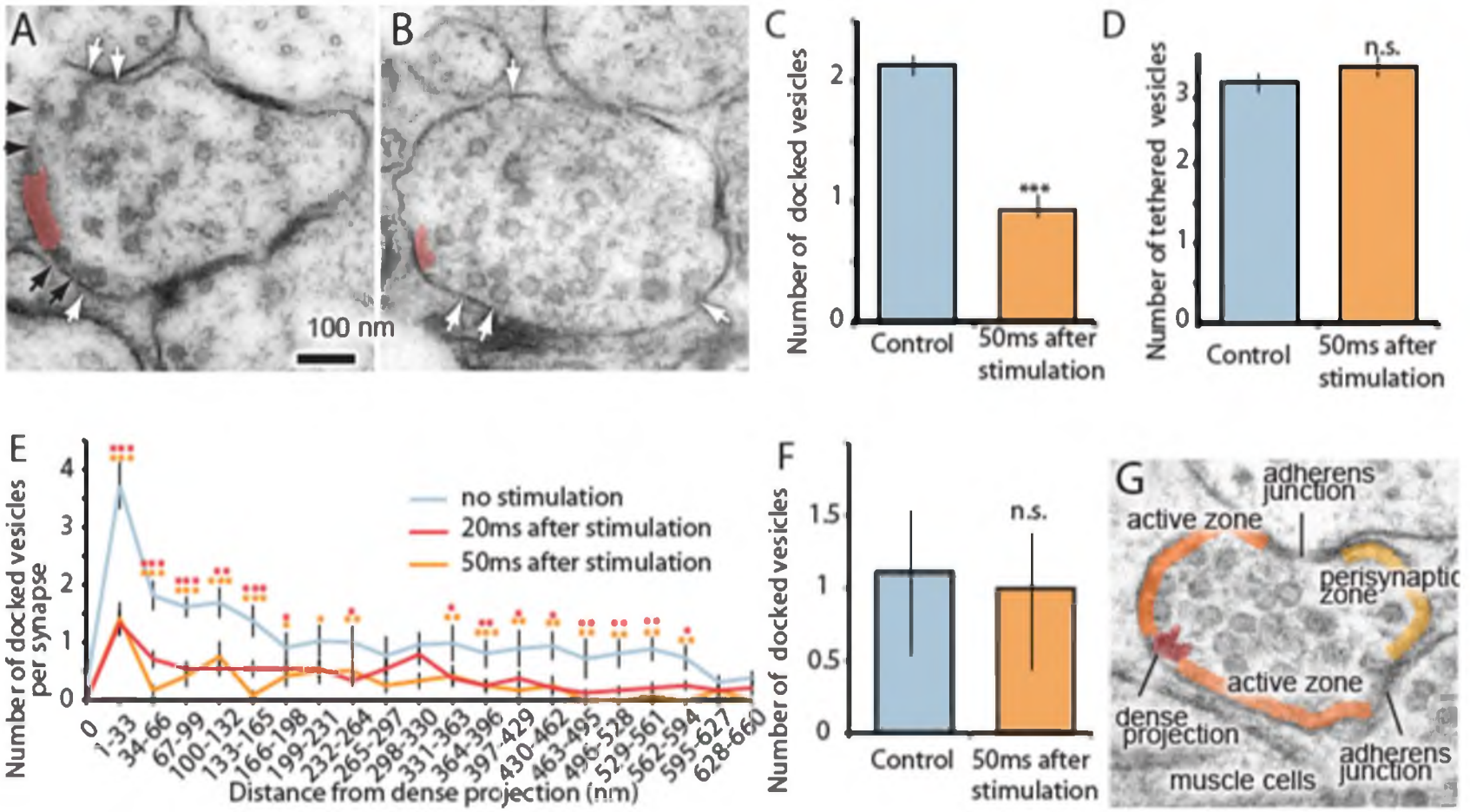
A
B
100 nm
C
Number of docked vesicles
***
Control
50ms after stimulation
D
Number of tethered vesicles
n.s.
Control
50ms after stimulation
E
Number of docked vesicles per synapse
no stimulation
20ms after stimulation
50ms after stimulation
0
1-33
34-66
67-99
100-132
133-165
166-198
199-231
232-264
265-297
298-330
331-363
364-396
397-429
430-462
463-495
496-528
529-561
562-594
595-627
628-660
Distance from dense projection (nm)
F
Number of docked vesicles
n.s.
Control
50ms after stimulation
G
adherens junction
active zone
perisynaptic zone
active zone
dense projection
adherens junction
muscle cells

Figure 7.5. Physiological recovery corresponds to replenishment of docking sites. (A) Sample traces for paired-pulse stimulations using channelrhodopsin recorded from an adult body muscle (*acr-16(ok789); oxSi91[Punc17::ChIEF::mCherry]).* The second pulses are indicated by colors: yellow, 100 ms; green, 300 ms; emerald, 1000 ms; blue, 3000 ms; and dark blue, 10000 ms. (B) Recovery of evoked responses in paired pulse stimulations. The ratios of the second current peak (P_i) to the first current peak (P_1) were calculated and plotted relative to the recovery intervals. There are two time constants for recovery: the first tau was 0.1 ms, and the second tau was 2.2 s. The rapid recovery (τ = 100 ms) is likely due to the resensitization of acetylcholine-gated ion channels (Mike et al., 2000) or the deactivation of presynaptic calcium-activated potassium channels (Dworetzky et al., 1996; Vergara et al., 1998) or a transition of docked vesicles from an incompetent to competent state (Zenisek et al., 2000), rather than the translocation and docking of vesicles. (C) Average number of vesicles per profile docked in the active zone are plotted relative to the intervals between stimulation and freezing. The intervals are indicated by colors: black, no stimulation; red, 20 ms; orange, 50 ms; yellow, 100 ms; green, 300 ms; emerald, 1000 ms; blue, 3000 ms; and dark blue, 10000 ms. The time constant for the recovery was 2.4 s. (D) Average number of vesicles docked in the active zone at various time points after the stimulus. Docked vesicles were reduced at time points before 3 s (non-stimulated: 3.0 ± 0.2, N = 102 profiles; no retinal 50 ms: 3.2 ± 0.1, p = 0.007; 20 ms: 1.0 ± 0.1, p<0.0001; 50 ms: 1.0 ± 0.1, p<0.0001; 100 ms: 1.1 ± 0.1, p<0.0001; 300 ms: 1.0± 0.1, p<0.0001;1 s: 1.5 ± 0.1, p<0.0001; 3 s: 2.8 ± 0.2, p=0.97; 10 s: 3.1 ± 0.1, p=0.01). (E) Total number of synaptic vesicles, averaged per profile. A slight reduction in the total number of synaptic vesicles was observed after stimulation (non-stimulated: 32 ± 1.0; no retinal 50 ms: 31 ± 1.2, p = 0.01; 20ms: 26 ± 1.4, p < 0.007; 50 ms: 27 ± 1.1, p < 0.001; 100 ms: 26 ± 1.3, p < 0.001; 300 ms: 31 ± 1.4, p = 0.007; 1 s: 30 ± 1.3, p = 0.042; 3 s: 30 ± 1.1, p = 0.032; 10 s: 31 ± 0.9, p = 0.01). (F) Percentage of vesicles per profile tethered in the active zone. The size of the tethered pool drops initially after stimulation (non-stimulated: 4.1 ± 0.3; no retinal 50 ms: 4.0 ± 0.2, p = 0.08; 20 ms: 4.3 ± 0.4, p = 0.41; 50 ms: 3.3 ± 0.3, p < 0.0001; 100 ms: 3.2 ± 0.4, p < 0.0001; 300 ms: 4.3 ± 0.4, p = 0.01; 1 s: 5.1 ± 0.4, p = 0.04; 3 s: 4.2 ± 0.4, p = 0.32; 10 s: 4.0 ± 0.2, p = 0.4). The numbers in (D-F) are normalized by the area of profiles to account for differences in the size of varicosities. All the p values were calculated against no stimulation control. Bonferroni correction was applied for multiple comparisons. ***, ** and * indicate p-values of <0.0001, <0.001 and <0.007, respectively. n.s., 'not significant'. N values: not-stimulated: 102 profiles; no retinal 50 ms: 51 profiles; 20 ms: 50 profiles; 50 ms: 104 profiles; 100 ms: 83 profiles; 300 ms: 89 profiles; 1 s: 111 profiles; 3 s: 91 profiles; 10 s: 121 profiles. The standard error of the mean is shown in each graph.

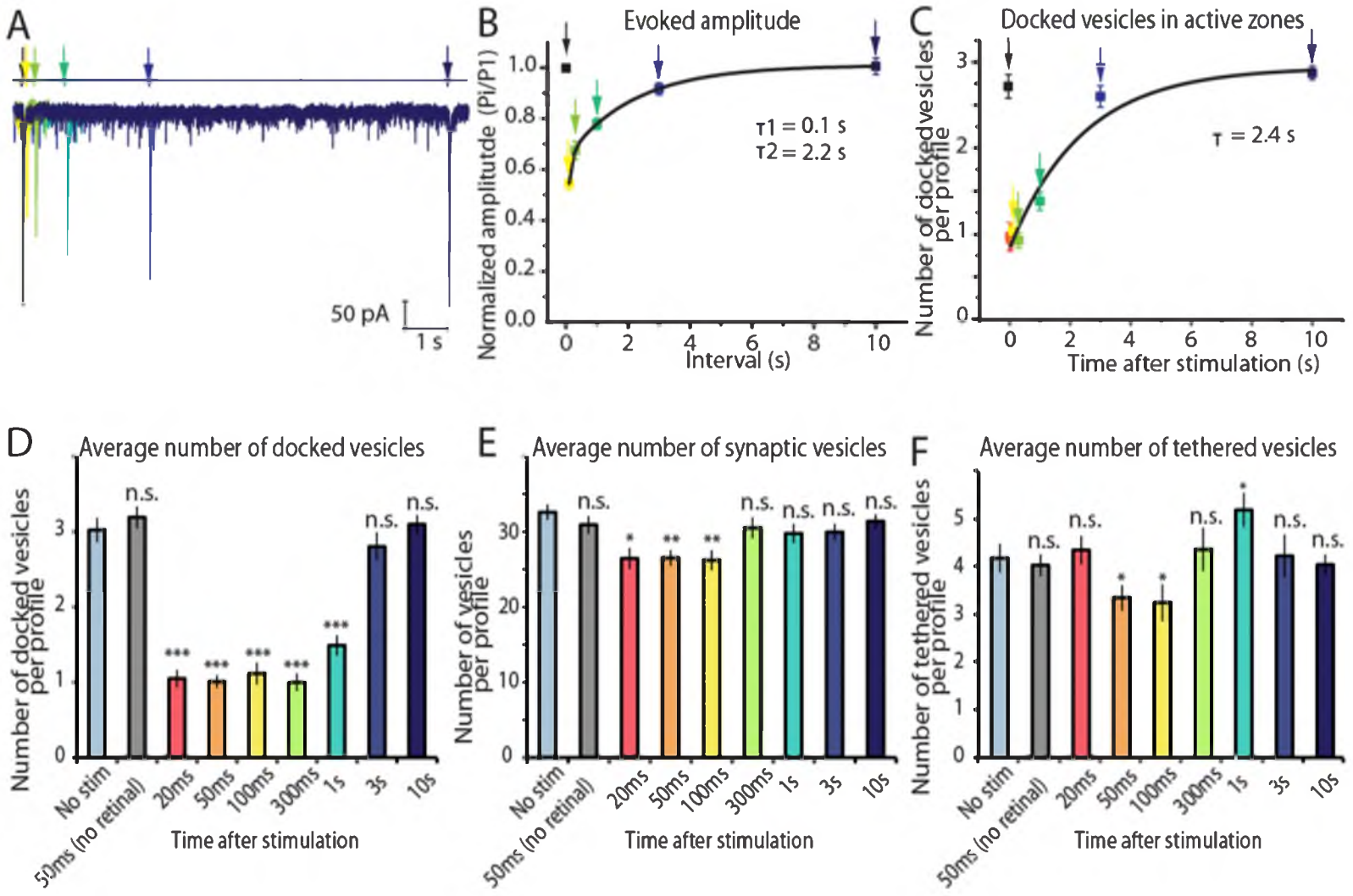
A
50 pA
1 s
B
Evoked amplitude
Normalized amplitude (P1/P1)
τ1 = 0.1 s
τ2 = 2.2 s
Interval (s)
C
Docked vesicles in active zones
Number of docked vesicles per profile
τ = 2.4 s
Time after stimulation (s)
D
Average number of docked vesicles
Number of docked vesicles per profile
Time after stimulation
E
Average number of synaptic vesicles
Number of vesicles per profile
Time after stimulation
F
Average number of tethered vesicles
Number of tethered vesicles per profile
Time after stimulation
No stim
50ms (no retinal)
20ms
50ms
100ms
300ms
1s
3s
10s
n.s.

Figure 7.6. Ultrafast endocytosis takes place near the dense projection. (A) Average size of exocytic pits in active zone and large invaginations at dense projections. The diameter of large structures at dense projections was ~ 1.5 times larger than that of exocytic pits observed at 20 ms after stimulation. N is 53 for exocytic pits and 35 for pits and large vesicles at dense projection. *** indicates a p-value of <0.0001. (B) Average number of large vesicles within a radial distance of 100 nm from the dense projection per synapse. These large vesicles only appear transiently near dense projections after the stimulation of channelrhodopsin (wild-type unstimulated: 0 ± 0; no retinal 50 ms: 0.2 ± 0.1 ; 20 ms: 0.6 ± 0.1; 50 ms: 2.3 ± 0.1; 100 ms: 1.4 ± 0.1; 300 ms: 1.1 ± 0.1; 1 s: 1.1 ± 0.1; 3 s: 0.5 ± 0.1; 10 s: 0.3 ± 0.4; *unc-13* unstimulated: 1.0 ± 0.1; *unc-13* stimulated: 0.5 ± 0.1). (C) Average number of large vesicles in the whole terminal per synapse is plotted from the wild type (P*unc-17::ChIEF::mCherry*) and *unc-13 (unc-13(s69);* P*unc-17::ChIEF::mCherry*) animals. A synapse is defined as a collection of profiles containing the same dense projection. Large vesicles are defined as clear-core vesicles with a diameter larger than 35 nm (wild-type unstimulated: 1.8 ± 0.1; no retinal 50 ms: 0.6 ± 0.1 ; 20 ms: 1.2 ± 0.2; 50 ms: 2.9 ± 0.2; 100 ms: 3.1 ± 0.1; 300 ms: 2.8 ± 0.1; 1 s: 2.1 ± 0.1; 3 s: 1.4 ± 0.1; 10 s: 1.3 ± 0.1; *unc-13* unstimulated: 1.6 ± 0.3; *unc-13* stimulated: 1.4 ± 0.3). (D-F) Example electron micrographs showing large invagination at the dense projection of an acetylcholine motor neuron 20 ms after stimulation (D) and large vesicles near dense projections 50 ms (E) and 100 ms (F) after stimulation. (G-H) An electron tomogram and a hand-segmented model of an acetylcholine motor neuron synapse captured at 20 ms after stimulation. A large invagination of membrane is visible next to the dense projection. (I) The numbers of large vesicles within 100 nm radius of a dense projection are plotted against their diameter. The background shading indicates the expected size distribution for vesicles composed of 1, 2 or 3 synaptic vesicles. There are two populations of large vesicles: one peaks at 38 nm and the other at 46 nm. R^2 value for bimodal distribution was 0.88 whereas that for unimodal was 0.78. Akaike information criterion for unimodal, bimodal, and trimodal distributions were 352.6, 346.4, and 353.9, respectively, supporting the bimodal distribution. Interestingly, the difference between the peaks is equivalent to the amount of membrane in a single synaptic vesicle. N for each condition in (A) and (B) was as follows: non-stimulated: 26 synapses; no retinal 50 ms: 12 synapses; 20 ms: 12 synapses; 50 ms: 24 synapses; 100 ms: 19 synapses; 300 ms: 20 synapses; 1 s: 23 synapses; 3 s: 19 synapses; 10 s: 26 synapses; *unc-13* unstimulated: 11 synapses; *unc-13* stimulated: 14 synapses. The standard error of the mean is shown in each graph.

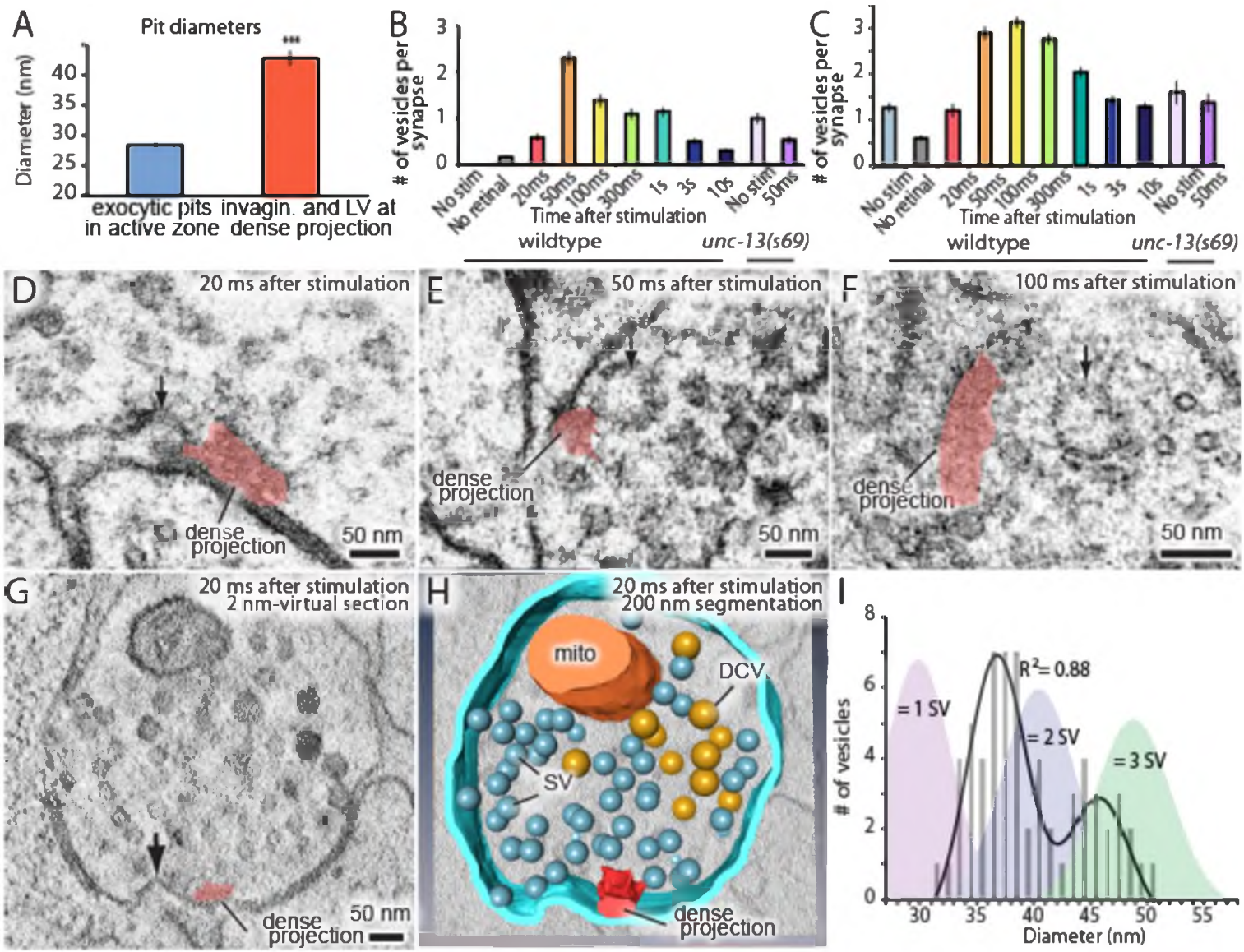
A
Pit diameters
Diameter (nm)
40
35
30
25
20
***
exocytic pits
invagin. and LV at
in active zone
dense projection
B
# of vesicles per synapse
3
2
1
0
No stim
No retinal
20ms
50ms
100ms
300ms
1s
3s
10s
No stim
50ms
Time after stimulation
wildtype
unc-13(s69)
C
# of vesicles per synapse
3
2
1
0
No stim
No retinal
20ms
50ms
100ms
300ms
1s
3s
10s
No stim
50ms
Time after stimulation
wildtype
unc-13(s69)
D
20 ms after stimulation
dense projection
50 nm
E
50 ms after stimulation
dense projection
50 nm
F
100 ms after stimulation
dense projection
50 nm
G
20 ms after stimulation
2 nm-virtual section
dense projection
50 nm
H
20 ms after stimulation
200 nm segmentation
mito
DCV
SV
dense projection
I
# of vesicles
8
6
4
2
0
R²= 0.88
= 1 SV
= 2 SV
= 3 SV
30
35
40
45
50
55
Diameter (nm)

Figure 7.7. Endocytosis adjacent to adherens junctions is fast. (A) A shallow pit is present adjacent to the adherens junction (arrow) 100 ms after stimulation. (B) A deep invagination at the adherens junction 1 s after stimulation. (C) A large clear vesicle near the adherens junction 3 s after stimulation. (D) Clathrin coats can be preserved through high-pressure freezing and freeze-substitution. An electron micrograph of a clathrin-coated vesicle in an endophilin mutant captured with the same fixation protocol and equipment. (E) Average number of shallow pits at adherens junctions (light orange) and large vesicles associated with adherens junctions (dark orange) per synapse. The decline of shallow pits is followed by an increase in large vesicles at adherens junctions. N values: non-stimulated: 26 synapses; no retinal 50 ms: 12 synapses; 20 ms: 12 synapses; 50 ms: 24 synapses; 100 ms: 19 synapses; 300 ms: 20 synapses; 1 s: 23 synapses; 3 s: 19 synapses; 10 s: 26 synapses. A synapse is defined as a collection of profiles containing the same dense projection. (F) Average number of shallow pits at adherens junctions per synapse. The time constant for the resolution of pits is 1.4 s. (G) Distance of shallow pits to adherens junctions after the stimulation. Average number per synapse is shown. The pits are next to adherens junctions. The standard error of the mean is shown in each graph.

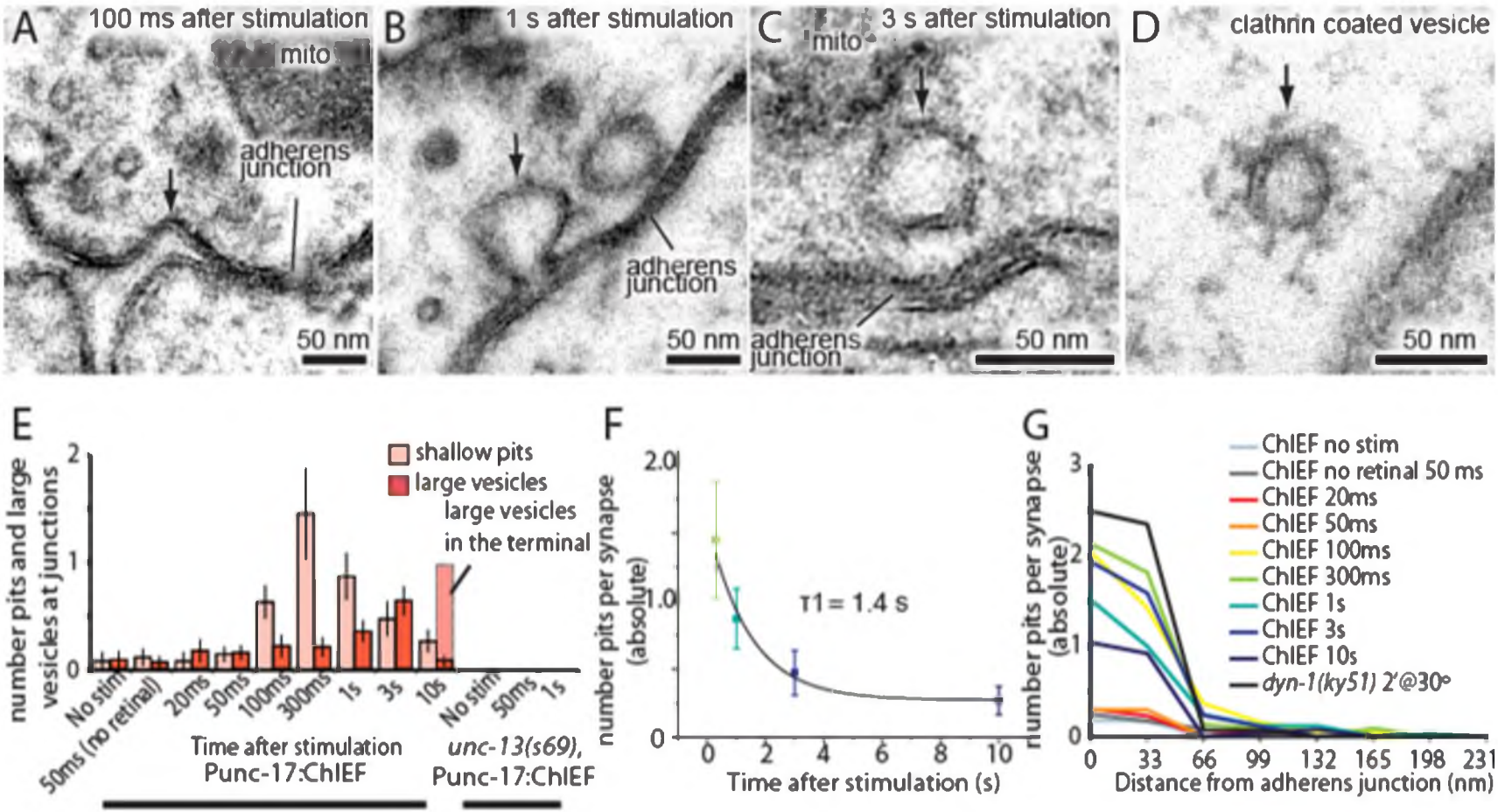
A
100 ms after stimulation
mito
adherens junction
50 nm
B
1 s after stimulation
adherens junction
50 nm
C
mito
3 s after stimulation
adherens junction
50 nm
D
clathrin coated vesicle
50 nm
E
number pits and large vesicles at junctions
shallow pits
large vesicles
large vesicles in the terminal
No stim
50ms (no retinal)
20ms
50ms
100ms
300ms
1s
3s
10s
No stim
50ms
1s
Time after stimulation
Punc-17:ChIEF
unc-13(s69),
Punc-17:ChIEF
F
number pits per synapse (absolute)
τ1 = 1.4 s
Time after stimulation (s)
G
number pits per synapse (absolute)
ChIEF no stim
ChIEF no retinal 50 ms
ChIEF 20ms
ChIEF 50ms
ChIEF 100ms
ChIEF 300ms
ChIEF 1s
ChIEF 3s
ChIEF 10s
dyn-1(ky51) 2'@30°
Distance from adherens junction (nm)

Figure 7.8. Dynamin is required for fast endocytosis. (A-D) DYN-1::tdEos localization using nano-resolution fluorescence electron microscopy (nano-fEM). (A) PALM localizations are overlaid on a scanning electron micrograph acquired from the same 70 nm section. 5000 frames were acquired to reconstruct PALM signals; diameter of signal represents full-width half-maximum, white represents density of fluorophores. (B) A magnification detail from (A). PALM localizations were assigned a 5nm arbitrary diameter to show the location of each fluorophore. (C) A schematic diagram showing the categories used to analyze the distribution of molecules. Signals within 50 nm of membrane and within 100 nm of the structure of interest (within dotted area) were counted in the pool. (D) Quantification of dynamin molecules in the different regions of a synapse. Dynamin accumulates at dense projections and adherens junctions ($p<0.001$). (E-G) Example electron micrographs showing morphology of an acetylcholine motor neuron from the dynamin temperature-sensitive mutant *dyn-1(ky51)* at the permissive temperature (E) and at the restrictive temperature (30ºC) for 2 min (F and G). Large vesicles near the dense projection (F) and adherens junction (G) are stabilized only when the mutants were exposed to the restrictive temperature.

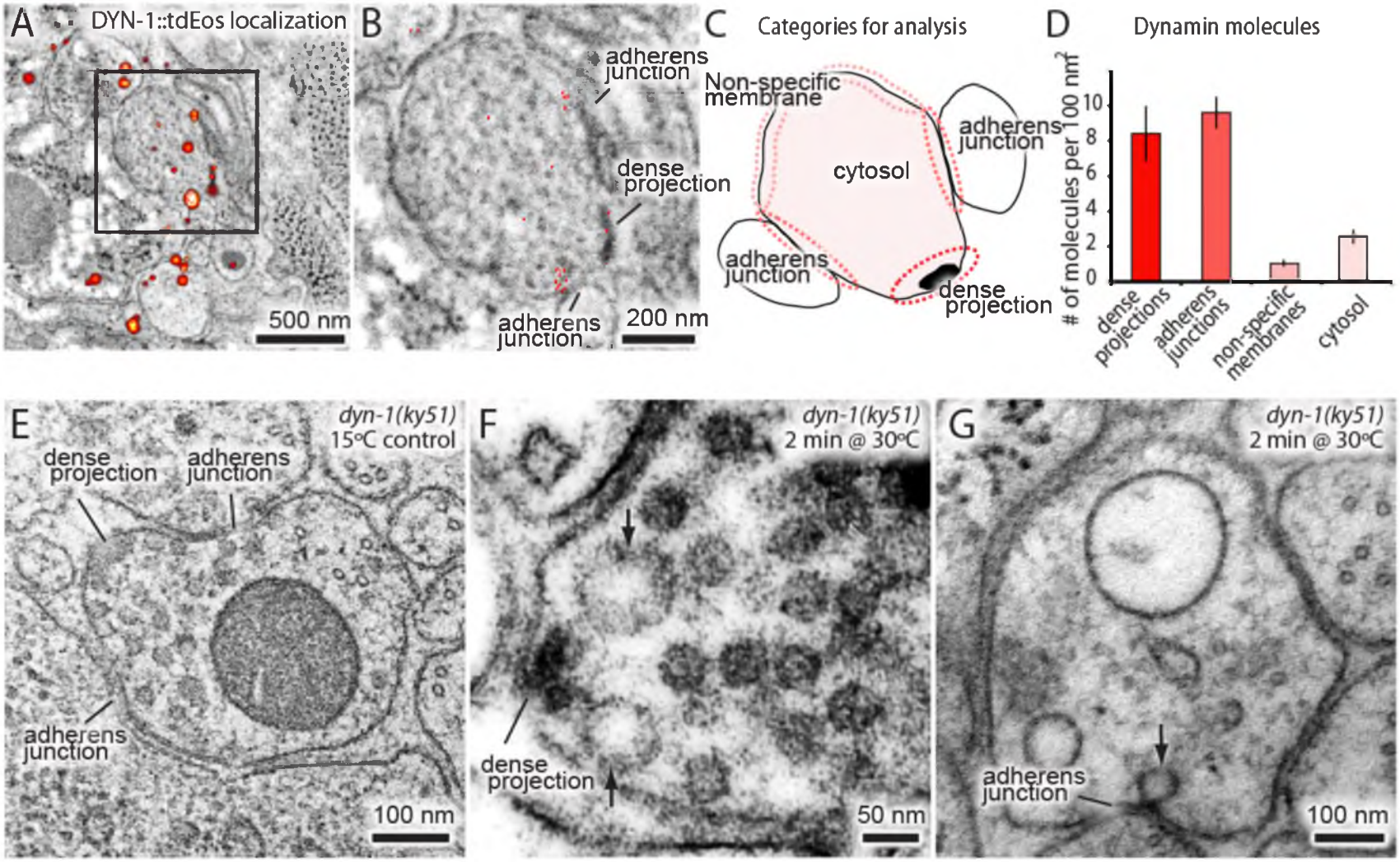
A
DYN-1::tdEos localization
500 nm
B
adherens junction
dense projection
adherens junction
200 nm
C
Categories for analysis
Non-specific membrane
adherens junction
cytosol
adherens junction
dense projection
D
Dynamin molecules
# of molecules per 100 nm²
0
2
4
6
8
10
dense projections
adherens junctions
non-specific membranes
cytosol
E
dyn-1(ky51)
15°C control
dense projection
adherens junction
adherens junction
100 nm
F
dyn-1(ky51)
2 min @ 30°C
dense projection
50 nm
G
dyn-1(ky51)
2 min @ 30°C
adherens junction
100 nm

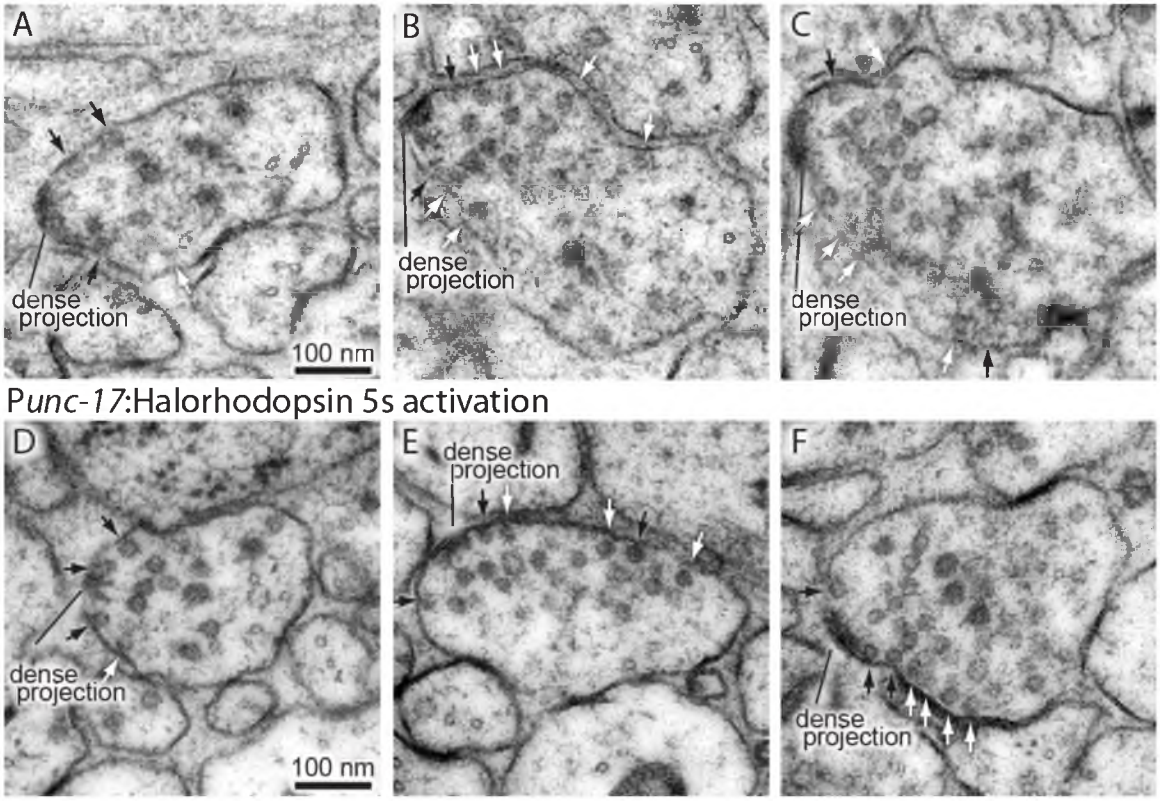

Figure 7.S1. Endogenous tonic release sites are in the proximity of the dense projection. Additional representative micrographs showing synapses from *C. elegans* acetylcholine motor neurons before (A-C) and 5 s after (D-F) activation of halorhodopsin. Docked vesicles are marked with black arrows, and tethered vesicles are indicated by white arrows.

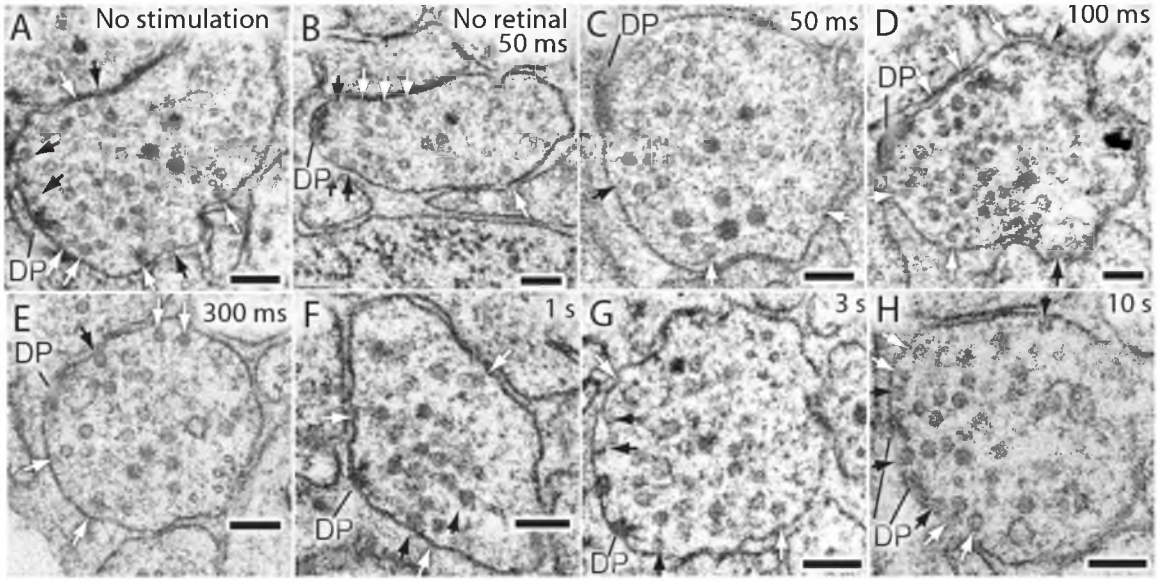

Figure 7.S2. The readily-releasable pool is solely constituted of docked vesicles. A representative micrograph showing synapses from the *C. elegans* acetylcholine motor neurons, expressing ChIEF channelrhodopsin, unstimulated (A), stimulated in the absence of trans-retinal (B), 50 ms after stimulation (C), 100 ms after stimulation (D), 300 ms after stimulation (E), 1 s after stimulation (F), 3 s after stimulation (G), and 10 s after stimulation (H). Docked vesicles are marked with black arrows, and tethered vesicles are indicated by white arrows. Note that the number of docked vesicles recovers with rest. DP, dense projection. The scale bars are 100 nm.

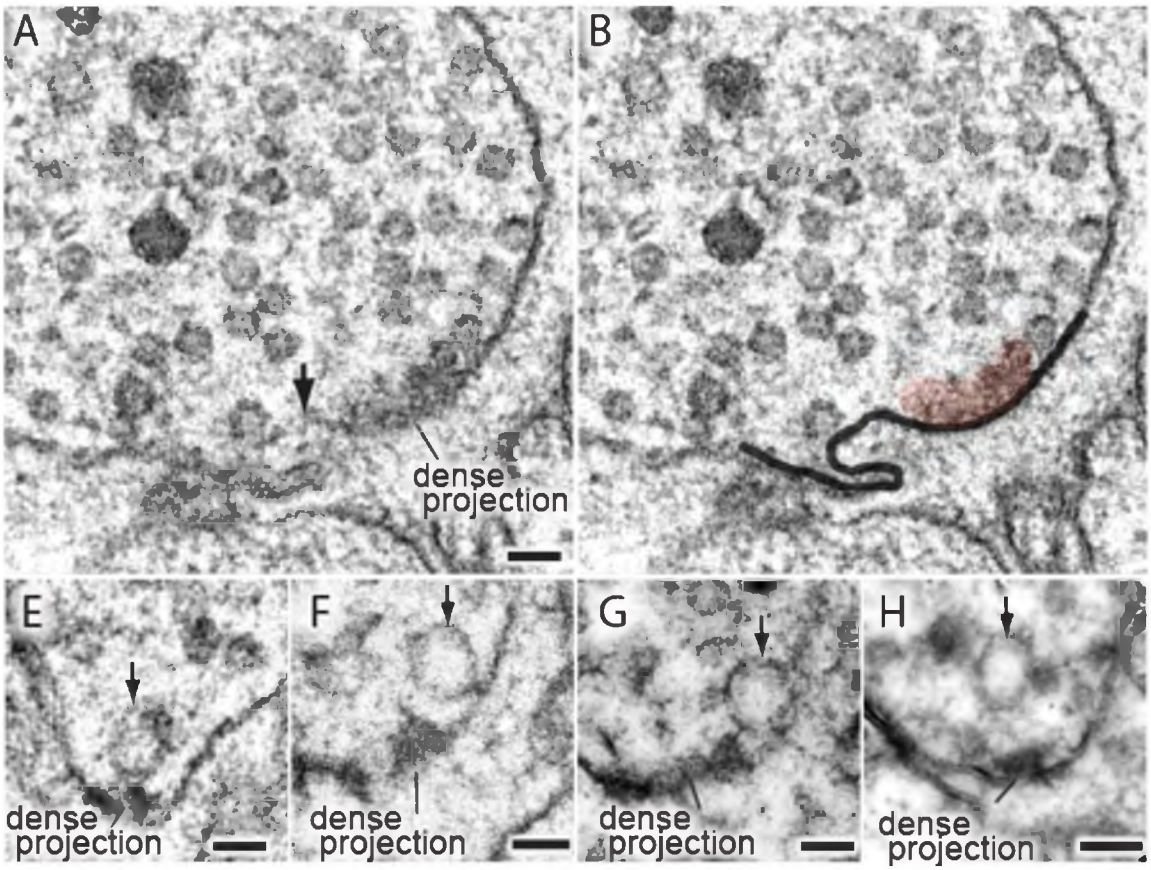

Figure 7.S3. Fast endocytosis takes place near the dense projection. Additional representative micrographs showing a large invagination (A,B) and large vesicles near the dense projections 20 ms (C), 50 ms (F,G), and 100 ms after stimulation (H). The large invagination in (A) is traced in (B). These large vesicles only appear transiently after the stimulation of channelrhodopsin. Black arrows indicate the large endocytic structures. The scale bars are 50 nm.

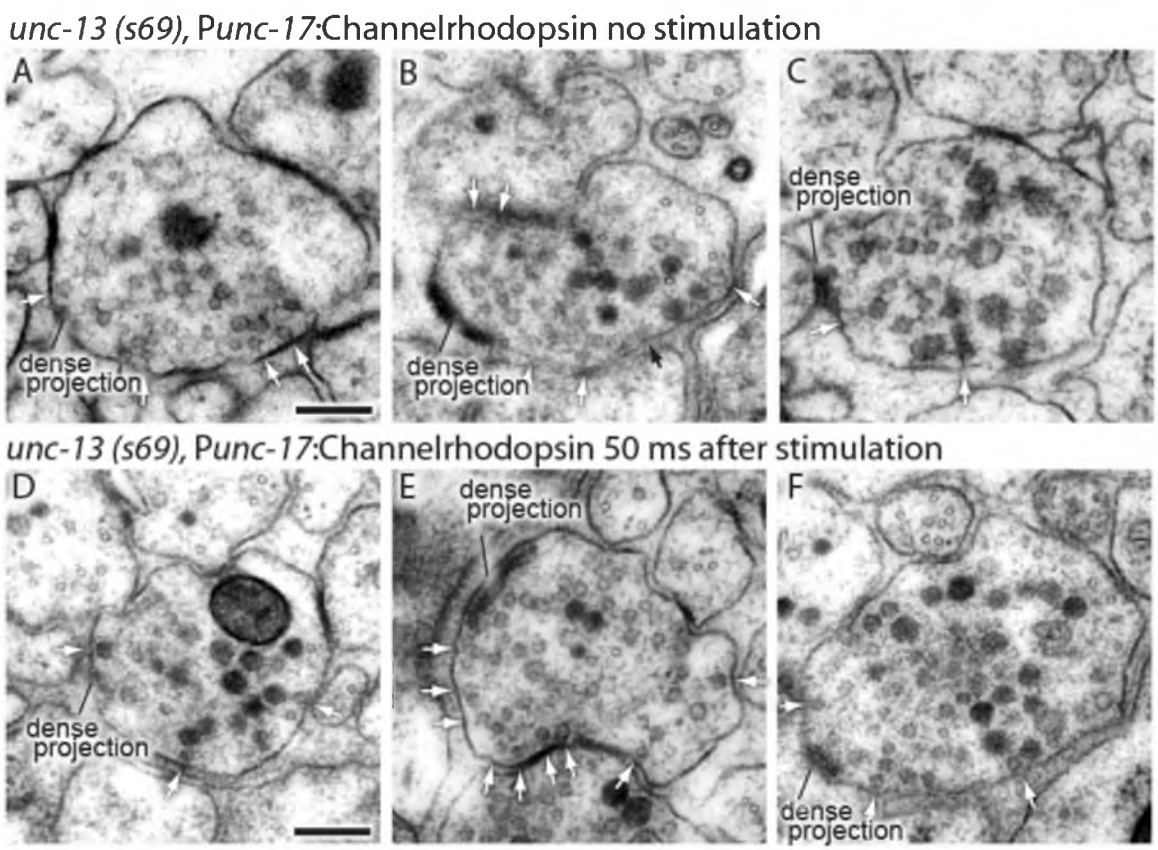

Figure 7.S4. Endocytosis is coupled to exocytosis. Representative micrographs showing synapses from *unc-13 (s69)* mutants unstimulated (A-C) and stimulated by light activation of ChIEF (D-F). Large vesicles do not appear in *unc-13* mutants, suggesting that endocytosis is triggered by neurotransmission. Docked vesicles are marked with black arrows, and tethered vesicles are indicated by white arrows. The scale bars are 100 nm.

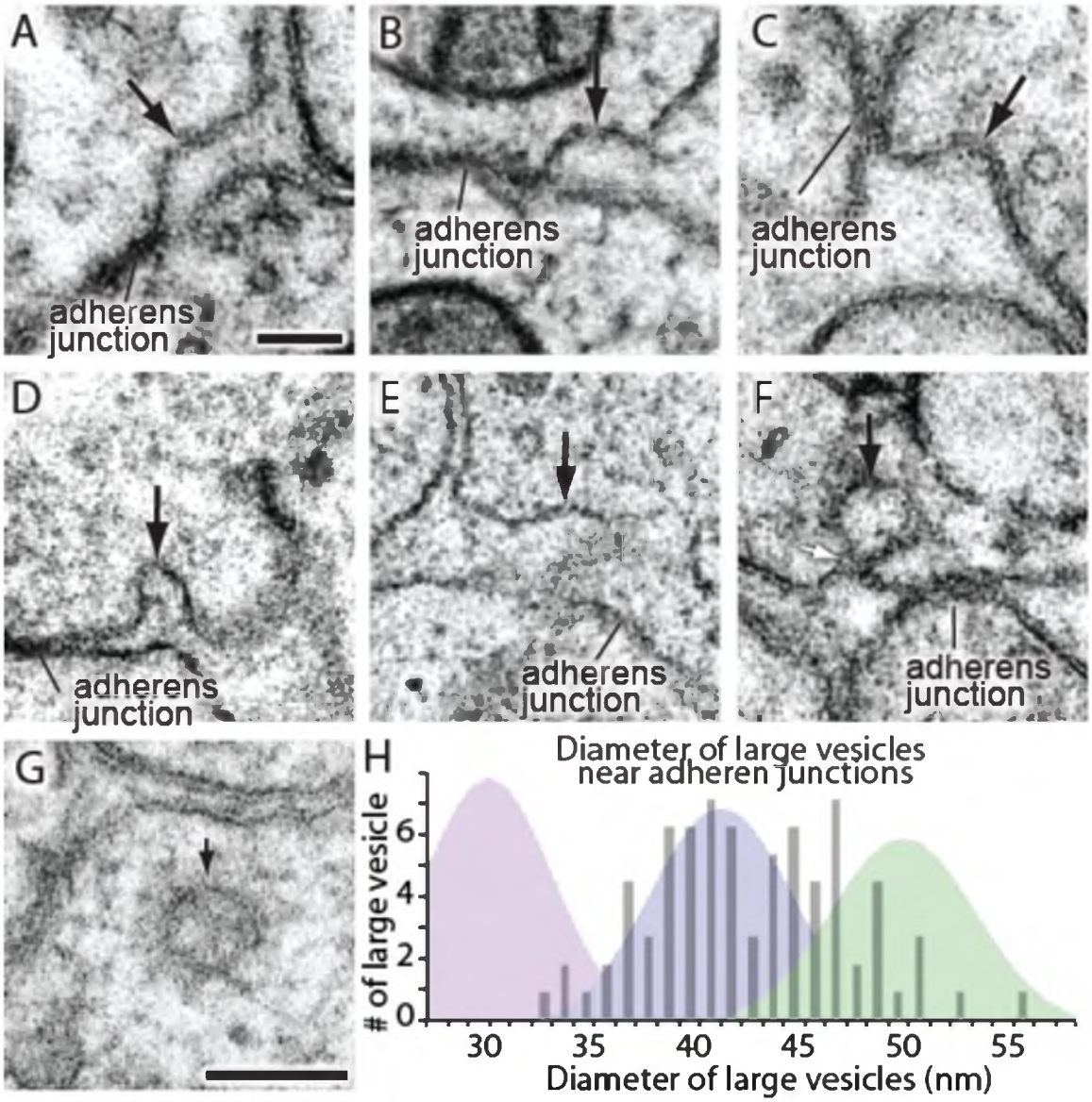

Figure 7.S5. Pits appear next to adherens junctions. Additional representative micrographs showing acetylcholine neuromuscular junctions from animals expressing ChIEF, 100 ms (A), 300 ms (B-C), and 1 s after stimulation (D-F). Black arrows indicate pits; the white arrow indicates the neck of the endocytic pit. (G) An additional representative micrograph showing a clathrin-coated vesicle. Clathrin-coats can be preserved in our fixation protocol. (H) The number of large vesicles near adherens junctions from 3 s and 10 s after stimulation is plotted against their diameter. The graph is shaded to indicate the number of synaptic vesicles that can be incorporated into the given size of the large vesicle; it is not clear if the distribution is unimodal or bimodal. The scale bars are 50 nm.

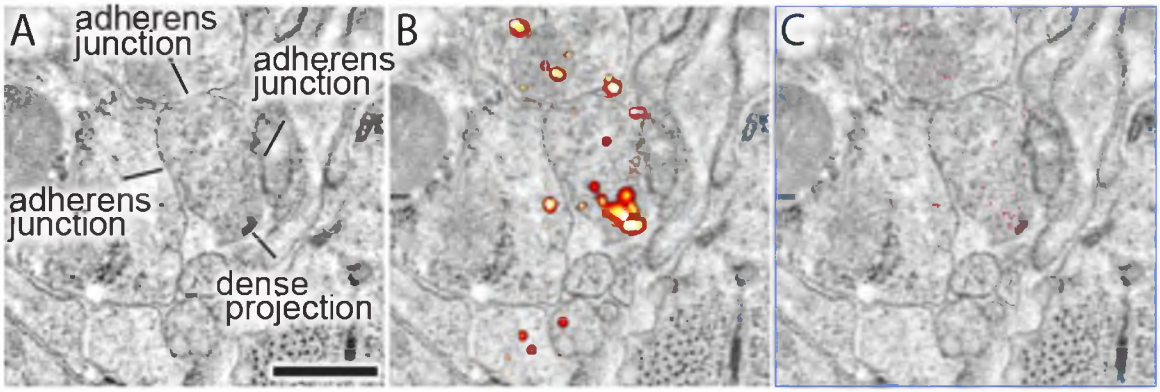

Figure 7.S6. Dynamin localizes to dense projections and adherens junctions. (A-C) Additional representative correlative image showing the localization of DYN-1::tdEos. (A) Scanning electron micrograph of section containing a neuromuscular junction. (B) PALM signals are overlaid on the corresponding electron micrograph. Diameter of spot represents the full-width half-maximum localization precision, intensity indicates density of localizations. (C) Arbitrary 5 nm dots representing the location of each fluorophore are overlaid on the corresponding scanning electron micrograph. The scale bar is 500 nm.

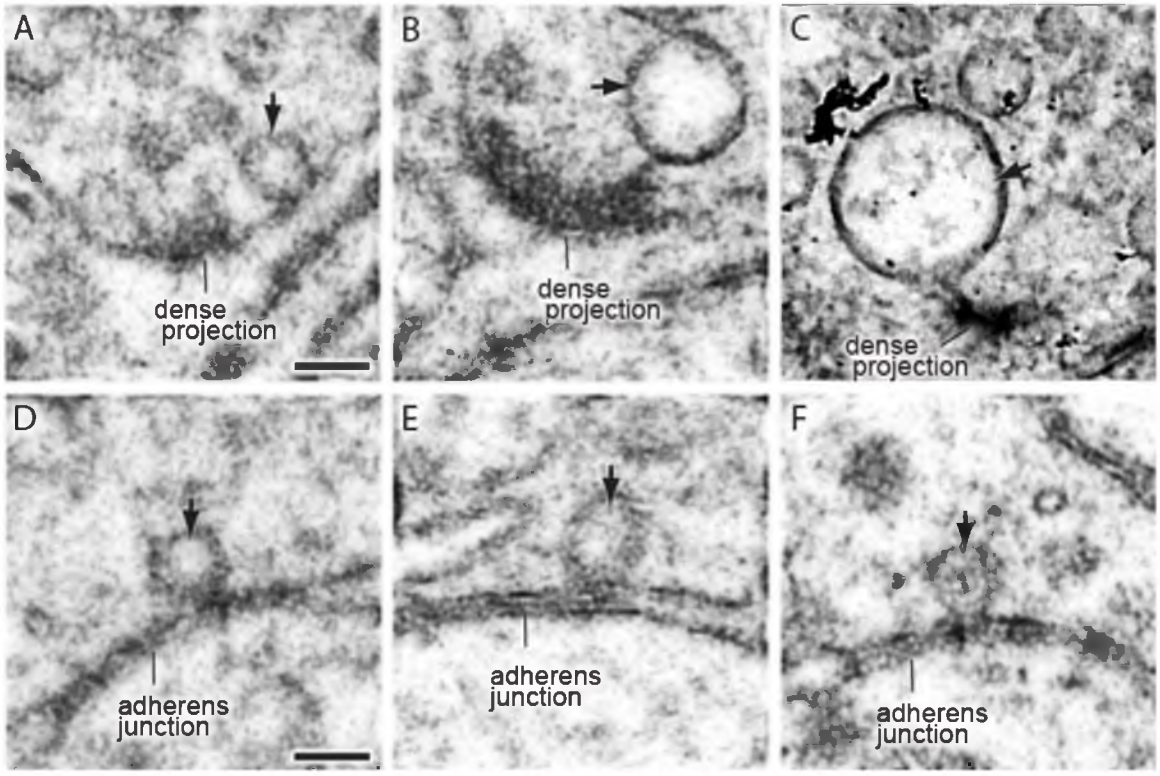

Figure 7.S7. Putative endocytic structures are trapped at dense projections (above) and adherens junctions (below) in *dyn-1 (ky51)* mutants. Additional representative micrographs showing large endocytic structures near the dense projection (A-C) and at adherens junctions (D-F) from the mutants shifted from the permissive temperature (15°) to the restrictive temperature (30ºC) for 2 min (A, B, and D-F) and for 5 min (C). Endocytic structures are trapped at dense projections and adherens junctions. Note that the neck of the endocytic structure is visible in an animal that was incubated at 30ºC for 5 min (C). Black arrows indicate the large endocytic structures. Only acetylcholine synapses are shown. The scale bars are 100 nm.

CHAPTER 8

DETECTION OF NEURON MEMBRANES IN ELECTRON MICROSCOPY IMAGES USING A SERIAL NEURAL NETWORK ARCHITECTURE

Reprinted with permission from the Elsevier Inc.

Jurrus, et al., 2010. Originally published in Medical Image Analysis. VOL. 14: 770-783

ARTICLE IN PRESS

Medical Image Analysis xxx (2010) xxx–xxx

Contents lists available at ScienceDirect

Medical Image Analysis

journal homepage: www.elsevier.com/locate/media

Detection of neuron membranes in electron microscopy images using a serial neural network architecture

Elizabeth Jurrus [a,b,*], Antonio R.C. Paiva [a], Shigeki Watanabe [c], James R. Anderson [e], Bryan W. Jones [e], Ross T. Whitaker [a,b], Erik M. Jorgensen [c], Robert E. Marc [e], Tolga Tasdizen [a,d]

[a] Scientific Computing and Imaging Institute, Salt Lake City, UT, United States
[b] School of Computing, University of Utah, 50 S. Central Campus Drive, Room 3190, Salt Lake City, UT 84112, United States
[c] Department of Biology, University of Utah, 257 South 1400 East, Salt Lake City, UT 84112, United States
[d] Department of Electrical and Computer Engineering, University of Utah, 50 S. Central Campus Dr., Rm. 3280 MEB Salt Lake City, UT 84112-9206, United States
[e] Moran Eye Center, University of Utah School of Medicine, 65 Medical Drive, 53881 Moran, Salt Lake City, UT 84132, United States

ARTICLE INFO

Article history:
Received 23 June 2009
Received in revised form 15 April 2010
Accepted 3 June 2010
Available online xxxx

Keywords:
Machine learning
Membrane detection
Artificial neural networks
Contour completion
Neural circuit reconstruction

ABSTRACT

Study of nervous systems via the connectome, the map of connectivities of all neurons in that system, is a challenging problem in neuroscience. Towards this goal, neurobiologists are acquiring large electron microscopy datasets. However, the shear volume of these datasets renders manual analysis infeasible. Hence, automated image analysis methods are required for reconstructing the connectome from these very large image collections. Segmentation of neurons in these images, an essential step of the reconstruction pipeline, is challenging because of noise, anisotropic shapes and brightness, and the presence of confounding structures. The method described in this paper uses a series of artificial neural networks (ANNs) in a framework combined with a feature vector that is composed of image intensities sampled over a stencil neighborhood. Several ANNs are applied in series allowing each ANN to use the classification context provided by the previous network to improve detection accuracy. We develop the method of serial ANNs and show that the learned context does improve detection over traditional ANNs. We also demonstrate advantages over previous membrane detection methods. The results are a significant step towards an automated system for the reconstruction of the connectome.

1. Introduction

Neural circuit reconstruction, i.e. the *connectome* (Sporns et al., 2005), is currently one of the grand challenges facing neuroscientists. Similarly, the National Academy of Engineering has listed reverse-engineering the brain as one its grand challenges.[1] While neural circuits are central to the study of the nervous system, relatively little is known about differences in existing neuronal classes, patterns, and connections. Electron microscopy (EM) is an unique modality for scientists attempting to map the anatomy of individual neurons and their connectivity because it has a resolution that is high enough to identify synaptic contacts and gap junctions. These are important indicators for types of neuron topology and are required for neural circuit reconstruction. Several researchers have undertaken extensive EM imaging projects in order to create detailed maps of neuronal structure and connectivity (Fiala and Harris, 2001; Briggman and Denk, 2006a). Early work in this area, by White et al. (1986), includes the complete mapping of the nematode *Caenorhabditis elegans* nervous system. This is a simple organism, containing just over 300 neurons and 6000 synapses, yet it took nearly a decade to identify all the relevant structures and reconstruct the connectivity.[2] In comparison, newer imaging techniques are producing much larger volumes of very complex organisms, with thousands of neurons and millions of synapses (Briggman and Denk, 2006b; Anderson et al., 2009). Thus, automating the reconstruction process is of paramount importance.

The ability to reconstruct neural circuitry at ultrastructural resolution is of substantial clinical importance. Retinal degenerative diseases, including pigmentosa and macular degeneration, result from a loss of photoreceptors. Photoreceptor cell stress and death induces subsequent changes in the neural circuitry of the retina resulting in corruption of the surviving retinal cell class circuitry. Ultrastructural examination of the cell identity and circuitry reveal substantial changes to retinal circuitry with implications for vision

* Corresponding author at: Scientific Computing and Imaging Institute, 72 South Central Campus Drive, Room 3750, Salt Lake City, UT 84112, United States.
E-mail address: liz@sci.utah.edu (E. Jurrus).

[1] William Perry, Farouk El-Baz, Wesley Harris, Calestous Juma, Raymond Kurzweil, and Robert Langer, the unveiling of the grand challenges for engineering, in *AAAS Meeting*, February 2008.

[2] Emily Singer, A wiring diagram of the brain, *Technology Review*, November 2007.

1361-8415/$ - see front matter © 2010 Elsevier B.V. All rights reserved.
doi:10.1016/j.media.2010.06.002

Please cite this article in press as: Jurrus, E., et al. Detection of neuron membranes in electron microscopy images using a serial neural network architecture. Med. Image Anal. (2010), doi:10.1016/j.media.2010.06.002

rescue strategies (Marc et al., 2008, 2007, 2003; Jones and Marc, 2005; Jones et al., 2003, 2005; Peng et al., 2000). These findings in retinal degenerative disease mirror findings in epilepsy where neural circuits also undergo remodeling in presumed response to abnormal electrical activity clinically manifested as seizures. Scientists are interested in examining normal and pathological synaptic connectivities and how neuronal remodeling contributes to neuronal pathophysiology (Sutula et al., 2002; Pollard et al., 1994; Koyama et al., 2004). Examination of synaptic and dendritic spine formation during development provide insight into the adaptivity of neural circuits (Sorra et al., 2000; DeBello et al., 2001). Ultrastructural evaluation of multiple canonical volumes of neural tissue are critical to evaluate differences in connectivity between wild type and mutants. The complexity and size of the these datasets, often approaching 17 terabytes, makes human segmentation of the complex textural information of electron microscopic imagery a difficult task. Moreover, population or screening studies become unfeasible since fully manual segmentation and analysis would require multiple years of manual effort per specimen. As a result, better image processing techniques are needed to help with automated segmentation of EM data including identification of neurons and the connections.

1.1. Serial-section transmission electron microscopy

The modality we have chosen for reconstructing the connectome at the individual cell level is serial-section transmission electron microscopy (TEM). It provides scientists with images that capture the relevant structures; however, it poses some interesting challenges for image processing. Most importantly, serial-section TEM offers a relatively wide field of view to identify large sets of cells that may wander significantly as they progress through the sections. It also has an in-plane resolution that is high enough for identifying synapses. In collecting images through TEM, sections are cut from a specimen and suspended so that an electron beam can pass through it creating a projection. The projection can be captured on a piece of film and scanned or captured directly as a digital image. An important trade-off occurs with respect to the section thickness. Thinner sections are preferable from an image analysis point of view because structures are more easily identifiable due to less averaging. However, from an acquisition point of view, thinner sections are harder to handle and impose a limit on the area of the section that can be cut. For instance, in the rabbit retina, scientists need to study sections with areas as large as 250 μm in diameter to gain a sufficient understanding of neural connectivity patterns. Sections of this size can be reliably cut at 50–90 nm thickness with the current serial-section TEM technology. This leads to an extremely anisotropic resolution, 2–5 nm in-plane compared to 50–90 nm out-of-plane, and poses two image processing challenges. First, the cell membranes can range from solid dark curves for neurons that run approximately perpendicular to the cutting-plane, to grazed grey swaths for others which run more obliquely and suffer more from the averaging effect. Consequently, segmentations of neurons in these 2-D images, are difficult given the change in membrane contrast and thickness. Second, due to the large physical separation between sections, shapes and positions of neurons can change significantly between adjacent sections.

There are alternative specimen preparation and EM imaging techniques that can be used for neural circuit reconstruction such as Serial-Block Face Scanning Electron Microscopy. Briggman and Denk proposed a specimen preparation which only highlights extracellular spaces removing almost all contrast from intracellular structures (Briggman and Denk, 2006b). However, it is not possible to identify synapses with that approach. Identification of synapses is an important part of neural circuit reconstruction because it determines which cells are communicating, and where in the circuitry they connect. To highlight synapses in TEM, scientists must use a stain that also highlights intracellular structures, such as vesicles and mitochondria, as well as neuron membranes. Therefore, image segmentation techniques must account for these data characteristics in order to identify and successfully track neurons across hundreds of sections.

1.2. Neuron segmentation

There are two general approaches for neuron segmentation. One approach focuses first on the detection of neuron membranes in each 2-D section (Jurrus et al., 2008; Macke et al., 2008; Venkataraju et al., 2009). These boundaries can be used to identify individual neurons, which are then linked across sections to form a complete neuron. Unfortunately, accurate detection of neuron membranes in EM is a difficult problem given the presence of intracellular structures. This makes simple thresholding, edge detection (i.e. Canny), and region growing methods ineffective for the detection of neuron membranes. Some example images and results with traditional image processing methods are shown in Fig. 1. The other approach to neuron segmentation is to directly use the 3-D characteristics of the data (Andres et al., 2008; Jain et al., 2007). However, full 3-D approaches are difficult due to the anisotropic nature of the data. As mentioned earlier, in serial-section EM, there is a trade-off between section thickness and section loss rate. The datasets used in this paper to demonstrate membrane detection are from the *C. elegans* ventral nerve cord and from the rabbit retina. For these datasets, the nerve cord has a resolution of 6 nm × 6 nm × 33 nm and the retina has a resolution of 2 nm × 2 nm × 80 nm. This large section thickness often causes features to shift significantly between sequential images, decreasing the potential advantages of a direct 3-D approach. For these reasons, we follow the first approach which is to first perform a

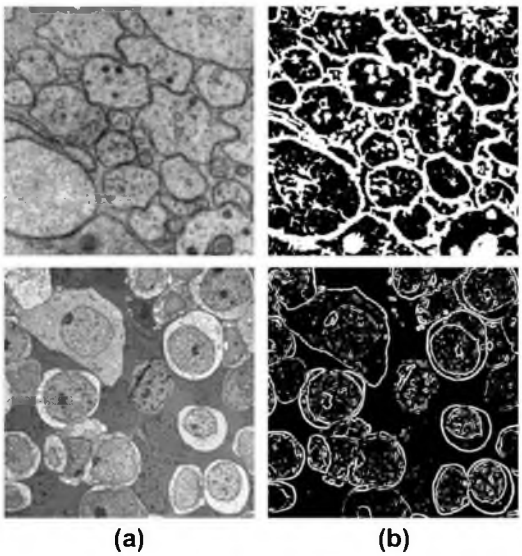

Fig. 1. (a) Example EM images. Top is from the *C. elegans*, bottom is from a rabbit retina. (b) Example membrane detection using thresholding after contrast enhancement and anisotropic directional smoothing to enhance membranes (top), and thresholding on the gradient magnitude (bottom). Both methods highlight the membrane boundaries but fail to remove internal structures.

Please cite this article in press as: Jurrus, E., et al. Detection of neuron membranes in electron microscopy images using a serial neural network architecture. Med. Image Anal. (2010), doi:10.1016/j.media.2010.06.002

2-D segmentation followed by a linking of the segmented regions in 3-D. This approach is particularly suitable for datasets in which a majority of the neurons run in a general direction which is roughly orthogonal to the sectioning plane such as the datasets considered in this paper. The main focus of this paper is to improve the 2-D neuron segmentation in each section. This information can then be used to link the segmentation in each section to obtain the full 3-D reconstruction.

Recent related work indicates that machine learning methods are an effective approach for detection of neuron membranes. These methods all use different representations for learning membrane pixels, most of which include training a single instance of a classifier on image derived features, such as Hessian eigenspaces (Venkataraju et al., 2009; Mishchenko, 2009) and local statistical features (Andres et al., 2008). Inspired by Tu's auto-context shape classification approach (Tu, 2008), the method described in this paper uses a series of classifiers to more accurately detect membranes in EM images, which is a necessary step for improved 3-D neuron segmentation as discussed above. However, unlike Tu's auto-context (Tu, 2008) which uses boosting to select features from a large pool of candidates such as Haar wavelet responses, we use a series of artificial neural networks (ANNs) that operate on a fixed set of features. The first ANN uses as input the intensity values sampled directly from the image. The input to the subsequent ANNs in the series is comprised of the same set of image values, in addition to the output of the previous ANN sampled on a stencil of nearby pixels (as depicted in Fig. 4). The ANNs in the series, therefore, have different inputs even though they have a common desired output. The advantages of this method are twofold. First, the classifier uses raw data, that is, the image intensities, rather than a constrained version of the image as given by responses to a large filter bank or statistical features that will not scale well for large datasets. Second, the use of the serial ANNs provides context, which is information from nearby pixels that contributes to the learning, providing increasing amounts of relative information at each stage of the network. As a result, the series of ANNs learns to remove vesicles and mitochondria from the membrane detection and close gaps in places where the membrane is weak. In this paper, we demonstrate the improvement from the combined use of stencils and the series of ANNs for two datasets with distinctly different characteristics.

2. Related work

There are several methods that attempt to segment EM images of neural tissue. Active contours, in both parametric and level set forms (Jurrus et al., 2009; Macke et al., 2008; Vazquez et al., 1998), can provide smooth, accurate segmentations of cells. However, they are very sensitive to initialization, which must be close to the neuron membrane, and often confuse internal structures for neuron membranes. If given an edge term that suppresses internal structures, such as one that is derived from the output of the classifier proposed in this paper, these methods may be more promising. Also, recent work using graph-cut segmentations on EM images produces promising neuron segmentations starting from a manual initialization (Vu and Manjunath, 2008). All of these methods require an initialization and are more appropriate for segmenting only a few cells. Our goal is the automatic segmentation of thousands of cells which renders manual initialization impractical.

Another set of approaches focus on segmenting the neurons by first performing membrane detection. Simple thresholding methods can be applied after anisotropic directional smoothing to improve membrane continuity (Tasdizen et al., 2005; Jurrus et al., 2008). This method does not remove internal cellular structures and simultaneously fails to detect a sufficiently high percentage of the true membranes to make accurate segmentations.

Supervised machine learning methods have proved to be useful for detecting membranes in EM images. For example, Jain et al. utilize a multilayer convolutional ANN to classify pixels as membrane or non-membrane in specimens prepared with an extracellular stain (Jain et al., 2007). The convolutional ANN has two important characteristics: it learns the filters for classification directly from data, and the multiple convolutions throughout the layers of the network account for an increasing (indirect) filter support region. On the other hand, the proposed ANN contains more than 30,000 parameters and, therefore, is computationally intensive and requires very large training sets. For these reasons, this approach has limited practical usefulness. Andres et al. propose a multi-part segmentation process that uses statistical learning and watersheds to segment neural tissue (Andres et al., 2008). Both of these methods produce clear segmentations of the membranes, however, they are aimed at datasets in which the stain used on the specimen suppresses the contrast of intracellular structures leaving only the cell membranes visible (Briggman and Denk, 2006b). This preparation technique simplifies the segmentation task but, on the other hand, it prevents a full neural circuit reconstruction since this requires the detection of synapses, which are characterized by certain intracellular structures.

In other work based on supervised learning, simple classifiers such as a single perceptron applied to a carefully chosen set of features has been shown to provide promising results in identifying membranes in EM images (Mishchenko, 2009). Nevertheless, this method still needs significant post-processing to connect membranes and remove internal cellular structures. Similarly, Venkataraju et al. propose using local context features computed from the Hessian matrix to train a boosted classifier to detect membranes, which highlights the importance of context for membrane detection (Venkataraju et al., 2009). The results obtained with these methods demonstrate not only the complexity of the problem, but also the potential of supervised machine learning for neuron segmentation.

Conceptually, of particular relevance to this work is Tu's auto-context framework (Tu, 2008), which uses a series of classifiers with contextual inputs to classify pixels in images. In Tu's method, the "continuous" output of a classifier, considered as a probability map, and the original set of features are used as inputs to the next classifier. The probability map values from the previous classifiers provide context for the current classifier, by using a feature set that consists of samples of the probability map at a large neighborhood around each pixel. This means that a classifier can utilize information relayed by previous classifiers from pixel values beyond the scope of its neighborhood, much like a convolutional network. This works well for the structures being detected in this paper. For example, when detecting smooth and elongated features, context helps identify pixels as belonging to membranes instead of other local structures, such as vesicles, by using information from a broader area. Hence, each subsequent classifier extends the support of the probability map, improving the decision boundary, and thus the system can learn the context, or shapes, associated with a pixel classification problem. Theoretically, the series of classifiers improves an approximation of a posteriori distribution (Tu, 2008). One of the main contributions of our work is the formulation of a series of ANNs in an architecture similar to auto-context. The particular implementation demonstrated by Tu uses 8000 nonspecific, spatially dispersed, image features, and a sampling of probability maps in very large neighborhoods. This is appropriate for methods that use a boosting classifier strategy (Freund and Schapire, 1995) and are being performed on smaller scale machine learning problems. However, in the proposed method, a much smaller set of features allows for flexibility and training of large datasets, such as the full rabbit retina dataset (Anderson et al., 2009), which in total is 16TB, and is more suitable for an ANN classifier.

Please cite this article in press as: Jurrus, E., et al. Detection of neuron membranes in electron microscopy images using a serial neural network architecture. Med. Image Anal. (2010), doi:10.1016/j.media.2010.06.002

More generally, the detection of complete membranes, even when portions of the membrane are low in contrast, is closely related to the contour completion and salient contour extraction problems which have been studied extensively in the computer vision literature. A detailed review of the literature on contour completion is beyond the scope of this paper. Various approaches have been proposed including spectral clustering and, graph analysis (Shashua and Ullman, 1988; Mahamud et al., 2003; Fowlkes et al., 2004; Zhu et al., 2007), tensor voting (Tang et al., 2002), probabilistic models (Ren and Malik, 2002) and conditional random fields (Ren et al., 2005). Some related work in this area also uses supervised classification that combines features across different scales to detect edges and close contours (Dollar et al., 2006; Shotton et al., 2008). This paper applies similar techniques in the use of auto-context, which uses incremental learning to gather information about features at different levels. Each stage of the network learns more information about nearby pixels, closing structures that would otherwise be difficult to identify without an incremental approach.

3. Method

The method developed here for neuron membrane detection combines ANN classifiers and image stencil neighborhood feature vectors. The following sections provide details on each of these components.

3.1. Artificial neural network

Given the success of ANNs for membrane detection (Mishchenko, 2009; Jain et al., 2007) and because auto-context is not specifically tied to any classifier, we implement a multilayer perceptron (MLP) ANN as our classifier. An MLP is a feed-forward neural network which approximates a classification boundary with the use of nonlinearly weighted inputs. The architecture of the network is depicted schematically in Fig. 2.

The output of each processing element (PE) (each of node of the ANN) is given as (Haykin, 1999; Principe et al., 2000)

$$y = f(\mathbf{w}^T\mathbf{x} + b), \tag{1}$$

where f is, in our case, the *tanh* nonlinearity, $\mathbf{w}$ is the weight vector, and b is the bias. The input vector $\mathbf{x}$ to PEs in the hidden layer is the input feature vector discussed in more detail in the next section. For the output PEs, $\mathbf{x}$ contains the outputs of the PEs in the hidden layer.

ANNs are a method for learning general functions from examples. They are well suited for problems without prior knowledge of the function to be approximated (a.k.a., "black box models"). They have been successfully applied to robotics (Pomerleau, 1993; Wells et al., 1996) and face and speech recognition (Rabi and Lu, 1998; Cottrell, 1990), and are robust to noise. Training uses gradient descent to solve for a solution which is guaranteed to find a minimum. However, several trade-offs occur in training ANNs regarding the size of the network and the number of inputs. An ANN with too many hidden nodes can lead to overfitting of the network (Haykin, 1999), resulting in a set of weights that fits well to the training data, but may not generalize well to test data. At the other extreme, if the number of hidden nodes is insufficient the ANN does not have enough degrees of freedom to accurately approximate the decision boundary. The number of inputs should also be keep small to mitigate the problem high-dimensional spaces, known as the "curse of dimensionality". Generally speaking, as the dimensionality of the input space increases, the data becomes increasingly sparse which makes it difficult to accurately learn a decision boundary. Additionally, the training time tends to scale with the amount of training data and size of the network, and therefore training smaller networks is generally preferable. Hence, the number of inputs to each ANN should be large enough to describe the data, while keeping this number to a minimal.

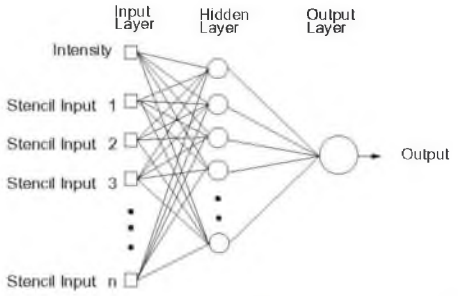

Fig. 2. Neural network diagram with one hidden layer. Inputs to the network include the image intensity and the values of the image at stencil locations.

3.2. Image stencil neighborhood

Choosing the best set of features to use in training an ANN is crucial for obtaining good segmentations. The field of machine learning has made available several possible strategies. A possible approach uses large sets of statistical features as the input to a learning algorithm. These features can include simple local and non-local properties, including the pixel values, mean, gradient magnitude, standard deviation, and Hessian eigenvalues (Andres et al., 2008; Tu, 2008; Venkataraju et al., 2009). These attempt to present the learning algorithm with a large variety of mathematical descriptors to train on, and are designed to work on a variety of data types. To achieve this generality, however, large numbers of these features are required to train a classifier. Training a classifier, and ANNs in particular, with a large number of features is challenging due to the "curse of dimensionality" which, if not done carefully, can complicate the decision space and make it difficult to find an optimal solution. Another approach is to design a set of match filters and apply them to an image to approximate a pixel's similarity to a membrane. This works well if the membranes in the image are uniform and respond well using cross-correlation (Leung and Malik, 2001; Schmid, 2001). Moreover, the design of the filter bank requires significant a priori knowledge of the problem. Yet, the fixed design may not be optimal for the dataset. Most importantly, the match filters have to be redesigned for datasets with different characteristics. On the other hand, learning these filters from training data, as in the case of convolutional networks (Jain et al., 2007), has the advantage that no a priori knowledge is required. A similar idea was been used in texture classification where is was shown that direct sampling of the image with a patch is actually a simpler and better approach for training a classifier compared to the use of filter banks (Varma and Zisserman, 2003). Image patches have also been used successfully for texture segmentation (Awate et al., 2006) and image filtering (Buades et al., 2005; Awate et al., 2006; Tasdizen, 2008). Similarly, using image neighborhoods in our case allows the ANNs to learn directly on the input data, giving the classifier more flexibility in finding the correct decision boundary. We define a square image neighborhood as an image patch, shown in Fig. 3a, centered at pixel k, l,

$$P_{k,l} = \left\{ I_{k+i,l+j} : i,j = -\frac{R-1}{2}, \ldots, \frac{R-1}{2} \right\}. \tag{2}$$

R is the width of the square image patch. Unfortunately, the size of the image patches required to capture sufficient context can be

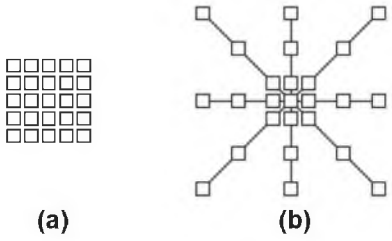

Fig. 3. Two image neighborhood sampling techniques: image pixels sampled using (a) a patch and (b) a stencil. For this example, the stencil contains the same number of samples, yet covers a larger area of the data. This is a more efficient representation for sampling the image space.

quite large. For this reason, we propose using as input to the ANNs the values from the image and probability map of the previous classifier sampled through a stencil neighborhood, shown in Fig. 3b. A stencil is also centered at pixel k, l and defined as,

$$S_{k,l} = \cup_{a=1}^{n} B_{k,l,a} \tag{3}$$

where

$$B_{k,l,a} = \{I_{k+ai,l+aj} : i,j = -1,0,1\}, \tag{4}$$

and n is the number of rows the stencil spans in the image. The stencil can cover large areas representing the desired feature space, but samples it with a spatially adaptive resolution strategy. In this way, an ANN can be trained using a small number of samples from image data, without having to use the whole image patch. Since the number of weights to be computed in an ANN are dominated by the connection between the input and the hidden layers, reducing the number of inputs reduces the number of weights and helps regularize the learned network. Moreover, using less inputs generally allows for faster training. With this, one aims to provide the classifier with sparse, but sufficient context information and achieve faster training, while obtaining a larger context which can lead to improve membrane detection. This strategy, combined with the serial use of ANNs (described in Section 3.3), grows the region of interest for classification within a smaller number of stages and without long training times.

3.3. Serial artificial neural networks

Using principles from auto-context, we implemented a series of classifiers that leverage the output of the previous network to gain knowledge of a large neighborhood. For the first classifier, the input is the image intensities around a pixel sampled using a stencil. For the ANNs in the remaining series, the input vector contains the samples from the original image, used as input to the first ANN, appended with the values from the output of the previous classifier sampled through the stencil neighborhood, yielding a larger feature vector. While the desired output labels remain the same, each ANN is dependent on the information from the previous network and therefore must be trained sequentially, rather than in parallel. Fig. 4 demonstrates this flow of data between classifiers. I denotes the image, S the image values sampled from the image using the stencil, C the output from the ANN, and T the threshold applied to C at zero, yielding the final membrane detection.

The serial structure allows the classifiers to gather with each step context information from a progressively larger image neighborhood to the pixel being classified, as occurs with a convolutional ANN. Indirectly, the classification from the previous ANN contains information about features in surrounding pixels, that is not represented in the original feature set. This allows the subsequent networks in the series (Fig. 4) to make decisions about the membrane classification utilizing non-local information. Put differently, each stage in the series accounts for larger structures in the data, taking advantage of results from all the previous networks. This results in membrane detection that improve after each network in the series. Fig. 5 visually demonstrates the classification improving between ANNs in the series as gaps in weak membranes are closed and intracellular structures are removed with each iteration in the series. The receiver operating characteristic (ROC) curves in Fig. 6 also demonstrate the increase in detection accuracy after each ANN in the series.

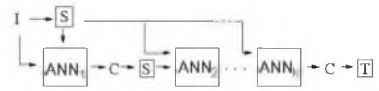

Fig. 4. Serial neural network diagram demonstrating the flow of information between ANNs. I is the original image, C is the output (probability map) from the classifier before thresholding, S is the stencil that samples the image data, and T is the final output from the classifier thresholded to produce a binary segmentation.

Combining the original image features with features sampled from the output of the previous classifier is important because, in this way, the membrane structure relevant for detection is enforced locally and then again at a higher level with each step in the series of classifiers. One of the advantages of this approach is that it provides better control of the training, allowing the network to learn in steps, refining the classification at each step as the context information it needs to correctly segment the image increases. Again, note that the membrane structure is learned directly from the data. Compared to a single large network with many hidden layers and nodes, such as the convolutional ANN of Jain et al. (2007) which requires 34,000 parameters, the proposed classifier is easier to train. This is mainly because each of the ANNs have a relatively small number of parameters. For example, given a single ANN used to compute the results in Section 4, the number of parameters needed is approximately 500 for the first ANN and 1100 for the remaining ANNs in the series. The number of weights in an ANN with a single-hidden layer is given by $(n+1)h+(h+1)$, where n is the number of inputs and h is the number of nodes in the hidden layer. For the first ANN in the series, $n = s$, where s is the number of points in the stencil. For the remaining ANNs in the series, $n = 2s$, since we sample the original image and the output from the previous classifier once. The total number of parameters across the whole series totals to approximately 5000. In contrast, a convolutional ANN needs $(n+1)h$ for the first layer, and $(nh+1)h$ for the remaining layers, an h^2 dependence (Jain et al., 2007). Hence, much less training data is needed, which is hard to obtain, since the ground truth must be hand labeled.[3] Furthermore, the training is simpler since backpropagation is less likely to get stuck on local minima of the performance surface (Haykin, 1999; Principe et al., 2000), and the network will train much faster.

4. Results

Two TEM datasets are used as test cases for the proposed method. The first dataset is a stack of 50 sections from the ventral nerve cord of the *C. elegans*. The second dataset is a single section from the 16TB rabbit retina dataset. These datasets contain very different types of neural cells. The *C. elegans* data has a resolution of 6 nm × 6 nm × 33 nm and each 2-D section is 662 × 697 pixels.

[3] According to the "rule-of-thumb" in (Principe et al., 2000), one needs at least 10× training samples pf the total number of parameters. Thus, compared to Jain et al. (2007) convolutional ANN, our approach needs about 27× less training samples, for the values given.

Please cite this article in press as: Jurrus, E., et al. Detection of neuron membranes in electron microscopy images using a serial neural network architecture. Med. Image Anal. (2010), doi:10.1016/j.media.2010.06.002

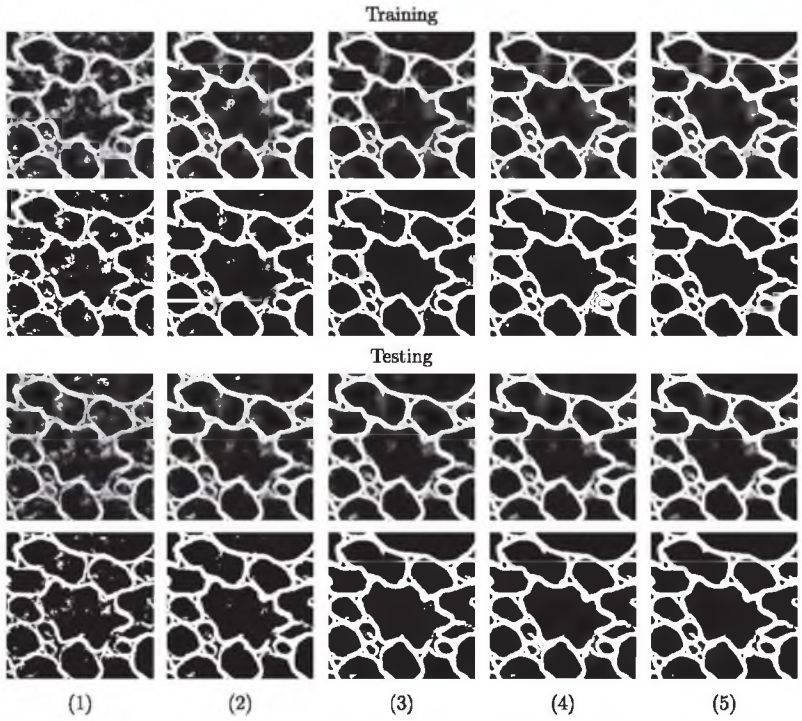

Fig. 5. An example of an image during training (top two rows) and testing (bottom two rows) at each stage (1–5) of the network series. The output from each network is shown in rows 1 and 3. Rows 2 and 4 demonstrate the actual membrane detection when that output is thresholded. The network quickly learns which pixels belong to the membranes within the first 2–3 stages, and then closes gaps in the last couple of stages.

Neuron membranes in the *C. elegans* data appear as intensity valleys; however, not all valleys in the data are neuron membranes, i.e. membranes of intracellular structures may also appear locally as valleys. The proposed method successfully learns the appropriate subset of ridges that need to be identified as neuron membranes as will be described in Section 4.2. The rabbit retina data has a resolution of 2 nm × 2 nm × 80 nm and each 2-D section is 7629 × 7351 pixels. Unlike the *C. elegans* dataset, neuron membranes in the retina data generally appear as intensity edges. Owing to the flexibility offered by the use of stencils rather than a predefined filter bank, the proposed method is also successful in learning to detect neuron membranes in this dataset as will be discussed in Section 4.3.

4.1. Experimental setup

Before discussing detailed results of experiments on the two dataset, we will outline the common experimental details. First, our setup for these datasets used 5 ANNs in series. Additional networks could be included; however, for these datasets, the performance converges to a limit (Fig. 6) and improvement in membrane detection is minimal. Each ANN used in the experiments contained one hidden layer with 20 nodes. We experimented with more layers and different numbers of nodes but did not find significant advantages. It is important that the number of nodes be large enough to approximate a nonlinear boundary and small enough that the ANN does not overfit to the training data (Cybenko, 1989; Hornik, 1991). Results using 10, 20, and 30 nodes turned out to be somewhat similar. Given the time versus performance trade-off, we chose 20 nodes. The networks were trained using backpropagation with a step size of 0.0001 and momentum term of 0.5. We used early stopping as the criterion to determine when to terminate training (Haykin, 1999; Principe et al., 2000). This means that a small portion of the training data (20% in our case), called the validation set, is used only to test the classifier generalization performance. The training terminates when the lowest error on the validation set is attained. To mitigate problems with local minima, each network is trained for 5 Monte Carlo simulations using randomly initialized weights.

Preprocessing is performed for each image using a contrast limited adaptive histogram equalization (CLAHE) (Pizer et al., 1990) filter. This enhances the contrast of the membranes. Window sizes of 64 × 64 and 256 × 256 were used for the *C. elegans* and retina datasets, respectively.

Each image used in the experiments was annotated by an expert who carefully marked neuron membranes with a one-pixel-wide contour. This contour was dilated using a disk shaped kernel with a radius of 2 pixels, ensuring that the positive training examples cover all of the actual membrane pixels. The negative training examples were selected as the remaining pixels in the image, after erosion to remove training pixels that are very close to the membranes. This strategy leaves a thin layer of pixels between the positive and negative training example pixels that are not used for training purposes. This ensures that the network learns on pixels that are either membrane or non-membrane, excluding those that are more prone to labeling errors.

Finally, to optimize network performance, the total number of training examples from each image includes all of the positive

Please cite this article in press as: Jurrus, E., et al. Detection of neuron membranes in electron microscopy images using a serial neural network architecture. Med. Image Anal. (2010), doi:10.1016/j.media.2010.06.002

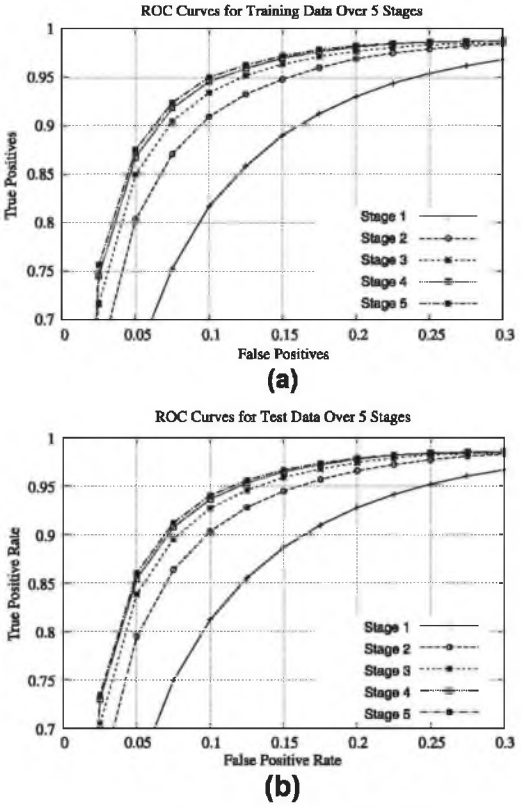

Fig. 6. ROC curves for the (a) training data and (b) testing data for each stage of the network.

examples and a random selection of negative examples such that there are twice the number of negative examples, than positive. Choosing the optimal number of training examples was difficult given there were many more negative than positive examples in this dataset. If all the negative training examples are used then the ANNS are biased towards classifying pixels as non-membrane. After conducting a series of experiments for considering the results from different ratios of positive and negative examples and the training times, we found the 2:1 ratio resulted in the best segmentation while achieving a reduced training time. Using all the training data (and other increased ratios, such as 4:1) produced a similar ROC curve but results were biased towards false negatives. Clearly, we could have adjusted the threshold in the final stage. Alternatively, one possible solution for this problem would be the use of a weighting factor chosen to obtain unbiased training. However, either approach would have much slower training than the previous described strategy without improving the overall segmentation. For each pixel in our training data, a stencil with a radius of 5 (or $n = 11$ in Eq. (3)) is used to sample the image data and form the feature vector.

4.2. Results on the C. elegans ventral nerve cord

The nematode *C. elegans* is an important dataset for neural circuit reconstruction. Despite being a well studied organism (White et al., 1986), there are still numerous open questions such as how genes regulate wiring (Jin et al., 1994) or how connectivity is altered to mediate different behaviors, for example between males and females (White et al., 2007). Reconstructions of the full nervous system reveals topological characteristics important for researchers studying neuron wiring. The particular dataset used in this paper is from the ventral nerve cord of the *C. elegans* and is important for studying the topological structure resulting from neurons making connections to local targets.

To validate the robustness of the method, fivefold cross-validation was used on a set of 50 annotated images, separated into 5 groups of 10 images in each. The network was trained on each fold according to the procedure described in Section 4.1, and tested on the remaining four. The improvement in the classification after each ANN in the series is visible in the classification of the training data after each stage, shown in Fig. 5, and in the receiver operating characteristic (ROC) curves in Fig. 6. The output from the network improves quantitatively and qualitatively with each network in the series. Directly sampling the image using a stencil and repeated uses of the network enables the method to accurately estimate the appearance of membrane pixels and pixels in surrounding neighborhoods.

Fig. 7a shows four sections from the *C. elegans* dataset chosen at random. The final membrane detection with the proposed method is shown in Fig. 7e. Note that these are testing results; that is, these four sections were not used as training data. To demonstrate the advantages of the proposed method, two other methods are presented. The first method, shown in Fig. 7b, performs thresholding after enhancing the membranes with anisotropic directional smoothing (Jurrus et al., 2008). Fig. 7c shows results from an approach similar to the approach in Mishchenko (2009), which learns boundary confidences using Hessian eigenvalues as input to a single layer neural network. It can be seen that the proposed method removes a substantially larger percentage of the intracellular structures from the detection results as well as providing better membrane continuity. It is important to note that in Mishchenko (2009) further post-processing is performed to interpolate between broken boundaries and complete contours, resulting in an improved result compared to the one shown here. However, we compare against only the single layer network part of that method since our goal is to demonstrate the improvement achieved by the use of ANNs and auto-context. Of course, the same preprocessing methods could be applied to the results of the proposed method as well. Fig. 8 shows enlarged regions demonstrating the removal of large intracellular structures and closing of weak membranes.

To demonstrate the advantages of directly sampling the image with a stencil, we also tested the proposed auto-context ANN strategy but with inputs to the ANNs that are derived from a line detection filter bank rather than sampling the image. We used a filter bank that consists of a set of 32 line detection filters oriented at different angles and five circle detection filters with different radii. The circle detection filters were included to help the auto-context ANN to learn to remove vesicles from the membrane detection results. Fig. 7d is the output obtained with the filter bank/series of ANN approach. While these results are better than the results in Fig. 7b and c, they contain more false positives than the results of the full stencil/auto-context ANN approach shown in Fig. 7e. The advantages of using the stencil becomes clearer in a quantitative comparison as discussed in the next paragraph. Furthermore, an important practical advantage of using the stencil is that it does not require any a priori knowledge. Therefore, it can be trained to detect different structures as will be shown for the retina dataset in Section 4.3. In comparison, a filter bank designed to capture the relevant structures for the *C. elegans* dataset is not expected to capture the relevant structures in a different dataset which necessitates the design of a new filter bank.

Please cite this article in press as: Jurrus, E., et al. Detection of neuron membranes in electron microscopy images using a serial neural network architecture. Med. Image Anal. (2010), doi:10.1016/j.media.2010.06.002

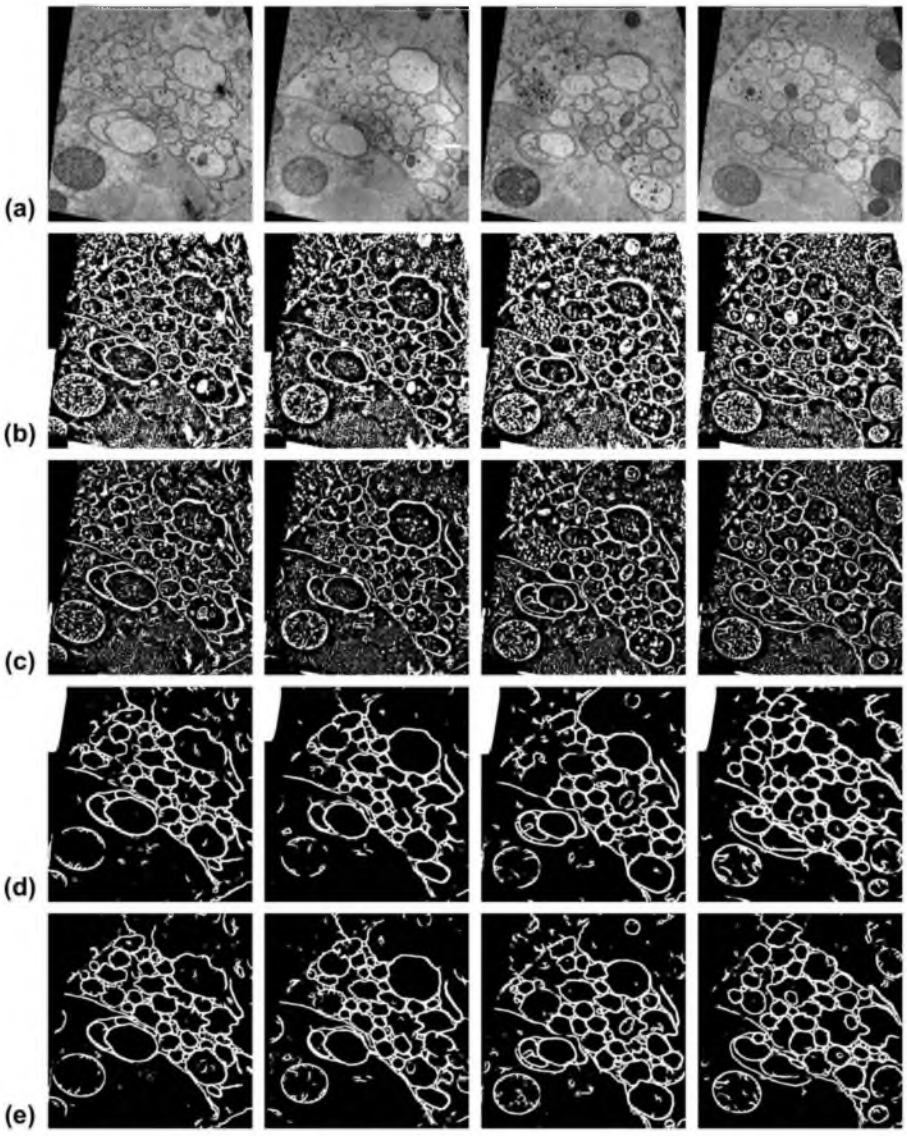

Fig. 7. (a) Cross-sections of the nematode *C. elegans* acquired using EM. Three demonstrated membrane detection techniques: (b) intensity thresholding after directional anisotropic smoothing (Jurrus et al., 2008), (c) thresholded boundary confidences from a single ANN trained using Hessian eigenvalues (Mishchenko, 2009), (d) membrane detection from serial ANNs, trained using membrane filter banks and auto-context, and (e) membrane detection from serial ANNs, trained using image data sampled from stencils and auto-context.

Fig. 9 compares the ROC curves for each method from Fig. 7. For this particular data, a single layer ANN using Hessian eigenvalues as inputs (labeled "Hessian") demonstrates no quantitative differences from thresholding after directional anisotropic diffusion (labeled "Jurrus et al."). These ROC curves correspond to the qualitative results in Fig. 7b and c, respectively. The other three curves all show a large improvement in performance. The use of membrane detection filters (labeled "Filters") demonstrates how a carefully chosen set of features can be used for learning to detect membranes. Image patches (labeled "Patches") are just as successful in training to detect membranes as filters. However, in testing, the patches outperform the filters. We argue that this is due to the fact that patches sample the image directly and give more flexibility to the classifier than a filter bank. Using a stencil (labeled "Stencil") results in the best performance. The stencil provides the classifier with two important features. First, similar to patches, it trains the classifier on image sample directly, as opposed to a fixed representation as obtained from the filters. Second, it samples a larger area than the patches, while maintaining the same number of features (as seen in Fig. 3). The latter feature is very helpful in

Please cite this article in press as: Jurrus, E., et al. Detection of neuron membranes in electron microscopy images using a serial neural network architecture. Med. Image Anal. (2010), doi:10.1016/j.media.2010.06.002

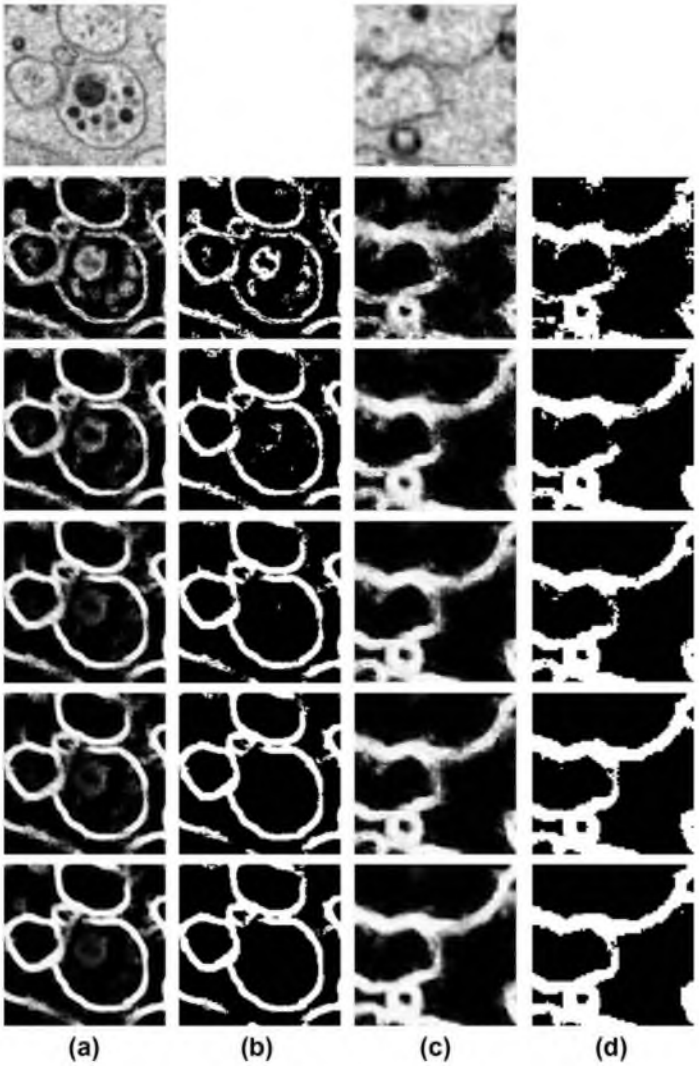

Fig. 8. Examples demonstrating how the proposed method removes intracellular structures (left two columns) and closes gaps in a weak membrane (right two columns). The top row is the original image, columns (a) and (c) show the classifier output, and columns (b) and (d) show the final thresholded segmentation.

practice since it ensures improved performance without sacrificing the network training time (actually, in our experiments, using the stencil improved the training reliability and time).

Fig. 10 demonstrates the final neuron segmentation, after a very simple region flood fill is applied to the image of detected membranes with the proposed method. This depicts how close the final segmentation is to the true segmentation. Fig. 11 is a full 3-D neuron segmentation for four key neurons and nearby muscles from this dataset. Neurons are segmented in each section using a region flood fill and linked across sections using a minimum path finding algorithm similar to Jurrus et al. (2008). Hand edits were required to correct some mistakes in the automatic segmentation. This 3-D model shows the motor neurons in the ventral nerve cord and their processes interdigitating along the lateral edge of the nerve bundle (Fig. 11a) to make contact with the muscles (Fig. 11b). Multiple muscles, in turn, must send processes to these motor neurons to receive input. Areas where this communication is occurring are marked in red. There are three motor neuron inputs into these muscles: the VA neurons release acetylcholine during backwards movement, the VB neurons release acetylcholine during forward movement, and the VD motor neurons release GABA to relax the muscle to allow sinusoidal movement. These data demonstrate that axons do not precisely interweave. GABA neurons run alongside a group of muscle arms and form multiple synapses to differing subsets of muscles before giving way to acetylcholine motor neurons. By contrast, the two types of acetylcholine neurons usually form contacts to the muscles simultaneously. Again, they form 2 to 3 contacts to the muscles for a segment of axon before giving

Please cite this article in press as: Jurrus, E., et al. Detection of neuron membranes in electron microscopy images using a serial neural network architecture. Med. Image Anal. (2010), doi:10.1016/j.media.2010.06.002

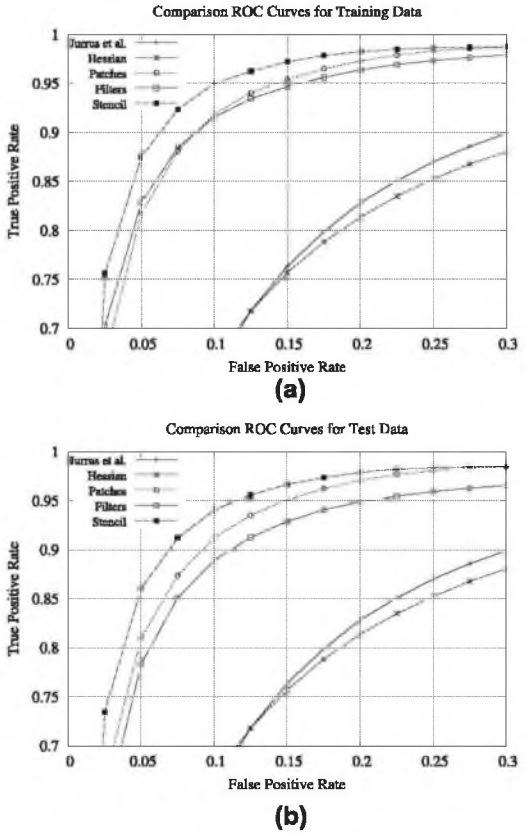

Fig. 9. [color] ROC curves for (a) training and (b) testing on the *C. elegans* data. "Jurrus et al.": thresholding after directional anisotropic smoothing (Jurrus et al., 2008). "Hessian": single layer neural network operating on Hessian eigenvalues similar to Mishchenko (2009). The remaining three curves demonstrate the results from different inputs to the proposed auto-context ANN approach.

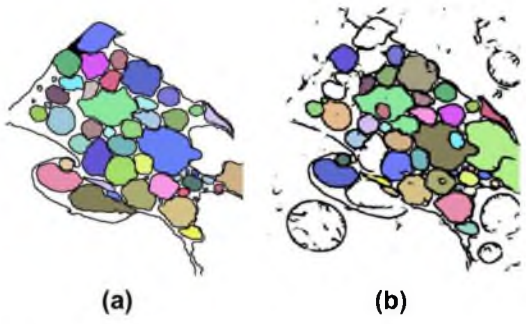

Fig. 10. Segmentation of neurons using a flood-fill on the image of detected membranes. (a) Ground truth and (b) membranes detected with proposed method.

way to the GABA motor neuron. This demonstrates the importance and diagnostic capabilities of full connectivity diagrams and renderings.

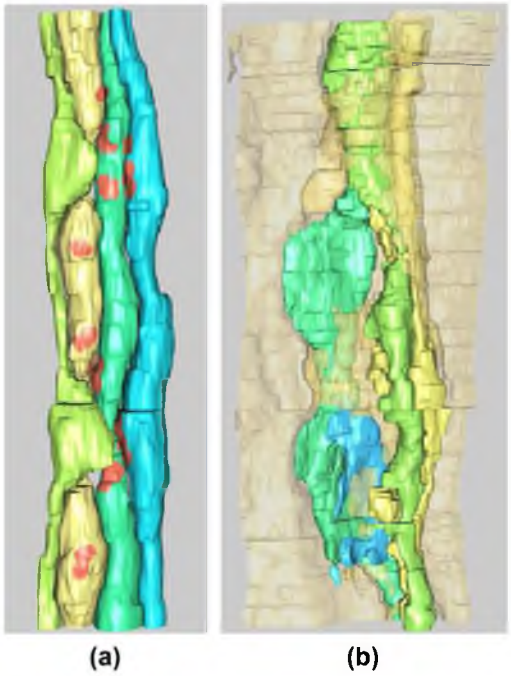

Fig. 11. (a) 3-D renderings of the four neurons competing for information from the muscles. The location of the synapses, which were extracted from user specified locations, are shown in red on the neurons. (b) Similar rendering of the muscles that run alongside the motor neurons.

4.3. Results on the rabbit retina

The retina is a complex structure containing several layers of neurons. Processing light sets off a series of chemical events and connections among these neurons that scientists would like to model. Most importantly, scientists would like to characterize neural circuitry that is damaged and in a diseased state. However, unraveling the connective patterns in this complex tissue is an enormous task.

To demonstrate the robustness of our method on a very different dataset, an expert hand segmented all of the bipolar, amacrine, and horizontal cells in a single 2-D section through the retina. This section is 7629 × 7351 pixels and contains approximately 500 neurons. The image was divided into four equal sections and a fourfold cross validation technique is used to assess the performance of the algorithm.

Fig. 12 shows the output on the test data. Fig. 12a shows portions of the TEM image, cropped to show the cellular details. Fig. 12b is a simple baseline membrane detection obtained by thresholding the intensity gradient after smoothing the input image with a Gaussian kernel (standard deviation 3 pixels). Thresholding the gradient results in some obvious problems. Differences in contrast and the presence of intracellular features make isolation of the neuron edges difficult. Fig. 12c shows the results of applying the series of ANN method with a filter bank as input. For this data, 25 Leung-Malik edge filters (Leung and Malik, 2001) were used. The Leung-Malik filter banks consists of first derivatives of a Gaussian kernel (standard deviation 3 pixels) at various orientations. The results in Fig. 12d are from the sten-

Please cite this article in press as: Jurrus, E., et al. Detection of neuron membranes in electron microscopy images using a serial neural network architecture. Med. Image Anal. (2010), doi:10.1016/j.media.2010.06.002

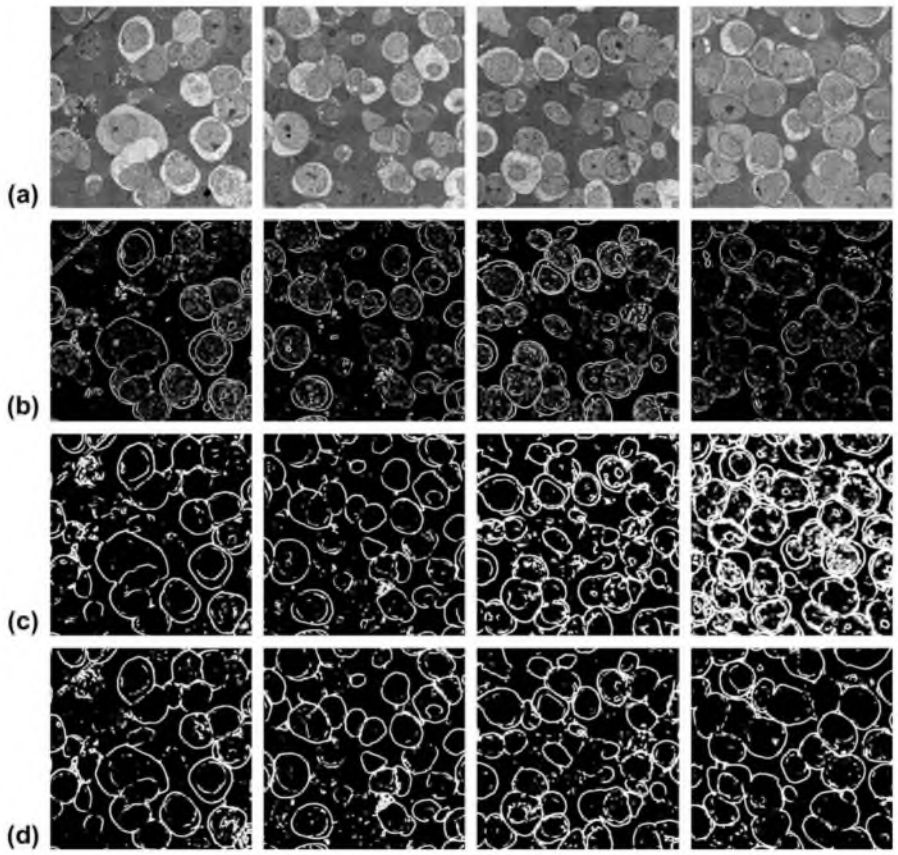

Fig. 12. (a) TEM images from a rabbit retina. Membrane detection with: (b) thresholding on the gradient magnitude, (c) serial ANNs using the output of an edge detection filter bank, and (d) serial ANNs using image intensities sampled from a stencil.

cil/serial ANN approach identical in architecture to the one used for the *C. elegans* dataset. From a qualitative perspective, the stencil removes more intracellular structures and is more robust to changes in contrast. When the weights from the final network, which was trained with a filter bank, are applied to the testing images, the edge detection performs poorly. However, sampling the image using a stencil is a more robust way to detect membrane edges and provides more consistent results across images. Fig. 13 gives clear examples of how this method removes non-membrane structures and closes complex gaps resulting from inconsistent membrane data. Most importantly, the results from this dataset demonstrate the flexibility of our method on different feature types. The feature vectors for both datasets are the same, that is, they are simply image values sampled from the input data.

Fig. 14 shows the quantitative comparison for the methods demonstrated in Fig. 12. The gradient magnitude provides a baseline for how well a simple edge detection method can be expected to perform. While it detects many of the neuron boundaries, it also has a lot of false positive responses for internal structures and fails to close gaps in weak parts of the membranes. The serial networks provide a very large improvement over this simple method when a filter bank is in place. However, the proposed stencil/auto-context ANN method is demonstrated to do still a significantly better job at detecting boundaries than the filters.

5. Conclusion and future work

In this paper a new approach for neuron membrane detection is proposed. Inspired by Tu's auto-context framework (Tu, 2008), our approach introduces two major contributions. The first contribution is the introduction of a serial ANN classifier and its application to neuron membrane detection. The use of context allows the classifier to close gaps in weak membranes and suppress intracellular structures by using increasingly non-local information with each ANN in the series. The second contribution is the use of raw image intensities sampled through a stencil as inputs to the series ANN rather than a predetermined filter bank. This provides increased flexibility to the classifier which can then be trained to detect neuron membranes in datasets with significantly different characteristics. Also, it must be noted the choice of sampling the image with a stencil rather than using the more traditional patch neighborhood. As shown in the results, utilizing a stencil yields significantly better results. This is because, for the same number of features, a stencil provides context information for a larger neighborhood. Although

Please cite this article in press as: Jurrus, E., et al. Detection of neuron membranes in electron microscopy images using a serial neural network architecture. Med. Image Anal. (2010), doi:10.1016/j.media.2010.06.002

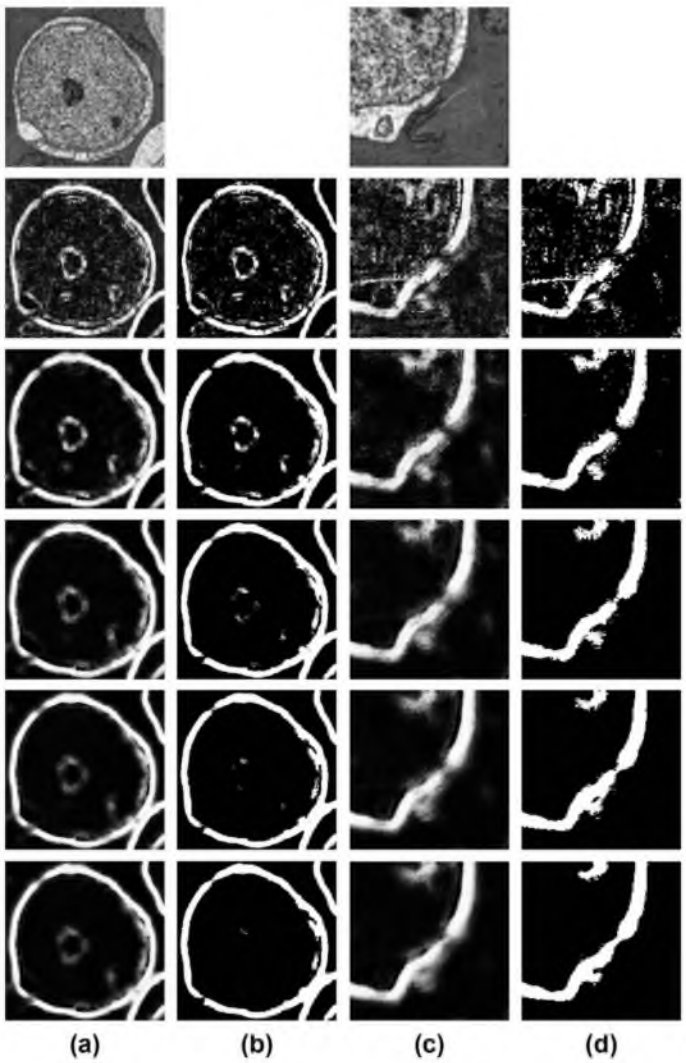

Fig. 13. Examples of locations in the data where intracellular structures are removed (left two columns) and gaps in membranes are closed (right two columns). The top row shows the raw images, columns (a) and (c) show the classifier output, and columns (b) and (d) are the final thresholded segmentations.

larger patches could be utilized, the number of features would grow more rapidly to impractical levels, and would be slower (and more complicated) to train the classifier. These two contributions result in a neuron membrane algorithm that outperforms other methods.

A direct comparison to Tu's auto-context classification using a probabilistic boosting tree is difficult to do. Applying the same filter bank to the data presented here results in storage complications and does not scale to larger datasets like the rabbit retina data, which is 16TB (Anderson et al., 2009). However, to compare the performances, our method was tested on the Weizmann Horse dataset (Borenstein et al., 2004), for which results using Tu's method are available, without significant changes in performance. The method used in this paper had an overall accuracy (or f-value) of 0.834, while Tu's accuracy was 0.84, and the qualitative differences were negligible (Paiva et al., 2010). Nevertheless, it must be emphasized that a major advantage in our method is that the filters are learning directly from data, tremendously simplifying the user's role. By incorporating a similar architecture into the form of a series of ANNs, we have designed a method that performs well on EM images and aids in the building of 3-D models for neural circuit reconstruction, as depicted in Fig. 11.

Given the challenge of full 3D reconstructions, and the extremely anisotropic resolution of serial-section TEM, we approach this problem with a two-stage solution that consists of first segmenting neurons in 2-D sections and then linking them up the segments in 3-D. Therefore, the motivation for improving the accuracy of automatic neuron membrane detection methods is to minimize user

Please cite this article in press as: Jurrus, E., et al. Detection of neuron membranes in electron microscopy images using a serial neural network architecture. Med. Image Anal. (2010), doi:10.1016/j.media.2010.06.002

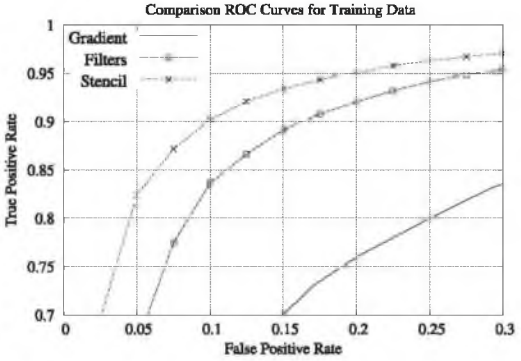

Fig. 14. ROC curves computed on the retina data for the (a) training data and (b) testing data. For comparison, an ROC curve is included that shows the best membrane detection when the gradient magnitude is thresholded.

interaction required to correct the segmentation. Fig. 10 demonstrates segmentations obtained by applying a simple flood fill operation to the image of detected membranes without any user corrections. In future work, segmentations obtained using the proposed method can be extended to other sections, taking advantage of segmentations in sequential sections having similar anatomy. Simple gap closing methods can also be applied to close small remaining holes in the membrane for a better 2-D neuron segmentation. Finally, a similar classifier strategy could prove successful also in segmenting long tubular structures such as vasculature in MRI due to the capability of closing gaps in weak areas of elongated structures.

Acknowledgments

This work was supported by NIH R01 EB005832 (T.T.), NIH EY0015128 (R.M.), EY002576 (R.M.), NEI Vision Core EY014800 (R.M.), HHMI (E.M.J.), and NIH NINDS 5R37NS34307-15 (E.M.J.). We also thank the anonymous reviewers whose comments helped improve this paper.

References

Anderson, J., Jones, B., Yang, J.-H., Shaw, M., Watt, C., Koshevoy, P., Spaltenstein, J., Jurrus, E., Whitaker, K.U.V.R., Mastronarde, D., Tasdizen, T., Marc, R., 2009. A computational framework for ultrastructural mapping of neural circuitry. PLoS Biol. 7 (3), e74.

Andres, B., Köthe, U., Helmstaedter, M., Denk, W., Hamprecht, F.A., 2008. Segmentation of SBFSEM volume data of neural tissue by hierarchical classification. In: Rigoll, G. (Ed.), Pattern Recognition, LNCS, vol. 5096. Springer, pp. 142–152. doi:10.1007/978-3-540-69321-5_15. ISBN: 978-3-540-69320-8.

Awate, S.P., Whitaker, R.T., 2006. Unsupervised, information-theoretic, adaptive image filtering for image restoration. In: IEEE Transactions on Pattern Analysis and Machine Intelligence, vol. 28 (3), pp. 364–376.

Awate, S.P., Tasdizen, T., Whitaker, R.T., 2006. Unsupervised texture segmentation with nonparametric neighborhood statistics. In: Proceedings of the European Conference on Computer Vision, pp. 494–507.

Borenstein, E., Sharon, E., Ullman, S., 2004. Combining top-down and bottom-up segmentation. In: Proceedings of the 2004 Conference on Computer Vision and Pattern Recognition Workshop (CVPRW'04), vol. 4. IEEE Computer Society, Washington, DC, USA, p. 46. ISBN: 0-7695-2158-4.

Briggman, K.L., Denk, W., 2006a. Towards neural circuit reconstruction with volume electron microscopy techniques. Curr. Opin. Neurobiol. 16 (5), 562–570. doi:10.1016/j.conb.2006.08.010. <http://dx.doi.org/10.1016/j.conb.2006.08.010>.

Briggman, K.L., Denk, W., 2006b. Towards neural circuit reconstruction with volume electron microscopy techniques. Curr. Opin. Neurobiol. 16 (5), 562–570.

Buades, A., Coll, B., Morel, J.-M., 2005. A non-local algorithm for image denoising. In: Proceedings of IEEE Conference on Computer Vision and Pattern Recognition, pp. 60–65.

Cottrell, G.W., 1990. Extracting features from faces using compression networks. In: Touretzky, D.S., Elman, J.L., Sejnowski, T.J., Hinton, G.E. (Eds.), Proceedings of the 1990 Connectionist Models Summer School. Morgan Kaufman, San Mateo, pp. 328–337.

Cybenko, G., 1989. Approximation by superpositions of a sigmoidal function. Math. Control, Signals, Syst. 2 (4), 303–314. doi:10.1007/BF02551274.

DeBello, W.M., Feldman, D.E., Knudsen, E.I., 2001. Adaptive axonal remodeling in the midbrain auditory space map. J. Neurosci. 21 (9), 3161–3174. <http://www.jneurosci.org/cgi/content/abstract/21/9/3161>.

Dollar, P., Tu, Z., Belongie, S., 2006. Supervised learning of edges and object boundaries. In: IEEE Computer Society Conference on Computer Vision and Pattern Recognition, vol. 2. IEEE Computer Society, Los Alamitos, CA, USA, pp. 1964–1971. doi:10.1109/CVPR.2006.298. ISSN: 1063-6919.

Fiala, J.C., Harris, K.M., 2001. Extending unbiased stereology of brain ultrastructure to three-dimensional volumes. J. Am. Med. Inform. Assoc. 8 (1), 1–16.

Fowlkes, C., Belongie, S., Chung, F., Malik, J., 2004. Spectral grouping using the Nyström method. In: IEEE Transactions on Pattern Analysis and Machine Intelligence, vol. 26, pp. 214–225.

Freund, Y., Schapire, R.E., 1995. A decision-theoretic generalization of on-line learning and an application to boosting. In: EuroCOLT '95: Proceedings of the Second European Conference on Computational Learning Theory. Springer-Verlag, London, UK, pp. 23–37. ISBN: 3-540-59119-2.

Haykin, S., 1999. Neural Networks – A Comprehensive Foundation, second ed. Prentice-Hall.

Hornik, K., 1991. Approximation capabilities of multilayer feedforward networks. Neural Networks 4 (2), 251–257. doi:10.1016/0893-6080(91)90009-T.

Jain, V., Murray, J., Roth, F., Turaga, S., Zhigulin, V., Briggman, K., Helmstaedter, M., Denk, W., Seung, H., 2007. Supervised learning of image restoration with convolutional networks. In: IEEE 11th International Conference on Computer Vision, pp. 1–8.

Jin, Y., Hoskins, R., Horvitz, H.R., 1994. Control of type-D GABAergic neuron differentiation by *C. elegans* UNC-30 homeodomain protein. Nature 372 (6508), 780–783.

Jones, B.W., Marc, R.E., 2005. Retinal remodeling during retinal degeneration. Exp. Eye Res. 81, 123–137.

Jones, B.W., Watt, C.B., Frederick, J.M., Baehr, W., Chen, C.K., Levine, E.M., Milam, A.H., Lavail, M.M., Marc, R.E., 2003. Retinal remodeling triggered by photoreceptor degenerations. J. Comp. Neurol. 464, 1–16.

Jones, B.W., Watt, C.B., Marc, R.E., 2005. Retinal remodelling. Clin. Exp. Optom. 88, 282–291.

Jurrus, E., Whitaker, R., Jones, B., Marc, R., Tasdizen, T., 2008. An optimal-path approach for neural circuit reconstruction. In: Proceedings of the 5th IEEE International Symposium on Biomedical Imaging: From Nano to Macro, pp. 1609–1612.

Jurrus, E., Hardy, M., Tasdizen, T., Fletcher, P., Koshevoy, P., Chien, C.-B., Denk, W., Whitaker, R., 2009. Axon tracking in serial block-face scanning electron microscopy. Med. Image Anal. 13 (1), 180–188.

Koyama, R., Yamada, M.K., Fujisawa, S., Katoh-Semba, R., Matsuki, N., Ikegaya, Y., 2004. Brain-derived neurotrophic factor induces hyperexcitable reentrant circuits in the dentate gyrus. J. Neurosci. 24, 7215–7224.

Leung, T., Malik, J., 2001. Representing and recognizing the visual appearance of materials using three-dimensional textons. Int. J. Comput. Vis. 43 (1), 29–44. doi:10.1023/A:1011126920638. ISSN: 0920-5691.

Macke, J., Maack, N., Gupta, R., Denk, W., Schölkopf, B., Borst, A., 2008. Contour-propagation algorithms for semi-automated reconstruction of neural processes. J. Neurosci. Methods 167, 349–357.

Mahamud, S., Williams, L., Thornber, K., Xu, K., 2003. Segmentation of multiple salient closed contours from real images. In: IEEE Transactions on Pattern Analysis and Machine Intelligence, vol. 25 (4), pp. 433–444. doi:10.1109/TPAMI.2003.1190570. ISSN: 0162-8828

Marc, R.E., Jones, B.W., Watt, C.B., Strettoi, E., 2003. Neural remodeling in retinal degeneration. Prog. Retinal Eye Res. 22, 607–655.

Please cite this article in press as: Jurrus, E., et al. Detection of neuron membranes in electron microscopy images using a serial neural network architecture. Med. Image Anal. (2010), doi:10.1016/j.media.2010.06.002

Marc, R.E., Jones, B.W., Anderson, J.R., Kinard, K., Marshak, D.W., Wilson, J.H., Wensel, T., Lucas, R.J., 2007. Neural reprogramming in retinal degeneration. Invest. Ophthalmol. Vis. Sci. 48, 3364–3371.

Marc, R.E., Jones, B.W., Watt, C.B., Vazquez-Chona, F., Vaughan, D.K., Organisciak, D.T., 2008. Extreme retinal remodeling triggered by light damage: implications for age related macular degeneration. Mol. Vis. 14, 782–806.

Mishchenko, Y., 2009. Automation of 3D reconstruction of neural tissue from large volume of conventional serial section transmission electron micrographs. J. Neurosci. Methods.

Venkataraju, K.U., Paiva, A., Jurrus, E., Tasdizen, T., 2009. Automatic markup of neural cell membranes using boosted decision stumps. In: Proceedings of the 6th IEEE International Symposium on Biomedical Imaging, pp. 1039–1042.

Paiva, A.R., Jurrus, E., Tasdizen, T., 2010. Using sequential context for image analysis. In: Proceedings of the International Conference on Pattern Recognition.

Peng, Y.W., Hao, Y., Petters, R.M., Wong, F., 2000. Ectopic synaptogenesis in the mammalian retina caused by rod photoreceptor-specific mutations. Nat. Neurosci. 3, 1121–1127.

Pizer, S., Johnston, R., Ericksen, J., Yankaskas, B., Muller, K., 1990. Contrast-limited adaptive histogram equalization: speed and effectiveness. In: Proceedings of the First Conference on Visualization in Biomedical Computing, pp. 337–345. doi:10.1109/VBC.1990.109340.

Pollard, H., Khrestchatisky, M., Moreau, J., Ben-Ari, Y., Represa, A., 1994. Correlation between reactive sprouting and microtubule protein expression in epileptic hippocampus. Neuroscience 61, 773–787.

Pomerleau, D., 1993. Knowledge-based training of artificial neural networks for autonomous robot driving. In: Connell, J., Mahadevan, S. (Eds.), Robot Learning. Kluwer Academic Publishing, pp. 19–43.

Principe, J.C., Euliano, N.R., Lefebvre, W.C., 2000. Neural and Adaptive Systems: Fundamentals Through Simulations. John Wiley & Sons.

Rabi, G., Lu, S., 1998. Visual speech recognition by recurrent neural networks. J. Electron. Imag. 7 (1), 61–69.

Ren, X., Malik, J., 2002. A probabilistic multi-scale model for contour completion based on image statistics. In: ECCV '02: Proceedings of the 7th European Conference on Computer Vision, Part I. Springer-Verlag, London, UK, pp. 312–327. ISBN: 3-540-43745-2.

Ren, X., Fowlkes, C., Malik, J., 2005. Scale-invariant contour completion using conditional random fields. In: Tenth IEEE International Conference on Computer Vision 2005, ICCV 2005, vol. 2, pp. 1214–1221. doi:10.1109/ICCV.2005.213. ISSN: 1550-5499.

Schmid, C., 2001. Constructing models for content-based image retrieval. In: Proceedings of the 2001 IEEE Computer Society Conference on Computer Vision and Pattern Recognition, CVPR 2001, vol. 2, pp. II–39–II–45. doi:10.1109/CVPR.2001.990922. ISSN: 1063-6919.

Shashua, A., Ullman, S. 1988. Structural saliency: the detection of globally salient structures using a locally connected network. In: Second International Conference on Computer Vision, pp. 321–327.

Shotton, J., Blake, A., Cipolla, R., 2008. Multiscale categorical object recognition using contour fragments. In: IEEE Transactions on Pattern Analysis and Machine Intelligence, vol. 30 (7), pp. 1270–1281. doi:10.1109/TPAMI.2007.70772. ISSN: 0162-8828.

Sorra, K.E., Harris, K.M., 2000. Overview on the structure, composition, function, development, and plasticity of hippocampal dendritic spines. Hippocampus 10, 501–511.

Sporns, O., Tononi, G., Kötter, R., 2005. The human connectome: a structural description of the human brain. PLoS Comput. Biol. 1, e42.

Sutula, T., 2002. Seizure-induced axonal sprouting: assessing connections between injury, local circuits, and epileptogenesis. Epilepsy. Curr. 2, 86–91.

Tang, C.-K., Medioni, G., 2002. Curvature-augmented tensor voting for shape inference from noisy 3D data. In: IEEE Transactions on Pattern Analysis and Machine Intelligence, vol. 24 (6), pp. 858–864. doi:10.1109/TPAMI.2002.1008395. ISSN: 0162-8828

Tasdizen, T., 2008. Principal components for non-local means image denoising. In: Proceeding of International Conference on Image Processing.

Tasdizen, T., Whitaker, R., Marc, R., Jones, B., 2005. Enhancement of cell boundaries in transmission electron microscopy images. In: ICIP, pp. 642–645.

Tu, Z., 2008. Auto-context and its application to high-level vision tasks. IEEE Conf. Comput. Vis. Patt. Recognit., 1–8.

Varma, M., Zisserman, A., 2003. Texture classification: are filter banks necessary? In: Proceedings of the 2003 IEEE Computer Society Conference on Computer Vision and Pattern Recognition, vol. 2, pp. II-691-8. doi:10.1109/CVPR.2003.1211534. ISSN: 1063-6919.

Vazquez, L., Sapiro, G., Randall, G., 1998. Segmenting neurons in electronic microscopy via geometric tracing. In: Proceedings of ICIP, pp. 814–818.

Vu, N., Manjunath, B., 2008. Graph cut segmentation of neuronal structures from transmission electron micrographs. In: 15th IEEE International Conference on Image Processing 2008, ICIP 2008, pp. 725–728. doi:10.1109/ICIP.2008.4711857. ISSN: 1522-4880.

Wells, G., Venaille, C., Torras, C., 1996. Promising research: vision-based robot positioning using neural networks. Image Vis. Comput. 14 (10), 715–732.

White, J., Southgate, E., Thomson, J., Brenner, F., 1986. The structure of the nervous system of the nematode *Caenorhabditis elegans*. Phil. Trans. Roy. Soc. Lond. Ser. B Biol. Sci. 314, 1–340.

White, J.Q., Nicholas, T., Gritton, J., Truong, L., Davidson, E.R., Jorgensen, E.M., 2007. The sensory circuitry for sexual attraction in *C. elegans* males. Curr. Biol. 17 (21), 1847–1857.

Zhu, Q., Song, G., Shi, J., 2007. Untangling cycles for contour grouping. In: IEEE 11th International Conference on Computer Vision 2007, ICCV 2007, pp. 1–8. doi:10.1109/ICCV.2007.4408929. ISSN: 1550-5499.

Please cite this article in press as: Jurrus, E., et al. Detection of neuron membranes in electron microscopy images using a serial neural network architecture. Med. Image Anal. (2010), doi:10.1016/j.media.2010.06.002

CHAPTER 9

SEMI-AUTOMATED NEURON BOUNDARY DETECTION AND NONBRANCHING PROCESS SEGMENTATION IN ELECTRON MICROSCOPY IMAGES

Reprinted with permission from Springer, Inc.

Jurrus, et al., 2012. Originally published in Neuroinformatics, doi:10.1007/s12021-012-9149-y

Neuroinform
DOI 10.1007/s12021-012-9149-y

ORIGINAL ARTICLE

Semi-Automated Neuron Boundary Detection and Nonbranching Process Segmentation in Electron Microscopy Images

Elizabeth Jurrus · Shigeki Watanabe · Richard J. Giuly · Antonio R. C. Paiva · Mark H. Ellisman · Erik M. Jorgensen · Tolga Tasdizen

Abstract Neuroscientists are developing new imaging techniques and generating large volumes of data in an effort to understand the complex structure of the nervous system. The complexity and size of this data makes human interpretation a labor-intensive task. To aid in the analysis, new segmentation techniques for identifying neurons in these feature rich datasets are required. This paper presents a method for neuron boundary detection and nonbranching process segmentation in electron microscopy images and visualizing them in three dimensions. It combines both automated segmentation techniques with a graphical user interface for correction of mistakes in the automated process. The automated process first uses machine learning and image processing techniques to identify neuron membranes that deliniate the cells in each two-dimensional section. To segment nonbranching processes, the cell regions in each two-dimensional section are connected in 3D using correlation of regions between sections. The combination of this method with a graphical user interface specially designed for this purpose, enables users to quickly segment cellular processes in large volumes.

Keywords Machine learning · Membrane detection · Artificial neural networks · Filter bank · Contour completion · Neural circuit reconstruction · Connectomics

E. Jurrus (✉) · A. R. C. Paiva · T. Tasdizen
Scientific Computing and Imaging Institute,
University of Utah, 72 S Central Campus Drive,
Salt Lake City, UT 84112, USA
e-mail: liz@sci.utah.edu

E. Jurrus
School of Computing, University of Utah,
Salt Lake City, UT, USA

S. Watanabe · E. M. Jorgensen
Department of Biology, University of Utah,
Salt Lake City, UT, USA

R. J. Giuly · M. H. Ellisman
National Center for Microscopy and Imaging Research,
University of California, San Diego, CA, USA

T. Tasdizen
Department of Electrical Engineering, University of Utah,
Salt Lake City, UT, USA

Introduction

Neural circuit reconstruction is an important method for studying neural circuit connectivity and its behavioral implications. The differences between neuronal classes, patterns, and connections are central to the study of the nervous system and critical for understanding how neural circuits process information. The ability to reconstruct neural circuitry at ultrastructural resolution is also of great clinical importance. With each new dataset generated, new details of well-known brain areas are being revealed, promising new insights into the basic biology and disease processes of nervous systems. For instance, for the first time, scientists can study the structural integrity of the transition zone of the optic nerve from unmyelinated to myelinated in the nervous system. This transition zone is now identified as one of the sites of pathology in glaucoma (Gonzalez-Hernandez et al. 2009). Other retinal degenerative

Published online: 30 May 2012

diseases, including retinitis pigmentosa and macular degeneration, result from a loss of photoreceptors. Photoreceptor cell stress and death induces subsequent changes in the neural circuitry of the retina resulting in corruption of the surviving retinal cell class circuitry. Ultrastructural examination of the cell identity and circuitry reveal substantial changes to retinal circuitry with implications for vision rescue strategies (Marc et al. 2003, 2007, 2008; Jones and Marc 2005; Jones et al. 2003, 2005; Peng et al. 2000). Ultrastructural evaluation of multiple canonical volumes of neural tissue are also critical towards the evaluation of differences in connectivity between different individuals.

Electron microscopy (EM) is a useful method for determining the anatomy of individual neurons and their connectivity because it has a resolution that is high enough to identify features, such as synaptic contacts and gap junctions. These features define connectivity, and therefore are required for neural circuit reconstruction. Manual analysis of this data is extremely time-consuming. Early work in mapping the complete nervous system of the relatively simple *C. elegans* took many years (White et al. 1986). Since then, several researchers have undertaken extensive EM imaging projects in order to create detailed maps of neuronal structure and connectivity (Fiala and Harris 2001; Briggman and Denk 2006a; Varshney et al. 2011). In comparison, newer imaging techniques are producing much larger volumes of very complex organisms, with thousands of neurons and millions of synapses (Briggman and Denk 2006b; Anderson et al. 2009). The complexity and size of the these datasets, often approaching tens of terabytes, makes human segmentation of the complex textural information of electron microscopic imagery both a difficult and very time-consuming task. Moreover, population or screening studies are unfeasible since fully manual segmentation and analysis would require years of manual effort per specimen. As a result, research in new imaging techniques and protocols, as well as automation of the reconstruction process, are critical for the study of these systems.

To assist in neural circuit reconstruction, this paper presents a method for segmenting 3D nonbranching cellular processes in EM images and visualize the results. The segmentation of neurons combines both automated neuron segmentation techniques with a graphical user interface for correction of mistakes in the automated process. The automated process first uses machine learning and image processing techniques to segment the neurons in each 2D section and then connect them in 3D. The combination of this process with a graphical user interface specially designed for this purpose, enable users to quickly segment neuron cell processes in large volumes.

Imaging Methods

Serial-section Transmission Electron Microscopy (ssTEM) and Serial Block Face Scanning Electron Microscopy (SSBFSEM) are the two methods used for image acquisition in this paper. Compared with other state of the art methods, such as MRI (Xiao et al. 2003) and scanning confocal light microscopy (Minsky 1961; Denk et al. 1990; Egner and Hell 2005; Rust et al. 2006; Betzig et al. 2006), electron microscopy methods provide much higher resolution and remain the primary tool for resolving the 3D structure and connectivity of neurons.

One of the modalities chosen for reconstructing neuronal circuits at the individual cell level is serial-section transmission electron microscopy (ssTEM) (Anderson et al. 2009, 2011; Chklovskii et al. 2010). Most importantly, through mosaicking of many individual images (Tasdizen et al. 2010; Saalfeld et al. 2010), ssTEM offers a relatively wide field of view to identify large sets of cells that may wander significantly as they progress through the sections. It also has an in-plane resolution that is high enough for identifying synapses. In collecting images through ssTEM, sections are cut from a specimen and suspended so that an electron beam can pass through it, creating a projection. The projection can be captured on a piece of film and scanned or captured directly as a digital image. An example ssTEM image is shown in Fig. 2a. An important tradeoff occurs with respect to the section thickness. Thinner sections are preferable from an image analysis point of view because structures are more easily identifiable due to less averaging. However, from an acquisition point of view, thinner sections are harder to physically handle and impose a limit on the area of the section that can be cut. Sections can be reliably cut at 30–90 nm thickness with the current ssTEM technology. This leads to an extremely anisotropic z resolution, compared to 2–10 nm in-plane. The *C. elegans* ventral nerve cord dataset used in this paper, for example, was imaged using ssTEM and has a resolution of 6 nm $\times$ 6 nm $\times$ 33 nm. This anisotropy poses two image processing challenges. First, the appearance of cell membranes can range from solid dark curves for neurons that run approximately perpendicular to the cutting-plane, to fuzzy grey swaths, commonly referred to as "grazed membranes," for membranes that run more obliquely and suffer more from the averaging effect. This is demonstrated in Fig. 1. Consequently, segmentations of neurons in these 2D images are difficult given the change in membrane

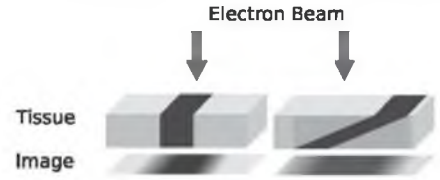

Fig. 1 Diagram demonstrating the formation of fuzzy membranes in ssTEM images

contrast and thickness. Second, due to the large physical separation between sections, shapes and positions of neurons can change significantly between adjacent sections. An example of this is shown in Fig. 3a.

Another specimen preparation and EM imaging technique commonly used for neural circuit reconstruction is Serial-Block Face Scanning Electron Microscopy (SBFSEM) (Denk and Horstmann 2004). In SBFSEM, successive slices are cut away and discarded, and the electron beam is scanned over the remaining block face to produce electron backscattering images. This method results in smaller deformations than ssTEM because the dimensions of the solid block remain relatively stable after slicing and thus deformation between sections is relatively small, usually eliminating the need for image registration between sections. The in-slice resolution (which is closer to 10nm) and signal-to-noise properties of SBFSEM are generally not as good as those of ssTEM, though. However, a specialized scanning electron microscope equipped with a high precision Gatan 3View ultramicrotome combined with an improved specimen staining protocol can produce high contrast images and increased detail of individual cells in the context of their surroundings (Deerinck et al. 2010). Specifically, by staining the tissue with a series of heavy metal stains, we were able to improve contrast and render the samples more conductive. The specimens were conductive enough to allow us to image at high vacuum, which results in images with improved resolution and signal/noise. This specimen preparation protocol was used to collect the neuropil of the molecular layer of the cerebellar cortex from an adult mouse, an exemplary image of which is shown in Fig. 2b. This image acquisition technique still results in anisotropic resolution, causing the separation between slices to be significant enough that positions of fine neurites and subcellular structures can shift and change significantly between sections (see Fig. 3b). In the case of SBFSEM mouse neuropil dataset, the resolution is 10 nm $\times$ 10 nm $\times$ 50 nm (SBFSEM).

Cellular Segmentation

There are two general approaches for neuron segmentation. One approach focuses first on the detection of neuron membranes in each 2D section. These boundaries can then be used to identify individual neurons, which are subsequently linked across sections to form a complete neuron (Jeong et al. 2010; Jurrus et al. 2008; Macke et al. 2008; Allen and Levinthal 1990). The other approach to neuron segmentation is to directly use the 3D characteristics of the data (Andres et al. 2008; Jain et al. 2007). Full 3D approaches are difficult due to the anisotropic nature of the data, however. As mentioned earlier, the large section thickness often causes features to shift significantly between sequential images, decreasing the potential advantages of a direct 3D approach.

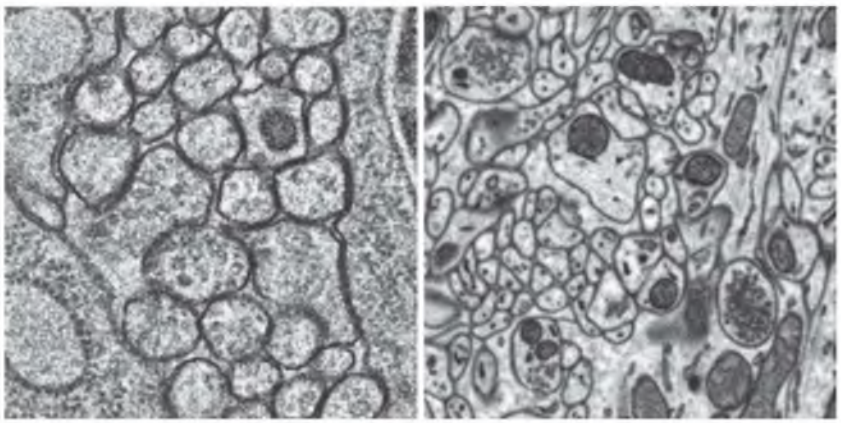

Fig. 2 **a** ssTEM image of the ventral nerve cord from the *C. elegans*. **b** SBFSEM image of the mouse neuropil

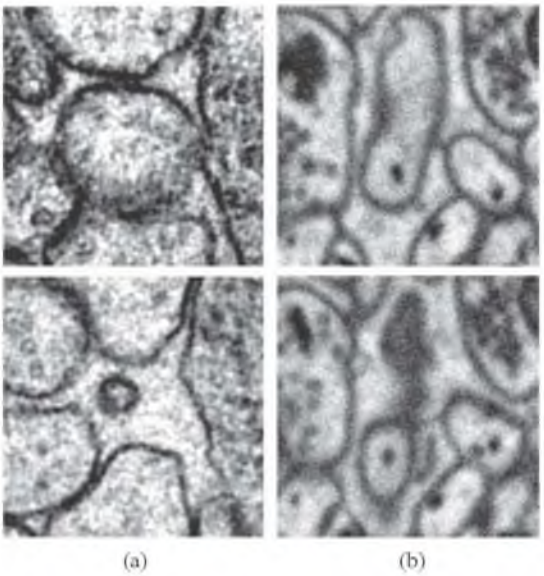

Fig. 3 Example showing how much change frequently occurs in neuron profiles between sequential sections from an **a** ssTEM image of the ventral nerve cord from the *C. elegans* and **b** SBFSEM image of the mouse neuropil

A number of methods exist for neuron membrane detection in 2D sections. Image processing methods for finding membranes include edge detection (i.e., Canny), region growing methods, and intensity thresholding on enhanced membrane features, either through Hessian-based diffusion (Tasdizen et al. 2005) or radon-like features (Kumar et al. 2010). Accurate detection of neuron membranes using these methods alone is a difficult problem given the presence of intracellular structures. There are several methods that attempt to segment EM images of neural tissue using active contours, in both parametric and level set forms (Jurrus et al. 2009; Bertalmío et al. 2000; Vazquez et al. 1998; Vazquez-Reina et al. 2009). 2D graph cuts can be used to segment images using region and boundary terms that separate intracellular structures from membranes (Vu and Manjunath 2008; Yang and Choe 2009). These can provide smooth, accurate segmentations of cells. However, when used alone they require a very specific energy minimization function so that neuron membranes are not confused with organelles making this method dependent on the type of cell being segmented. Additionally, their success can depend on their initialization (Vu and Manjunath 2008). Combined with machine learning methods (Kaynig et al. 2010), they have an improved detection accuracy and can be used more reliably in 3D.

Recent related work indicates that supervised machine learning methods are an effective approach for detection of neuron membranes in 2D and 3D (Jain et al. 2010; Andres et al. 2008). Simple classifiers such as a single perceptron applied to a carefully chosen set of features have been shown to provide promising results in identifying membranes in EM images (Mishchenko 2008). Nevertheless, this method still needs significant post-processing to connect membranes and remove internal cellular structures. Similarly, Venkataraju et al. proposed using local context features computed from the Hessian matrix to train a boosted classifier to detect membranes, which highlights the importance of context for membrane detection (Venkatataju et al. 2009). Jain et al. use a multilayer convolutional ANN to classify pixels as membrane or non-membrane in specimens prepared with an extracellular stain (Jain et al. 2007; Turaga et al. 2009). The convolutional ANN has two important characteristics: it learns the filters for classification directly from data, and the multiple convolutions throughout the layers of the network account for an increasing (indirect) filter support region. The serial neural network architecture (Jurrus et al. 2010) used in this paper also takes advantage of context and samples the image pixels directly to learn membrane boundaries, but given the anisotropic data, focuses only on 2D sections. New cost functions used during training are being developed to take into account the topological constraints of neuron boundaries (Turaga et al. 2010; Jain et al. 2010). The results obtained with these methods demonstrate not only the complexity of the problem, but also the potential of supervised machine learning as a tool towards neuron segmentation.

One of the goals of this work is to combine machine learning and segmentation algorithms with three-dimensional rendering capabilities for users to better understand how to process the data and visualize the results. Towards this aim, there are several existing software efforts that incorporate many of the above algorithms specifically for reconstructing neural circuits from biological volumetric images. These tools provide an interface to the data and contour tools to segment structures in a stack of EM images. One of most widely used software tools is Reconstruct (Fiala and Harris 2002, 2010) which enables users to view and outline structures of interest and then render them as 3D volumes. Combining Reconstruct with automated methods, such as the ones proposed by Mishchenko (Mishchenko et al. 2010) resulted in scientific discoveries regarding the predicted location of synapses within a neuron. IMOD (Kremer et al. 1996) and TrakEM2 (Cardona et al. 2010) have also proved to be useful tools for mosaicking, segmenting, and rendering

structures from a variety of biological volumetric image data. A more comprehensive set of tools for reconstruction is the Cell Centered Database (Martone et al. 2008) which performs not only annotation on EM images, but also provides data management and protein knowledge base interfaces. While these tools are critical in the segmentation and reconstruction of EM data, the goal of this paper is to segment many structures from large sets of images through the design of automated memory efficient algorithms while also building a tool capable of streaming large datasets for volume viewing and interaction. Towards this goal, two software programs, the Serial Section Reconstruction and Tracing Tool (SSECRETT) and NeuroTrace can segment large image databases (Jeong et al. 2009, 2010). SSECRETT is an interface for slice-based viewing of large volumes using a client-server architecture to request only the data needed by the user. NeuroTrace incorporates 2D level set segmentation tools for segmenting individual sections, and then using those segmentations to identify long neuronal processes. These combined tools produce vital reconstruction data, however the interface to the data is specific to the implemented algorithms and still requires the user to initialize each neuron for segmentation. The software program designed for this paper similarly manages memory for large datasets, but also is designed to incorporate automated segmentation algorithms. In addition, it provides an interface specific to the segmentation method presented in this paper to make corrections, and most importantly, view the raw image data with its 3D segmentation.

Methods

The overall method proposed in this paper for reconstructing nonbranching neuron cell processes consists of two steps. First, neuron membranes are segmented in 2D and neuronal cross-sections are identified. Second, the regions are linked across all the sections to form 3D renderings of parallel processes. The initial neuron segmentation used for each 2D section builds upon previous work which uses a series of artificial neural networks (ANNs) to detect neuron membranes. To improve the membrane detection, that method is extended here by incorporating learned membranes from sequential sections into another ANN and applying tensor voting post-processing. Also drawing from previous work, we incorporate an optimal path algorithm to connect similar regions through the volume to form complete 3D segmentations. Furthermore, this paper combines all of the above techniques into an interactive tool, called the Neuron Reconstruction Viewer (NeRV), that lets the user view large EM datasets, evaluate the segmentations, and make corrections to both the 2D membrane detection and the joining of regions through the sections to segment a neuron in 3D.

2D Membrane Detection

The method developed here for neuron membrane detection extends previous work, which uses a series of ANN classifiers and image stencil neighborhood feature vectors to detect neuron membranes in 2D images (Jurrus et al. 2010). In that paper, membrane detection was limited to features within a 2D section. An example output from this algorithm is shown in Fig. 4b–d. This work is extended here to train on information from neighboring sections, using the confidence from sequential sections. Given the anisotropic nature of the data, sequential sections have very poor membrane correspondence. To account for this, classified results representing the membrane probability image are registered and a 3D stencil that spans 3 sections is formed for training. Finally, tensor voting, a method for closing remaining gaps, is used. This provides significantly improved segmentation results over the original method (Jurrus et al. 2010). The output from these additional steps is shown in Fig. 4e and f. Quantitatively, the improvement of these new methods can be seen in Figs. 16, 17, 22 and 23.

Serial Neural Network Architecture

In previous work, a serial classifier architecture was implemented that used a series of classifiers, each operating on input from the previous classifier, to incrementally gain knowledge of a large neighborhood (Jurrus et al. 2010; Paiva et al. 2010). This architecture is particularly useful for two reasons. First, the data used for training requires no preprocessing with filter banks or statistics, and the classifier is trained directly on sampled image intensities. Second, by applying several classifiers in series, each classifier uses the classification context provided by the previous network to improve membrane detection accuracy. To initialize this architecture, the first classifier is trained only on image intensities. Each remaining classifier in the series then uses an input vector containing samples from the original image appended with the values from the output of the previous classifier, yielding a larger feature vector. While the desired output labels remain the same, each classifier is dependent on the information from the previous network and therefore must be trained sequentially. The output from each

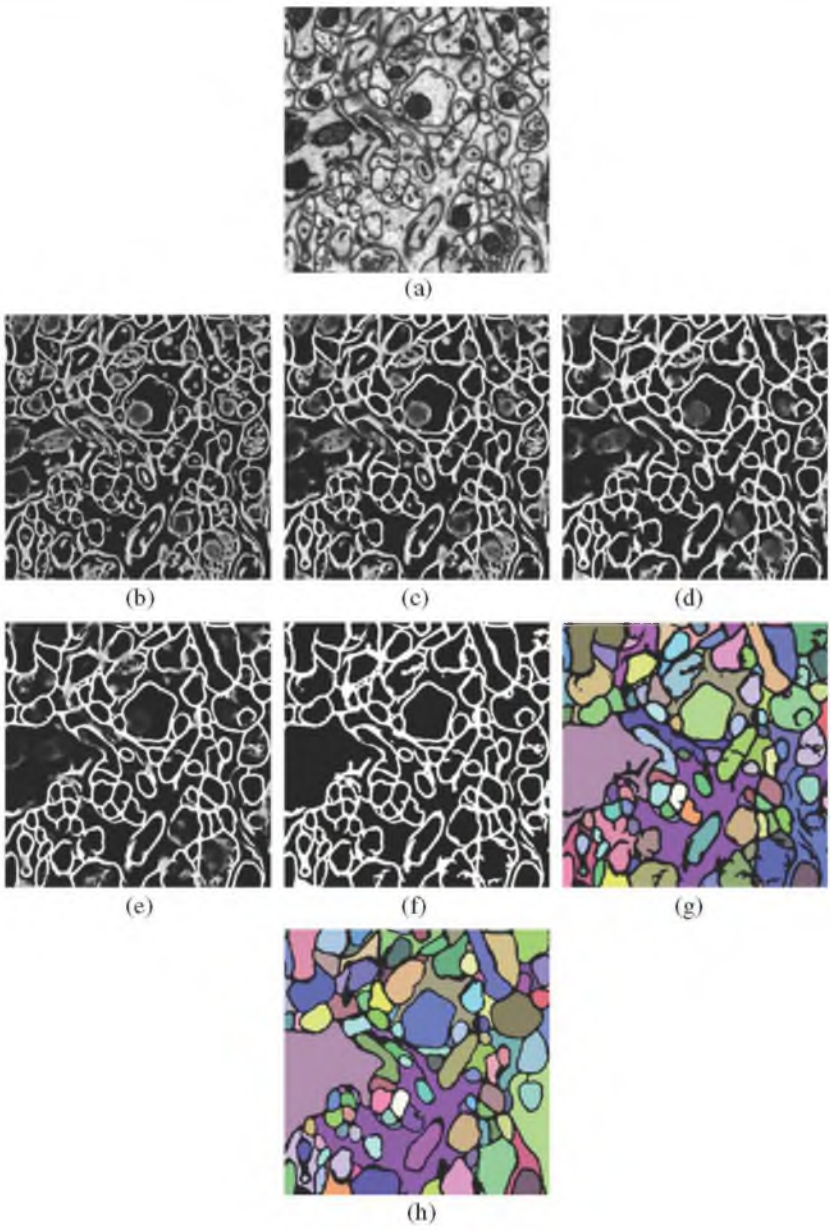

Fig. 4 Output of the method on a test image from an SBFSEM dataset. **a** is the raw image, **b**–**d** are stages 1, 2 and 5 of the series ANN, **e** is the output from the sequential series ANN, **f** is the output from the tensor voting, **g** is the region segmentation after a simple flood fill, and **h** the gold standard, generated by an expert, for membranes and neuron regions

network is used to generate an image that represents the membrane probability map at that stage. Figure 5 demonstrates this flow of data between classifiers: ML is the classifier, I denotes the image, S represents the sampling of image intensities from the image using the stencil, and C denotes the output from the classifier, yielding the membrane detection.

Since the serial classifier architecture is not specific to any classifier and given the success of ANNs for membrane detection (Mishchenko 2008; Jain et al. 2007), the classifier chosen for this architecture is a multilayer perceptron (MLP) ANN (shown in Fig. 6). An MLP is a feed-forward neural network which approximates a classification boundary with the use of nonlinearly

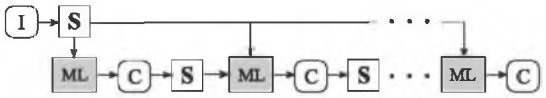

Fig. 5 Serial classifier diagram demonstrating the flow of information between classifiers. *I* is the original image, *C* is the output image from the classifier (*ML*), and *S* is the stencil (shown in Fig. 7) that samples the image data to form the feature vector for the classifier

weighted inputs. The output of each processing element (PE) (each node of the ANN) is given as (Haykin 1999; Principe et al. 2000)

$$y = f\left(\mathbf{w}^T\mathbf{x} + b\right), \tag{1}$$

where f is, in our case, the *tanh* nonlinearity, $\mathbf{w}$ is the weight vector, and b is the bias. The input vector $\mathbf{x}$ to PEs in the first hidden layer is the input feature vector discussed in more detail in the next section. For the PEs in subsequent layers, $\mathbf{x}$ contains the outputs of the PEs in the previous layer. ANNs are a method for learning general functions from examples. They are well suited for problems without prior knowledge of the function to be approximated (a.k.a., "black box models"). They have been successfully applied to robotics (Pomerleau 1993; Wells et al. 1996) and face and speech recognition (Rabi and Lu 1998; Cottrell 1990), and are robust to noise.

To learn the weight vector and bias, back-propagation was used to minimize the minimum squared error(MSE) criterion (Haykin 1999; Principe et al. 2000). Back-propagation is a gradient descent procedure that maps the output layer error to the error at the output of each node, yielding a local update rule that depends only on the node's input and output error. It is obtained by direct application of the chain rule to the derivative of the criterion with regards to each one of the ANN parameters. Because back-propagation depends only on the local gradient and that information is available directly from the optimization criterion, there is no need to explicitly characterize the parameter space.

The serial classifier is trained by simply using raw image intensities. Training a classifier on raw image data yielded improved results over filter banks and neighborhood statistical information (Jurrus et al. 2009; Paiva et al. 2010). The stencil, shown in Fig. 7, can cover large areas representing the desired feature space, but samples it with a spatially adaptive resolution strategy. In this way, an ANN can be trained using a low dimensional feature vector without having to use the whole image patch. Pixels are selected close to the stencil center, along a radius, at a high resolution, and then further from the center at a more coarse resolution. This gives more detail for the training of our classifier around the feature of interest, while maintaining a large area in which to apply context. Since the number of weights to be computed in an ANN are dominated by the connection between the input and the hidden layers, reducing the number of inputs also reduces the number of weights and helps regularize the learned network. Moreover, using fewer inputs generally allows for faster training. With this, one aims to provide the classifier with sparse, but sufficient context information and achieve faster training, while obtaining a larger context which can lead to improvements in membrane detection. This strategy, combined with the serial use of ANNs, grows the region of interest for classification within a smaller number of stages and without long

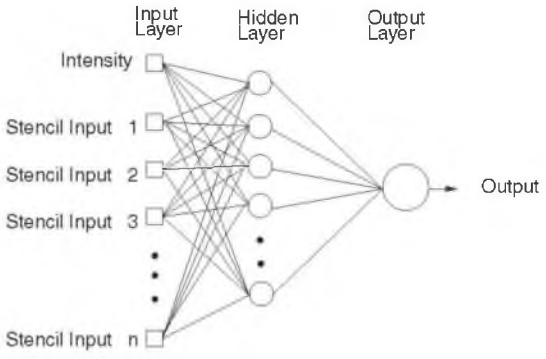

Fig. 6 Artificial neural network diagram with one hidden layer

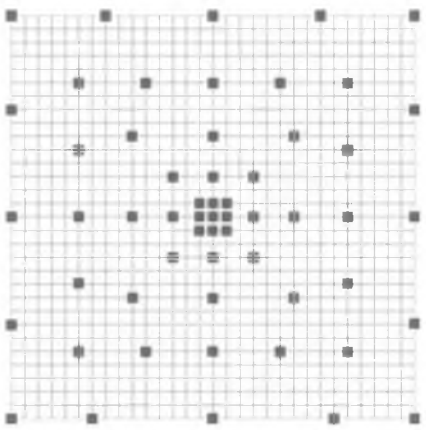

Fig. 7 Image neighborhood sampling technique: image pixels sampled using a stencil. For this example, the stencil contains a small number of samples, yet covers a larger area of the data. This is an efficient representation for sampling the image space

training times. Example output from the serial classifier is shown in Fig. 4b–d.

The training data used to train the classifier is generated by hand by domain experts. For each dataset, a user annotated all the membrane boundaries with curves that were one pixel wide on a subset of the images. We dilated this boundary to cover the width of the neuron membrane and these pixels were used as positive training examples for our classifier. Unannotated pixels, which included intercellular features such as vesicles, mitochondria, and nucleus, were used as negative training examples. From these pixels, we randomly chose a balanced set of positive and negative training examples for our classifier. This is discussed in more detail for each dataset in Sections "Results for the *C. Elegans* Ventral Nerve Cord" and "Results on the Mouse Neuropil".

Sequential Section Serial Neural Network Architecture

Sequential sections from EM data often contain similar structures that we would like to use as context to improve the quality of the 2D segmentation. One way to do this would be with a stencil that spans multiple sections. However, the membrane locations between sections have poor correspondence. This is partly because of the anisotropic nature of the data, which often results in large movement of membranes between sections, and membranes sometimes do not run perpendicular to the cutting plane causing membranes to have low contrast and appear fuzzy. The differences between two sections is seen in Fig. 8a which shows two sequential images with detected membranes overlaid with each other. Membranes in sequential sections are near each other, but they do not correspond well enough to use them directly in a 3D stencil that would span multiple sections. One way to resolve this problem is to perform a nonrigid registration across the whole volume to align as best as possible all the membrane boundaries. There are two problems with this approach. First, internal structures in the neurons complicate the registration process introducing possible errors to the segmentation. Second, this process introduces warping, changing the anatomy of the neurons. To account for this, we propose a novel approach which aligns sequential membrane probability map images between only two sections using a correlation-based nonlinear registration. We register only the membrane probability images because the classification process has removed many of the internal structures that would make an extremely fine-scale nonlinear registration on raw image data difficult. Also, we perform the registration between only two sections to keep the location of the neurons intact. Once registered, a 3D stencil that spans 3 adjacent sections samples the classification results from the previous stage and provides information to be used in the final classification step.

More specifically, after the membrane detection is complete for each section using the serial ANN architecture, images are registered in pairs to the center section and used as input to a new ANN. The serial ANN with the registration step and final ANN is depicted in Fig. 9. The registration method proposed is a B-spline deformable registration (Ibanez et al. 2005). Given an image to be registered and a static template image, a nonlinear deformation can be generated which minimizes the mean squared difference energy, given by,

$$\int_{\Omega} \left(C^M \circ t(x) - C^S(x)\right)^2 dx. \tag{2}$$

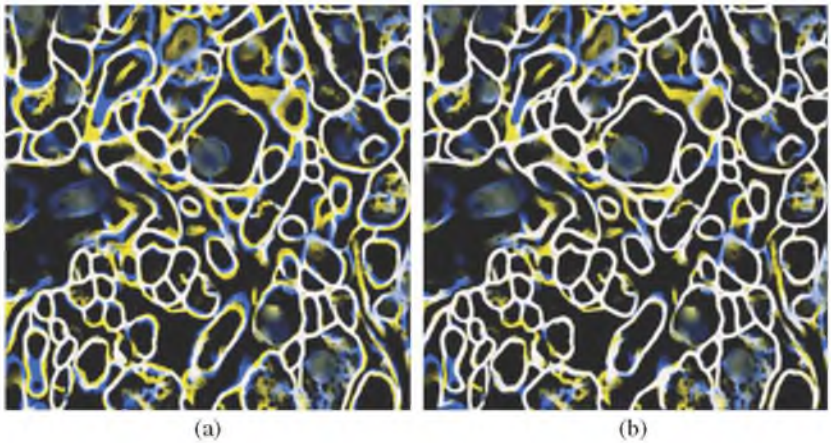

Fig. 8 (Color) Two sequential sections from the mouse neuropil with membranes detected after the serial ANN overlaid with each other with **a** no registration and **b** after the intensity-based nonlinear registration. *Blue* and *yellow colors* indicate membrane overlay mismatches and *white* indicates shared membranes

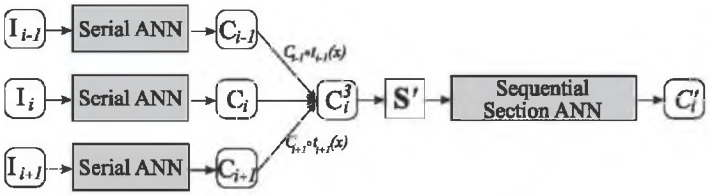

Fig. 9 Diagram demonstrating the flow of data for the sequential section ANN architecture on a single image. I_i are the input images, *SerialANN* is the diagram in Fig. 5 collapsed, and C_i is the output of the classifier on image I_i. $C_{i-1} \circ t_{i-1}(x)$ is the registration of C_{i-1} to C_i and $C_{i+1} \circ t_{i+1}(x)$ is the registration of C_{i+1} to C_i. C_i^3 is the stack of all three registered images. S' is the 3D stencil used on the combined images as input to the classifier. C_i' is the final classification

where Ω is the image domain and $t(x)$ is the deformation $\mathbb{R}^2 \rightarrow \mathbb{R}^2$, in our case given by a 2D tensor product B-spline transform of order 2 (Rueckert et al. 1999). C^M is the moving classification image, and C^s is the static classification image. For our purposes, C_i (the center section) is the static image and C_{i-1} and C_{i+1} are the moving images.

Each section has its own set of neighboring registered sections. The change in the membrane locations after two images are registered is shown in Fig. 8b. Now that membranes are more carefully aligned across neighboring sections, a new stencil can be used to sample the 3D space. The 3D, three section, stencil is similar to the one shown previously in Fig. 7. This stencil is used on the middle slice, while the stencil on the top and bottom slice have a shorter radius. The output from the ANN using this stencil is show in Fig. 4e. Using information from the sequential sections, the ANN learns to identify membranes in C_i that were not previously detected, because the membranes were detected in C_{i-1} and C_{i+1} improving the overall segmentation. This helps specifically in cases where C_i contains grazed membranes, but C_{i-1} and C_{i+1} do not. A good example of this is shown in Fig. 14, second column. Membranes in the raw image appear fuzzy and are not well detected after the serial ANN. Using information from the registered sequential sections strengthens these boundaries. In this way, the ANN also learns the possible shapes of membranes across several sections.

Tensor Voting

Tensor Voting (TV) is a method first proposed by Medioni et al. (2000) for extraction or enhancement of local features (lines, curves or surface) extraction results. Local feature extraction by itself is often unreliable in noisy and complicated images. That is, the lines or curves are often noisy and interrupted. TV enhances or predicts local features by integrating clues from nearby features. In our case, the influence of nearby features is based on a given voting field designed to extract smooth curves.

In tensor voting, a 2-D tensor can be represented by a symmetric, positive semidefinite 2×2 matrix as follows:

$$\mathbf{T} = \begin{pmatrix} a_{xx} & a_{xy} \\ a_{xy} & a_{yy} \end{pmatrix} = \lambda_1 \mathbf{e}_1 \mathbf{e}_1^T + \lambda_2 \mathbf{e}_2 \mathbf{e}_2^T \tag{3}$$

where λ_1 and λ_2 are the eigenvalues ($\lambda_1 \geq \lambda_2 \geq 0$); $\mathbf{e}_1$ and $\mathbf{e}_2$ are the orthonormal eigenvectors. Graphical representation of this kind of tensor is ellipse, as shown in Fig. 10a. One common parameterization is to define

Fig. 10 Tensor and tensor voting field

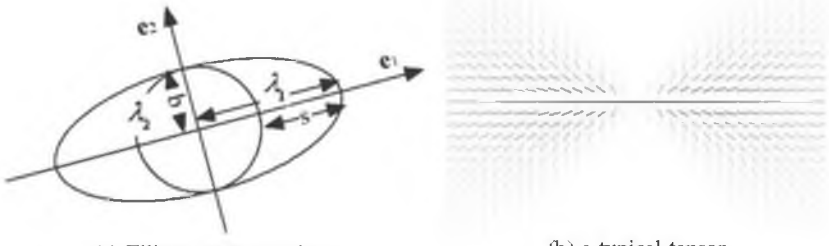

(a) Ellipse representation of a tensor

(b) a typical tensor **voting field**

a tensor with three parameters: orientation β, stickness s and ballness b.

$$\beta = arccos\left(\mathbf{e}_x^T \mathbf{e}_1\right) \tag{4}$$

$$s = \lambda_1 - \lambda_2 \tag{5}$$

$$b = \lambda_2 \tag{6}$$

where $\mathbf{e}_x = (1, 0)^T$. A tensor with ballness equal to 0 is called stick tensor and represents a curve passing through that pixel. A tensor with stickness equal to 0 is called ball tensor. In our work the initial tensors are computed from the classifier output image as

$$\mathbf{T}_{x,y} = I_{x,y} \begin{pmatrix} \cos(\alpha_{x,y}) \\ \sin(\alpha_{x,y}) \end{pmatrix} \left(\cos(\alpha_{x,y}), \sin(\alpha_{x,y})\right) \tag{7}$$

where $I(x, y)$ is the membrane strength at pixel (x, y) and $\alpha(x, y)$ is the local orientation computed as the orientation of the eigenvector corresponding to the smaller eigenvalue of the local second order derivative matrix (Hessian).

In TV, the "vote" is a tensor calculated from the geometric relation between the voter and the votee. All the votes to a pixel will be summed and form the output tensor of that pixel. The voting field is shown in Fig. 10b. A typical voting method is to filter the tensor image with a nonholonomic filter, called voting field, aligned with the local tensor orientation. Since this is a computationally intensive method, it is typically applied in a sparse manner such that only a subset of the pixels in the image, those where curve features are detected, are allowed to cast votes. However, in problems where detection is hard, such as with neuron membranes, it can be advantageous to allow every pixel to cast votes proportional to their strength, as determined by our classifier, and to postpone detection until after this step. To achieve this in a computationally efficient manner, we used a rapid tensor voting algorithm which uses steerable filters as a basis for the voting field (Franken et al. 2006; Leng et al. 2011). In this algorithm, a set of basis voting fields are convolved with the image and then linearly combined to form the desired voting field at each pixel.

Region Segmentation

Given detected membranes in each 2D section, neurons can be segmented in each section using either a watershed segmentation (Gonzalez and Woods 1992; Ibanez et al. 2005) or a simple flood fill algorithm on the thresholded probability map. The flood fill algorithm operates on thresholded data and works best when a user has corrected segmentations with hand editing and wants a precise neuron membrane representation at every section. For larger problems, the watershed algorithm has the advantage in that it can close gaps automatically. For our method, we apply a watershed segmentation to the blurred output from the tensor voting and select the watershed depth that best segments the neuron regions. However, there are two trade-offs to consider when choosing to use the watershed for region segmentation. The first is a trade-off between the ability to close large gaps and the ability to segment smaller features. This is controlled by the parameter σ which is used to smooth the image as part of the watershed process. Large σ enables the watershed to close large gaps but also loses the ability to segment smaller features. Another trade-off of the watershed is that depending on the level (or depth) of the watershed, chosen by the user, over-segmentation can occur of regions, meaning areas that should be one whole region are instead two or three regions. The user has to balance these trade-offs when choosing the level to proper set of required parameters. This is discussed more in Section "Results on the Mouse Neuropil" when the watershed is applied to the mouse neuropil data.

Region Linking

In segmenting the structures relevant for the datasets described in this paper, we present a method that identifies only parallel processes through a stack of images. For this paper, neuron identification across a stack of EM images is formulated as an optimal path problem with a graph data structure (Jurrus et al. 2008). The vertices of the graph are defined as the regions obtained by 2D segmentation of the individual sections, as described in Section "2D Membrane Detection". Edges in the graph represent possible linkages between regions in neighboring sections. Linking together the neuron regions in the graph is performed using Dijkstra's shortest path algorithm. The resulting path through the graph is used to reconstruct the neuron in 3D.

Linking Method for Neuron Regions

Let $R_{s,i}$ be the ith region from the 2D segmentation in section s. A directed graph containing a set of nodes that correspond to the set of segmented regions in section s is constructed. The set of directed edges on the graph is between all nodes in adjacent sections. That is,

$$E = \left\{ \bigcup_{s,i,j=1}^{N, Q_s, Q_{s+1}} E_{s,i,j} \right\} \text{ where } E_{s,i,j} = [R_{s,i}, R_{s+1,j}], \tag{8}$$

N is the total number of sections, and Q_s denotes the number of segmented regions in section s.

A path through the graph is defined as a sequence of nodes connected by edges. We are interested in paths that span all sections $P = (R_{1,i_1}, R_{2,i_2}, \ldots, R_{N,i_N})$, and the cost of the path is defined as the sum of the costs of the edges

$$K(P) = \sum_{s=0}^{N-1} W(E_{s,i_s,i_{s+1}}), \tag{9}$$

where $i_1, \ldots i_N$ is the set of indices that the path follows on each section; because of the directed nature of the graph, paths cannot cross back to previous sections.

For biologists, the identification of neurons between sections relies on texture, shape, and proximity. These properties motivate the construction of the edge cost as the negative of the log-product of the correlation between regions and a Gaussian penalty on in-section displacement. That is:

$$W(E_{s,i,j}) = -\log\left[C(R_{s,i}, R_{s+1,j}) \times \exp\left(\frac{-D(R_{s,i}, R_{s+1,j})^2}{\phi^2}\right)\right], \tag{10}$$

where $D(R_{s,i}, R_{s+1,j})$ is the Euclidean distance between region center of mass in the $x-y$ coordinates of the section. ϕ is the maximum distance we expect the neurons to move between sections. C is the maximum value of the normalized cross-correlation of the two segmented regions. Correlation is used most commonly in image processing and computer vision for locating or matching specific features across scenes. In this case, it is used to measure how well a region in section s matches with another region in section $s+1$. The two section images are multiplied with the characteristic function of the regions (0 outside, 1 inside) corresponding to $R_{s,i}$ and $R_{s+1,i}$ to obtain the masked images $I_{s,i}$ and $I_{s+1,j}$, respectively. Then, the normalized cross-correlation between two vertices of the graph is computed as

$$C(R_{s,i}, R_{s+1,j}) = \max_{t_x,t_y} \frac{\sum_{x,y} I'_{s,i}(x - t_x, y - t_y) I'_{s+1,j}(x, y)}{\sqrt{\left(\sum_{x,y} I'_{s,i}(x, y)^2\right)\left(\sum_{x,y} I'_{s+1,j}(x, y)^2\right)}}. \tag{11}$$

For computational efficiency, the cross-correlation is computed in the Fourier Domain. The log is used so that the formulation is equivalent to a product through the sections, and the system avoids seeking out very good connections at the expense of very bad ones. Cell identity is lost if a connection between sections is not sufficiently strong. Finally, the log-product, which can be seen as an edge connection weight, is negated to create a cost function.

An important extension to this basic framework allows paths to skip sections, in order to avoid poor quality sections, which can happen regularly. To accomplish this, edges are added to the graph that allow connections up to M sections away:

$$E = \left\{ \bigcup_{k,s,i,j=1}^{M,N,Q_s,Q_{s+k}} E_{s,i,j,k} \right\} \text{ where } E_{s,i,j,k} = [R_{s,i}, R_{s+k,j}] \tag{12}$$

where k is the number of skipped sections. For the datasets in this paper, $M = 2$, thereby allowing connections between sections separated at most by a single intermediate section. This gives Dijkstra's algorithm a choice in calculating the best path in the case where an immediately adjacent section does not have the best match. This changes the construction of costs for these edges, because we want to avoid cost functions that favor skipping sections when there is sufficient data to support a path through a section. The function in Eq. 10 is adjusted to penalize the correlation and distance terms for the skipped sections. Generally we have

$$W(E_{s,i,j}) = -\log\left[\alpha^{k-1} C(R_{s,i}, R_{s+1,j}) \times \exp\left(\frac{-D(R_{s,i}, R_{s+1,j})^2}{k\phi^2}\right)\right], \tag{13}$$

α is the typical normalized correlation penalty between a cell in two adjacent sections, which was found empirically to be about 0.6. The displacement Gaussian's variance is multiplied by k, allowing more spatial movement when a section is skipped. The effect of these changes is to normalize the correlation, but allow for more displacement between the skipped regions. Overall, this increases the edge cost for $k > 1$.

Dijkstra's algorithm, which finds a minimum distance path in a directed graph is used to find the optimal connectivity for each neuron (region) in the first section. Dijkstra is run with a zero cost for all the regions in the first section. The region with the best cost is found on the last section, and tracing the solution backwards results in the optimal path (best cell) for the whole data set. Of course in this solution, cells can share paths, which is not normally what we want for this particular application. To account for this, we enforce uniqueness iteratively, in a greedy optimization strategy. That is,

we solve for the best path, remove those nodes from the graph, and repeat, producing a sequence of cells associated with a decreasing degree of evidence for connectivity.

One of the constraints required by this method is that the user know how far a neuron will likely go across an image volume. This linking algorithm is designed to identify as many neurons as possible that start on slice s and end on slice $s+n$. This limits this method to parallel processes. However, for certain datasets, such as the *C. elegans* where neurons rarely branch or terminate, scientists can potentially use this automatic linking algorithm to reconstruct as many paths, P, as possible of the ventral nerve cord.

Neuron Reconstruction Viewer

The automatic methods described up until this point all work fairly well on their own, but in the end, require the ability for viewing and editing of the segmentation results. The Neuron Reconstruction Viewer (NeRV) (shown in Fig. 11) attempts to bridge these two requirements by providing a visual interface to large volumes of EM images and neuron segmentations, with the option to make corrections that will, in the long term improve the segmentation.

Primarily, NeRV is an interface for the user to view the raw image data and the 3D reconstruction. Interacting with the image data and the rendered neuron provides insight for the scientist on the arrangement of the neurons within the data. The pane on the left, in Fig. 11, is mainly a slice viewer. The user can view the membrane detection, the region segmentation, and the raw data all in one viewer. Spheres highlight the paths neurons take through the volume. The keyboard arrow keys or the slider in the middle lets the user scroll through the sections. The pane on the right, is a 3D viewer of the reconstructed neuron. Raw image data can be turned off and on in this view, and users can select other sections simply by clicking on the area of the neuron.

Users can interact with this using the graphical interface on the far left. First, users can correct segmentations to close gaps with a simple drawing tool, then recompute the regions and correlations to improve the optimal path calculation (as discussed in Section "Region Linking"). Users can manually select regions in slices and create their own 3D renderings with the automatic path calculation. For precomputed and segmented neurons, a separate window allows users to select different neurons for viewing, deleting, or joining.

Figure 12 is an overview of all the software and data used to generate results in this paper. Before NeRV can load any image data, a sequence of command line tools needs to be executed to generate the membrane detection, segmentations, correlations, optimal paths, and isosurfaces. NeRV could easily interact with all these tools at each step; however, because of the time it takes to process the data, it is easier to do the early steps off line. However, once generated, NeRV has the

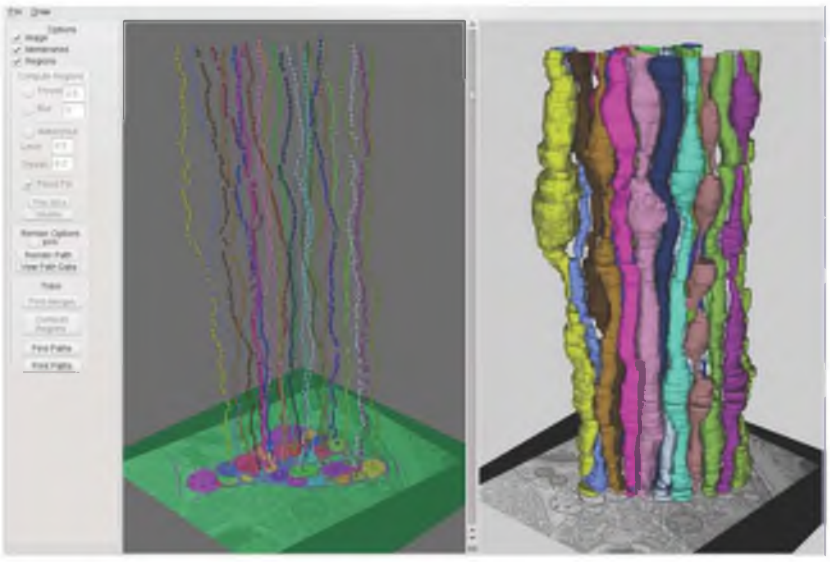

Fig. 11 (Color) Screen capture of NeRV displaying the automatic segmentation results on the *C. elegans* ventral nerve cord for a portion of the data

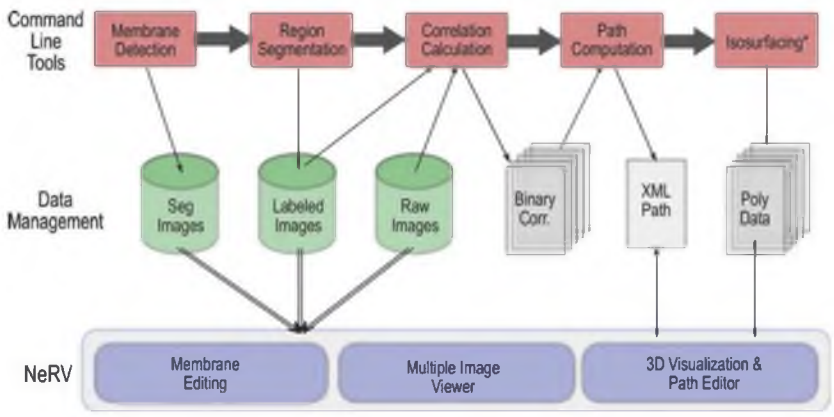

Fig. 12 (Color) Diagram demonstrating how the command line tools for segmenting EM images and NeRV interact with the EM images and data files. Directions of *arrows* indicate reads and writes. *Double arrows* designate data that is being streamed by VTK. The isosurfacing command line tool also takes, as input, the labeled images. "Binary Corr." are the correlations files for all the section to section edge weights, stored in binary for fast reading and writing of large files

ability to quickly edit membranes and view segmentations through streaming of the image data. Only the data that the user is viewing is loaded into memory. The 3D visualization and path editor give the user an opportunity to view full models of neurons and join paths, one of the most crucial steps in the reconstruction.

NeRV is built primarily using VTK (Schroeder et al. 2010) and Qt (Nokia 2012). To handle large datasets, the VTK image data streamer is used to load only the images required for viewing and requested by the user. Since slices are loaded as needed, the memory of this system is limited only by the size of a single section. Other optimizations, such as down sampling and memory management, enable efficient building of the isosurfaces for the 3D reconstruction in the right pane.

Neuron Segmentation Results

Two EM datasets are segmented using the proposed methods. The first dataset is a stack of 400 sections from the ventral nerve cord of the *C. elegans* worm. The second dataset is a stack of 400 sections from the mouse neuropil. These datasets contain very different types of neural cells. Furthermore, the *C. elegans* data has a resolution of 6 nm $\times$ 6 nm $\times$ 33 nm and each 2D section is 4008 $\times$ 2672 pixels, whereas the mouse neuropil data has a pixel resolution of 10 nm $\times$ 10 nm $\times$ 50 nm and each 2D section is 4096 $\times$ 4096 pixels. Figure 2 shows images from each of these datasets. Note that the membranes in the mouse and worm images, shown in Fig. 2, are very different. The section from the worm nerve cord (Fig. 2a) has a low signal-to-noise ratio and the neuron membranes have varying thickness and contrast. While the membranes from the mouse neuropil (Fig. 2b) are strong in contrast and have a high signal-to-noise ratio, they contain more variable internal structures. Both datasets contain grazed membranes, corresponding to neurons cut at nonperpendicular angles. This makes it difficult for even the human eye to identify all the membrane structures. More traditional statistics-based machine learning methods would require a specific filter design for each dataset. However, the use of stencils, rather than a predefined filter bank, means the proposed method can adapt to the idiosyncrasies of different samples and is successful in learning to detect neuron membranes in both datasets.

To segment the neurons in these datasets we focused on identifying parallel processes. The *C. elegans* data was ideal for this solution because nerves running along the ventral nerve cord rarely branched or terminated. In contrast, the mouse neuropil contains a higher number of branching structures, although in our close examination of the data, most parallel processes found in this data branched very little, maybe two to three slices. In an effort to segment as many neurons as possible, we also restrict our segmentation to processes that span a specific number of sections.

The results presented in this paper were generated using two different computers. The first was on a desktop computer containing 8, 2.8 GHz Intel CPUs and 8G of Memory. The second machine was a 32 node, 2.93 Ghz, shared memory computer containing 200 Gb of memory. The raw *C. elegans* data, if loaded entirely into memory at once, requires 4.2 Gb of memory, while the mouse neuropil data requires 25 Gb. Because of these memory requirements, distribution of the processing was done across computers, in parallel, for the most efficient computation of results as possible. Details regarding the time for each computation are described in detail in the following sections.

Results for the *C. Elegans* Ventral Nerve Cord

The nematode *C. elegans* is an important organism for neural circuit reconstruction because it is the only organism for which the connectivity has been determined (White et al. 1986; Varshney et al. 2011). Nevertheless, there are still numerous questions that require the determination of the connectivity, such as how genes regulate wiring (Jin et al. 1994) or how connectivity is altered to mediate different behaviors, for example, between males and females (White et al. 2007). In addition, reconstructions of the full nervous system reveal topological characteristics of the neurons that are important for studies of neuronal functions. The particular dataset used in this paper is from the ventral nerve cord of the *C. elegans* and is important for studying the interwoven topology of neurons making connections to local targets.

To segment the membranes in this dataset and create a 3D reconstruction, we first had to align all the

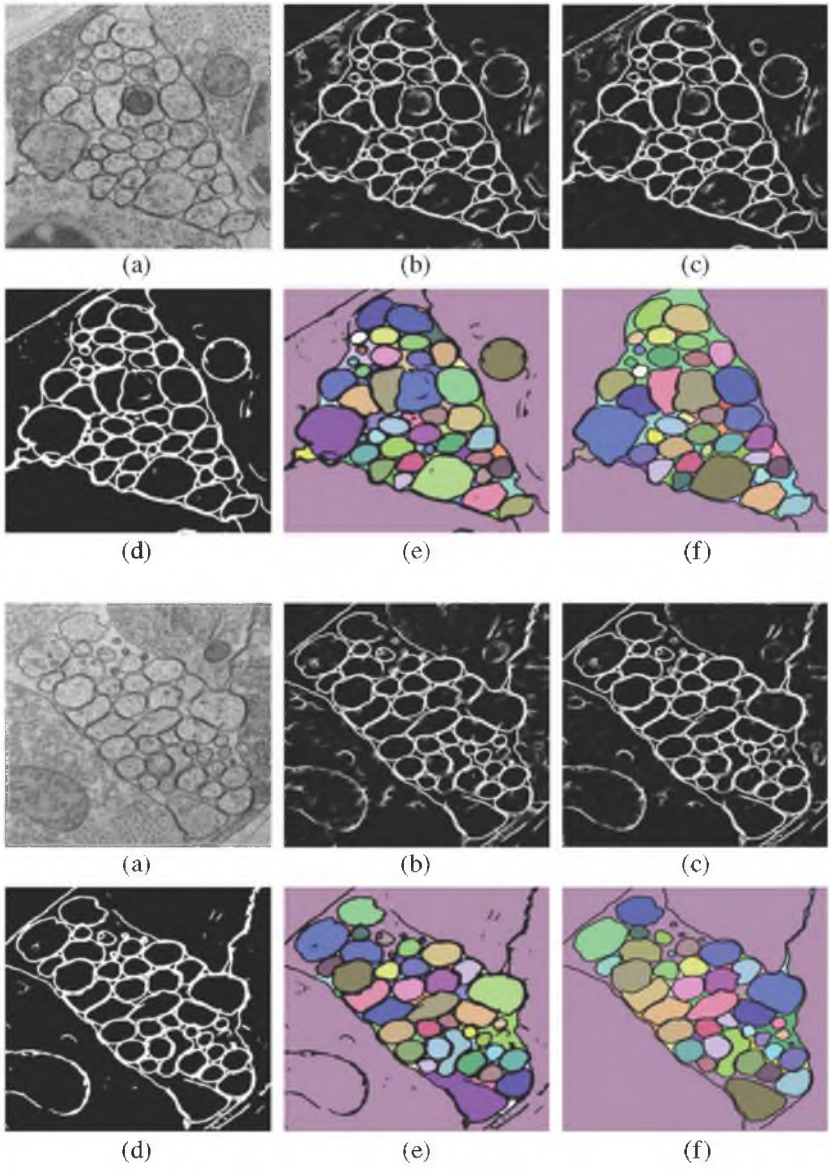

Fig. 13 (Color) Output of the method on *C. elegans* test images. **a** is the raw image, **b** is the output from the final stage of the series ANN (Section "Serial Neural Network Architecture"), **c** is the output from the sequential section ANN (Section "Sequential Section Serial Neural Network Architecture"), **d** is the output after tensor voting (Section "Tensor Voting"), and **e** is the segmentations of the neuron regions from a flood fill

ssTEM images into a volume. We performed a ridged alignment using a brute-force search for the unknown rotation and translation between adjacent pairs of sections (Tasdizen et al. 2010). This was a challenging task because there are significant changes between the sections resulting from slicing artifacts and missing sections. Approximately 10% of the images required user intervention to remove images of poor quality or realign sections that had little correspondence. Using the tools described in Tasdizen et al. hand alignment of two sections took just a couple of minutes. We did not perform a nonlinear alignment on these sections because we wanted to maintain the shape of the neurons and prevent distortion.

For validation, we had experts segment 40 selected images from the first 400 sections. Each expert placed

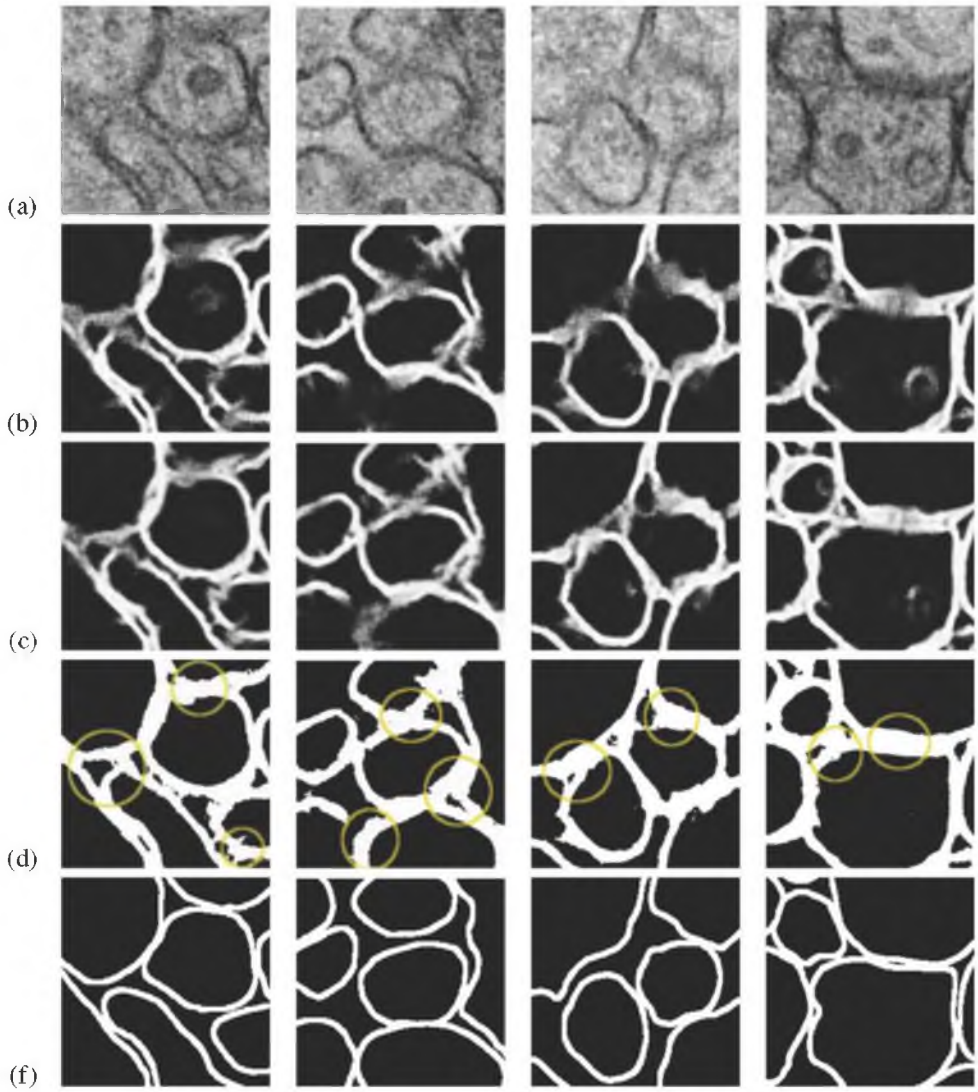

Fig. 14 (Color) Example images demonstrating how the different elements of the proposed method contribute to strengthen undetected or grazed membranes, and close gaps on the *C. elegans* ventral nerve cord data. **a** is the raw image, **b** is the output from the final stage of the series ANN (Section "Serial Neural Network Architecture"), **c** is the output from the sequential section ANN (Section "Sequential Section Serial Neural Network Architecture"), and **d** is the final output after tensor voting. *Yellow circles* highlight improved membrane detection and gap closing that results from these methods. **f** is the expert annotated gold standard

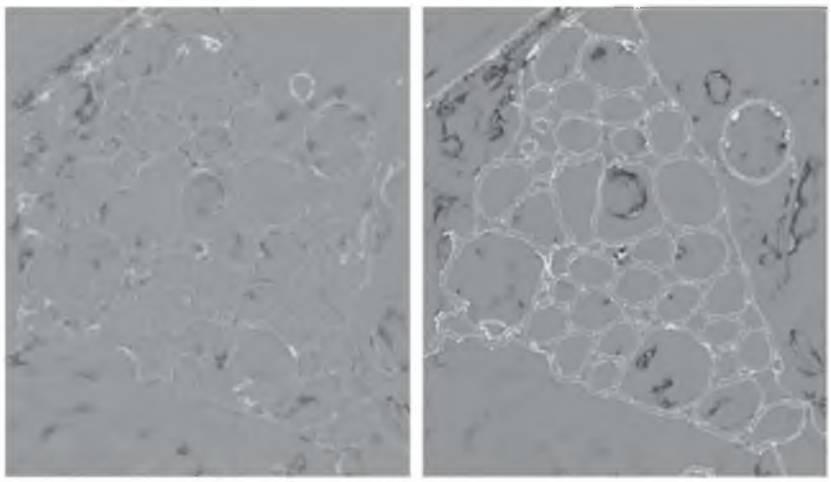

Fig. 15 Difference images for the image in Fig. 13, middle row, showing the change in membrane detection between **a** the series ANN and the sequential section ANN and **b** the sequential section ANN and tensor voting. *White pixels* indicate added membranes, *black* indicates removed membrane pixels, and *grey* is unchanged

a one pixel wide line along the membranes of the neurons, which we dilated using a 5 pixel wide structuring element, to cover most of the membrane pixels. Before training, we performed Gaussian blurring of the EM images with a small $\sigma = 2$ to remove noise, and down sampled by 2 to reduce the computational complexity. Then we used a contrast limited adaptive histogram equalization (CLAHE) (Pizer et al. 1990) filter to enhance the contrast in the neuron membranes. For the training data, 30 images were randomly selected for training and the remaining 10 were used for validation. From those images, 1 million samples were randomly selected from the manually marked images. Because of the relatively small percentage of positive examples (representing membrane pixels), these 1 million samples were chosen to contain $\frac{1}{3}$ positive and $\frac{2}{3}$ negative examples. The stencil used to sample the image values had a radius of 10 and was similar to the one in Fig. 7. The ANN we used was implemented in C++ and had one hidden layer of 20 nodes. To mitigate problems with local minima in training, each network was trained for 5 Monte Carlo simulations using randomly initialized weights. Each stage of the serial ANN took between 9 and 12 h to complete. The ANN for the sequential sections took about 22 h to train. Applying the weights from the ANNs takes a total of 7 min per section. Finally, the tensor voting implemented in Matlab was completed in 6 min per section.

Figure 13a shows three selected sections from the *C. elegans* dataset. The final membrane detection with the proposed method is shown in Fig. 13e. The sequential section ANN uses information about membranes also detected in neighboring sections to improve the current segmentation. The tensor voting uses, as input, the final classification and closes remaining gaps. This is demonstrated in closer detail in Fig. 14. Improved membrane detection is annotated with yellow circles. Most often a strong membrane in a neighboring section provides confidence for enhancing membranes with poor contrast in the current section. Using difference images, Fig. 15 demonstrates the improvements between the different methods. Figure 16 gives a numerical eval-

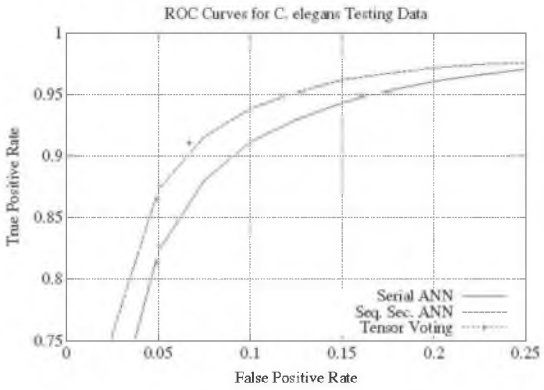

Fig. 16 These ROC curves show the improvement for the *C. elegans* data using the true positive and false negative membrane pixel classification rate with the use of the sequential section ANN (Seq. Sec. ANN) and the tensor voting, compared to using the serial ANN alone. Each curve the results over a series of threshold values from the output of the ANNs. The output from the tensor voting is binary and, thus, is represented by a single point

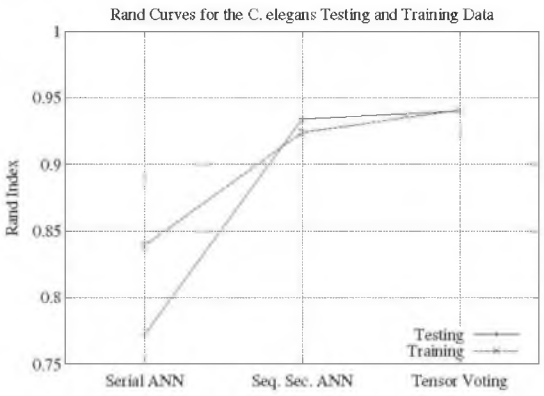

Fig. 17 This plot shows the improvement of the Rand index, which measures the similarity between two segmentations after the new methods, proposed in this paper, are applied. For each point in this plot, the segmentation for the methods is compared to the segmentation from the truth data

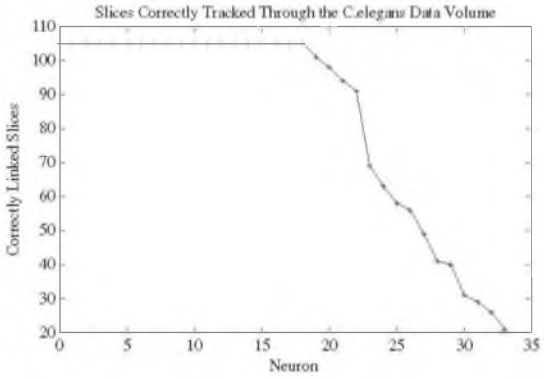

Fig. 19 This plot shows, in descending order, the number of regions correctly linked across slices for a continues series of images from the *C. elegans* volume

uation of the improvement between the serial ANN and the sequential section ANN on the validated test images using ROC curves. While the impact from the tensor voting method to close gaps is demonstrated qualitatively, its true positive and false positive values do not change as much. This is partly due to the dilation that results from the tensor voting and that the addition of pixels for closing is small compared to the overall segmentation. Figure 15b demonstrates this dilation effect. To evaluate the effectiveness of the sequential section ANN and the tensor voting applied to the output of the serial ANN, Fig. 17 uses the Rand index (Rand 1971) to validate our methods. For the *C. elegans* data, the value of using detected membranes from sequential sections to improve the classification is quite large, while the tensor voting contribute is smaller. Since we developed the tensor voting to work with both datasets, we suspect the lack of improvement for the *C. elegans* dataset is because the tensor voting was better tuned for the mouse neuropil image data.

Figure 18 shows the 3D reconstruction of 10 neurons through the first 300 sections of the *C. elegans* ventral nerve cord. Building this reconstruction was a two part

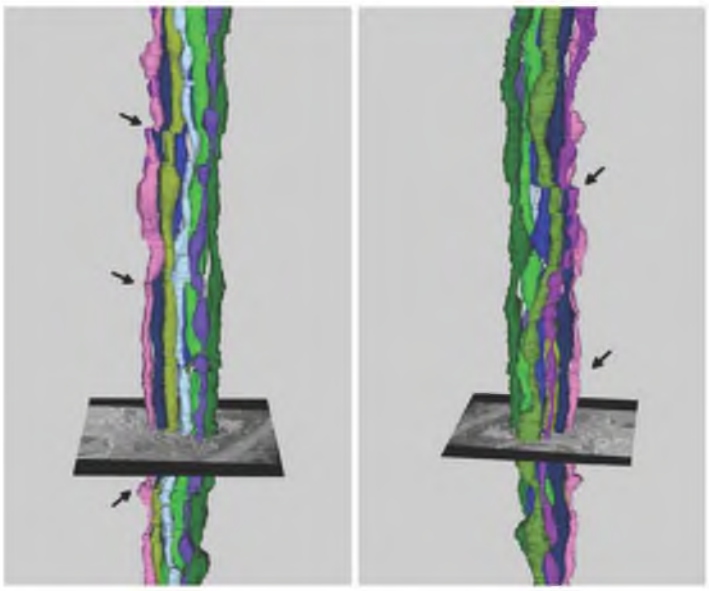

Fig. 18 (Color) Two views of 10 neurons spanning 300 sections of the ventral nerve cord of the *C. elegans*. Neuron paths were generated automatically between six pairs of sections where known breaks in the image data existed. NeRV was used to connect paths between the breaks. *Arrows* identify discontinuities in neurons where some of these breaks occurred

process. First, we identified six significant breaks in the image volume where there was missing data due to lost or badly imaged sections. These were places where the data had significant changes and would cause the region linking algorithm to fail. As a result, neuron regions were linked only between the sections without breaks, producing six sets of paths that spanned the whole volume. To completely reconstruct these paths through the all 300 sections, NeRV was used to manually merge neurons in sequential sections, forming complete reconstructions through the volume. This final step, computing the isosurface for all the neurons, took approximately 5 min per neuron to complete. Figure 18 is the final output from this process.

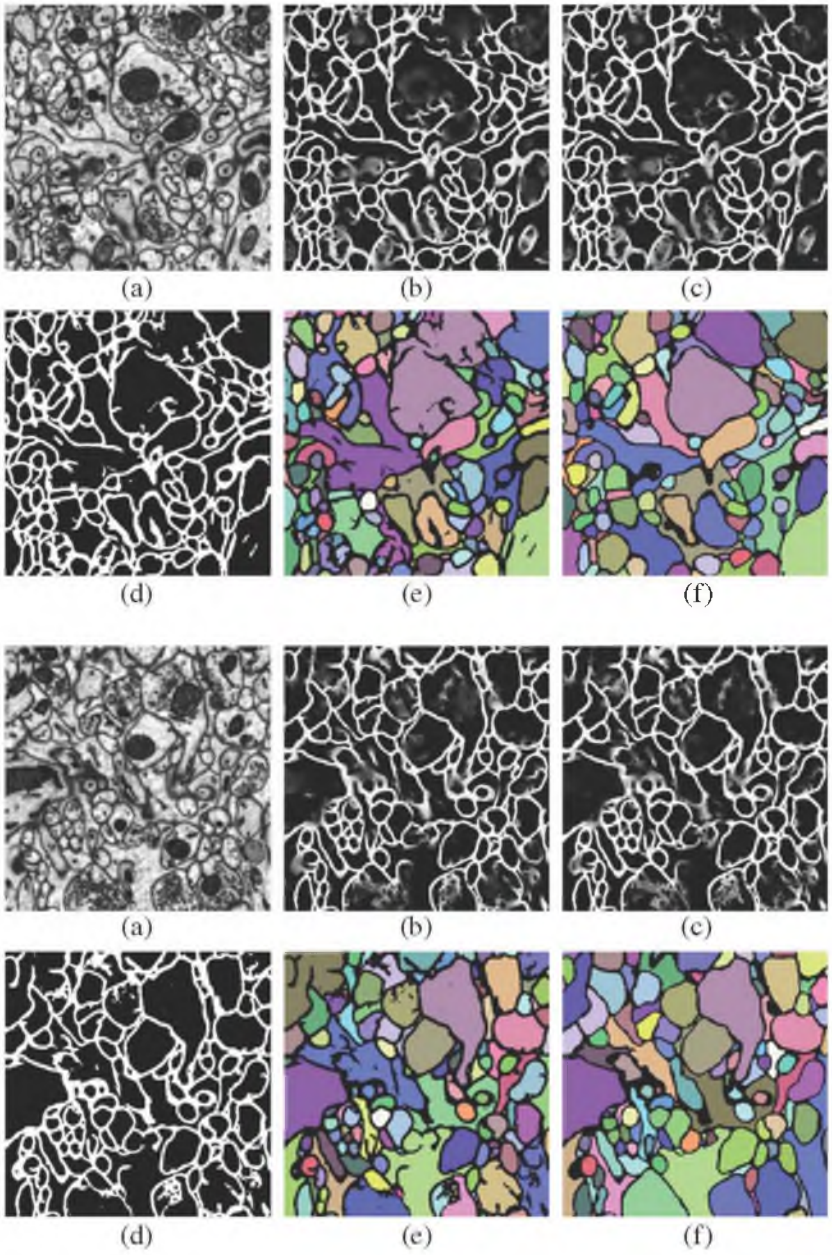

Fig. 20 (Color) Output of the method on a three different test images from the mouse neuropil. **a** is the raw image, **b** is the output from the final stage of the series ANN (Section "Serial Neural Network Architecture"), **c** is the output from the sequential section ANN (Section "Sequential Section Serial Neural Network Architecture"), **d** is the output after tensor voting (Section "Tensor Voting") and **e** is the segmentations of the neuron regions from a flood fill

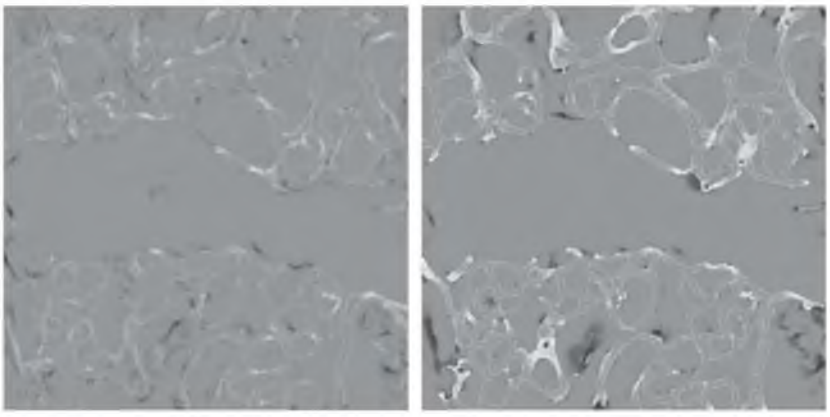

(a) (b)

Fig. 21 Difference images for the mouse neuropil section in Fig. 20, middle row, showing the change in membrane detection between **a** the series ANN and the sequential section ANN and **b** the sequential section ANN and tensor voting. *White pixels* indicate added membranes, *black* indicates removed membrane pixels, and *grey* is unchanged

To validate the accuracy of the 3D reconstruction automatically generated by the neuron region linking method, we manually inspected the top 34 total paths returned for a sequence of images. We picked the series of images 85–190 to be our test volume. This sequence of images had the longest continuous set of sections without significant breaks. Figure 19 shows the number of regions each neuron successfully tracked through the volume. Of these 34 paths, 19 (58%) went through the entire dataset with no errors. Of the remaining paths, nine correctly linked neuron regions for over half of the sections and six paths correctly linked regions through less than half of the sections. Despite the continuity of the set of sections, significant changes between neuron shape and location still existed within this block of images. One example of this is shown in Fig. 3. These cases sometimes caused neuron paths to sometimes follow intercellular spaces (also included in the graph) or other neuron regions. Overall, the automatic segmentation still has the potential to reduce the amount of time a scientist is required to perform annotation by half for this dataset.

Results on the Mouse Neuropil

Understanding the connectivity, types of connections, and roles of different cells in the mouse neuropil is an increasingly common area of study. The 3D organization of these structures provides insight into how the nervous system functions at very basic levels (Watanabe et al. 2010). In an effort to better understand and statistically quantify these structures, we are segmenting a large volume of the mouse neuropil.

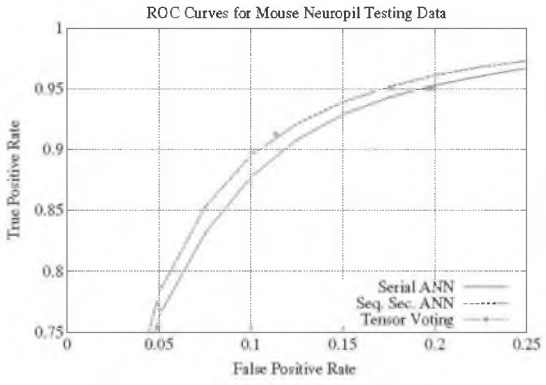

Fig. 22 ROC curves showing the improvement of the membrane pixel classification rates on the mouse neuropil data using the two methods highlighted in this paper

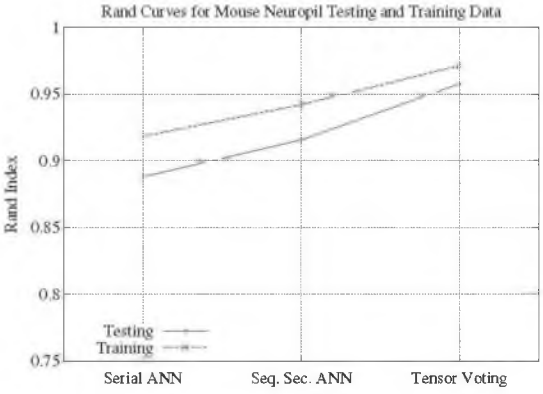

Fig. 23 The Rand index is used to demonstrate the similarity between the segmentations produced after a flood fill of the output from the sequential section ANN and tensor voting when compared to the true neuron regions

The entire neuropil dataset is $4096 \times 4096 \times 400$. To train and validate our neural networks, a subset of this data ($700 \times 700 \times 70$) was manually segmented using Amira (Imaging 2012) by an expert. From that set, 42 images were randomly selected and used for training in our classifier. The training set contained 4.5 million examples. To decrease training time, the ANN was trained first on 1 million examples for 50 iterations. The weights from this network were used to initialize the ANN for the 4.5 million training examples. The ANN contained one hidden layer of ten nodes. The images required no preprocessing to remove noise or enhance contrast and were sampled with a stencil of radius 10.

Figure 20 shows the segmentation results on three images from different sections. Figure 24 demonstrates in more detail the gap closing that occurs when the

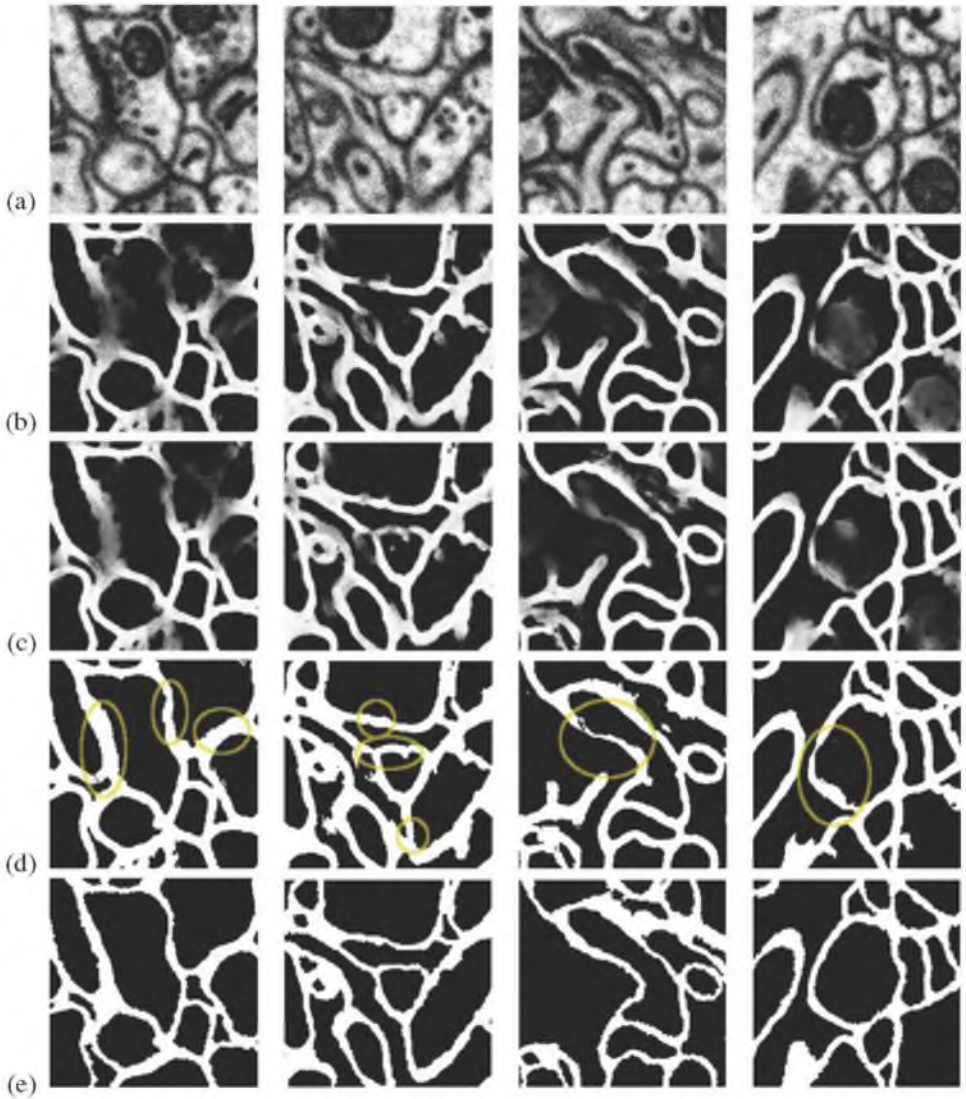

Fig. 24 (Color) Example images demonstrating this method closing gaps on neuropil data. **a** is the raw image, **b** is the output from the final stage of the series ANN (Section "Serial Neural Network Architecture"), **c** is the output from the sequential section ANN (Section "Sequential Section Serial Neural Network Architecture"), and **d** is the final output after tensor voting. *Yellow circles* highlight membranes that were enhanced and detected using these methods. Finally, row **e** is the ground truth

sequential section ANN and tensor voting are used. Figures 21 and 22 give a quantitative comparison on the improvement of the different methods. While the improvement in the ROC curve for the sequential section ANN is evident, the improvement after the tensor voting is more difficult to distinguish. However, evaluation of the difference images and the Rand index, shown in Figs. 21 and 23, shows a much greater improvement towards closing gaps and strengthening boundaries.

Final reconstruction of the volume on the entire dataset turned this task into a large data challenge, since the actual size of the full volume is much larger than the training data. First, neuron membranes needed to be detected in each 4K $\times$ 4K section, which took about 40 min for each section, including applying all the weights in series from the ANNs and using tensor voting. As a reminder, the output from each step of this process is depicted in Fig. 24b–d. We then used the watershed segmentation algorithm on the blurred output from the tensor voting. As discussed in Section "Region Segmentation", the user chose a level for the watershed that gave us a slightly over segmented set of regions, ensuring that gaps were closed. Using the watershed implementation from ITK (Ibanez et al. 2005), a level of 0.15 was used. These became the regions used in the correlations and linking methods. The computation of the watersheds was much faster, taking only about 1 min per section. Calculating the correlations between every two sections took between 40 min and 1.5 h, depending on the number of regions in each section. To reduce computational time and the required memory, correlations were only calculated for regions within β distance away. For this dataset $\beta = 150$. Once all the correlations are calculated, a graph can be constructed and Dijkstra can be used to find paths through the volume. The generic implementation of Dijkstra's algorithm has a complexity of $O(r^2)$, where r is the number of nodes in the graph. However, for this case, since the edges in the graph are limited to connections between sections, the complexity is $O(\frac{r^2}{N})$. The graph can be made even more sparse by limiting the number of edges to regions by $D(R_{s,i}, R_{s+1,j}) < d$, where d is the maximum distance a region is allowed to connect between region centers. For this dataset $d = 100$. This means the algorithm can scale more easily to larger graphs. To scale the path calculation even further, we divided the volume into smaller slabs and found paths through every 25 sections. Each path then took approximately 4 min to compute and paths were easily joined by matching paths with overlapping sections. To view in 3D, each path that spanned more than 300 sections was rendered in 45 min. We used, to our advantage, multiple processor machines to compute these results as efficiently as possible, in parallel. NeRV easily handles the size of this data because it only loaded into memory what was requested by the user. Finally, users

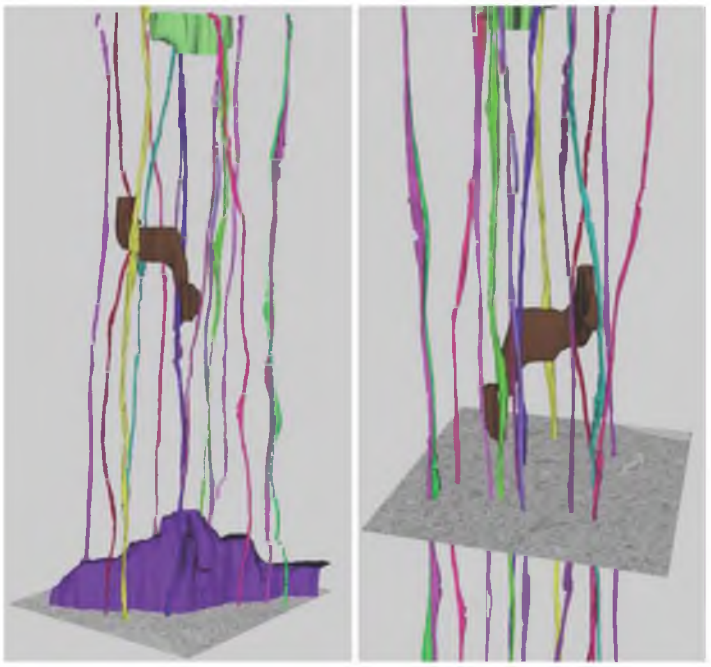

Fig. 25 (Color) Two views of 14 fully automatically segmented parallel fibers spanning 400 sections of the mouse neuropil. The larger three structures, Purkinje cells, were segmented manually using the NeRV interface. Discontinuities in the neuron renderings indicate sections of the automatic algorithm that were skipped because of changing neuron regions

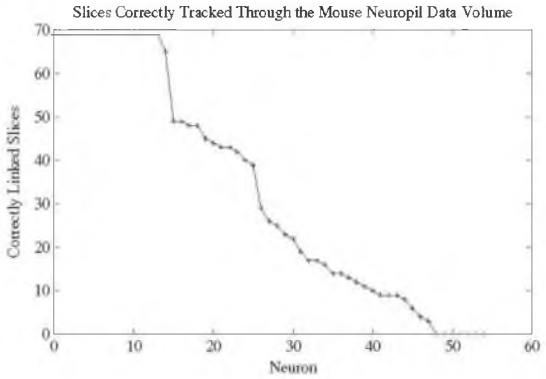

Fig. 26 This plot shows, in descending order, the number of regions correctly linked, for each neuron, across the subset volume of the mouse neuropil

can easily select the neurons they want to view in the volume. The final 3D visualization of this dataset can be seen in Fig. 25.

Our neuron linking method was validated for this dataset using the small training volume, discussed earlier, which is a subset of the main volume. We calculated every possible path that would pass from the top of the stack to the bottom of the stack. After we eliminated paths that attempted to link neurons that passed through the edge and outside of the volume subset, we had 56 possible paths. Of these, 14 were correctly segmented neurons through the whole stack, 12 were correctly segmented through more than half of the dataset, 23 were correctly segmented through less than half of the dataset, and finally 7 paths had no regions correctly linked. Figure 26 is a plot of these results, demonstrating the accuracy of the neuron linking through a small volume that is representative of the main dataset.

Conclusion and Future Work

This paper presents a method for the segmentation and extraction of neurons from electron microscopy images. Membranes in each 2D section are initially detected using a series of ANNs. The output image from this algorithm is used in a final ANN which uses registered images to improve the classification. Examining the detected membranes in sequential sections, above and below the current section, helps the classifier learn to detect membranes that are grazed or complicated by internal cellular structures. In the last step, tensor voting closes remaining gaps in the image. A software tool, NeRV, provides an interface for users to correct 2D segmentations and manually assign neuron paths through sections. Users can also view automatically generated paths and join sections. This aids the user in visualizing the reconstruction data.

Future work in this area includes extending this framework to detect synapses and vesicles. In addition, we would like to incorporate a multiscale context sampling method to train the series ANNs. One of the drawbacks of this method is that the classifier is very sensitive to the data it uses in training. As a result, applying this method to new image data without first training a classifier is not possible. Recent, related work in this field is available in a tool called Ilastic (Sommer et al. 2011) which computes segmentations based on user inputs. Building on these concepts, we would like to improve the performance and flexibility of our algorithms to enable the incorporation of interactive user input into our model. The path computation and linking of neuron membranes might also be more efficient to compute using a more flexible graph matching algorithm, incorporating recent work by Funke et al. (2011). This would be beneficial because it could more easily handle neuron branching and termination. Finally, NeRV should be extended with more user interfaces for editing neuron segmentations, such as making corrections and handling branching.

We plan on extending this method on the full *C. elegans* ventral nerve cord dataset. This would reveal in 3D the physical layout of neurons and can be compared to the data from White et al. which is the current gold-standard for neuron connectivity in the *C. elegans*. Further work to segment the synapses in the neurons and the muscles that surround the nerve cord would provide insight into communication and wiring in the *C. elegans*. Likewise, a more thorough analysis of the 3D reconstructions in the mouse neuropil need to be completed so we can develop a better understanding of the types of connections present in this dataset.

Information Sharing Statement

NeRV and related command line tool software are available at http://www.sci.utah.edu/~liz/nerv.html for download. The mouse neuropil image data is available from ccdb.ucsd.edu as a microscopy product with the ID 8192.

Acknowledgements This work was supported by NIH R01 EB005832 (TT), HHMI (EMJ), NIH NINDS 5R37NS34307-15 (EMJ) and 1R01NS075314 (MHE, TT) as well as NIH NCRR for support of the National Center for Microscopy and Imaging Research at UCSD, 5P41RR004050 (MHE). We are grateful to Nikita Thomas, Nels B. Jorgensen, Jeremy B. Thompson, and

Blake Paulin for their help in imaging the c. elegans VNC and Eric Bushong and Thomas Deerinck for their work in preparing the examples from the mouse cerebellum.

References

Allen, B. A., & Levinthal, C. (1990). CARTOS II semi-automated nerve tracing: Three-dimensional reconstruction from serial section micrographs. *Computerized Medical Imaging and Graphics, 14*(5), 319–329.

Anderson, J. R., Jones, B. W., Watt, C. B., Shaw, M. V., Yang, J. H., Demill, D., et al. (2011). Exploring the retinal connectome. *Molecular Vision, 17*, 355–379.

Anderson, J. R., Jones, B. W., Yang, J.-H., Shaw, M. V., Watt, C. B., Koshevoy, P., et al. (2009). A computational framework for ultrastructural mapping of neural circuitry. *PLoS Biology, 7*(3), e74.

Andres, B., Köthe, U., Helmstaedter, M., Denk, W., & Hamprecht, F. A. (2008). Segmentation of SBFSEM volume data of neural tissue by hierarchical classification. In G. Rigoll (Ed.), *Pattern recognition. LNCS* (Vol. 5096, pp. 142–152). Berlin: Springer.

Bertalmío, M., Sapiro, G., & Randall, G. (2000). Morphing active contours. *IEEE Transactions on Pattern Analysis and Machine Intelligence, 22*, 733–737.

Betzig, E., Patterson, G. H., Sougrat, R., Lindwasser, O. W., Olenych, S., Bonifacino, J. S., et al. (2006). Imaging intracellular fluorescent proteins at nanometer resolution. *Science, 313*(5793), 1642–1645.

Briggman, K. L., & Denk, W. (2006a). Towards neural circuit reconstruction with volume electron microscopy techniques. *Current Opinion in Neurobiology, 16*(5), 562–570.

Briggman, K. L., & Denk, W. (2006b). Towards neural circuit reconstruction with volume electron microscopy techniques. *Current Opinion in Neurobiology, 16*(5), 562–570.

Cardona, A., Saalfeld, S., Preibisch, S., Schmid, B., Cheng, A., Pulokas, J., et al. (2010). An integrated micro- and macroarchitectural analysis of the *Drosophila* brain by computer-assisted serial section electron microscopy. *PLoS Biol, 8*(10), e1000502.

Chklovskii, D. B., Vitaladevuni, S., & Scheffer, L. K. (2010). Semi-automated reconstruction of neural circuits using electron microscopy. *Current Opinion in Neurobiology, 20*(5), 667–675.

Cottrell, G. W. (1990). *Extracting features from faces using compression networks: Face, identity, emotion and gender recognition using holons* (pp. 328–337). San Mateo: Morgan Kaufmann.

Deerinck, T. J., Bushong, E. A., Thor, A., & Ellisman, M. H. (2010). NCMIR methods for 3D EM: A new protocol for preparation of biological specimens for serial block face scanning electron microscopy. In *Microscopy* (pp 6–8).

Denk, W., & Horstmann, H. (2004). Serial block-face scanning electron microscopy to reconstruct three-dimensional tissue nanostructure. *PLoS Biol, 2*(11), 1900–1909.

Denk, W., Strickler, J. H., & Webb, W. W. (1990). Two-photon laser scanning microscopy. *Science, 248*, 73–76.

Egner, A., & Hell, S. W. (2005). Fluorescence microscopy with super-resolved optical sections. *Trends in Cell Biology, 15*(4), 207–215.

Fiala, J. C., & Harris, K. M. (2001). Extending unbiased stereology of brain ultrastructure to three-dimensional volumes. *Journal of the American Medical Informatics Association, 8*(1), 1–16.

Fiala, J. C., & Harris, K. M. (2002). Computer-based alignment and reconstruction of serial sections. *Microscopy and Analysis, 87*, 5–8.

Fiala, J. C., & Harris, K. M. (2010). Synapseweb. http://synapses.clm.utexas.edu/tools/reconstruct/reconstruct.stm.

Franken, E., Almsick, M., Rongen, P., Florack, L. M. J., & Haar Romeny, B. M. (2006). An efficient method for tensor voting using steerable filters. In *ECCV06* (pp. IV:228–IV:240).

Funke, J., Andres, B., Hamprecht, F. A., Cardona, A., & Cook, M. (2011). Multi-hypothesis crf-segmentation of neural tissue in anisotropic em volumes. *CoRR*, abs/1109.2449.

Gonzalez, R. C., & Woods, R. E. (1992). *Digital image processing*. Boston: Addison-Wesley Longman.

Gonzalez-Hernandez, M., Pablo, L. E., Armas-Dominguez, K., Rodriguez de la Vega, R., Ferreras, A., & Gonzalez de la Rosa, M. (2009). Structure-function relationship depends on glaucoma severity. *British Journal of Ophthalmology, 93*(9), 1195–1199.

Haykin, S. (1999). *Neural networks—A comprehensive foundation* (2nd ed.). New York: Prentice-Hall.

Ibanez, L., Schroeder, W., Ng, L., & Cates, J. (2005). *The ITK software guide* (2nd ed.). Kitware, Inc. ISBN 1-930934-15-7. http://www.itk.org/ItkSoftwareGuide.pdf.

Jain, V., Bollmann, B., Richardson, M., Berger, D. R., Helmstaedter, M. N., Briggman, K. L., et al. (2010). Boundary learning by optimization with topological constraints. In *2010 IEEE conference on computer vision and pattern recognition (CVPR)* (pp. 2488–2495).

Jain, V., Murray, J. F., Roth, F., Turaga, S., Zhigulin, V., Briggman, K. L., et al. (2007). Supervised learning of image restoration with convolutional networks. In *IEEE 11th international conference on computer vision* (pp. 1–8).

Jain, V., Sebastian Seung, H., & Turaga, S. C. (2010). Machines that learn to segment images: A crucial technology for connectomics. *Current Opinion in Neurobiology, 20*(5), 653–666.

Jeong, W.-K., Beyer, J., Hadwiger, M., Blue, R., Law, C., Vazquez-Reina, A., et al. (2010). Ssecrett and neurotrace: Interactive visualization and analysis tools for large-scale neuroscience data sets. *IEEE Computer Graphics and Applications, 30*, 58–70.

Jeong, W.-K., Beyer, J., Hadwiger, M., Vazquez, A., Pfister, H., & Whitaker, R. T. (2009). Scalable and interactive segmentation and visualization of neural processes in EM datasets. *IEEE Transactions on Visualization and Computer Graphics, 15*, 1505–1514.

Jin, Y., Hoskins, R., & Horvitz, H. R. (1994). Control of type-D GABAergic neuron differentiation by *C. elegans* UNC-30 homeodomain protein. *Nature, 372*(6508), 780–783.

Jones, B. W., & Marc, R. E. (2005). Retinal remodeling during retinal degeneration. *Experimental Eye Research, 81*, 123–137.

Jones, B. W., Watt, C. B., Frederick, J. M., Baehr, W., Chen, C. K., Levine, E. M., et al. (2003). Retinal remodeling triggered by photoreceptor degenerations. *Journal of Comparative Neurology, 464*, 1–16.

Jones, B. W., Watt, C. B., & Marc, R. E. (2005). Retinal remodelling. *Clinical and Experimental Optometry, 88*, 282–291.

Jurrus, E., Hardy, M., Tasdizen, T., Fletcher, P. T., Koshevoy, P., Chien, C.-B. et al. (2009). Axon tracking in serial block-face scanning electron microscopy. *Medical Image Analysis, 13*(1), 180–188.

Jurrus, E., Paiva, A. R. C., Watanabe, S., Anderson, J. R., Jones, B. W., Whitaker, R. T., et al. (2010). Detection of neuron membranes in electron microscopy images using a serial

neural network architecture. *Medical Image Analysis, 14*(6), 770–783. doi:10.1016/j.media.2010.06.002.

Jurrus, E., Paiva, A. R. C., Watanabe, S., Whitaker, R., Jorgensen, E. M., & Tasdizen, T. (2009). Serial neural network classifier for membrane detection using a filter bank. In *Proc. workshop on microscopic image analysis with applications in biology.*

Jurrus, E., Whitaker, R. T., Jones, B., Marc, R., & Tasdizen, T. (2008). An optimal-path approach for neural circuit reconstruction. In *Proceedings of the 5th IEEE international symposium on biomedical imaging: From nano to macro* (pp. 1609–1612).

Kaynig, V., Fuchs, T., & Buhmann, J. M. (2010). Neuron geometry extraction by perceptual grouping in ssTEM images. In *IEEE Computer Society conference on computer vision and pattern recognition* (pp. 2902–2909).

Kremer, J. R., Mastronarde, D. N., & McIntosh, J. R. (1996). Computer visualization of three-dimensional image data using imod. *Journal of Structural Biology, 116*(1), 71–76.

Kumar, R., Vázquez-Reina, A., & Pfister, H. (2010). Radon-like features and their application to connectomics. In *2010 IEEE computer society conference on computer vision and pattern recognition workshops (CVPRW)* (pp. 86–193). doi:10.1109/CVPRW.2010.5543594. http://ieeexplore.ieee.org/stamp/stamp.jsp?tp=&arnumber=5543594&isnumber=5543135.

Leng, Z., Korenberg, J. R., Roysam, B., & Tasdizen, T. (2011). A rapid 2-D centerline extraction method based on tensor voting. In *2011 IEEE international symposium on biomedical imaging: From nano to macro* (pp. 1000–1003). doi:10.1109/ISBI.2011.5872570. http://ieeexplore.ieee.org/stamp/stamp.jsp?tp=&arnumber=5872570&isnumber=5872340.

Macke, J. H., Maack, N., Gupta, R., Denk, W., Schölkopf, B., & Borst, A. (2008). Contour-propagation algorithms for semi-automated reconstruction of neural processes. *Journal of Neuroscience Methods, 167*, 349–357.

Marc, R. E., Jones, B. W., Anderson, J. R., Kinard, K., Marshak, D. W., Wilson, J. H., et al. (2007). Neural reprogramming in retinal degeneration. *Investigative Ophthalmology & Visual Science, 48*, 3364–3371.

Marc, R. E., Jones, B. W., Watt, C. B., & Strettoi, E. (2003). Neural remodeling in retinal degeneration. *Progress in Retinal and Eye Research, 22*, 607–655.

Marc, R. E., Jones, B. W., Watt, C. B., Vazquez-Chona, F., Vaughan, D. K., & Organisciak, D. T. (2008). Extreme retinal remodeling triggered by light damage: Implications for age related macular degeneration. *Molecular Vission, 14*, 782–806.

Martone, M. E., Tran, J., Wong, W. W., Sargis, J., Fong, L., Larson, S., Lamont, S. P., et al. (2008). The cell centered database project: An update on building community resources for managing and sharing 3D imaging data. *Journal of Structural Biology, 161*(3), 220–231. The 4th International Conference on Electron Tomography.

Medioni, G., Lee, M.-S., & Tang, C.-K., (2000). *Computational framework for segmentation and grouping*. New York: Elsevier.

Minsky, M. (1961). Microscopy apparatus. U.S. Patent number 301467.

Mishchenko, Y. (2008). Automation of 3D reconstruction of neural tissue from large volume of conventional serial section transmission electron micrographs. *Journal of Neuroscience Methods*.

Mishchenko, Y., Hu, T., Spacek, J., Mendenhall, J., Harris, K. M., & Chklovskii, D. B. (2010). Ultrastructural analysis of hippocampal neuropil from the connectomics perspective. *Neuron, 67*, 1009–1020.

Nokia (2012). Qt: Cross-platform application and UI framework. http://qt.nokia.com.

Paiva, A. R. C., Jurrus, E., & Tasdizen, T. (2010). Using sequential context for image analysis. In *2010 20th international conference on pattern recognition (ICPR)* (pp. 2800–2803).

Peng, Y. W., Hao, Y., Petters, R. M., & Wong, F. (2000). Ectopic synaptogenesis in the mammalian retina caused by rod photoreceptor-specific mutations. *Nature Neuroscience, 3*, 1121–1127.

Pizer, S. M., Johnston, R. E., Ericksen, J. P., Yankaskas, B. C., & Muller, K. E. (1990). Contrast-limited adaptive histogram equalization: Speed and effectiveness. In *Proceedings of the first conference on visualization in biomedical computing, 1990* (pp. 337–345).

Pomerleau, D. (1993). Knowledge-based training of artificial neural networks for autonomous robot driving. In J. Connell, & S. Mahadevan (Eds.), *Robot learning* (pp. 19–43). Dordrecht: Kluwer Academic.

Principe, J. C., Euliano, N. R., & Lefebvre, W. C. (2000). *Neural and adaptive systems: Fundamentals through simulations*. New York: Wiley.

Rabi, G., & Lu, S. W. (1998). Visual speech recognition by recurrent neural networks. *Journal of Electronic Imaging, 7*(1), 61–69. doi:10.1117/1.482627.

Rand, W. M. (1971). Objective criteria for the evaluation of clustering methods. *Journal of the American Statistical Association, 66*(336), 846–850.

Rueckert, D., Sonoda, L. I., Hayes, C., Hill, D. L. G., Leach, M. O., & Hawkes, D. J. (1999). Nonrigid registration using free-form deformations: Application to breast MR images. *IEEE Transactions on Medical Imaging, 18*(8), 712–721.

Rust, M. J., Bates, M., & Zhuang, X. (2006). Sub-diffraction-limit imaging by stochastic optical reconstruction microscopy (storm). *Nature Methods, 3*(10), 793–796.

Saalfeld, S., Cardona, A., Hartenstein, V., & Tomančák, P. (2010). As-rigid-as-possible mosaicking and serial section registration of large ssTEM datasets. *Bioinformatics, 26*(12), i57–i63.

Schroeder, W., Martin, K., & Lorensen, B. (2010). *The VTK user's guide* (11th ed.). Kitware, Inc. ISBN 1-930934-19-X. http://www.vtk.org.

Sommer, C., Straehle, C., Köthe, U., & Hamprecht, F. A. (2011). ilastik: Interactive learning and segmentation toolkit. In *2011 IEEE international symposium on biomedical imaging: From nano to macro* (pp. 230–233). doi:10.1109/ISBI.2011.5872394. http://ieeexplore.ieee.org/stamp/stamp.jsp?tp=&arnumber=5872394&isnumber=5872340.

Tasdizen, T., Whitaker, R., Marc, R., & Jones, B. (2005). Enhancement of cell boundaries in transmission electron microscopy images. In *ICIP* (pp. 642–645).

Tasdizen, T., Koshevoy, P., Grimm, B. C., Anderson, J. R., Jones, B. W., & Watt, C. B. (2010). Automatic mosaicking and volume assembly for high-throughput serial-section transmission electron microscopy. *Journal of Neuroscience Methods, 193*(1), 132–144.

Turaga, S. C., Briggman, K. L., Helmstaedter, M., Denk, W., & Seung, H. S. (2009). Maximin affinity learning of image segmentation. *CoRR*, abs/0911.5372.

Turaga, S. C., Murray, J. F., Jain, V., Roth, F., Helmstaedter, M., & Briggman, K. (2010). Convolutional networks can learn to generate affinity graphs for image segmentation. *Neural Computation, 22*(2), 511–538.

Varshney, L. R., Chen, B. L., Paniagua, E., Hall, D. H., Chklovskii, D. B. (2011). Structural properties of the *Caenorhabditis elegans* neuronal network. *PLoS Computational Biology, 7*(2), e1001066. doi:10.1371/journal.pcbi.1001066.

Vazquez, L., Sapiro, G., & Randall, G. (1998). Segmenting neurons in electronic microscopy via geometric tracing. In *Proc. of ICIP* (pp. 814–818).

Vazquez-Reina, A., Miller, E., & Pfister, H. (2009). Multiphase geometric couplings for the segmentation of neural processes. *IEEE Computer Society conference on computer vision and pattern recognition* (pp. 2020–2027).

Venkatataju, K. U., Paiva, A., Jurrus, E., & Tasdizen, T. (2009). Automatic markup of neural cell membranes using boosted decision stumps. In *Proceedings of the 6th IEEE international symposium on biomedical imaging* (pp. 1039–1042).

Visage imaging (2012). Amira. http://www.amira.com.

Vu, N., & Manjunath, B. S. (2008). Graph cut segmentation of neuronal structures from transmission electron micrographs. In *15th IEEE international conference on image processing, 2008. ICIP 2008* (pp. 725–728).

Watanabe, K., Takeishi, H., Hayakawa, T., & Sasaki, H. (2010). Three-dimensional organization of the perivascular glial limiting membrane and its relationship with the vasculature: A scanning electron microscope study. *Okajimas Folia Anatomica Japonica, 87*(3), 109–121.

Wells, G., Venaille, C., & Torras, C. (1996). Promising research: Vision-based robot positioning using neural networks. *Image and Vision Computing, 14*(10), 715–732.

White, J. Q., Nicholas, T. J., Gritton, J., Truong, L., Davidson, E. R., & Jorgensen, E. M. (2007). The sensory circuitry for sexual attraction in *C. elegans* males. *Current Biology, 17*(21), 1847–1857.

White, J. G., Southgate, E., Thomson, J. N., & Brenner, F. R. S. (1986). The structure of the nervous system of the nematode *Caenorhabditis elegans. Philosophical Transactions of the Royal Society of London. Series B, Biological Sciences, 314*, 1–340.

Xiao, Y. P., Wang, Y., & Felleman, D. J. (2003). A spatially organized representation of colour in macaque cortical area v2. *Nature, 421*(6922), 535–539.

Yang, H.-F., & Choe, Y. (2009). Cell tracking and segmentation in electron microscopy images using graph cuts. In *IEEE international symposium on biomedical imaging: From nano to macro, 2009. ISBI '09* (pp. 306–309).

CHAPTER 10

PERSPECTIVES

For circuits to function, neurons must wire with their appropriate partners and communicate with each other in a coordinated fashion. In this dissertation, I have developed two techniques in electron microscopy to characterize the basis of neurotransmission. First, I coupled optogenetics with high-pressure freezing to capture rapid events that take place during neurotransmission. Second, I combined super-resolution fluorescence microscopy with electron microscopy to localize proteins in electron micrographs at nanometer resolution. These two techniques were used to address how synaptic vesicles are organized for neurotransmission and how they are recovered after fusion. In short, we found that synaptic vesicles are organized around the presynaptic density, that only vesicles directly in contact with the plasma membrane fuse upon stimulation, and that the same synaptic vesicle pool was likely consumed for both tonic and evoked neurotransmission. Following synaptic vesicle fusions, synaptic vesicle membrane was removed from the surface at the edges of active zones within 50 ms – 1 s, much faster than previously thought. In this chapter, I will speculate on potential mechanisms for synaptic transmission and synaptic vesicle endocytosis, propose experiments to test the predictions, and present my preliminary data. Furthermore, I will discuss the semi-automated reconstruction

technique we developed and a potential tool that could add a molecular map to a connectivity map.

Synaptic vesicle pools

Neurotransmission can occur spontaneously at rest or actively following an action potential. Synaptic vesicles are organized into three functional pools at synapses: the readily-releasable pool, the recycling pool, and the reserve pool. Previously, evoked release was thought to draw vesicles from the readily-releasable pool (Stevens and Tsujimoto, 1995; Schikorski and Stevens, 1997; Zenisek et al., 2000) whereas spontaneous release was thought to involve vesicles in the reserve pool (Sara et al., 2005; Matthews and Sterling, 2008; Fredj and Burrone, 2009; Chung et al., 2010). However, emerging evidence suggests that the same vesicles may be used for both types of neurotransmission (Rizzoli and Betz, 2002; Groemer and Klingauf, 2007; Ikeda and Bekkers, 2009; Wilhelm et al., 2010). In this dissertation, I investigated how these two types of neurotransmission are regulated by the organization of vesicles at synapses using time-resolved electron microscopy (Chapter 7). Inducing evoked neurotransmission by channelrhodopsin showed reduction of release-ready vesicles from a region spanning from the dense projection to the neighboring adherens junctions, suggesting that the active zone is broad in *C. elegans* neuromuscular junctions. On the other hand, blocking of the tonic neurotransmission by halorhodopsin showed an accumulation of vesicles near dense projections, which is the center of active zone. These results suggested

that the locations of tonic and evoked pool of vesicles overlap near the dense projection.

To confirm that tonic release is mediated by vesicles at the dense projection, I propose to capture fusion of these spontaneous fusions. Tonic release can be blocked by hyperpolarizing the membrane. Activation of halorhodopsin by light pumps chloride ions into the cell and hyperpolarizes the membrane. Turning the light off allows the synapse to return to resting potential, and tonic release will resume. The synapses could be frozen synapses 20 ms after 'light-off' and the positions of fusing vesicles determined. If synaptic vesicles near the dense projections are, in fact, consumed for tonic release, then exocytic intermediates should be captured around the dense projection. This result will provide further evidence that the domains of vesicle fusion for tonic and evoked neurotransmission overlap, suggesting that the same vesicles may be used for both types of neurotransmission. However, ultimately, the use of vesicle tracers such as FM dyes in combination with pHluorin may be necessary to test whether the same vesicle can be used during tonic and evoked neurotransmission.

My data here suggest that the spatial organization of synaptic vesicles likely contribute to the regulation of synaptic vesicles for different types of neurotransmission. If this prediction is correct, how do neurons regulate the number of vesicles released by tonic versus evoked transmission. During tonic release, only one vesicle is fused at a time whereas about 4-11 vesicles fuse at *C. elegans* neuromuscular junctions during evoked neurotransmission. In the

previous study, we demonstrrated that about 34 synaptic vesicles are docked (Hammarlund et al., 2007). In fact, about one third of these vesicles are found within 100 nm of the dense projection, the same region that showed an accumulation of vesicles when tonic neurotransmission was blocked by halorhodopsin activation. One possibility is that the spatial organization of voltage-gated calcium channels and the amount of calcium influx may determine the number of vesicle fusions. N-type voltage-gated calcium channels are associated with the dense projection (Kittel et al., 2006; Gracheva et al., 2008), and it is likely that weakly depolarized membrane potential and brief calcium channel openings lead to tonic vesicle fusions. By contrast, a more sustained opening of calcium channels causes an elevation of calcium across the entire active zone during the evoked stimulation. To test the idea that the amount of calcium influx regulates the number of vesicle fusion during each type of neurotransmission, synapses lacking functional voltage-gated calcium channels were examined by electrophysiology (Fig. 10.1 and 10.2) and time-resolved electron microscopy (Fig. 10.3).

At *C. elegans* neuromuscular junctions, calcium influx through two types of voltage-gated calcium channels (N-type and L-type) contributes to synaptic vesicle fusion during tonic and evoked neurotransmission (Fig. 10.1). N-type calcium channels possess fast activation kinetics and inactivate rapidly (Tsien et al., 1988; Kisilevsky and Zamponi, 2008). Calcium entering through voltage-gated calcium channels is rapidly buffered, and thus vesicles are thought to be held within 50 nm of N-type channels for fusion (Neher and Sakaba, 2008). On

the other hand, L-type calcium channels are activated by strong depolarization of the membrane and have the largest calcium conductance due to slow inactivation (Tsien et al., 1988; Kisilevsky and Zamponi, 2008), and thus it may trigger vesicle fusion from a larger area (Heidelberger et al., 2005; Innocenti and Heidelberger, 2008). My preliminary results show that in the absence of N-type calcium channels, release-ready vesicles held within 100 nm of the dense projection did not fuse while vesicles held distant from the dense projections were triggered to fuse following a single stimulus, likely due to intact L-type calcium channels (Fig. 10.3). In the absence of functional L-type channels, I observed the opposite effect – fusion of vesicles near but not distant from the dense projection (Fig. 10.3). These results suggest that N-type channels are likely responsible for vesicle fusion near the dense projection whereas the vesicle fusion distant from the dense projections is likely triggered by the calcium influx through the L-type channels during evoked neurotransmission.

The results from N-type calcium channel mutants suggested that they affect vesicle fusion in the proximity of dense projections. Because synaptic vesicles likely fuse in this region during the tonic release (Chapter 7) and synaptic vesicles must be held within 50-100 nm of the N-type calcium channels for fusion (Neher, 2010), the vesicle fusion sites during tonic neurotransmission may be constrained by the amount of calcium influx through the N-type channels. To test if the N-type is exclusively responsible for tonic neurotransmission, we observed the frequency of miniature excitatory postsynaptic currents (mEPSCs) in mutants lacking the N-type calcium channel. Consistent with the idea, the

frequency of mEPSC decreased dramatically in animals lacking N-type channels (Fig. 10.2). However, the reduction of mEPSCs was also observed in animals lacking functional L-type channels, suggesting that calcium influx through both N-type and L-type calcium channels contributes to vesicle fusion during tonic neurotransmission (Fig. 10.2). Thus, the vesicle fusion sites for tonic neurotransmission may not be constrained by the type of calcium channels localized at dense projections. However, recent evidence suggests that L-type calcium channels may compensate for the loss of N-type channels during development (Bauer Huang et al., 2007), and thus the L-type channels may relocalize to dense projections to compensate for the loss of N-type channels. To test this possibility, L-type calcium channels should be localized using nano-fEM at synapses in the presence and absence of N-type calcium channels.

The alternative explanation for spatial constraints for tonic release sites is that synaptic vesicles for each type of neurotransmission are regulated by different molecules. Recent studies have suggested that the calcium sensors required for each type of neurotransmission may be different at vertebrate synapses. Synaptotagmin-1 is required for evoked neurotransmission (Brose et al., 1992). On the other hand, another calcium sensor, Doc2, is associated with release-ready vesicles for spontaneous neurotransmission (Groffen et al., 2006) although its calcium sensing domain does not seem necessary for spontaneous vesicle fusion (Pang et al., 2011). Moreover, we have shown that two isoforms of UNC-13 may differentially regulate synaptic vesicle docking at particular regions of the active zones (Hammarlund et al., 2007). The long isoform seems to

regulate docking of vesicles in the proximity of dense projections whereas the short isoform is likely responsible for docking in the distal region of active zones (Hammarlund et al., 2007). These different regions correspond to the release sites for tonic and evoked neurotransmission, respectively. In the future, it will be interesting to perform time-resolved electron microscopy in the mutants defective in either isoform of UNC-13 to determine if these isoforms differentially regulate tonic and evoked pool of vesicles at synapses.

Synaptic vesicle endocytosis

To sustain neurotransmission, synaptic vesicles must be recycled locally at synapses. Two models for synaptic vesicle endocytosis were proposed by the classical ultrastructural analyses using a freeze-slammer. Heuser and Reese proposed that endocytosis occurs via a slow mechanism using clathrin scaffolds (Heuser and Reese, 1973, 1981; Miller and Heuser, 1984). By contrast, Ceccarelli and his coworkers proposed a fast mechanism, called kiss-and-run (Ceccarelli et al., 1972; Torri-Tarelli et al., 1985). However, in each case, intense stimulation was applied to samples under non-physiological conditions. To address how endocytosis takes place under physiological conditions, I combined optogenetics with high-pressure freezing to observe membrane dynamics following a single stimulus in the intact nematode.

'Clathrin-mediated endocytosis' predicts that vesicles will collapse into the membrane, that membrane will endocytose lateral to the active zone, and that endocytosis will occur slowly (~20 s). By contrast, 'kiss-and-run' predicts that

vesicles will not collapse into the membrane, that vesicles will endocytose at the site of release, that they will be the same size as synaptic vesicles, and that endocytosis will be fast (~1 s). In contrast to these models, my data demonstrated that vesicles collapse into the membrane, that a large surface area of membrane is endocytosed at the edges of active zones on a very rapid timescale (20 ms - 300 ms). The detailed interpretations of the results are described in Chapter 7, and thus in this chapter, I will focus on the following three topics. 1) Is the ultrafast membrane retrieval universal first step of synaptic vesicle endocytosis? 2) Where does clathrin act to regenerate vesicles? 3) What molecules are responsible for this endocytic pathway?

Ultrafast membrane retrieval

Following a single stimulus in the intact nervous system, we observed ultrafast membrane retrieval at the edges of active zones. Unlike cultured neurons, neurons in the intact nervous system are bundled together in the confined space. Therefore, when vesicle membrane is added to the surface by fusion, the plasma membrane does not have an infinite amount space to expand. This space limitation may trigger compensatory membrane retrieval at synapses. The compensatory mechanism, called bulk endocytosis, has been observed at synapses of many organisms following intense repetitive stimulation (Miller and Heuser, 1984; de Hoop et al., 1994; Holt et al., 2003, 2004; Voglmaier et al., 2006; Wu and Wu, 2009; Teng et al., 2007; Wu and Wu, 2007; Cousin, 2009; Clayton et al., 2010; Hoopmann et al., 2010). However, our results suggested

that a single physiological stimulus might trigger bulk membrane retrieval at *C. elegans* neuromuscular junctions.

Is this pathway conserved in other organisms or is it specific to *C. elegans* neuromuscular junctions? The freeze-slamming experiment using *ex vivo* frog neuromuscular junction showed large endocytic structures appearing within 1 s of an action potential (Miller and Heuser, 1984; Heuser, 1989). Although Heuser argued that this structure was likely caused by the non-physiological stimulation employed in the study (Heuser, 1989), it is possible that this large endocytic structures may be parallel to the structures we observed in the *C. elegans* neuromuscular junctions. Moreover, capacitance measurements in Calyx of Held showed that large surface of membrane is internalized following physiological stimulation (10 stimuli applied at 10 Hz). Thus, ultrafast endocytosis may occur under physiological conditions.

To test if ultrafast endocytosis can be triggered by a single stimulus in different organisms, I froze cultured mouse hippocampal neurons expressing Channelrhodopsin at defined time points after a single pulse of light. My preliminary results show that membrane invaginations are captured in regions lateral to the active zone 100 ms after the stimulation (Fig. 10.4). Some of these invaginations are larger than the size of a synaptic vesicle. Interestingly, although the clathrin coats can be well preserved in this preparation (Fig. 10.4), none of these invaginations are clathrin-coated, suggesting that clathrin is likely not at work here. These results are consistent with our observations in *C. elegans* neuromuscular junctions and may suggest that rapid bulk membrane

retrieval is a conserved endocytic pathway. To fully characterize endocytic pathways in the hippocampal neurons, more data from different time points after stimulation must be analyzed.

Clathrin-mediated vesicle regeneration

If the ultrafast membrane retrieval is the first step in synaptic vesicle endocytosis, where does clathrin act to regenerate vesicles? The general consensus has been that clathrin acts on the plasma membrane to regenerate synaptic vesicles. On the other hand, clathrin could act to regenerate synaptic vesicles from endosomes. Some ultrastructural studies observe clathrin on endosomes (Heuser and Reese, 1973; Takei et al., 1998). In fact, the acute photo-inactivation of clathrin in *Drosophila* showed an accumulation of endosomal structures in terminals (Heerssen et al., 2008; Kasprowicz et al., 2008). However, the disruption of dynamin in *Drosophila* neuromuscular junctions show that the terminal is depleted with vesicles and that clathrin-coated pits are trapped on the plasma membrane following exhaustive stimulation (Koenig and Ikeda, 1989). The accumulation of clathrin coated pits has been observed in many organisms (Shupliakov et al., 1997; Jockusch et al., 2005; Granseth et al., 2006).

How do we reconcile this discrepancy? One possibility is that clathrin-coated pits may be an artifact caused by glutaraldehyde fixation of tissues. Glutaraldehyde preserves tissue morphology by polymerizing macromolecules such as proteins but produces aggregation artifacts (Payne, 1973; Cheung and

Nimni, 1982). One extreme example is that glutaraldehyde can cause fusion of synaptic vesicles, perhaps by aggregating SNARE proteins (Rosenmund and Stevens, 1997). Are clathrin coats artificially stabilized in the endocytic pits? At this point, we do not have an answer to this question. However, one observation may bring insight to this question. When mutants defective in uncoating clathrin coats are characterized by electron microscopy following the conventional aldehyde fixation, clathrin coated vesicles and pits accumulated in the terminal of *C. elegans* neuromuscular junctions (Harris et al., 2000). However, the same mutant fixed by high-pressure freezing and freeze-substitution techniques did not show an accumulation of such structures (Jospin et al., 2007). This result is not due to the inability of the high-pressure freezing technique to preserve clathrin-coated vesicles or pits, as described in Chapter 7 (Fig. 7.7D). Characterizing the endocytic pathways in the cultured hippocampal neurons frozen at different time points after the light stimulation may resolve this issue.

Molecular mechanisms of ultrafast endocytosis

How is bulk membrane retrieved from the surface? The fission of bulk membrane is likely mediated by dynamin (Clayton et al., 2010). However, how membrane invagination is initiated from the surface is poorly understood. One potential mechanism is that excess membrane is simply folded passively into the cytosol. Alternatively, membrane-curvature generating or sensing proteins such as endophilin may initiate membrane invagination. To test these models, I analyzed synaptic morphology of the transgenic nematode lacking endophilin

before and after light stimulation. I found that endocytic intermediates became even larger in the absence of endophilin (Fig. 10.6). I also found endocytic invaginations with abnormal shapes (Fig. 10.6). These results suggest that endophilin may have a role in ultrafast endocytosis.

What are the roles of endophilin in ultrafast endocytosis? Endophilin has two major functional domains: a BAR domain and an SH3 domain (McMahon and Boucrot, 2011). The BAR domain is thought to bind or create membrane curvature while the SH3 domain is thought to interact with dynamin or synaptojanin. Recent studies have shown two opposite roles for endophilin at synapses. Structure and function analysis of endophilin by truncations in *C. elegans* showed that endocytic function of endophilin is mediated by its BAR domain and that the function of the SH3 domain is dispensable (Bai et al., 2010). On the other hand, triple knock-outs of endophilin in mouse resulted in coated vesicles (late structures) but not coated pits (early structures) accumulating in the terminal and showed that the recruitment of synaptojanin, presumably via the SH3 domain, is required for its endocytic function (Milosevic et al., 2011). My results may suggest that both domains are important for the endocytic functions of endophilin. Based on the results obtained, three potential roles of endophilin can be postulated: accelerating the fission reaction possibly by recruiting dynamin to the sites and resolving large endosomes into small vesicles.

Dynamin recruitment. One possible role of endophilin is to recruit dynamin via its SH3 domain to the fission site of the endocytic structures. In the absence of endophilin, dynamin may not localize properly to the neck of endocytic

structures, and thus, the fission may be delayed, resulting in the enlarged structures. To test the role of endophilin in the recruitment of dynamin, dynamin localization should be investigated in the absence of endophilin using nano-resolution fluorescence electron microscopy. In Chapter 7, I have shown that dynamin is localized to dense projections and adherens junctions. My preliminary data suggest that endophilin also localizes to these locations (Fig. 10.5). If the role of endophilin in ultrafast endocytosis is to recruit dynamin to the fission site of endocytic structures, in the absence of endophilin, dynamin would be mislocalized or would localize slowly to the neck of the endocytic structures.

Endosomes. Another potential role of endophilin is to generate membrane curvature through its BAR domain and resolve the large vacuoles into synaptic vesicles. In the absence of endophilin, synaptic vesicles are not regenerated, resulting in the accumulation of the larger endocytic structures. To test if endophilin is required to resolve large endocytic structures into small synaptic vesicles, the time course for disappearance of the large endocytic structures should be fully characterized by time-resolved electron microscopy. My preliminary results show that large endocytic structures disappear with a slower time constant, suggesting that endophilin may accelerate the reaction but may not be essential for resolving the large endocytic structures.

Together, these preliminary results suggest that endophilin may have roles in the bulk membrane retrieval and that this pathway is likely an active process mediated by proteins. However, in the absence of endophilin, membrane invagination still takes place, suggesting that some other molecules

may be involved. To elucidate the molecular mechanism of bulk membrane retrieval, a candidate protein approach may be necessary. However, such studies likely require tremendous amount of time since the phenotype of mutants must be analyzed by electron microscopy. A large-scale screen using pHluorin may speed up the process. However, pHluorin-based assay may not be possible because the large endocytic structure observed here is not likely reacidified, and thus pHluorin in the endocytic structures cannot be distinguished from pHluorin on the surface. The proteomic analysis of large membrane invagination would allow us to identify molecules required in the process. However, these endocytic structures cannot be purified biochemically for mass spectrometry. In the future, I will develop a technique to use electron microscopy to identify a structure of interest and extract it directly from the specimen for proteomic analysis (this technique is discussed further in the next section).

Connectomes

A nervous system must be wired properly for it to function. To understand how a complex behavior is mediated by the wiring of neural circuits, we need to map connections between neurons, that is, determine the 'connectome'. However, drawing these maps requires tremendous effort for three reasons. First, synapses are too small to resolve by conventional light microscopy. Second, serial section electron microscopy, the only method thus far that allows the visualization of synapses, is very labor-intensive and time-consuming. Third, after acquisition of serial electron micrographs, neurons need to be traced

through the entire volume. In this dissertation, we developed a semiautomated method to reconstruct neurons from a simple neural circuit of *C. elegans* (Jurrus et al., 2010, 2012), aiming to circumvent these problems. We showed that the connectivity among motor neurons in the ventral nerve cord of *C. elegans* obtained in this study was similar to the previously published connectomes (White et al., 1976), suggesting that our method is valid to reconstruct neurons that do not branch (Jurrus et al., 2012). However, applying this technique to reconstruct more complex nervous system requires several improvements: modification of the algorithm to trace branching processes, automated image acquisition, and molecular mapping. The future work on the algorithm has been discussed extensively in Chapter 8 and 9, and thus, I will focus on the latter two points in this chapter.

Automated image acquisition

Typically, acquisition of electron micrographs for reconstruction requires one to collect serial thin sections (~50 nm thick), image each, and align all of the images. However, because one electron micrograph typically covers a volume of 5 µm x 5 µm x 50 nm and neuronal arbors are typically a few hundred micrometers across, these tasks are prohibitively laborious for the reconstruction of more than a dozen neurons. For imaging the entire *C. elegans* nervous system, the number of sections would be ~20,000, and the number of images would be even more because multiple images must be acquired from each

section to capture all the neurons in cross-section. Thus, this step is extremely time-consuming.

I chose to reduce the amount of labor required by automating the sectioning and imaging. To do this, I adopted a recently developed technique called serial block-face scanning electron microscopy (Denk and Horstmann, 2004; Knott et al., 2008). In this technique, plastic embedded tissues are mounted in a scanning electron microscope, and the back-scattered electrons are imaged from the tissue on the surface of the block. A thin layer of the surface (typically 5-30 nm) is then trimmed using a diamond knife (Denk and Horstmann, 2004) or a focused ion beam (Knott et al., 2008). Imaging and trimming processes are repeated until the desired volume is generated in a fully automated fashion. In collaboration with Joel Mancuso (Gatan Inc.), a plastic embedded *C. elegans* animal was imaged using serial block-face scanning electron microscopy. Serial sections were successfully collected from the ventral nerve cord of *C. elegans* in an automated fashion. However, neuronal membrane appeared fuzzy in these images (Fig. 10.7) because of the limited resolution of a scanning electron microscope and the lack of extra membrane staining with heavy metals (Fig. 10.8). To achieve sharper membrane, I applied the osmium bridging technique to enhance the membrane contrast (Seligman et al., 1966; Tapia et al., 2012). Unfortunately, osmiophilic thiocarbohydrazide (TCH) did not dissolve in the organic solvent used for freeze-substitution. Thus, 10% water (v/v) was added into the solution to dissolve TCH. The use of osmium bridging was sufficient to enhance membrane contrast for human eyes

(Fig. 10.8). However, membrane boundaries were not sufficiently defined for automated detection of neuronal profiles by a computer program. Therefore, further refinement is necessary to adopt this automated imaging scheme into the framework of the automated reconstruction.

For automated image acquisition, membrane contrast must be further enhanced using other heavy metals such as uranyl acetate and lead citrate. Unfortunately, these heavy metals do not dissolve well in organic solvents. To apply these heavy metals, freeze-substituted tissues may require rehydration (Van Donselaar et al., 2007; Ripper et al., 2008). Alternatively, the use of a transmission microscope (Anderson et al., 2009) or a scanning electron microscope with higher resolution (Knott et al., 2009) is necessary. The image acquisition can be automated using computer programs such as Legionon (Carragher et al., 2000) or SerialEM (Mastronarde, 2005). Furthermore, automated sectioning technique called automated tape-collecting ultramicrotomy (ATUM) has been recently developed (Tapia et al., 2012). Although the sections are collected onto a tape that is not compatible with transmission electron microscopy imaging, the modification of this technique may allow us to collect serial sections for transmission electron microscopy imaging (Briggman and Bock, 2012). These refinements will likely allow us to collect images with membrane contrast sufficient for a computer program for automated reconstruction.

Molecular maps

A connectome shows how a neural circuit is wired. However, the interpretation of these reconstructed circuits will be limited due to the lack of molecular identities in electron micrographs of neurons. What types of neurons are connected to the particular neuron reconstructed? What neurotransmitters do this particular neuron use to communicate? What adhesion molecules are required to form a specific connection between two reconstructed neurons? To add molecular maps to connectomes, a new approach called array tomography has been developed.

Array tomography adds molecular maps to connectomes by preserving antigenicity of proteins through sample preparation for electron microcopy and staining particular proteins in plastic sections using antibodies (Micheva and Smith, 2007). Because an array of tissue sections are mounted permanently on a microscope slide, these sections can be probed with multiple antibodies, allowing the proteomic mapping of these neurons. By imaging the underlying structures by electron microscopy and reconstructing a three-dimensional volume, the connectivity between neurons as well as the types of synapses such as inhibitory and excitatory can be mapped using this technique (Micheva and Smith, 2007; Micheva et al., 2010; Oberti et al., 2011). There are currently three limitations of this technique. First, the morphology of neuronal membrane is not well preserved because membrane contrast enhancing agents such as osmium tetroxide degrades proteins and thus cannot be used during the sample preparation. Second, antibodies compatible with plastic sections are limited.

Third, only one protein is probed at a time, and thus probing multiple proteins is time consuming. To circumvent these problems, I aim to develop a technique to perform proteomic analysis using mass spectrometry on samples prepared for electron microscopy in the future.

Mass spectrometry allows high-throughput identification of proteins from biochemically-isolated materials, but the extraction method imposes a limitation to the technology. Many proteins and structures are not biochemically tractable. For example, proteins associated with membrane can only be extracted by use of detergents in addition to cell lysis (Bodzon-Kulakowska et al., 2007). These chemical treatments often result in degradation of proteins by proteolytic activities of a cell or dissociation of protein complexes (Bodzon-Kulakowska et al., 2007). Therefore, extraction methods must be optimized for each sample, and this process is tedious. Thus, proteomic approaches rely heavily on the sample preparation. On the other hand, structures are visible by electron microscopy, even if they are not biochemically tractable. Thus, the proteomic approach will be very powerful if structures and proteins of interest can be extracted directly from or probed directly on specimens in an electron microscope (Szakal et al., 2011; Lanni et al., 2012). By combining focused ion beam milling with nano-manipulation system (Omniprobe) or MALDI-TOF MS, I aim to develop such a technique and study how specific synaptic connections are produced by identifying adhesion molecules in the synaptic junctions.

References

Anderson, J.R., Jones, B.W., Yang, J.-H., Shaw, M.V., Watt, C.B., Koshevoy, P., Spaltenstein, J., Jurrus, E., UV, K., Whitaker, R.T., et al. (2009). A Computational Framework for Ultrastructural Mapping of Neural Circuitry. PLoS Biol *7*,.

Bai, J., Hu, Z., Dittman, J.S., Pym, E.C.G., and Kaplan, J.M. (2010). Endophilin functions as a membrane-bending molecule and is delivered to endocytic zones by exocytosis. Cell *143*, 430–441.

Bauer Huang, S.L., Saheki, Y., VanHoven, M.K., Torayama, I., Ishihara, T., Katsura, I., van der Linden, A., Sengupta, P., and Bargmann, C.I. (2007). Left-right olfactory asymmetry results from antagonistic functions of voltage-activated calcium channels and the Raw repeat protein OLRN-1 in C. elegans. Neural Dev *2*, 24.

Bodzon-Kulakowska, A., Bierczynska-Krzysik, A., Dylag, T., Drabik, A., Suder, P., Noga, M., Jarzebinska, J., and Silberring, J. (2007). Methods for samples preparation in proteomic research. J. Chromatogr. B Analyt. Technol. Biomed. Life Sci. *849*, 1–31.

Briggman, K.L., and Bock, D.D. (2012). Volume electron microscopy for neuronal circuit reconstruction. Curr. Opin. Neurobiol. *22*, 154–161.

Brose, N., Petrenko, A.G., Südhof, T.C., and Jahn, R. (1992). Synaptotagmin: a calcium sensor on the synaptic vesicle surface. Science *256*, 1021–1025.

Carragher, B., Kisseberth, N., Kriegman, D., Milligan, R.A., Potter, C.S., Pulokas, J., and Reilein, A. (2000). Leginon: an automated system for acquisition of images from vitreous ice specimens. J. Struct. Biol *132*, 33–45.

Ceccarelli, B., Hurlbut, W.P., and Mauro, A. (1972). Depletion of vesicles from frog neuromuscular junctions by prolonged tetanic stimulation. J. Cell Biol *54*, 30–38.

Cheung, D.T., and Nimni, M.E. (1982). Mechanism of crosslinking of proteins by glutaraldehyde I: reaction with model compounds. Connect. Tissue Res. *10*, 187–199.

Chung, C., Barylko, B., Leitz, J., Liu, X., and Kavalali, E.T. (2010). Acute dynamin inhibition dissects synaptic vesicle recycling pathways that drive spontaneous and evoked neurotransmission. J. Neurosci. *30*, 1363–1376.

Clayton, E.L., Sue, N., Smillie, K.J., O'Leary, T., Bache, N., Cheung, G., Cole, A.R., Wyllie, D.J., Sutherland, C., Robinson, P.J., et al. (2010). Dynamin I phosphorylation by GSK3 controls activity-dependent bulk endocytosis of synaptic vesicles. Nat. Neurosci *13*, 845–851.

Cousin, M.A. (2009). Activity-dependent bulk synaptic vesicle endocytosis--a fast, high capacity membrane retrieval mechanism. Mol. Neurobiol *39*, 185–189.

Denk, W., and Horstmann, H. (2004). Serial block-face scanning electron microscopy to reconstruct three-dimensional tissue nanostructure. PLoS Biol *2*, e329.

van Donselaar, E., Posthuma, G., Zeuschner, D., Humbel, B.M., and Slot, J.W. (2007). Immunogold labeling of cryosections from high-pressure frozen cells. Traffic *8*, 471–485.

Fredj, N.B., and Burrone, J. (2009). A resting pool of vesicles is responsible for spontaneous vesicle fusion at the synapse. Nat Neurosci *12*, 751–758.

Granseth, B., Odermatt, B., Royle, S.J., and Lagnado, L. (2006). Clathrin-mediated endocytosis is the dominant mechanism of vesicle retrieval at hippocampal synapses. Neuron *51*, 773–786.

Groemer, T.W., and Klingauf, J. (2007). Synaptic vesicles recycling spontaneously and during activity belong to the same vesicle pool. Nat. Neurosci. *10*, 145–147.

Groffen, A.J.A., Friedrich, R., Brian, E.C., Ashery, U., and Verhage, M. (2006). DOC2A and DOC2B are sensors for neuronal activity with unique calcium-dependent and kinetic properties. Journal of Neurochemistry *97*, 818–833.

Hammarlund, M., Palfreyman, M.T., Watanabe, S., Olsen, S., and Jorgensen, E.M. (2007). Open syntaxin docks synaptic vesicles. PLoS Biol *5*, e198.

Harris, T.W., Hartwieg, E., Horvitz, H.R., and Jorgensen, E.M. (2000). Mutations in Synaptojanin Disrupt Synaptic Vesicle Recycling. J Cell Biol *150*, 589–600.

Heerssen, H., Fetter, R.D., and Davis, G.W. (2008). Clathrin dependence of synaptic-vesicle formation at the Drosophila neuromuscular junction. Curr. Biol. *18*, 401–409.

Heidelberger, R., Thoreson, W.B., and Witkovsky, P. (2005). Synaptic transmission at retinal ribbon synapses. Progress in Retinal and Eye Research *24*, 682–720.

Heuser, J. (1989). The role of coated vesicles in recycling of synaptic vesicle membrane. Cell Biol. Int. Rep *13*, 1063–1076.

Heuser, J.E., and Reese, T.S. (1973). Evidence for recycling of synaptic vesicle membrane during transmitter release at the frog neuromuscular junction. J. Cell Biol *57*, 315–344.

Heuser, J.E., and Reese, T.S. (1981). Structural changes after transmitter release at the frog neuromuscular junction. J. Cell Biol *88*, 564–580.

Holt, M., Cooke, A., Neef, A., and Lagnado, L. (2004). High mobility of vesicles supports continuous exocytosis at a ribbon synapse. Current Biology.

Holt, M., Cooke, A., Wu, M.M., and Lagnado, L. (2003). Bulk Membrane Retrieval in the Synaptic Terminal of Retinal Bipolar Cells. J. Neurosci. *23*, 1329–1339.

de Hoop, M.J., Huber, L.A., Stenmark, H., Williamson, E., Zerial, M., Parton, R.G., and Dotti, C.G. (1994). The involvement of the small GTP-binding protein Rab5a in neuronal endocytosis. Neuron *13*, 11–22.

Hoopmann, P., Punge, A., Barysch, S.V., Westphal, V., Bückers, J., Opazo, F., Bethani, I., Lauterbach, M.A., Hell, S.W., and Rizzoli, S.O. (2010). Endosomal sorting of readily releasable synaptic vesicles. Proc. Natl. Acad. Sci. U.S.A *107*, 19055–19060.

Ikeda, K., and Bekkers, J.M. (2009). Counting the number of releasable synaptic vesicles in a presynaptic terminal. Proc. Natl. Acad. Sci. U.S.A. *106*, 2945–2950.

Innocenti, B., and Heidelberger, R. (2008). Mechanisms Contributing to Tonic Release at the Cone Photoreceptor Ribbon .... Journal of Neurophysiology.

Jockusch, W.J., Praefcke, G.J.K., McMahon, H.T., and Lagnado, L. (2005). Clathrin-dependent and clathrin-independent retrieval of synaptic vesicles in retinal bipolar cells. Neuron *46*, 869–878.

Jospin, M., Watanabe, S., Joshi, D., Young, S., Hamming, K., Thacker, C., Snutch, T., Jorgensen, E., and Schuske, K. (2007). UNC-80 and the NCA ion channels contribute to endocytosis defects in synaptojanin mutants. Curr Biol *17*, 1595–1600.

Jurrus, E., C. Paiva, A.R., Watanabe, S., Whitaker, R., Jorgensen, E.M., and Tasdizen, T. (2010). Detection of neuron membranes in electron microscopy images using a serial neural network architecture. Medical Image Analysis, Elsevier.

Jurrus, E., Watanabe, S., Giuly, R.J., Paiva, A.R.C., Ellisman, M.H., Jorgensen, E.M., and Tasdizen, T. (2012). Semi-Automated Neuron Boundary Detection and Nonbranching Process Segmentation in Electron Microscopy Images. Neuroinformatics *14*, 770-783.

Kasprowicz, J., Kuenen, S., Miskiewicz, K., Habets, R.L.P., Smitz, L., and Verstreken, P. (2008). Inactivation of clathrin heavy chain inhibits synaptic recycling but allows bulk membrane uptake. J. Cell Biol *182*, 1007–1016.

Kisilevsky, A.E., and Zamponi, G.W. (2008). Presynaptic calcium channels: structure, regulators, and blockers. Handb Exp Pharmacol 45–75.

Knott, G., Marchman, H., Wall, D., and Lich, B. (2008). Serial section scanning electron microscopy of adult brain tissue using focused ion beam milling. J. Neurosci *28*, 2959–2964.

Knott, G.W., Holtmaat, A., Trachtenberg, J.T., Svoboda, K., and Welker, E. (2009). A protocol for preparing GFP-labeled neurons previously imaged in vivo and in slice preparations for light and electron microscopic analysis. Nat. Protocols *4*, 1145–1156.

Koenig, J.H., and Ikeda, K. (1989). Disappearance and reformation of synaptic vesicle membrane upon transmitter release observed under reversible blockage of membrane retrieval. J. Neurosci *9*, 3844–3860.

Lanni, E.J., Rubakhin, S.S., and Sweedler, J.V. (2012). Mass spectrometry imaging and profiling of single cells. Journal of Proteomics *75*, 5036-5051.

Mastronarde, D.N. (2005). Automated electron microscope tomography using robust prediction of specimen movements. Journal of Structural Biology *152*, 36–51.

Matthews, G., and Sterling, P. (2008). Evidence that vesicles undergo compound fusion on the synaptic ribbon. Journal of Neuroscience *28*, 5403–5411.

McMahon, H.T., and Boucrot, E. (2011). Molecular mechanism and physiological functions of clathrin-mediated endocytosis. Nat Rev Mol Cell Biol *12*, 517–533.

Micheva, K.D., O'Rourke, N., Busse, B., and Smith, S.J. (2010). Array tomography: high-resolution three-dimensional immunofluorescence. Cold Spring Harb Protoc *2010*, pdb.top89.

Micheva, K.D., and Smith, S.J. (2007). Array tomography: a new tool for imaging the molecular architecture and ultrastructure of neural circuits. Neuron *55*, 25–36.

Miller, T.M., and Heuser, J.E. (1984). Endocytosis of synaptic vesicle membrane at the frog neuromuscular junction. J. Cell Biol *98*, 685–698.

Milosevic, I., Giovedi, S., Lou, X., Raimondi, A., Collesi, C., Shen, H., Paradise, S., O'Toole, E., Ferguson, S., Cremona, O., et al. (2011). Recruitment of endophilin to clathrin-coated pit necks is required for efficient vesicle uncoating after fission. Neuron *72*, 587–601.

Neher, E. (2010). What is rate-limiting during sustained synaptic activity: vesicle supply or the availability of release sites. Front Synaptic Neurosci *2*, 144.

Neher, E., and Sakaba, T. (2008). Multiple Roles of Calcium Ions in the Regulation of Neurotransmitter Release. Neuron *59*, 861–872.

Oberti, D., Kirschmann, M.A., and Hahnloser, R.H.R. (2011). Projection neuron circuits resolved using correlative array tomography. Front Neurosci *5*, 50.

Pang, Z.P., Bacaj, T., Yang, X., Zhou, P., Xu, W., and Südhof, T.C. (2011). Doc2 supports spontaneous synaptic transmission by a Ca(2+)-independent mechanism. Neuron *70*, 244–251.

Payne, J.W. (1973). Polymerization of proteins with glutaraldehyde. Soluble molecular-weight markers. Biochem J *135*, 867–873.

Ripper, D., Schwarz, H., and Stierhof, Y.-D. (2008). Cryo-section immunolabelling of difficult to preserve specimens: advantages of cryofixation, freeze-substitution and rehydration. Biol. Cell *100*, 109–123.

Rizzoli, S.O., and Betz, W.J. (2002). Effects of 2-(4-morpholinyl)-8-phenyl-4H-1-benzopyran-4-one on synaptic vesicle cycling at the frog neuromuscular junction. J. Neurosci. *22*, 10680–10689.

Rosenmund, C., and Stevens, C.F. (1997). The rate of aldehyde fixation of the exocytotic machinery in ultured hippocampal synapses. Journal of Neuroscience Methods *76*, 1–5.

Rubakhin, S.S., Romanova, E.V., Nemes, P., and Sweedler, J.V. (2011). Profiling metabolites and peptides in single cells. Nat Meth *8*, S20–S29.

Sara, Y., Virmani, T., Deák, F., Liu, X., and Kavalali, E.T. (2005). An isolated pool of vesicles recycles at rest and drives spontaneous neurotransmission. Neuron *45*, 563–573.

Schikorski, T., and Stevens, C.F. (1997). Quantitative ultrastructural analysis of hippocampal excitatory synapses. J. Neurosci *17*, 5858–5867.

Seligman, A.M., Wasserkrug, H.L., and Hanker, J.S. (1966). A new staining method (OTO) for enhancing contrast of lipid--containing membranes and droplets in osmium tetroxide--fixed tissue with osmiophilic thiocarbohydrazide(TCH). J. Cell Biol. *30*, 424–432.

Shupliakov, O., Löw, P., Grabs, D., Gad, H., Chen, H., David, C., Takei, K., De Camilli, P., and Brodin, L. (1997). Synaptic vesicle endocytosis Impaired by disruption of dynamin-SH3 domain interactions. Science *276*, 259–263.

Stevens, C.F., and Tsujimoto, T. (1995). Estimates for the pool size of releasable quanta at a single central synapse and for the time required to refill the pool. Proc. Natl. Acad. Sci. U.S.A *92*, 846–849.

Szakal, C., Narayan, K., Fu, J., Lefman, J., and Subramaniam, S. (2011). Compositional mapping of the surface and interior of mammalian cells at submicrometer resolution. Anal. Chem. *83*, 1207–1213.

Takei, K., Haucke, V., Slepnev, V., Farsad, K., Salazar, M., Chen, H., and De Camilli, P. (1998). Generation of coated intermediates of clathrin-mediated endocytosis on protein-free liposomes. Cell *94*, 131–141.

Tapia, J.C., Kasthuri, N., Hayworth, K.J., Schalek, R., Lichtman, J.W., Smith, S.J., and Buchanan, J. (2012). High-contrast en bloc staining of neuronal tissue for field emission scanning electron microscopy. Nat Protoc *7*, 193–206.

Teng, H., Lin, M.Y., and Wilkinson, R.S. (2007). Macroendocytosis and endosome processing in snake motor boutons. J. Physiol. (Lond.) *582*, 243–262.

Torri-Tarelli, F., Grohovaz, F., Fesce, R., and Ceccarelli, B. (1985). Temporal coincidence between synaptic vesicle fusion and quantal secretion of acetylcholine. J. Cell Biol *101*, 1386–1399.

Tsien, R.W., Lipscombe, D., Madison, D.V., Bley, K.R., and Fox, A.P. (1988). Multiple types of neuronal calcium channels and their selective modulation. Trends Neurosci *11*, 431–438.

Voglmaier, S.M., Kam, K., Yang, H., Fortin, D.L., Hua, Z., Nicoll, R.A., and Edwards, R.H. (2006). Distinct endocytic pathways control the rate and extent of synaptic vesicle protein recycling. Neuron *51*, 71–84.

White, J.G., Southgate, E., Thomson, J.N., and Brenner, S. (1976). The structure of the ventral nerve cord of Caenorhabditis elegans. Philos. Trans. R. Soc. Lond., B, Biol. Sci *275*, 327–348.

Wilhelm, B.G., Groemer, T.W., and Rizzoli, S.O. (2010). The same synaptic vesicles drive active and spontaneous release. Nat. Neurosci. *13*, 1454–1456.

Wu, W., and Wu, L.-G. (2007). Rapid bulk endocytosis and its kinetics of fission pore closure at a central synapse. Proc. Natl. Acad. Sci. U.S.A. *104*, 10234–10239.

Wu, X.-S., and Wu, L.-G. (2009). Rapid endocytosis does not recycle vesicles within the readily releasable pool. J. Neurosci. *29*, 11038–11042.

Zenisek, D., Steyer, J.A., and Almers, W. (2000). Transport, capture and exocytosis of single synaptic vesicles at active zones. Nature *406*, 849–854.

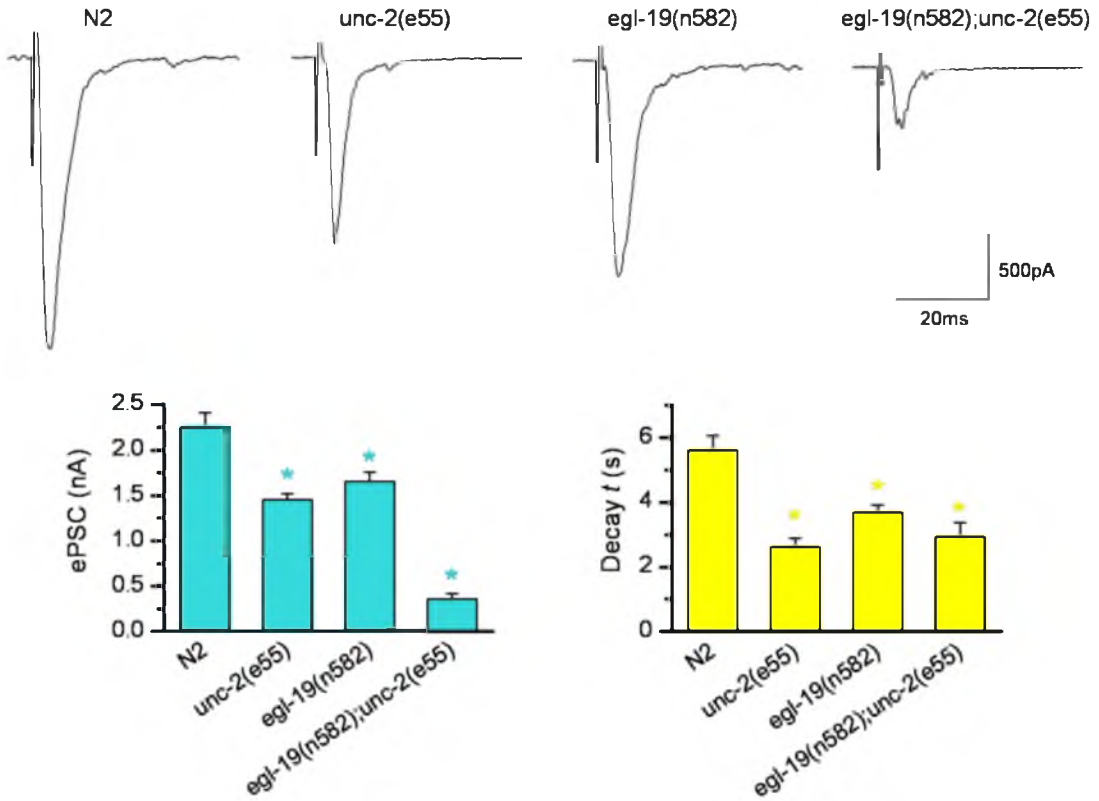

Fig. 10.1. Excitatory postsynaptic current measurement from nematodes lacking functional calcium channels. (top) Sample EPSC traces (bottom) Quantification of the evoked amplitude (left) and the kinetics of decay. Note that the ePSC is significantly reduced in N-type (*unc-2*) and L-type (*egl-19*) calcium channel mutants. ePSC is almost abolished in the double mutants (*egl-19;unc-2*).

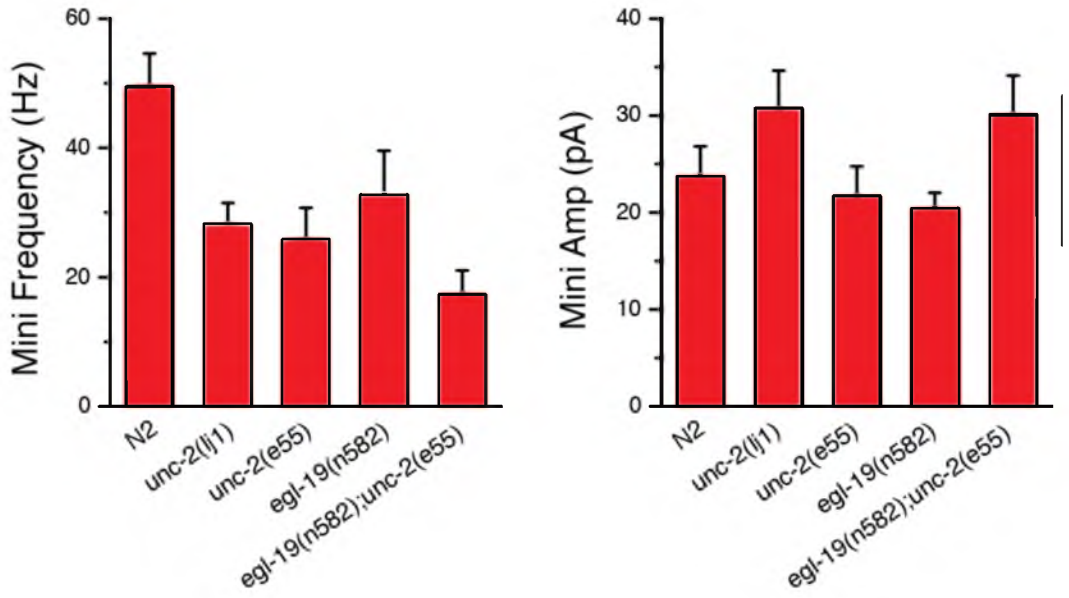

Fig. 10.2. mEPSC measurement from nematodes lacking functional calcium channels. (left) mini frequency (right) mini amplitude. The frequency of mEPSC is reduced to ~50% in both N-type and L-type mutants.

Fig. 10.3. Different types of calcium channels are required in the specific regions of an active zone. Each graph shows distance of docked vesicles along the plasma membrane relative to the dense projection in acetylcholine neurons before and after stimulation in different genetic background. The first column along the x-axis labeled as 0 nm in this figure shows the number of docked vesicles that are touching the dense projection, and each column thereafter is binned by 33 nm. In wild type, vesicle fusion occurs from a broad region in the active zone. N-type calcium channel mutant (*unc-2*) shows a defect in vesicle fusion in the proximity of a dense projection whereas L-type calcium channel mutant (*egl-19*) shows a defect in vesicle fusion from distal regions of an active zone.

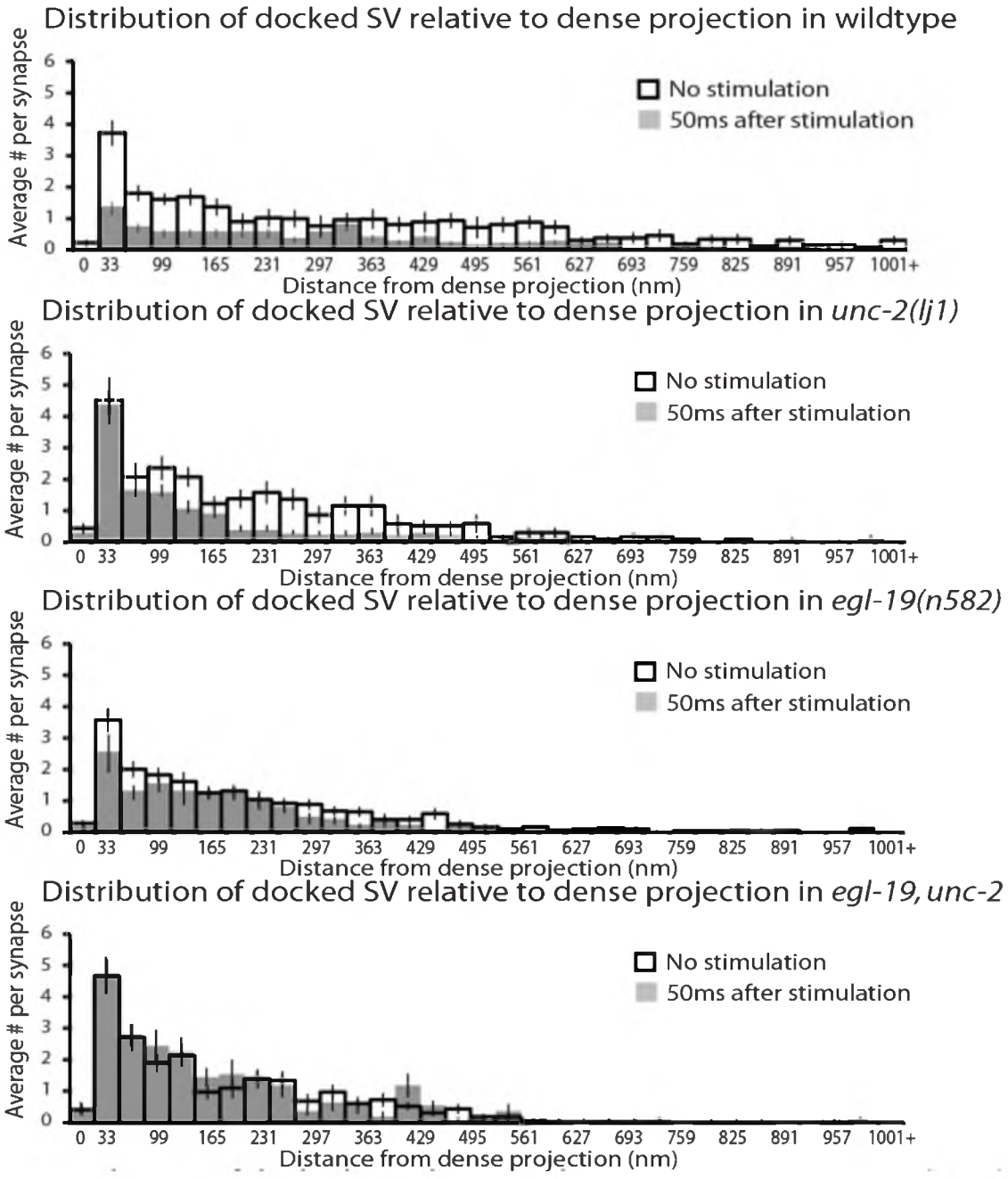
Distribution of docked SV relative to dense projection in wildtype
Average # per synapse
No stimulation
50ms after stimulation
0 33 99 165 231 297 363 429 495 561 627 693 759 825 891 957 1001+
Distance from dense projection (nm)
Distribution of docked SV relative to dense projection in unc-2(lj1)
Average # per synapse
No stimulation
50ms after stimulation
0 33 99 165 231 297 363 429 495 561 627 693 759 825 891 957 1001+
Distance from dense projection (nm)
Distribution of docked SV relative to dense projection in egl-19(n582)
Average # per synapse
No stimulation
50ms after stimulation
0 33 99 165 231 297 363 429 495 561 627 693 759 825 891 957 1001+
Distance from dense projection (nm)
Distribution of docked SV relative to dense projection in egl-19, unc-2
Average # per synapse
No stimulation
50ms after stimulation
0 33 99 165 231 297 363 429 495 561 627 693 759 825 891 957 1001+
Distance from dense projection (nm)

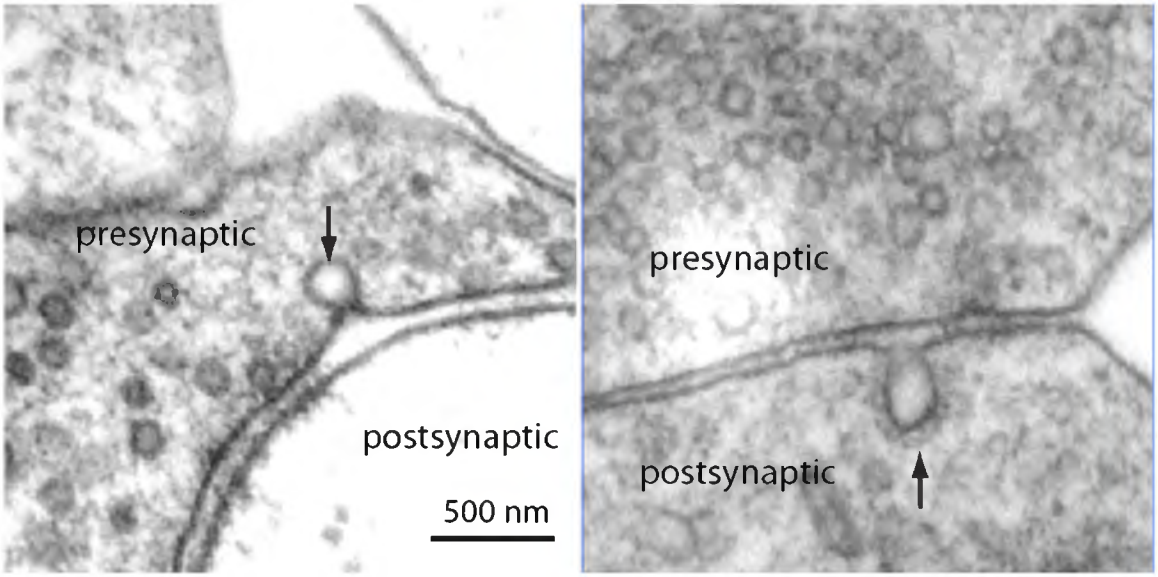

Fig. 10.4. Invaginations in the mouse hippocampal neurons 100 ms after stimulation. The endocytic invagination in presynaptic cells (left) is not coated whereas that in postsynaptic cells is coated (right).

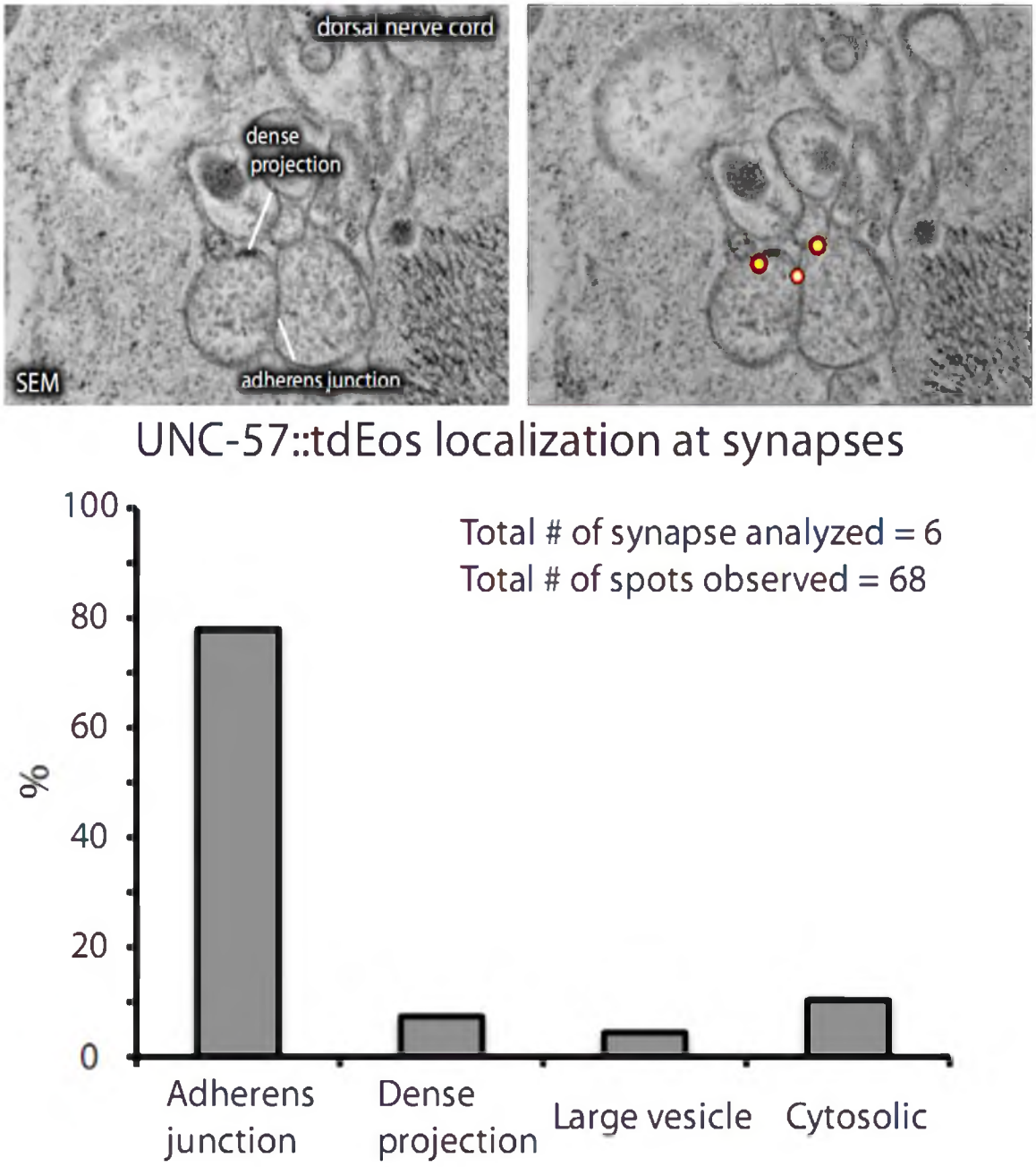

Fig. 10.5. Endophilin localization using nano-fEM. (top) Example micrographs showing the localization of endophilin to a dense projection and adherens junctions. (bottom) Quantification of endophilin localization. Most of the signals are localized to adherens junctions. Endophilin is found in every dense projection analyzed.

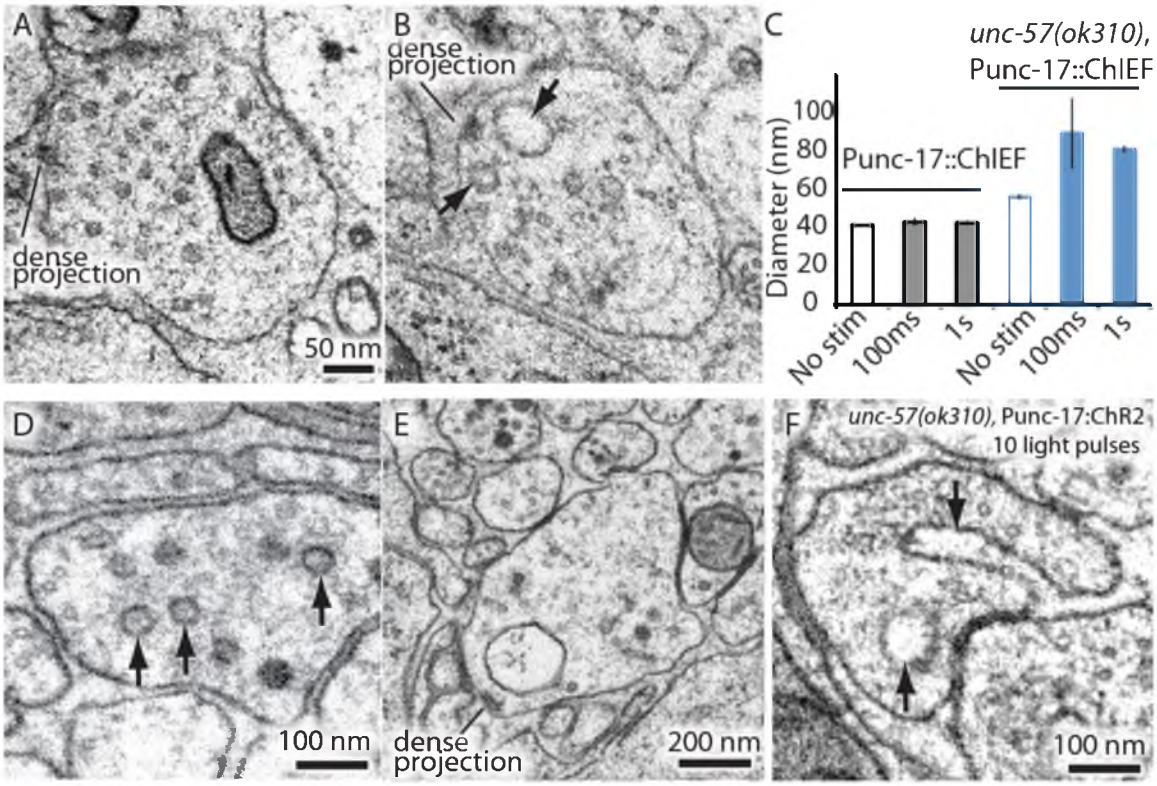

Fig. 10.6. Endocytic structures are larger in endophilin mutants (*unc-57*). Representative electron micrographs showing an acetylcholine synapse of the mutant before (A) and after a single stimulus (B). Endocytic intermediates are captured near the dense projection. (C) A graph showing the diameter of large vesicles. The diameter is twice as large in the endophilin mutants after the stimulation. Representative electron micrographs of wild type (D) and endophilin mutant (E, F) expressing ChIEF following 10 light pulses. Multiple endocytic structures with a diameter of 40-45 nm were observed in wild type synapses (D) whereas a single enlarged structure was observed near a dense projection in endophilin mutant (E). Additionally, an abnormal invagination was captured next to the adherens junctions in the endophilin mutants (F), suggesting that endophilin may function to shape the endocytic membrane.

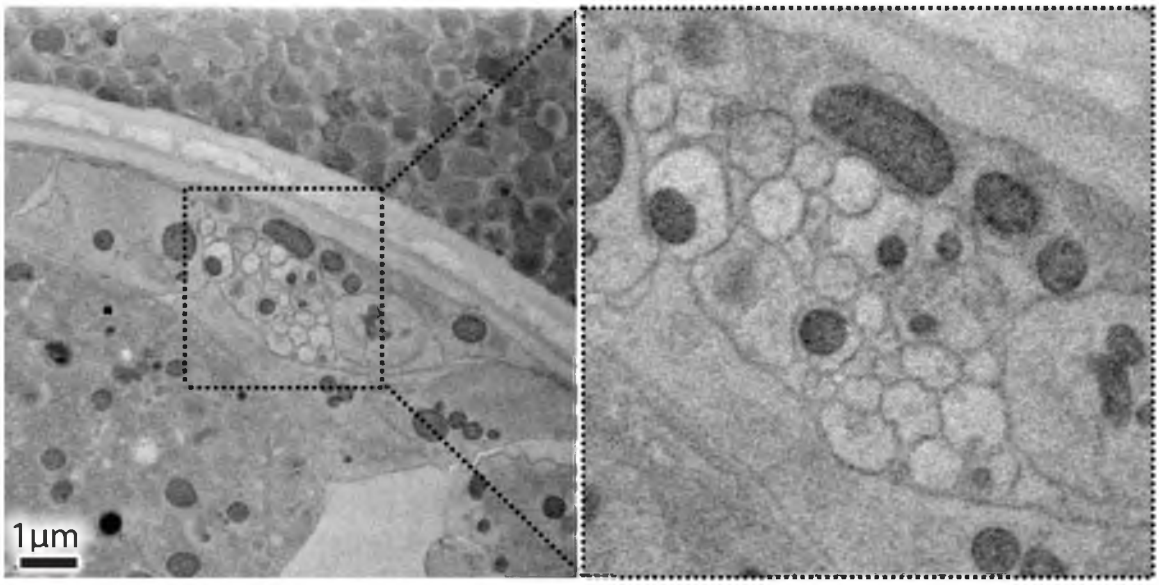

Fig. 10.7. Membrane contrast in an image acquired from the serial-block face SEM is not sufficient for automated reconstruction. Representative electron micrograph from *C. elegans* ventral nerve cord imaged using serial-block face SEM. Note that the membrane is fuzzy when zoomed in.

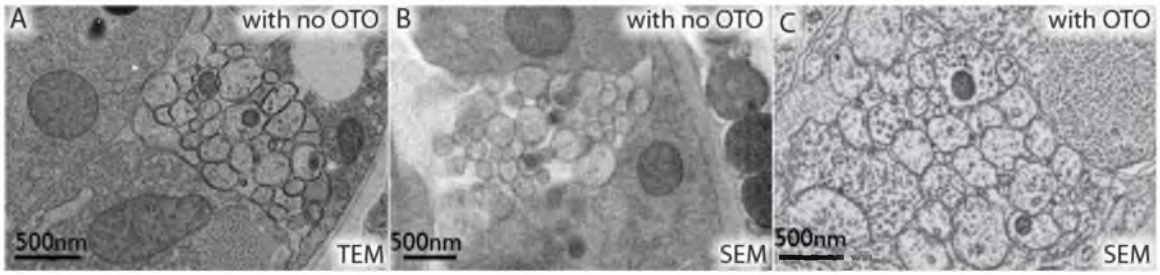

Fig. 10.8. Membrane contrast is enhanced by the OTO staining technique. Representative images from *C. elegans* ventral nerve cord acquired in TEM (A) and SEM (B, C). Note that animals in (A) and (B) were not stained using the OTO bridging.